Probabilistic Structural Integrity Assessment Based on Direct Methods

A thesis in fulfilment of the requirements for the degree of Doctor of Philosophy

By

Xiaoxiao Wang

Department of Mechanical and Aerospace Engineering
University of Strathclyde
Glasgow
UK

2023

Declaration of Authenticity and Author's Rights

This thesis is the result of the author's original research. It has been composed by the author and has not been previously submitted for the examination which has led to the award of a degree.

Xiaoxiao Wang

March 28, 2023

Acknowledgements

Firstly, I would like to thank my supervisor, Dr Haofeng Chen, for the help during my PhD study, which made me finish this research with high quality.

I would also thank all the team members in Structure Integrity and Lifetime Assessment research group and colleagues in the Mechanical and Aerospace Engineering Department. And I will always remember the time we worked together.

Finally, I would like to express my special gratitude to my family for their continuous support and encouragement all the time.

Abstract

Structural integrity assessment is an effective way to measure the safety of critical infrastructures under the complicated combination of high-temperature and varying load conditions. However, under the urgent need for carbon peaking and carbon neutrality, the current industry has to pursue extreme operating parameters and precise design solutions, which inevitably involve a multiplicity of uncertainties in design considerations. Unfortunately, the majority of basic evaluation procedures are dependent on deterministic analysis approaches, with expert experience based-safety factors accounting for the randomness. Due to the lack of statistical characterization of key parameters for failure analysis, this scheme tends to cause conservativeness and offset the benefits gained from the development of advanced computational methods. Therefore, it is crucial to develop a plausible probabilistic structural integrity assessment framework in terms of computational efficiency and accuracy.

This thesis reviews the latest research progress on the structural integrity assessment for high-temperature structures and delivers a new insight into the probabilistic structural integrity assessment framework based on the direct method and artificial intelligence technology. Firstly, by systematically comparing three different creep rupture analysis methods, a quasi-efficient deterministic analysis method for high-temperature structure is identified for the subsequent probabilistic structural integrity assessment framework. Secondly, the cyclic plastic response of the cracked specimen is investigated by Linear Matching Method (LMM) considering the crack constraint effect on the alternating plasticity and ratchet limit, where the capability of the selected numerical method to deal with the structures in the presence of the defect is demonstrated in detail. Thirdly, aiming at predicting the structural failure probability of violating shakedown condition, the probabilistic shakedown analysis under the Linear Matching Method (pLMM) framework is proposed based on the LMM shakedown procedure and First Order Reliability Method (FORM). Furthermore, taking advantage of the Artificial Neural Network (ANN) technique, the probabilistic Low Cycle Fatigue (LCF), ratcheting and creep-fatigue analyses are also established, with the physics-based surrogate model constructed and trained by LMM-driven dataset. The key design parameters that influence the structural ratcheting limit, LCF life and creep-fatigue life are revealed and discussed in depth, and the probabilistic assessment curves for engineering components are built in terms of ratcheting, LCF and creep-fatigue failure modes, with the reliability-based safety factors calibrated considering multi-reliability requirements. This study is dedicated to the

probabilistic structural integrity assessment strategies covering extensive failure mechanisms and conducive to achieving better reliability-centred risk management for critical infrastructures.

Publications

Journal papers:

1. ***Wang X***, Chen H, Xuan F. Direct method-based probabilistic shakedown analysis for the structure under multiple uncertain design conditions[J]. Ocean Engineering, 2023, 280: 114653.

2. ***Wang X***, Yang J, Chen H, et al. Physics-based probabilistic assessment of creep-fatigue failure for pressurized components[J]. International Journal of Mechanical Sciences, 2023, 250: 108314.

3. ***Wang X***, Chen H, Xuan F. Physics-based neural network for probabilistic low cycle fatigue and ratcheting assessments of pressurized elbow pipe component[J]. International Journal of Fatigue, 2023, 172: 107598.

4. ***Wang X,*** Yang J, Chen H, et al. Effect of constraint on cyclic plastic behaviours of cracked bodies and the establishment of unified constraint correlation[J]. European Journal of Mechanics-A/Solids, 2023, 97: 104857.

5. ***Wang X,*** Ma Z, Chen H, et al. Creep rupture limit analysis for engineering structures under high-temperature conditions[J]. International Journal of Pressure Vessels and Piping, 2022, 199: 104763.

6. Ma Z, ***Wang X,*** Chen H, et al. A unified direct method for ratchet and fatigue analysis of structures subjected to arbitrary cyclic thermal-mechanical load histories[J]. International Journal of Mechanical Sciences, 2021, 194: 106190.

Conference papers:

7. ***Wang X***, Ma Z, Chen H, et al. Direct Method-Based Probabilistic Structural Integrity Assessment for High-Temperature Components Considering Uncertain Load Conditions[C]. Pressure Vessels and Piping Conference. American Society of Mechanical Engineers, 2022, 86144: V001T01A053.

Book chapters:

8. ***Wang X***, Chen H. An Introduction to the Probabilistic Linear Matching Method Framework for Structural Integrity Assessment under Uncertain Design Conditions, Direct Methods for Limit State of Materials and Structures: Advanced Computational Algorithms and Material Modelling, Lecture Notes in Applied and Computational Mechanics. May 2023, ISBN: 978-3-031-29121-0.

Contents

List of Figures

List of tables

Nomenclature

$\tilde{F}$	Approximation function
Γ	global trend function
δ	additional identification of a stochastic process
A_i	creep date of strain rate parameter
B_i	creep date of Omega parameter
ε_{total}	total strain
$\varepsilon_{elastic}$	elastic strain
$\varepsilon_{plastic}$	plastic strain
ε_{creep}	creep strain
$\Delta\varepsilon_{ij}^{c}$	compatible strain increment over a cycle
$\Delta\varepsilon_{ij}^{new'}$	deviatoric component of new compatible strain increment
$\dot{\varepsilon}$	creep strain rate
$\dot{\varepsilon}_{oc}$	initial creep strain rate at the start of the time period being evaluated based on the stress state and temperature
$\dot{\varepsilon}_{ij}^{c}$	kinematically admissible strain rate
$\bar{\dot{\varepsilon}}$	effective strain rate
$\dot{\varepsilon}_{ij}^{new'}$	deviatoric component of new strain rate history in the next cycle
$\dot{\varepsilon}_{kk}^{new}$	hydrostatic component of the new strain rate history in the next cycle
$\bar{\dot{\varepsilon}}^{i}$	effective strain rate
σ_e	equivalent effective stress
$\hat{\sigma}_{ij}$	linear elastic stress field solution

σ_{ij}^{c}	stress yield at yield associated with $\dot{\varepsilon}_{ij}^{c}$
$\sigma_{ij}^{\prime in}$	deviatoric component of initial stress condition
$\hat{\sigma}_{ij}^{\prime}$	deviatoric component of linear elastic solution
σ_y	revised yield stress
σ_r	creep rupture stress
σ_s	material's yield stress
p	hydrostatic pressure stress
$\bar{\rho}_{ij}^{new}$	constant residual stress field
$\bar{\rho}^{\prime f}_{ij}$	deviatoric component of constant residual stress field
t_r	creep rupture time, hours
t_{rA}	creep failure time for verification, hours
t_{rB}	creep failure time for verification, hours
Δt	period during the load cycle
m	Norton's exponent to describe the rate increase because of the cross-section reduction effect
p	microstructural damage
c	deficiencies in Norton's exponent and other microstructural factors related to the stress change
λ	load parameter
λ_{UB_LIMIT}	upper bound load parameter
μ	matching condition parameter
$\bar{\mu}$	average of matching condition parameter over a cycle
μ_n	matching condition parameter during a cycle

D_c	creep damage variable
$\dot{D}_C$	creep damage rate
T	temperature
E	Young's modulus
ν	Poisson's ratio
Ω	Omega parameters used in Omega creep model
A_{PEEQ}	area surrounded by equivalent alternative plastic strain isoline
A_p	unified parameter for quantifying both in-plane and out-of-plane constraints
A_{ref}	area surrounded by equivalent alternative plastic strain isoline in a standard test
F	cyclic time-dependent surface load
$\bar{F}$	constant component of surface load
I	strain energy function
P	Load condition
R^2	correlation coefficient
S_T	surface subjected to surface load
S_u	surface subjected to displacement constraint
V	body volume
W	width parameter of CT and CCT specimens
M_{max}	peak value of the bending moment within the load cycle
a	initial crack length
$\hat{\sigma}_{ij}^{\bar{F}}$	constant elastic stresses
$\hat{\sigma}_{ij}^{\Delta}$	time-dependent elastic stresses
σ_{ij}	stress solution of the general cyclic load condition

σ_{ij}^{c}	stress at yield state to derive the Minimum Theorem
σ_{ij}^{*}	stress state under yield condition
σ_0	subsequent yield strength in DSCA iteration
$\bar{\rho}_{ij}$	constant residual stress
ρ_{ij}^{r}	time-dependent residual stress
ρ_{kk}^{nf}	hydrostatic component of residual stress under equilibrium condition
$\Delta\rho_{ij}^{nf'}$	deviatoric component of residual stress under equilibrium conditon
$\dot{\varepsilon}_{ij}^{p}$	plastic strain rate
$\dot{\varepsilon}_{ij}^{c}$	kinematically admissible strain rate
$\dot{\varepsilon}_{ij}^{s}$	exact stress solution
$\varepsilon_{ratcheting}$	equivalent ratcheting strain
ε^{pl}	plastic strain tensor
$\Delta\varepsilon_{ij}^{n}$	increment of plastic strain in terms of time t_n
$\Delta\varepsilon_{ij}^{ni}$	initial estimation of $\Delta\varepsilon_{ij}^{n}$
$\Delta\varepsilon_{ij}^{Tf'}$	deviatoric component of compatible strain increment
$\Delta\varepsilon_{ij}^{nf'}$	deviatoric component of plastic strain increment
$\Delta\varepsilon_{kk}^{Tf}$	hydrostatic component of compatible strain increment
f	yield condition function
$\dot{\alpha}$	a plastic multiplier
$\bar{\mu}_{ni}$	shear modulus
$\Delta\varepsilon_{ij}$	compatible strain increment
σ_{ij}^{in}	weighted average stress combination

$\boldsymbol{J}$	Jacobian matrix
P_1	horizontal tensile load
$P_{1i,j}$	horizontal tensile loads applied in benchmark
P_2	vertical tensile load
$P_{2i,j}$	vertical tensile loads applied in benchmark
ΔP	uncertain fluctuation of tensile load P
ΔP_1	uncertain fluctuation of tensile load P_1
P_f	failure probability
R	structural resistance
S	structural loading conditions
$\boldsymbol{X}$	n-dimensional vector including all the random variables
$\boldsymbol{Y}$	n-dimensional vector including independent standard normal variables
Φ	standard normal cumulative distribution function
f_R	probability density function of resistance
f_S	probability density function of loading conditions
G	state function
g	state function in standard normal space
g_T	linear approximation of state function
∇	gradient information
β	reliability index
n_f	total number of failed cases due to non-shakedown
I_f	indicator function of failed cases due to non-shakedown

$\Delta\varepsilon$	total strain range for LCF life calculation
t_n	nominal wall thickness
λ_{LCF}	multiplier of low cycle fatigue life
$\lambda_{ratcheting}$	ratchet limit multiplier
$\boldsymbol{C}$	covariance matrix
$\boldsymbol{\mu}$	centre of known data
ΔT	temperature difference within the whole body
α_i	weight of input parameter
ϕ_i	basis function
β_k	weight of intermediate parameter
$\boldsymbol{H}$	expansion of coefficients matrix
$\boldsymbol{G}$	coefficients matrix of linear equations system
$\boldsymbol{\alpha}$	weights matrix of the neural network
α_m	average coefficient of thermal expansion
$\bar{E}$	multi-axial Young's modulus
k	thermal conductivity
L_f	low cycle fatigue life
L_{design}	low cycle fatigue e life that meets design needs
N_{LCF}	predicted LCF life
N_{LDNN}	number of training points used in training process of LDNN
N_{RSM}	number of training points used in training of RSM
N_{MCS}	number of elastoplastic simulations during MCS

N_{P_1}	acceptable LCF life of high reliability under loading path 1
N_{P_2}	acceptable LCF life of high reliability under loading path 2
u	displacement
λ_θ	load factor of time-dependent thermal conditions
λ_p	load factor of time-dependent mechanical conditions
$\hat{\sigma}_{ij}^{\theta}$	elastic stress induced by thermal conditions
$\hat{\sigma}_{ij}^{p}$	elastic stress induced by surface loads
θ	thermal conditions
ρ_{ij}	time-dependent residual stress
$\Delta\sigma_{ij}^{in}$	input stress field
$\Delta\hat{\sigma}_{ij}$	solution of elastic stress
$\Delta\rho_{ij}$	increment of cyclic residual stress
$\boldsymbol{K}$	stiffness matrix
$\boldsymbol{B}$	strain-displacement matrix
$\Delta\boldsymbol{u}$	increment of displacement
$\bar{\mu}_m$	shear modulus
$\Delta\bar{\varepsilon}_c$	creep strain increment
A	creep parameter
n^*	creep parameter
m^*	creep parameter
$\dot{\bar{\varepsilon}}_c$	creep strain rate
σ_{sij}	creep stress at the start of the dwell period
$\bar{\sigma}_c$	creep flow stress

$\Delta\rho_{cij}$	creep effect-induced residual stress
$\bar{\dot{\varepsilon}}^F$	creep strain rate at the end of dwell
σ_0^m	either plastic yield stress or creep flow stress
$\bar{\sigma}$	mean stress during creep dwell period
$\dot{\omega}_{cr}$	creep damage rate
$\dot{\omega}_f$	fatigue damage rate
$\Delta\varepsilon_{total}$	total cyclic strain range
N_f	fatigue life absent of creep effect
D	prediction function of creep-fatigue damage
L	prediction function of creep-fatigue life
β_i	weight of input parameter
φ_i	basis functions of EBF
α_{N+1}	bias term
β_{N+1}	bias term
$\boldsymbol{S}$	covariance matrix
$\boldsymbol{H}$	matrix containing Mahalanobis distance
$\boldsymbol{Q}$	matrix of the linear equations system
$\boldsymbol{\alpha}$	weights matrix
$\boldsymbol{y}$	matrix containing given dataset
$R_{p0.2}$	0.2% proof stress of the cyclic steady-state stress-strain curves
t_{n1}	nominal thickness of main vessel
t_{n2}	nominal thickness of lower head
h_n	nominal height of air chamber

ρ	density
C_p	specific heat
h_1	convection coefficient at inner surface
h_2	convection coefficient at outer surface
ε	emissivity
N_m	lifetime calculated by the mean values of design parameters
n_{G1}	reliability-based safety factor of Grade 1
N_{G1}	lower bound life of Grade 1
n_{G2}	reliability-based safety factor of Grade 2
N_{G2}	lower bound life of Grade 2

Acronyms

CDM	Continuum Damage Mechanics
EPP	Elastic-Perfectly Plastic
FEA	Finite Element Analysis
ISS	Isochronous Stress-Strain
LMM	Linear Matching Method
LRFD	Load and Resistance Factor Design
MPC	Material Properties Council
SDV	Solution Dependent State Variables
XFEM	Extended Finite Element Method
3D	Three-Dimensional
BCs	Boundary Conditions
CT	Compact Tension
CCT	Central-Cracked Tension
DSCA	Direct Steady Cyclic Analysis
LCF	Low Cycle Fatigue
PEMAG	Plastic Strain Magnitude
CDF	Cumulative Distribution Function
CV	Coefficient of Variation
DOE	Design of Experiments
FORM	First-Order Reliability Methods
MCS	Monte Carlo Simulation

PDF	Probability Density Function
PEEQ	Equivalent Plastic Strain
pLMM	probability Linear Matching Method
SLSIF	Shakedown Limit State Indicator Function
RSM	Response Surface Method
SORM	Second-Order Reliability Methods
A-V	Ahmadzadeh-Varvani
CJK	Chen-Jiao-Kim
EBF	Elliptical Basis Function
MLP	Multi-Layer Perceptron
LDNN	Linear Matching Method-driven Neural Network
LHS	Latin Hypercube Sampling
P-S-N	Probabilistic S-N curve
RO	Ramberg-Osgood
ULSI	Unified Limit State Indicator
3T-RDM	Three-Term Reference Damage Model
AMWD	Applied Mechanical Work Density Function
ANN	Artificial Neural Network
eDSCA	extended Direct Steady Cyclic Analysis
EDDNN	eDSCA-driven neural network
ML	Machine Learning
MLP	Multi-Layer Perceptron
RBSF	Reliability-Based Safety Factor

DE	Ductility Exhaustion Model
SMDE	Stress Modified Ductility Exhaustion Model
SEDE	Strain Energy Density Exhaustion Model
TF	Time Fraction Model

1 Introduction

1.1 Research background

Environmental issues are closely related to the energy industry, which have become the main challenge of current social development. To better cope with environmental protection, the urgent need for emission peak and carbon neutrality all over the world makes the future industry has to pursue extreme operating parameters and precise design solutions. For instance, Fig. 1.1 shows the high-pressure heat exchanger working in the coal chemical industry with 20 MPa and 525 ºC. And to solve the current energy crisis, more nuclear power plants that are about to reach their initial service life face the demand for equipment life extension [1] after a long period of running. All of these technical requirements, inevitably, involve a multiplicity of uncertainties in design and operation conditions of critical engineering infrastructures, such as load condition fluctuation, manufacturing tolerance and material property degeneration, etc.

Fig. 1.1. Heat exchanger under high pressure and elevated temperature conditions in energy industry

The uncertain conditions tend to unavoidably affect structural resistance and lifespan and result in unpredictable structural responses. For instance, on 11 March 2011, the accident at Fukushima Dai-ichi Nuclear Power Plant was damaged by the earthquake and tsunami [2], which posed a serious security threat to the local area. Hence, it is impossible to be measured with a deterministic evaluation, which further changes the safety assessment of structures to a risk management problem. According to current high-temperature assessment procedures, including the ASME Boiler and Pressure Vessel Code (NH) [3], API 579 Fitness-For-Service Code [4], R5 procedure [5] and RCC-MR Code [6], the underlying approach to consider the uncertain effect of

the design parameters is to directly adopt the bounding values of the input parameters and set a safety factor [7] for the deterministic analysis results regarding a certain failure mode. Pessimistically, the potential redundancy created in this process often leads to the over-conservative scheme, due to the expert experience-based security coefficients, with limited statistical information on the key structural response reflected.

Nowadays, the design and assessment of high-temperature engineering concentrate on reliability, durability and robustness, and the reliability-centred maintenance method is well established in the nuclear and aerospace industry with the continuous pursuit of maximizing efficiency and performance. The development of Stochastic Finite Element Analysis (SFEA) technology [8] makes it possible to numerically calculate the reliability of complicated engineering structures. Recently, R5 Volume 2/3 Appendix 15 [9] provides an additional technical guideline of the probabilistic creep-fatigue assessment to tackle the uncertain design factors, working as the extension of the deterministic analysis procedure in terms of high-temperature components.

Generally, a feasible methodology of probabilistic structural integrity assessment mainly embraces two core sections: the efficient procedure for failure analysis and the probabilistic analysis framework. At the physical level, various advanced material constitutive relationships and damage models were proposed to describe the high-temperature material behaviours during the detailed non-linear Finite Element Analysis. However, this step-by-step analysis is unable to avoid relying on a large number of nonlinear iterative processes and related poor control of convergence. Alternatively, the direct methods have been developed over many years and are now accepted as the suitable substitution for the conventional non-linear FEA to alleviate the unaffordable computational cost and further improve analysis efficiency. On the other hand, data-driven surrogate model technology paves the way for the reliability analysis of the large-scale numerical model with direct Monte Carlo Simulation (MCS). And assisted by Machine Learning (ML) and Artificial Intelligence (AI), the versatility and applicability of reliability analysis are broadened to address more comprehensive engineering failure patterns.

1.2 Objectives of this thesis

The purpose of this study is to propose a comprehensive probabilistic structural integrity assessment framework in terms of efficiency and accuracy, where several key failure modes related to high-temperature circumstances are to be tackled. To reflect the physics-based failure mechanisms, the developed direct method, Linear Matching Method (LMM) framework, is utilized,

and further extended to form the probabilistic Linear Matching Method (pLMM) framework. And the Artificial Intelligence (AI) technology and the data-driven surrogate model are also adopted to improve the applicability of the proposed probabilistic structural integrity assessment framework. The reliability-based evaluation scheme is dedicated to meeting precise design, getting rid of the over-conservativeness from conventional safety factors.

To accomplish the research goal, three main objectives and corresponding research methods are given as follows:

1. To satisfy the design requirement for extreme working conditions, the direct method-based creep rupture analysis and the structural integrity assessment for the cracked body are demonstrated.

2. The semi-analytical solution for the reliability analysis of the shakedown condition is delivered by combining the LMM shakedown procedure and First Order Reliability Method (FORM).

3. The physics-based surrogate models of structural cyclic plasticity and creep-fatigue responses are established with the Artificial Neural Network (ANN) technology, by which the reliability-based evaluation diagrams are built for different failure risks.

1.3 Methodology

The technical roadmap of this study is presented in Fig. 1.2, and the main methodologies adopted in this thesis are summarized below:

1. The structural integrity assessments are performed by the LMM framework with extreme design conditions involved.

2. Regarding the reliability analysis of the shakedown condition, First Order Reliability Method (FORM) is utilized to derive the failure probability.

3. The elliptical basis function (EBF) neural network is applied to build the surrogate models of structural cyclic plasticity and creep-fatigue responses, with Monte Carlo Simulation (MCS) utilized to calculate the statistical distribution of key response and failure probability.

4. The validations are based on the ABAQUS step-by-step analysis with pertaining material constitutive functions.

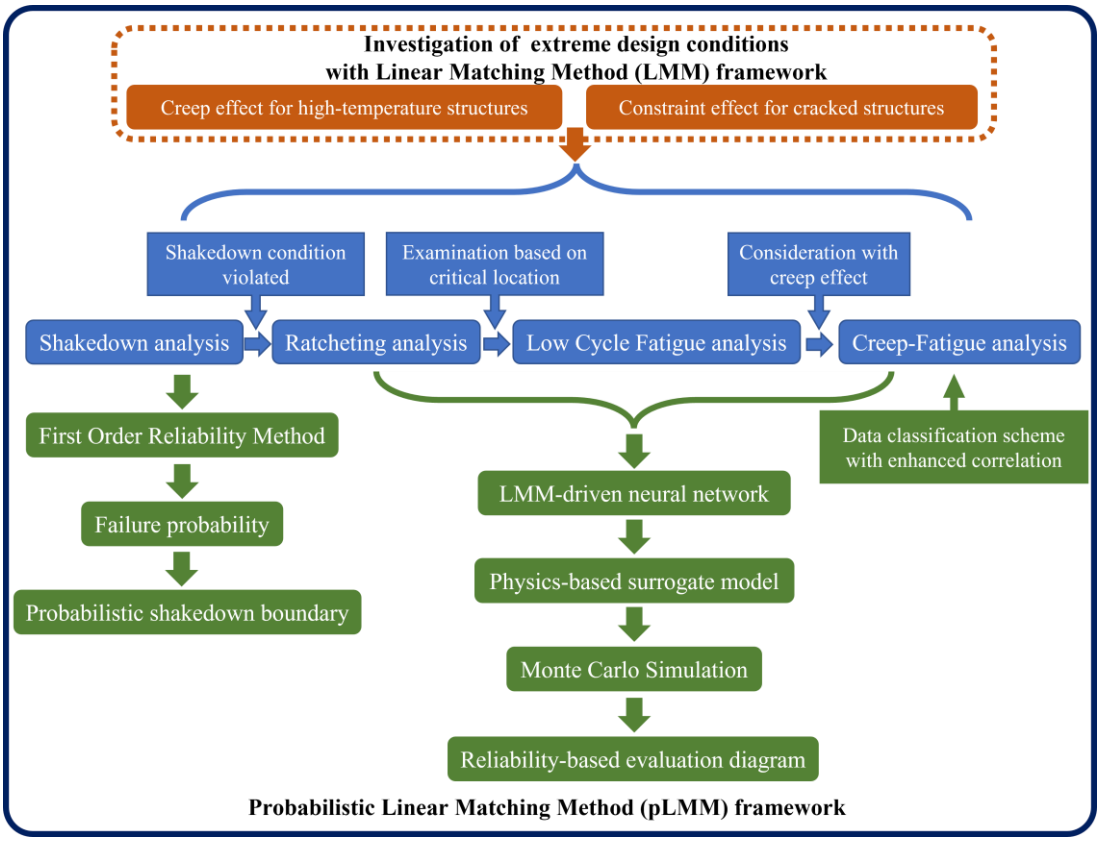

Fig. 1.2. Technical roadmap and the key methodologies of this study

1.4 Outline of the thesis

The main chapters of this thesis are outlined below:

Chapter 2 presents the general background of the structural integrity assessment for high-temperature structures. And the related reliability analysis strategies are summarized.

Chapter 3 delivers a comparative investigation of the main creep rupture assessment techniques, including the isochronous stress-strain (ISS) curve-based creep rupture limit analysis, the Omega creep damage model-based creep analysis and the direct method-based creep rupture assessment by LMM. New virtual creep test curves are generated from the Omega creep model to produce the unified material creep data. To establish a reasonable strategy for evaluating high-temperature structures, the balance between computational efficiency and accuracy is comprehensively analyzed.

Chapter 4 focuses on the constraint effect existing in the cracked structures with LMM Direct Steady Cycle Analysis (DSCA) and ratcheting analysis procedures. And the unified constraint parameter $\sqrt{A_p}$ is well applied to measure the strength of the compound constraint effect under cyclic loads on structural cyclic plastic responses (including ratchet limit and alternating plastic strain range).

Chapter 5 proposes a novel direct method-based probabilistic shakedown analysis under the new probabilistic Linear Matching Method (pLMM) framework. The risk of losing the shakedown state is predicted by the physics-based estimation model, where the efficient iteration is employed to derive the reliability index. And in the benchmark, the probabilistic shakedown boundary is constructed, with the additional influence of the uncertain cyclic loading pattern on the reliability fully reflected.

Chapter 6 deals with the risk evaluation of important pipelines with cyclic plasticity. Under the pLMM framework, quantitative prediction of the statistical distribution of LCF life and ratchet limit by the surrogate model is given out with the novel Linear Matching Method-driven neural network (LDNN). With the numerical investigations on the elbow pipe, the probabilistic assessment boundaries and reliability-based evaluation diagrams in terms of LCF life and ratchet limit are established respectively.

Chapter 7 develops the physics-based probabilistic assessment for creep-fatigue failure under the pLMM framework. To express the relationship between design parameters and structural responses implicitly, the extended Direct Stable Cycle Analysis-driven neural network (EDDNN) is built with superior fitting quality. The reliability-based evaluation diagram is established for high-temperature components, and a novel data classification scheme is proposed to address the randomness in creep damage-dominated assessment.

Chapter 8 provides the main conclusions of the research work of this thesis and the recommendations for future work.

2 Failure analysis and probabilistic structural integrity assessments for high-temperature structures

2.1 Introduction

Generally, under cyclic load conditions, the high-temperature structures are mainly susceptible to cyclic plasticity and the creep effect. To maintain structural integrity according, it is indispensable for the industry to implement engineering failure analysis experimentally or numerically against certain failure modes to classic design standards. During this process, not only accurate material constitutive relationships and damage models but also efficient calculation methods are widely used. As extreme operating environments are required to satisfy the high-efficiency running in the energy industry, the uncertainty among all the conditions is involved in the current structural safety assessment as well. Facing such a challenge, the experience-based safety factor with the deterministic analysis seems arbitrary and conservative, providing limited statistical information on failure behaviours. Therefore, a multiplicity of reliability analysis technologies begins to draw widespread attention from industry and academia, and reliability-centred designs are being developed for the risk management of critical infrastructures in sophisticated engineering. In this chapter, the structural cyclic response, high-temperature evaluation, direct method for structural integrity assessment and reliability analysis technology are reviewed comprehensively.

2.2 Cyclic responses of the high-temperature structure

2.2.1 Typical structural responses under cyclic load conditions

The Bree diagram comprehensively describes the interactive states of multiple structural responses under cyclic thermo-mechanical load conditions, as shown in Fig. 2.1, with the horizontal axis and vertical axis representing the normalized constant mechanical load and the normalized cyclic thermal condition, respectively. And generally, there are five significant structural responses produced in terms of different load combinations:

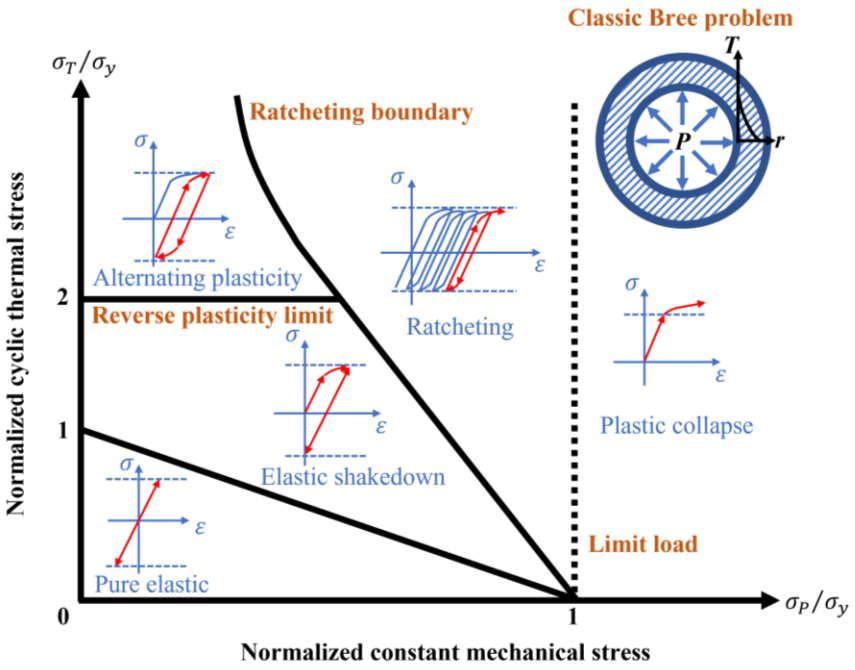

Fig. 2.1. Bree diagram of structural responses under cyclic load conditions

A. Instantaneous plastic collapse

If the mechanical load is large enough to cause global instantaneous plastic collapse, the structure is failed due to reaching the plastic limit load at the initial loading stage, which can be reduced to an extreme case of structures subjected to cyclic load conditions.

B. Pure elastic behaviour

Without the maximum stress among the whole structure satisfying the yield condition, the structural response appears pure elastic behaviour in the subsequent loading and unloading steps.

C. Elastic shakedown

As the load conditions exceed the pure elastic region, the structural response tends to show plastic behaviours within the first limited cycles, while after the adaptive stage, the structure exhibits the elastic response with constant residual stress.

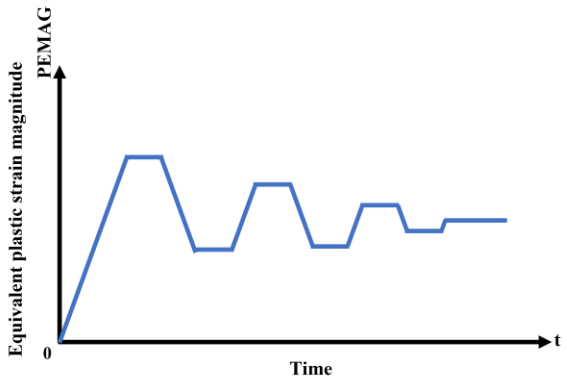

Fig. 2.2. Time-dependent equivalent plastic strain magnitude with elastic shakedown

D. Alternating plasticity

Since the applied cyclic normalized thermal condition is larger than the reverse plasticity limit, the time-dependent stress-strain relationship formulates the saturated hysteresis loop, with no incremental plastic strain during the overall loading history. This alternating plasticity phenomenon is closely related to the Low Cycle Fatigue (LCF) life assessment.

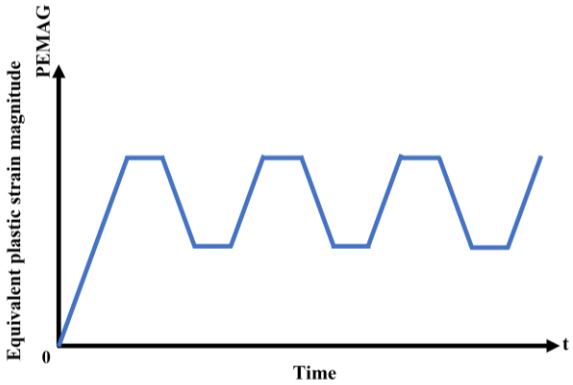

Fig. 2.3. Time-dependent equivalent plastic strain magnitude with alternating plasticity

E. Ratcheting

Structural ratcheting behaviour occurs when the load condition breakout the ratcheting boundary, and, consequently, the accumulative plastic strain raises the incremental collapse. Structural ratcheting should be strictly avoided in the majority of design cases, as facing such a failure mechanism drastically shortens the potential lifetime of the engineering components.

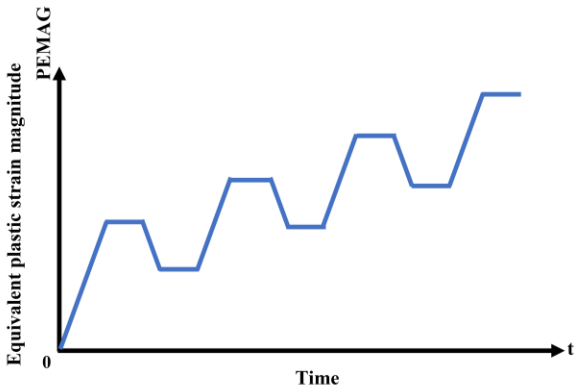

Fig. 2.4. Time-dependent equivalent plastic strain magnitude with ratcheting mechanism

2.2.2 Predictions of creep rupture under monotonic load conditions

Creep rupture is a crucial time-dependent failure mode of high-temperature structures that occurs under monotonic load conditions after the creep behaviour fully develops through the primary and second stages, for which the creep crack initiates and propagates very fast until the final rupture. And to prevent creep rupture failure, various design and assessment procedures against creep rupture behaviour have been developed.

2.2.2.1 Isochronous strain stress (ISS) curve

As a widely used simplified creep rupture calculation, the isochronous strain stress (ISS) curve has been seen as a powerful and concise tool to evaluate the structural creep behaviour, and it has been incorporated into ASME Boiler & Pressure Vessel Code Section III (including the Code Case), offering ISS curves for the majority of materials suitable for high-temperature engineering components (Division 1, Subsection NH) [3]. The origins and background of the ISS curve were described in detail by Douglas L. Marriott [10].

Ideally, the material's ISS curve database comes from a large number of uniaxial creep tests, creating a series of long-term creep strain curves [11], during which the stress and temperature are kept constant for a certain creep period. As explained in Fig. 2.5. By extracting the stress and strain data at the same time point from the creep test curves above, an isochronous stress-strain curve similar to the material's elastoplastic constitutive relationship is constructed. Repeating the same steps and choosing the next time point, the ISS curves over a range of creep times and temperature magnitudes can be acquired sequentially. Through this transformation, the time-dependent creep

process has been described in a time-independent form [12], reflecting the relationship between stress and total strain including elastic strain, creep strain, and plastic strain (defined in Equation (2.1) under a fixed creep time.

By substituting this ISS-based constitutive relationship for inelastic material's property, the structural creep rupture limit is able to be calculated by the general elastoplastic FEA program. And the rupture failure state is determined at the physical instability point of the non-linear iterations, where the creep dwell period is considered implicitly in the material's constitutive relationship [13].

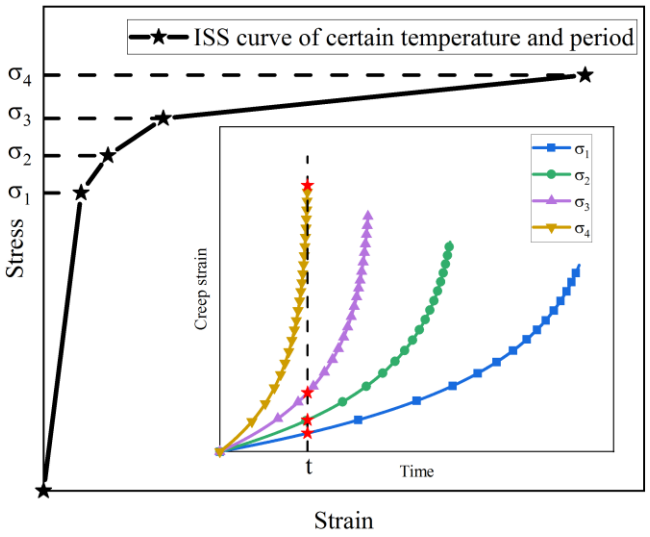

Fig. 2.5. Scheme of the isochronous stress-strain curve

$$\varepsilon_{total} = \varepsilon_{elastic} + \varepsilon_{plastic} + \varepsilon_{creep} \quad (2.1)$$

2.2.2.2 Omega creep damage model

Another plan to implement creep prediction is to make use of the creep laws derived from a large number of creep tests and the fitting of experimental parameters [14]. By means of continuum damage mechanics (CDM) and the creep damage state variables, it is possible to numerically depict all three stages of creep to rupture, especially for the tertiary creep behaviour.

Combined with commercial FEA software, Omega model-based engineering approach [15], has been applied to high-temperature structure design and evaluation of pressure vessels, which may have a risk of creep-induced failure. Both API 579-1/ASME FFS-1 [4] and ASME Boiler and

Pressure Vessel Code Case 2605-3 [16] include the Omega model-based method and provide detailed parameters and numerical procedures for the users.

The omega creep model was developed under the Material Properties Council (MPC) Omega Project, based on a large number of material tests and Kachanov's CDM concept [17]. Unlike the fundamental Norton's law that treats the secondary creep stage as the key factor, the Omega damage model focuses on the tertiary creep phase under the design stress level [18]. By utilizing the exponential form of creep rate and its integral form below,

$$\dot{\varepsilon} = \dot{\varepsilon}_{oc} e^{(m+p+c)\varepsilon} \tag{2.2}$$

$$\frac{1}{\dot{\varepsilon}_{oc}(m+p+c)}\left(1 - e^{-(m+p+c)\varepsilon}\right) = t \tag{2.3}$$

The damage term Ω is defined by Equation (2.4) physically and mathematically, including m, Norton's exponent to describe the rate increase because of the cross-section reduction effect; p, microstructural damage; and c, deficiencies in Norton's exponent and other microstructural factors related to the stress change, and calibrated by using the coefficient of the relative (logarithmic) change in strain rate during a creep test. Therefore, the time to creep rupture, t_r, is able to be estimated below,

$$\frac{1}{\dot{\varepsilon}_{oc}(m+p+c)} = t_r = \frac{1}{\dot{\varepsilon}_{oc}\Omega}$$
$$\Omega = m + p + c \tag{2.4}$$

where the creep damage rate is also determined by $\dot{D}_c = \frac{1}{t_r} = \dot{\varepsilon}_{oc}\Omega$.

As shown in Fig. 2.6, there is a strong connection between the strain rate and the amount of damage, which can be defined by Equation (2.5),

$$\dot{\varepsilon} = \frac{\dot{\varepsilon}_{oc}}{1 - D_c} \tag{2.5}$$

When the creep damage accumulates to nearly 1.0, the creep rupture occurs with the creep strain rate tending to infinity.

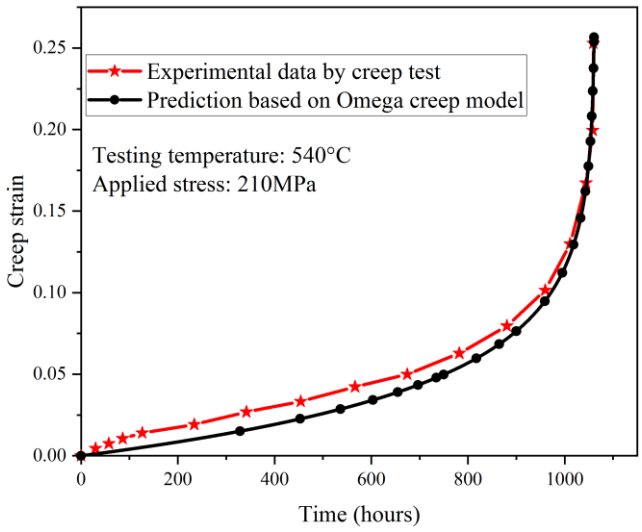

Fig. 2.6. Creep data of 2.25Cr-1Mo-V comparison between experiment and Omega model prediction

The omega model can be integrated to clearly describe the relationship between the creep strain and time. A more practical and effective way to utilise this method is to embed the creep damage model into commercial FEA software such as ANSYS and ABAQUS, making this creep model function as a creep constitutive equation during the calculation of creep strain, damage and creep rupture time. Both ASME Code Case 2605-3 and API 579-1/ASME FFS-1 incorporate the Omega creep model into the assessment options of creep-induced failures, where the creep damage at the critical locations is restricted to below 1.0 in order to prevent the whole structure from the risk of creep rupture. The detailed algorithms and specified material property parameters for programming via the creep user subroutine are illustrated in Appendix A.

2.2.3 Creep-fatigue evaluation

2.2.3.1 Damage models

In nuclear engineering, the core facility operates frequently under the combinations of high-temperature and cyclic load conditions, hence, the creep-fatigue is viewed as one of the underlying failure modes due to the accumulated damage at critical locations [19]. Even though dominated by different damage mechanisms, creep damage and fatigue damage may exist simultaneously when high-temperature structures operate under cyclic load conditions, with the interaction between two types of damages remarkably affecting the lifetime. On the one hand, the cyclic plastic behaviour

elevates the stress level at the start of creep dwell, which is called cyclic-enhanced creep. On the other hand, the creep strain within each cycle enlarges the inelastic strain range when evaluating the cyclic strain range, known as creep-induced plasticity.

Although a number of the non-linear viscoplastic constitutive models [20] have been developed to describe the creep-fatigue interaction under cyclic loads, currently, the guidelines of creep-fatigue evaluation mainly rely on the well-established procedures for structural integrity assessment, including the R5 high-temperature assessment procedure [5], API 579-1/ASME FFS-1 [4], and ASME Boiler & Pressure Vessel Code Section III Subsection NH [3]. A multiplicity of feasible analysis approaches such as the simplified analysis, the inelastic analysis and the creep-fatigue damage envelope are outlined in terms of specified engineering materials. Besides, the ASME Code Case 2605 [16] is dedicated to providing another advanced option to perform the creep-fatigue evaluation for the pressure vessel made from 2.25Cr-1Mo-V steel at an elevated temperature circumstance, with the Omega damage model involved in the creep strain and damage determination. During creep-fatigue damage determination, the fatigue damage is commonly obtained by the linear damage cumulative theory [21], while different kinds of damage models are adopted to measure the creep damage within the dwell period, including the time fraction (TF) model, ductility exhaustion (DE) model, stress modified ductility exhaustion (SMDE) model, strain energy density exhaustion (SEDE) model [22, 23], and the damage models based on the Continuum Damage Mechanics (CDM) [18, 24].

2.2.3.2 Evaluation procedure

Simplified structural analysis [25] or detailed Finite Element Analysis (FEA) [26-28] is indispensable for acquiring the important parameters related to structural cyclic response (e.g., stress, stress relaxation, plastic strain amplitude and creep strain).

After the steady structural responses of high-temperature structures under cyclic load conditions are identified by the numerical simulations, the subsequent evaluation of creep-fatigue damage and life contains four key steps which are illustrated by the flowchart in Fig. 2.7.

Step 1. Construction of the stress relaxation during the dwell period

According to the stress history (including the stress at the start of the dwell and the stress at the end of the creep dwell), the relationship between the changing stress and the time is given out

by using the elastic follow-up factor. Hence, the mean stress during creep dwell is able to be acquired.

Step 2. Determination of creep damage rate per cycle by rupture curve

With the linear damage summation assumption and TF rules, the creep damage rate $\dot{\omega}_{cr}$ is expressed in terms of the ratio of creep dwell time Δt to creep rupture time t_r shown in Equation (2.6), which is obtained by the creep rupture data, with the mean stress $\bar{\sigma}$ during dwell time considered by Equation (2.7).

$$\dot{\omega}_{cr} = \frac{\Delta t}{t_r} = \frac{\Delta t}{t_r(\bar{\sigma})} \tag{2.6}$$

$$\bar{\sigma} = \frac{1}{\Delta t}\int_0^{\Delta t} \sigma(t, \sigma_1, Z)dt \tag{2.7}$$

Step 3. Estimation of fatigue damage rate by E-N curve

In this step, the analysis output of the total cyclic strain range $\Delta\varepsilon_{total}$ is examined including the components of elastic strain, plastic strain and creep strain. The fatigue damage rate $\dot{\omega}_f$ at the critical node is characterized by Equation (2.8), based on the cycles to fatigue failure N_f.

$$\dot{\omega}_f = \frac{1}{N_f} = \frac{1}{N_f(\Delta\varepsilon_{total})} \tag{2.8}$$

Step 4. Evaluation of the lifetime to the creep-fatigue failure

The acceptable creep-fatigue life is N characterized by Equation (2.9), where the maximum life should satisfy the requirement of bi-linear interaction envelop that the summation of the creep damage and fatigue damage does not exceed 1.0 [29]. Regarding different materials, the turning point (c, f) is a variable parameter [30] (e.g., for 316L steel, the turning point is (0.3,0.3), while for 2.25Cr1Mo steel, it is (0.1,0.1)).

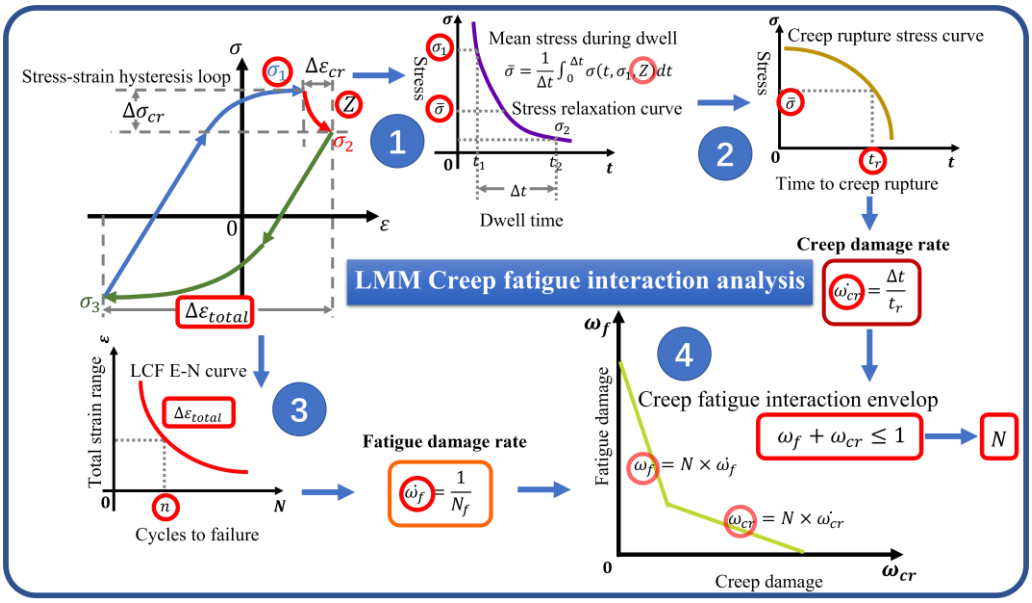

Fig. 2.7. Evaluation scheme of creep-fatigue damage and life by LMM

$$N = \begin{cases} \left(\omega_f + \dfrac{\omega_c(1-f)}{c}\right)^{-1}, & \omega_c < \omega_f \\ \left(\omega_c + \dfrac{\omega_f(1-c)}{f}\right)^{-1}, & \omega_c \geq \omega_f \end{cases} \tag{2.9}$$

2.3 Constraint effect in structural integrity assessment in presence of defects

To appropriately arrange the repair and replacement, the safety evaluation of components containing defects is an important part of the structural integrity assessment for in-service equipment. The development of fracture mechanics-based analysis methods is dedicated to addressing the structural integrity assessment for cases in the presence of defects. For this purpose, the accurate calibration of fracture toughness is needed, with the constraint effect fully reflected. The constraint is the resistance of a structure against plastic deformation [31], which is closely related to the specimen dimension and can be segregated into in-plane constraint and out-of-plane constraint based on the crack plane. The specimen dimensions in the direction of the growing crack, including the crack depth and specimen width, directly affect the in-plane constraint. By contrast, the specimen dimension parallels the crack front, which includes specimen thickness, directly determining the out-of-plane constraint. When evaluating the structural integrity of pressure vessels and pipelines with a low constraint effect, the material fracture toughness calibrated with a high

constraint level results in a conservative outcome, leading to unnecessary repair and replacement schemes. On the contrary, low constraint effect-derived fracture toughness may give out a dangerous analysis result for the high constraint components.

Given that constraint can significantly affect the material fracture resistance, it is essential to understand its influence on material fracture behaviour clearly. A lot of studies have been done on the effect of constraint on the material fracture behaviour under monotonic loading, and different fracture constraint parameters [32] and theories have been developed to characterise and analyse the constraint effect strength, such as *K*-*T* [33], *J*-*Q* [34, 35], *J*-A_2 [36], T_Z [37-39], φ [40, 41], A_p [42, 43], and A_d [44]. In addition, to deal with the high-temperature structural integrity assessment falling into the creep regime, the constraint parameters *Q** [45] and *C**-*Q** [46] were proposed, with the recent findings of the constraint effect on creep crack initiation reported in Ref. [47].

In this study, to characterise the in-plane and out-of-plane constraint effect numerically in a concise but clear manner, the unified measure parameter A_p proposed by Yang et al. [48] is adopted in the subsequent structural integrity assessment for the components containing defects. The constraint parameter A_p is defeined by Equation (2.10)

$$A_p = A_{PEEQ}/A_{ref} \tag{2.10}$$

Here, A_{PEEQ} is the area surrounded by the equivalent plastic strain isolines ahead of the crack tip, and A_{ref} is the reference area surrounded by the isolines in the standard specimen, which is selected following the requirement of Refs. [37, 49].

2.4 R5 procedure for high-temperature structure assessment

The R5 procedure [5] was developed and issued in the United Kingdom by EDF Energy Nuclear Generation Ltd, which includes five volumes and is dedicated to providing a comprehensive assessment procedure for evaluating structural responses in high-temperature environments. In this study, several fundamental structural failure mechanisms and analysis schemes are well-defined within the scope of Volume 2/3 “Procedure for Assessing Defects under Creep and Creep-Fatigue Loading”, which is intended to prevent the defect-free structures from the failure mechanisms including excessive plastic deformation, creep rupture, ratcheting, initiation of cracking due to combined creep and fatigue and creep deformation enhanced by the cyclic load.

This volume includes a series of simplified calculation methods based on the concept of reference stress, which was initially exploited based on the material creep ductility to deal with the phenomenon of creep deformation under monotonic load conditions, and then the variant was also adopted to tackle cases with cyclic loads. The key steps with this structural integrity assessment procedure are listed out below:

Step 1. Resolve load history into cycle types.

Step 2. Perform elastic stress analysis.

Step 3. Demonstrate sufficient margins against plastic collapse.

Step 4. Determine whether creep is significant.

Step 5. Demonstrate that creep rupture endurance is satisfactory.

Step 6. Perform simple test for shakedown and check for insignificant cyclic loading.

Step 7. Perform global shakedown check and calculate cyclic plastic zone size.

Step 8. Calculate shakedown reference stress, reference temperature and the start of dwell stress.

Step 9. Estimate elastic follow-up factor and associated stress drop during creep dwell.

Step 10. Calculate the total strain range.

Step 11. Check limits on cyclically enhanced creep and calculate creep usage factor.

Step 12. Summarise assessment parameters.

Step 13. Treatment of weldments.

Step 14. Calculate fatigue damage per cycle.

Step 15. calculate creep damage per cycle.

Step 16. Calculate total damage.

2.5 Direct methods for structural integrity assessment

2.5.1 Development of direct methods

As the core step in structural integrity assessment, the determination of structural cyclic responses under a high-temperature environment used to be performed by detailed FEA or expert knowledge-based simplified approaches. The former tends to provide more accurate analysis results, but it relies heavily on computing resources when dealing with large-scale modelling with plasticity and viscoplasticity included in the non-linear program, and it is difficult to guarantee computing efficiency. The latter is often based on some appropriate assumptions in order to improve computational efficiency and is only applicable to problems within a certain range.

Alternatively, by combining the advantages of both detailed FEA and simplified calculation approaches to balance computational accuracy and efficiency, several direct methods have been proposed, which are generally divided into two categories: the mathematical programming methods [50, 51] and the modified elastic modulus methods. In recent years, The modified elastic modulus-based methods have developed particularly rapidly and have derived many different variants, including the Reduced Modulus Method [52], the Generalised Local Stress-Strain Method [53], the Elastic Compensation Method [54], the Modified Elastic Compensation Method [55], the Non-linear Superposition Method [56], the Stress Compensation Method [57].

2.5.2 Linear Matching Method (LMM) framework

The Linear Matching Method (LMM) framework [58, 59] is a variant of the Reduced Modulus Method containing a series of linear analysis tools that are able to give out structural non-linear responses by solving linear problems. The core conception of this methodology is to establish the appropriate linear matching conditions which are formulated and adjusted iteratively to precisely match the structural non-linear behaviour due to complicated load conditions. As a result, the constant residual stress fields and changing residual stress fields are determined during the iteration process, with the associated inelastic strain increment generated for the subsequent structural integrity evaluations. Currently, the LMM framework supports the Elastic-Perfectly Plastic (EPP) model and the strain hardening model depicted by Ramberg-Osgood (R-O) form to consider cyclic plastic behaviours. For cases with the creep dwell effect, the material yield stress is replaced by the creep flow stress.

The history of the development of the LMM framework is shown in Fig. 2.8 below, and each analysis module is developed corresponding to the analysis requirements in the R5 Volume 2/3.

The shakedown modulus was designed firstly to calculate the structural shakedown limit based on the upper bound shakedown theory. With the revised yield stress proposed by the lower value of the material yield stress and the creep rupture stress, the extended shakedown modulus was proposed to derive the structural creep rupture limit. When tackling cases including time-dependent residual stress, the DSCA modulus is able to provide the cyclic plastic response related to the LCF life evaluation, by which the ratcheting modulus was then developed by combing the varying residual stress by DSCA and the extended shakedown procedure to give out the structural ratchet limit against the additional constant load conditions. Recently, in order to break through the limitation that the original ratchet analysis can only focus on the combination of cyclic loads and constant loads, the Unified Procedure for Fatigue and Ratchet Analysis (UPFRA) [60] was established to incorporate more complicated cyclic load conditions and build the constant LCF life boundary in terms of different load levels. In this thesis, the LMM is further extended to the pLMM framework, aiming at providing a probabilistic structural integrity assessment platform to process the uncertain design and operating factors. And the pLMM is dedicated to delivering technical support for reliability-centred design and risk management of critical infrastructures, which balances computational efficiency and accuracy simultaneously.

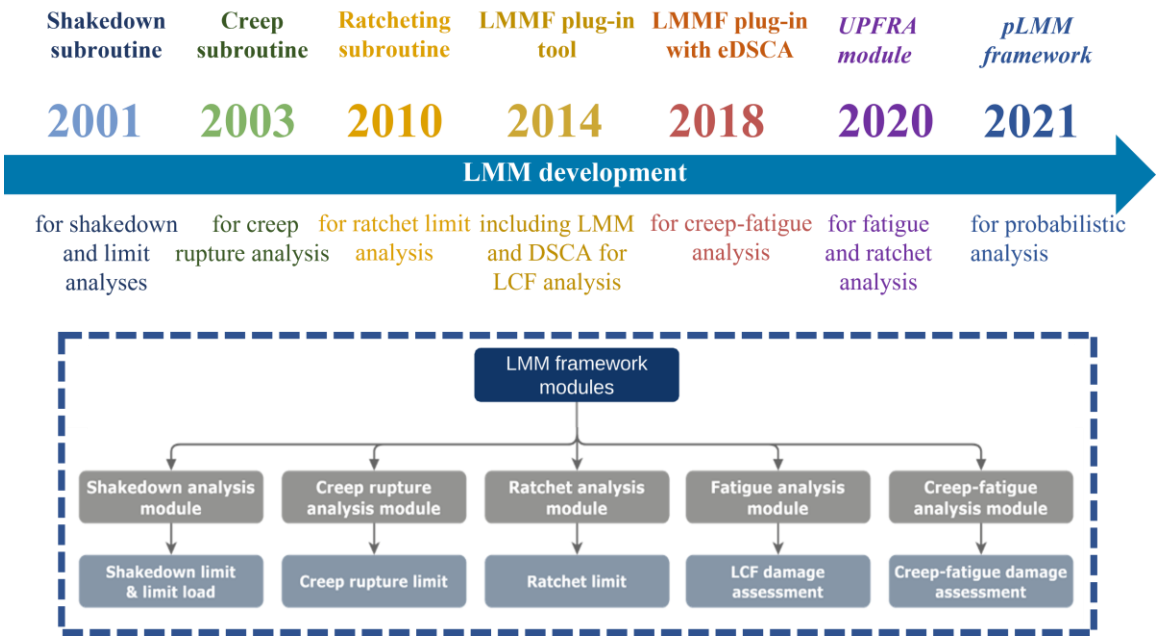

Fig. 2.8. Development of the LMM framework and the related analysis modules

2.6 Reliability analysis in structural integrity assessment

Structural integrity assessment for high-temperature components largely depends on deterministic analysis to prevent specified failure modes. However, due to the current energy crisis and the urgent need for efficient use of energy, high-temperature equipment in the energy industry often has to operate in extreme environments for a long period, which may raise numerous unpredictable multiplicity of uncertainty in the actual extreme design parameters. Aiming at pursuing an absolutely reliable scheme, traditional deterministic calculations need a safety factor conservative enough to cope with uncertain conditions [61]. However, this strategy reflects limited statistical information on the structural key responses related to the failure behaviours. The reliability-centred structural integrity assessment is dedicated to measuring the structural behaviours in a probabilistic manner, allowing the potential failure risk to be predicted and facilitating the risk management of critical infrastructures in the energy industry.

2.6.1 Identification of failure probability

The main purpose of probabilistic failure analyses is to investigate the failure risk of engineering structures when not satisfying a specific function, with a variety of uncertain factors taken into account. The prototype is the Load and Resistance Factor Design (LRFD) [62]. Different from the conventional allowable stress-based design scheme, LRFD incorporates multi-safety factors into the assessment process, with different weighted load effects considered separately. Then, the concept of performance function G is arisen and employed to compare the structural resistance $\boldsymbol{R}$ and the load conditions $\boldsymbol{S}$ [63]. Here, an n-dimensional vector $\boldsymbol{X} = (X_1, X_1, \dots, X_n)$, including all the random variables, is defined to consider the uncertainties in design parameters, and in Equation (2.11) the limit state of the G function identifies the safe and failure regions by the hyper-surface $G(\boldsymbol{X}) = 0$. There are three possible states: if $G = \boldsymbol{R} - \boldsymbol{S} > 0$, that means survival; when the equation is lower than zero, the assessment result is failed; with $G = \boldsymbol{R} - \boldsymbol{S} = 0$, the limit state is established. The failure probability P_f is given by the non-positive state of the G, and, as shown in Fig. 2.9, the failure probability is calculated by the integral value of the interference region $P_f = P(G(\boldsymbol{X}) < 0)$.

$$G(\boldsymbol{X}) = R(\boldsymbol{X}) - S(\boldsymbol{X}) \begin{cases} < 0, \text{Failed} \\ = 0, \text{Limit state} \\ > 0, \text{Safe} \end{cases} \tag{2.11}$$

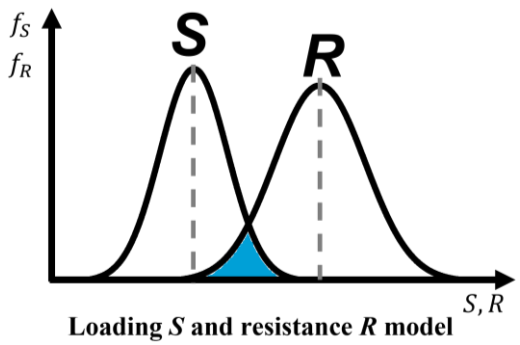

Fig. 2.9. Comparison of loading R and resistance S and determination of failure probability

2.6.2 First-Order Reliability Methods (FORM)

To avoid the huge number of repeated deterministic calculations in the direct Monte Carlo Simulation (MCS), the semi-theoretical approaches, including the Mean-value First-Order Second-Moment analysis (MFOSM), the First-Order Reliability Method (FORM), also known as Advanced First-Order Second-Moment analysis (AFOSM), and the Second-Order Reliability Method (SORM) [64], was proposed by exploiting the efficient Taylor series expansion of nonlinear performance function to enhance the computational efficiency in reliability analysis.

The most commonly used FORM was first developed by Hasofer [65] to estimate structural reliability. firstly, the basic random variables in vector X are transformed into the independent standard normal variables stored in another vector Y. Next, the reliability index β is defined from the analytical view which characterizes failure probability if the performance function satisfies the normal distribution. Here, $g(\boldsymbol{Y})$ is the SLSIF expressed in the new space Y composed of uncorrelated random variables obeying standard normal distribution. And the tangential hyper-plane of SLSIF hyper-surface $g(\boldsymbol{Y}) = 0$ is prescribed by the following formulation:

$$g_T(\boldsymbol{Y}) = \nabla g(\boldsymbol{Y}^*)^T \cdot (\boldsymbol{Y} - \boldsymbol{Y}^*) \tag{2.12}$$

where $\nabla g(\mathbf{Y}^*)$ is the gradient of SLSIF $g(\boldsymbol{Y})$ at the design point. The reliability index also indicates the shortest distance (see the red line in Fig. 2.10) in space Y, from the origin to the design point $\boldsymbol{Y}^*$ on the hyper-surface of $g(\boldsymbol{Y}) = 0$, which can be determined by

$$\beta = -\left(\frac{\nabla g(\boldsymbol{Y}^*)}{\|\nabla g(\boldsymbol{Y}^*)\|}\right)^T \cdot \boldsymbol{Y}^* \tag{2.13}$$

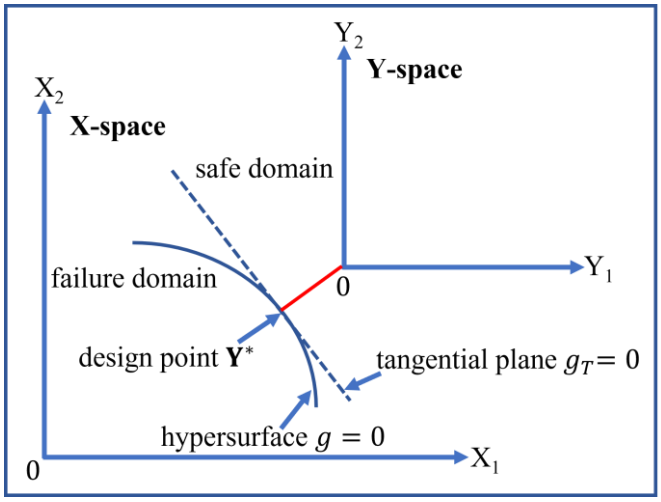

Fig. 2.10. Linear approximation scheme and calculation of reliability index

Then, for seeking the location of the design point and the minimum value of the reliability index, a non-linear optimization problem is posed by the form below,

$$\begin{cases} \quad min \ \sqrt{\mathbf{Y}^T \cdot \mathbf{Y}} \\ \quad s.t. \ \mathrm{g}(\mathbf{Y}) \leq 0 \end{cases} \tag{2.14}$$

With the gradient information acquired by partial differentiation of each random variable, the searching process is performed according to the iteration Equation (2.15).

$$\boldsymbol{Y}_{k+1} = \frac{\nabla g(\boldsymbol{Y}_k)}{|\nabla g(\boldsymbol{Y}_k)|^2}\left[\boldsymbol{Y}_k^T \nabla g(\boldsymbol{Y}_k) - g(\boldsymbol{Y}_k)\right] \tag{2.15}$$

It searches and advances along the gradient of the performance function at the design point, applies the value of the performance function to determine the step length, and updates the new design point at the end of each iteration.

To estimate the failure probability, Equation (2.16) is approximated linearly at the design point by the Taylor series expansion,

$$g(\mathbf{Y}) \approx g(\mathbf{Y}^*) + \nabla g(\mathbf{Y}^*)^T \cdot (\mathbf{Y} - \mathbf{Y}^*) \tag{2.16}$$

so that the hyper-surface of SLSIF $g(\mathbf{Y}) = 0$ is substituted by the above tangential hyper-plane $g_T(\mathbf{Y}) = 0$, and the failure probability relies on the approximation in Equation (2.17),

$$P_f = P(g(\mathbf{Y}) \le 0) \approx P(g_T(\mathbf{Y}) \le 0)$$

$$= P(\nabla g(\mathbf{Y}^*)^T \cdot (\mathbf{Y} - \mathbf{Y}^*) \le 0)$$

$$= P\left(\left(\frac{\nabla g(\mathbf{Y}^*)}{\|\nabla g(\mathbf{Y}^*)\|}\right)^T \cdot \mathbf{Y} + \beta \le 0\right) \tag{2.17}$$

$$= P\left(\left(\frac{\nabla g(\mathbf{Y}^*)}{\|\nabla g(\mathbf{Y}^*)\|}\right)^T \cdot \mathbf{Y} \le -\beta\right) = \Phi(-\beta)$$

where $\left(\frac{\nabla g(\boldsymbol{Y}^*)}{\|\nabla g(\boldsymbol{Y}^*)\|}\right)^T \cdot \boldsymbol{Y}$ obeys standard normal distribution.

2.6.3 Surrogate modelling technology

Surrogate modelling technology is an effective way to capture the approximation relationship between the input parameters and the output responses implicitly or explicitly, without losing too much calculation accuracy. This black-box modelling strategy is very conducive to simplifying probability analysis by replacing detailed FEA calculations. Such methods commonly adopted in modelling engineering problems include Response Surface Method (RSM) [66], Kriging Model [67], Artificial Neural Network (ANN) [68], and their variants.

RSM employs the polynomials with different orders to fit the response of the actual physical problem [69] based on a given dataset and is frequently applied to perform reliability analysis and optimization with a low computational burden. The fitting parameters of the polynomials are determined by solving the linear system of equations, and the basic approximation $\tilde{F}$ is expressed in the following form with the first-order and second models:

$$\tilde{F}(\boldsymbol{x}) = \alpha_0 + \sum_{i=1}^{N} b_i x_i \tag{2.18}$$

$$\tilde{F}(\boldsymbol{x}) = \alpha_0 + \sum_{i=1}^{N} b_i x_i + \sum_{i=1}^{N} c_{ii} x_i^2 + \sum_{ij(i<j)} c_{ij} x_i x_j \tag{2.19}$$

Kriging Model is named after the South African mining engineer, D. G. Krige, and then developed in geostatistics [70], a hybrid discipline of mining, engineering, geology, mathematics, and statistics [71]. The interpolation form of the Kriging model is formulated by considering global and local behaviours [72], as shown in Equation (2.20) below,

$$y(x) = \Gamma(x) + \delta(x) \tag{2.20}$$

where $\Gamma(x)$ is the global trend expressed by the polynomial function and $\delta(x)$ is the additional identification of a stochastic process with mean zero, variance σ^2, and nonzero covariance.

Due to the excellent generalization ability, the feedforward ANN [73], is built and employed as the multi-layer perceptron (MLP) for modelling and prediction purposes. Based upon the universal approximation theorem [74], the rationality and effectiveness of the three-layer neural network have been proved by Refs. [75, 76], and the general network structure contains three layers: the input layer, the hidden layer and the output layer, as displayed in Fig. 2.11.

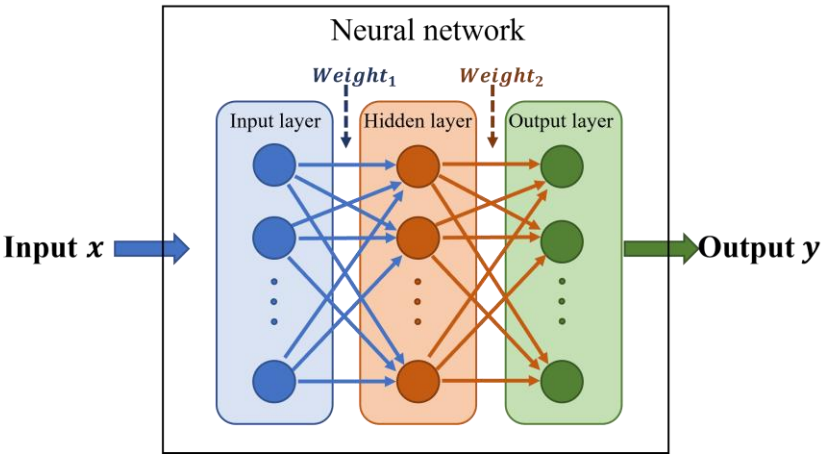

Fig. 2.11. The general structure of a three-layer neural network

The data flow commences with the input data vector $\boldsymbol{x}$ passed in through the input layer to the hidden layer, during which the weight of each parameter is also considered. Next, in the middle or hidden layer, the activation function existing in each neuron plays a key role in the non-linear mapping process to process the summation of weighted input with bias. Usually, the number of neurons used in the hidden layer depends on the size of the training data set for a certain type of analysis, and it should be guaranteed to be larger than the dimensionality of the input vector being processed. Then, the output layer is responsible for generating the final predictions. In this study, the construction process of ANN is implemented by adopting the Isight software.

2.7 R5 Volume 2/3 Appendix A15: Advice on probabilistic assessments

The R5 Volume 2/3 Appendix A15 "Advice on probabilistic assessments" [77] delivers a complement to the deterministic analysis approaches when dealing with the uncertainty of design

input parameters in creep-fatigue crack initiation assessments. Within this scope, structural integrity is demonstrated by the failure probability, instead of the pessimistic margin values, such as bounding working conditions or lower-bound material endurance. And this probabilistic assessment is able to predict:

1. The probability that initiation occurs at a single location in an individual component by a given time, or within a given time period;

2. The probability that initiation occurs at one of multiple locations in an individual component by a given time, or within a given time period;

3. The number of cracks initiating, by a given time or within a given time period, in a population of components where the variation within the population can be characterised by statistical distributions in terms of material properties, geometry and loading.

This probabilistic assessment guidance also prescribes the analysis steps, including :

Step 1. Specify values for the various quantities required to perform an assessment.

Step 2. Specify which quantities from Step 1 are to be treated as having a distribution of input values.

Step 3. Specify the failure condition.

Step 4. Select a random sample of input variable quantities which, together with the quantities that do not vary, leads to a complete set of inputs for an assessment.

Step 5. Perform a deterministic assessment and record whether the failure is conceded or not.

Step 6. Repeat Steps 4 and 5 a total number of times.

Step 7. Calculate the failure probability

Step 8. Carry out checks to confirm the probability or frequency being estimated has numerically converged to within acceptable tolerance.

Step 9. Carry out sensitivity analysis within the probabilistic assessment on the assumed probability distributions, number of calculations and deterministic inputs to determine which variables have the greatest impact on component lifetime and therefore the probability of failure.

Step 10. Perform studies on the impact of correlations in input quantities.

2.8 Summary

In this chapter, the typical structural responses under high-temperature conditions are introduced comprehensively, with ratcheting, LCF, creep rupture and creep-fatigue failure behaviours illustrated clearly. Regarding the evaluations of components with defects, the constraint effect is clarified as well, which affects the material fracture resistance significantly. Besides, as a powerful structural integrity assessment procedure for high-temperature components, the UK R5 procedure Volume 2/3 is exemplified, where the core analysis steps in Volume 2/3 related to creep-fatigue failure analysis are delivered in detail. And to implement such an assessment process, the direct method, especially the LMM is fully reviewed which is dedicated to dealing with structural integrity assessment according to R5 procedure Volume 2/3. Compared with conventional detailed FEA, the LMM avoids the numerous non-linear iterations, and directly captures the structural steady responses under complicated load conditions, with a good balance achieved between computational efficiency and accuracy [78].

In addition to the review of deterministic analysis, the basic background of the reliability-based structural integrity assessment is elaborated to handle the uncertain design parameters in extreme engineering conditions. And to further extend the applicability of probabilistic analysis approaches, several fundamental surrogate modelling technologies that are frequently adopted in the reliability-based structural integrity assessment are given out, which can be considered as the underlying technical solutions for building a reliability-based structural integrity assessment framework. Finally, the recent research progress on the guidance of probabilistic assessment concerning creep-fatigue failure in the R5 procedure Volume 2/3 is summarized, with the specific analysis steps listed.

3 Direct method-based creep rupture limit analysis for engineering structures under high-temperature conditions

3.1 Introduction

With modern industrial equipment expecting higher temperature and pressure design requirements, the problems of how to prevent creep rupture failure, the crucial failure mode when the equipment works in this harsh environment, and how to make this design or assessment more efficient and accurate have been focused on for a long time [79]. Considering that the equipment running under high-temperature conditions often has an expensive cost and will produce huge security risks and economic losses after failure [80], various design and assessment procedures against creep rupture behaviour have been developed by both industry and researchers.

Instead of tracking the entire process of creep rupture failure, a different type of technique to deal with the creep rupture endurance was put forward by the high-temperature structure assessment procedure R5 [5], where creep rupture data can be utilised directly to acquire rupture reference stress by simplified elastic analysis and subsequently to quantify the creep significance by the creep usage factor. Following such a methodology, Chen [81] proposed the extended Linear Matching Method (LMM) creep rupture procedure by combining both material's revised yield stress and the traditional shakedown analysis algorithm to provide an alternative to implementing non-linear creep rupture assessment and to minimize the conservativeness of simplified elastic analyses. It now has been integrated within the LMM framework to analyse the structures subjected to both monotonic and cyclic load conditions under elevated operating temperatures. Because of its concise linear iteration form, this algorithm can overcome the convergence difficulties faced by other non-linear creep simulation methods. The LMM framework is then further extended to address the creep-fatigue interaction problem by Chen and Yevgen, with the creep damage evaluated by the time fraction rule [82].

The aforementioned creep rupture assessment techniques, including the ISS curve, Omega creep damage model and LMM creep rupture analysis, have their characteristics, however, so far, there is no systematic research delivered before on these methods. It is necessary to recommend an

in-depth examination to bridge the gap, providing a sufficient basis for selecting the appropriate creep rupture analysis method in engineering applications. Besides, inevitably, the material constitutive models and parameters to describe the creep behaviour are not consistent for different approaches due to unequal experimental calibrations, as a result, leading to unfair comparison. Therefore, this thesis focuses on proposing a robust assessment technique to deal with creep rupture failure of high-temperature structures based on the unbiased comparative investigation of mainstream assessment techniques. And a deep and comprehensive understanding of the creep rupture failure mechanism is demonstrated with a complicated 3D benchmark. In addition, applicable creep rupture limit boundaries in terms of both monotonic and cyclic load conditions are established not only for design purposes but also for evaluating the in-service high-temperature component against creep rupture failure, where the correlations between different mechanisms of shakedown, creep rupture and creep induced ratcheting are identified and clarified for the first time. Furthermore, aiming at confirming the effectiveness of such design curves, the creep rupture evaluation curves are validated in a new way through detailed step-by-step non-linear creep analyses, which makes such an engineering design tool reliable and robust when dealing with the assessment of creep rupture failure for the high-temperature components.

This chapter is organized as follows. In Section 3.2, there is a detailed illustration of the LMM-based creep rupture analysis procedure. Next, by applying the above three methods to a typical high-temperature structure, a hydrogenation reactor operating in the chemical industry is investigated numerically to calculate the creep rupture limit load in Sections 3.3 and 3.4. And, in Section 3.5, the creep rupture boundary acquired by the LMM creep rupture analysis is illustrated and an effective numerical verification strategy for the calculated creep rupture boundary above is proposed based on the step-by-step non-linear FEA. Finally, additional discussions of the case with cyclic load conditions are elaborated in Section 3.6, and the main conclusions are listed briefly in the last section.

3.2 The numerical procedure of the LMM-based creep rupture analysis

The LMM creep rupture limit analysis is developed on the basis of an extended shakedown analysis procedure, depending on the concept of revised yield stress which is employed to substitute the original yield stress with the minimum of the material yield stress and the creep rupture stress at a specified creep temperature range.

3.2.1 Determination of the creep rupture limit multiplier

The description of this program [83] is shown below:

It can be assumed that for the conservative design purpose, the material is isotropic and elastic-perfectly plastic (EPP), following the Mises yield condition. In the beginning, a linear solution $\lambda\hat{\sigma}_{ij}$ is determined in which λ is a parameter controlling the scaling of the load history applied. The process is based on incompressible and kinematic admissible strain rate history $\dot{\varepsilon}_{ij}^{c}$ which is associated with a compatible strain increment $\Delta\varepsilon_{ij}^{c}$ by integrating the following equation:

$$\int_0^{\Delta t} \dot{\varepsilon}_{ij}^{c}\, dt = \Delta\varepsilon_{ij}^{c} \tag{3.1}$$

where Δt is the period during the load cycle.

According to the shakedown upper boundary theory, a limit parameter λ_{UB_LIMIT} is calculated by

$$\lambda_{UB\_LIMIT} \int_V \int_0^{\Delta t} \left(\hat{\sigma}_{ij}\dot{\varepsilon}_{ij}^{c}\right) dtdV = \int_V \int_0^{\Delta t} \sigma_{ij}^{c}\dot{\varepsilon}_{ij}^{c}\, dtdV \tag{3.2}$$

When implementing a creep rupture limit analysis, σ_{ij}^{c} stands for either the stress near creep rupture or the stress at yield state with the strain rate history $\dot{\varepsilon}_{ij}^{c}$, and $\hat{\sigma}_{ij}$ is the linear elastic stress defined above, associated with the applied reference load history. Considering the associated flow rule, Equation (3.2) can be transformed and the creep rupture limit multiplier is derived by the equation below:

$$\lambda_{UB\_LIMIT} = \frac{\int_V \int_0^{\Delta t} \sigma_y(t, t_r, T)\bar{\dot{\varepsilon}}\left(\dot{\varepsilon}_{ij}^{c}\right) dtdV}{\int_V \int_0^{\Delta t} \left(\hat{\sigma}_{ij} \cdot \dot{\varepsilon}_{ij}^{c}\right) dtdV} \tag{3.3}$$

where $\bar{\dot{\varepsilon}}$ is the effective strain and σ_y is the revised yield stress introduced before which is determined in Equation (3.4) by the minimum of the creep rupture stress σ_r under certain creep dwelling time and the yield stress σ_s at the corresponding temperature.

$$\sigma_y(t, t_r, T) = min\{\sigma_r(t, t_r, T), \sigma_s(t, T)\} \tag{3.4}$$

3.2.2 Iteration procedure of the LMM creep rupture analysis

This program consists of a series of iterations, starting with a history of plastic strain rate $\dot{\varepsilon}_{ij}^{i}$ and leading to a new strain history in the next iteration $\dot{\varepsilon}_{ij}^{new'}$,

$$\dot{\varepsilon}_{ij}^{new'} = \frac{1}{\mu}\left(\lambda_{UB\_LIMIT}^{i}\hat{\sigma}_{ij} + \bar{\rho}_{ij}^{new}\right)' \tag{3.5}$$

$$\dot{\varepsilon}_{kk}^{new} = 0 \tag{3.6}$$

where the symbol $'$ represents the deviatoric component, $\bar{\rho}_{ij}^{new}$ is the constant residual stress field, and $\dot{\varepsilon}_{kk}^{new}$ is the hydrostatic component of the new strain rate history in the next cycle. The condition below provides the matching relationship to strictly guarantee that both EPP and linear material properties give the same response due to $\dot{\varepsilon}_{ij}^{i}$ defined at the beginning of this iterative step.

$$\mu = \frac{\sigma_y(t, t_r, T)}{\bar{\dot{\varepsilon}}^{i}} \tag{3.7}$$

The integral forms of these equations are as follows,

$$\Delta\varepsilon_{ij}^{new'} = \frac{1}{\bar{\mu}}\left(\bar{\rho}'^{f}_{ij} + \sigma_{ij}'^{in}\right) \tag{3.8}$$

$$\sigma_{ij}'^{in} = \bar{\mu}\left\{\int_0^{\Delta t}\frac{1}{\mu(t)}\lambda_{UB}^{i}\hat{\sigma}_{ij}'(t)dt\right\} \tag{3.9}$$

$$\frac{1}{\bar{\mu}} = \int_0^{\Delta t}\frac{1}{\mu(t)}dt \tag{3.10}$$

which gives the amount of these variables after an iteration. Next, as illustrated in Fig. 3.1, the modulus is modified according to the magnitude of the calculated strain in order to make the stress equal to the revised yield stress.

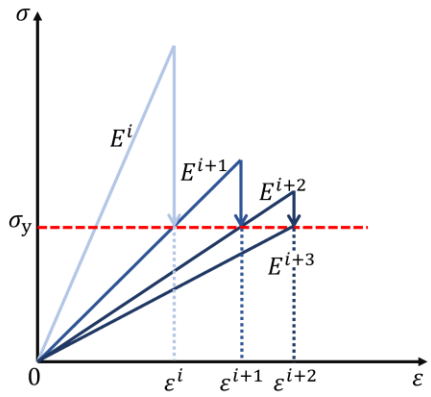

Fig. 3.1. Iteration process of the LMM-based creep rupture analysis

Repeating the steps above produces a set of monotonically decreasing upper bound multipliers, given by the following Equation (3.11) until the iteration converges to a stable value.

$$\lambda_{UB\_LIMIT}^{new} \leq \lambda_{UB\_LIMIT}^{i} \tag{3.11}$$

Under the LMM framework, the creep rupture analysis generates both the upper bound multiplier and the lower bound multiplier for the creep rupture limit simultaneously. Although the upper bound solution based on energy criterion may give rise to non-conservative estimations, it is more accurate than the lower bound solution which is very model-sensitive and depends on the stress solutions at the most critical location. Therefore, the LMM upper bound creep rupture limit results are utilised for all the discussions in this study.

According to a convex yield condition, several straight-line paths and vertices in the load space are adopted for engineering problems to predefine the load history. As these vertices correspond to the appearance of plastic strain, the sum of plastic strain increments at each vertex results in the strain increment over a certain cycle. In particular, if the load path is prescribed by only one condition point in the load space, this iteration form degenerates to a creep rupture limit analysis under the monotonic load condition, which paves the way for solving the creep rupture limit problem by the extended LMM algorithm.

3.3 Problem description of creep rupture assessment for hydrogenation reactor

In this section, a typical high-temperature structure, the hydrogenation reactor component, is chosen as the benchmark to investigate the aforementioned creep rupture limit analyses numerically. As a large-scale pressure vessel, the hydrogenation reactor is the core operating unit of the petroleum refining and coal chemical industry, running under elevated temperatures and complex mechanical load conditions. Hence, when designing and assessing this equipment, creep rupture is the most crucial failure mode among several potential failure behaviours.

3.3.1 FEA model description

Due to the symmetry of this structure, a quarter model of the hydrogenation reactor with a normal nozzle is created in ABAQUS CAE, with the inner radius and the thickness of the main vessel set as 1,500 mm and 130 mm, respectively. And this structure is meshed by the 20-node quadratic brick element C3D20 and refined around the welding transition zone between the main vessel and nozzle (see Figs. 3.2 and 3.3) to capture the high-stress gradient effect. As to the nozzle part, its inner radius is 108mm and its thickness is 122 mm. Along the thickness direction, the pressure vessel is discretised into 9 elements, with the adopted minimum element size of 4.2 mm, which is sensitive enough to meet the requirement for the mesh convergence check.

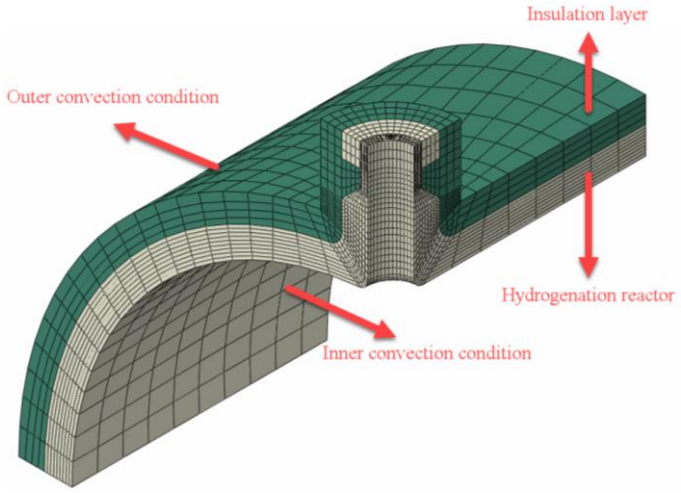

Fig. 3.2. Finite element model and Convection conditions for thermal analysis (insulation layer and steel pressure vessel)

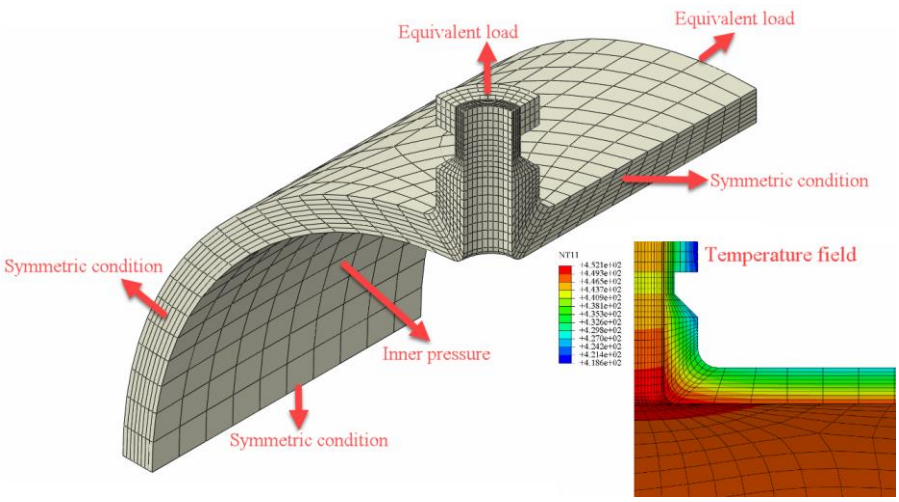

Fig. 3.3. Finite element model and boundary conditions for creep rupture analysis (only pressure vessel)

This hydrogenation reactor is made of 2.25Cr-1Mo-V steel because of its high strength, superior anti-hydrogen embrittlement property, and creep rupture resistance [35]. The basic material's properties including Young's modulus E, yield stress σ_s, and coefficient of thermal expansion α are presented in Table 3.1 and the Poisson's ratio ν at all design temperatures is set to 0.3.

Table 3.1. Material properties of 2.25Cr-1Mo-V steel for a given temperature from Ref. [84]

Temperature (°C)	E (GPa)	σ_s (MPa)	α (10^{-6}/°C)
400	184	353	15.9
425	/	346	16.1
450	180	339	16.4
475	/	332	16.5

Indeed the adoption of the same material properties is the key assumption to guarantee the effectiveness of this investigation, however, the direct use of real creep properties in different forms inevitably makes the comparative study biased since different methods rely on unequal material

parameters calibrations to describe creep behaviour and these material parameters in different forms may not be consistent. To avoid such an issue, an alternative is adopted that the same creep deformation curves acquired from the virtual creep test, where the Omega creep model plays the role of the constitutive relationship to generate the ISS curve and related creep rupture stress for the other two methods respectively, hence, making later investigation on the unified material base.

Therefore, in this study, the ISS curves and the creep rupture stresses for given service lives and temperatures are derived by a series of virtual creep experiments numerically in which the Omega creep constitutive Equation (2.5) is integrated via the ABAQUS user subroutine, acting as the creep strain rate function in the FEA test with a single element. In this way, different methods are placed under the same material data source, and the study fully reflects the inherent differences between these methods. The virtual experimentally generated creep test curves for 2.25Cr-1Mo-V steel are shown in Fig. 3.4, and Fig. 3.5 displays the related ISS curves, with the typical operating temperatures (425 °C and 450 °C) and working period (250,000 hours) of the hydrogenation reactor selected. Fig. 3.6 provides the revised yield stress data used by the LMM creep rupture analysis to consider the creep rupture failure, which is determined according to the minimum of the normal material's yield stress and creep rupture stress under specified temperature levels and service life. The calculation paths of the three strategies are summarised in the flowchart in Fig. 3.7, where the input requirements and result forms of each are exhibited.

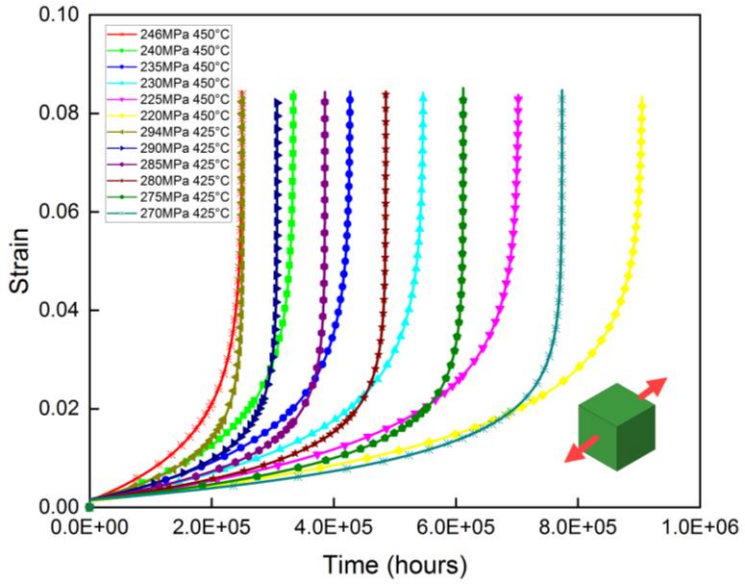

Fig. 3.4. Virtual creep experiments curves for 2.25Cr-1Mo-V under different conditions derived from the Omega creep model

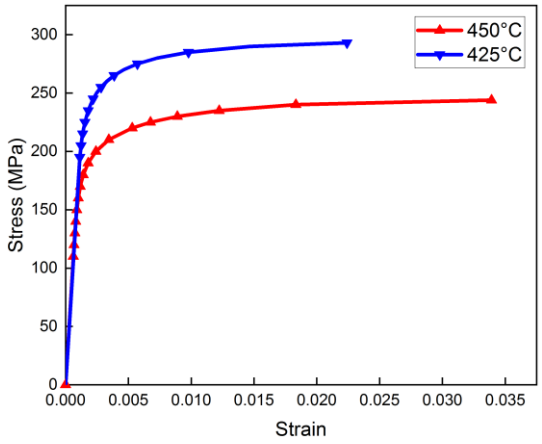

Fig. 3.5. ISS curves of 2.25Cr-1Mo-V steel for 2.5 ×105 hours

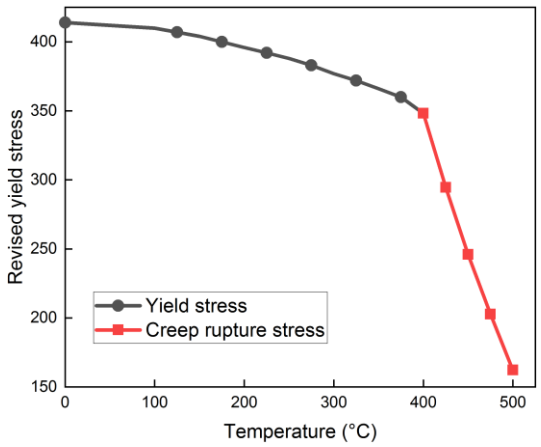

Fig. 3.6. Revised yield stress of 2.25Cr-1Mo-V steel for 2.5 ×105 hours

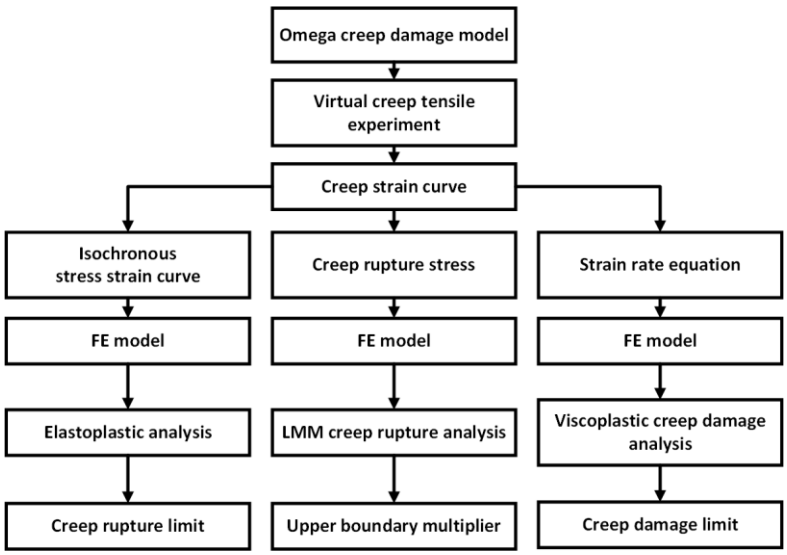

Fig. 3.7. Flowchart of three creep rupture limit analysis strategies

3.3.2 Boundary conditions

Aiming at determining the temperature distribution among the structure, a hydrogenation reactor model covered with an insulation layer is created for the thermal analysis, where two convection conditions (shown in Table 3.2) are applied on both inner and outer surfaces, respectively, providing the temperature field for subsequent creep rupture limit analyses. For creep rupture limit analysis, in addition to the temperature field (displayed in Fig. 3.3) imported from the above thermal analysis, the inner surface of the vessel is subjected to a high-pressure load, with the

related equivalent loads at the end of the nozzle and right side of the main vessel added. The symmetric boundary conditions are also applied to the other three end surfaces.

Table 3.2. Convection condition parameters for thermal analysis

Convection condition	Inner surface	Outer surface
Film coefficient (W/mm2 · °C)	1.2×10-3	1.2×10-5
Temperature (°C)	454	-20

For the ISS-based method, the applied pressure should be large enough to reach the rupture limit load during the non-linear FEA. As to the Omega model-based creep approach, a series of trial and error searches are performed continually to seek the final acceptable load condition which leads to the threshold of creep damage. By contrast, in LMM creep rupture analysis, only a reference load is needed, which is usually set to one unit (1 MPa in this case).

3.4 Comparative investigation of creep rupture analyses

In this section, with the creep rupture analysis for the hydrogenation reactor elaborated, the detailed comparison between the ISS curve-based approach, Omega model-based method and LMM creep rupture analysis are demonstrated in terms of computational efficiency and accuracy.

3.4.1 Discussion on calculation processes and results

From the results displayed in Fig. 3.8, different result layouts are plotted to describe the creep rupture failure mechanism after running for 250,000 hours, and the maximum creep strain, up to 0.0208, occurs at the inner corner of the nozzle connected to the main vessel cylinder. The creep strain produced around the inner corner gradually decays to the minimum level along the axial direction of both the nozzle and vessel cylinder, respectively, while the rest of the material remains undamaged.

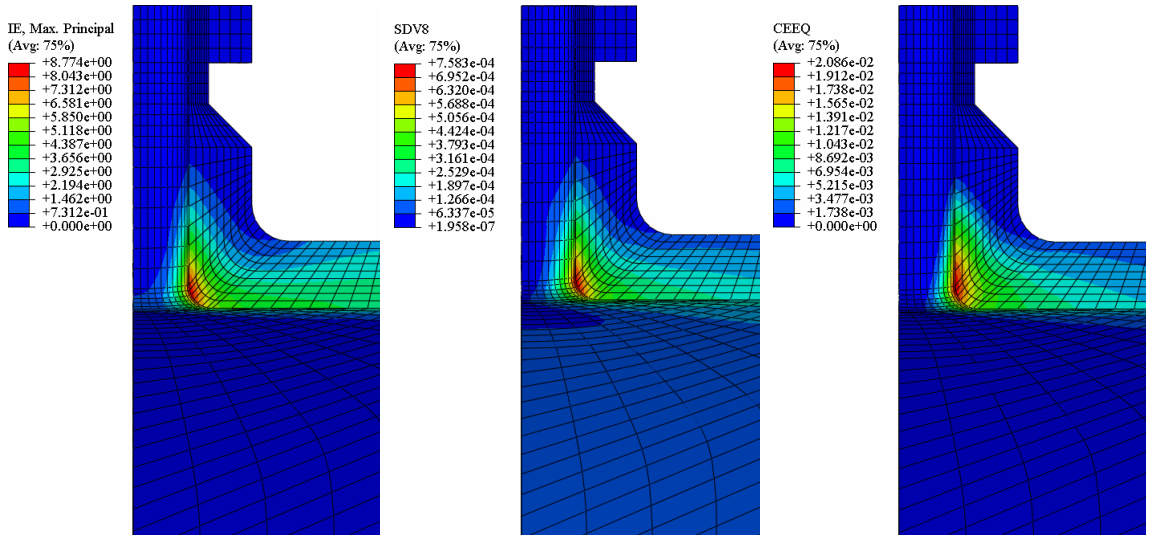

(a) (b) (c)

Fig. 3.8. Failure mechanism by creep rupture analyses after 250,000 hours: (a) Inelastic strain by ISS curve-based analysis; (b) Effective strain increment by LMM creep rupture analysis; (c) Creep strain by Omega model-based analysis

Based on the elastoplastic analysis, the ISS curve-based approach considers the inelastic strain (see Fig. 3.8 (a)) as the creep strain. Alternatively, the distribution of inelastic strain increment (see Fig. 3.8 (b)) is employed by the LMM creep rupture analysis to demonstrate the failure mode. While, only by Omega model-based creep simulation, the creep strain (Fig. 3.8 (c)) can be acquired by embedding a creep user subroutine into the FEA procedure.

Additionally, the interpretations of the stress result further explain their features. Relying on the stress level to define the material's failure state, both the ISS curve-based analysis and LMM creep rupture analysis present a final stress state after 250,000 hours described in Fig. 3.9 that is similar to the plastic flow state due to yielding. The stress values of the keypoint defined by the maximum creep strain (in Fig. 3.8) correspond to either maximum isochronous stress or revised creep rupture stress under specified temperature and dwell time.

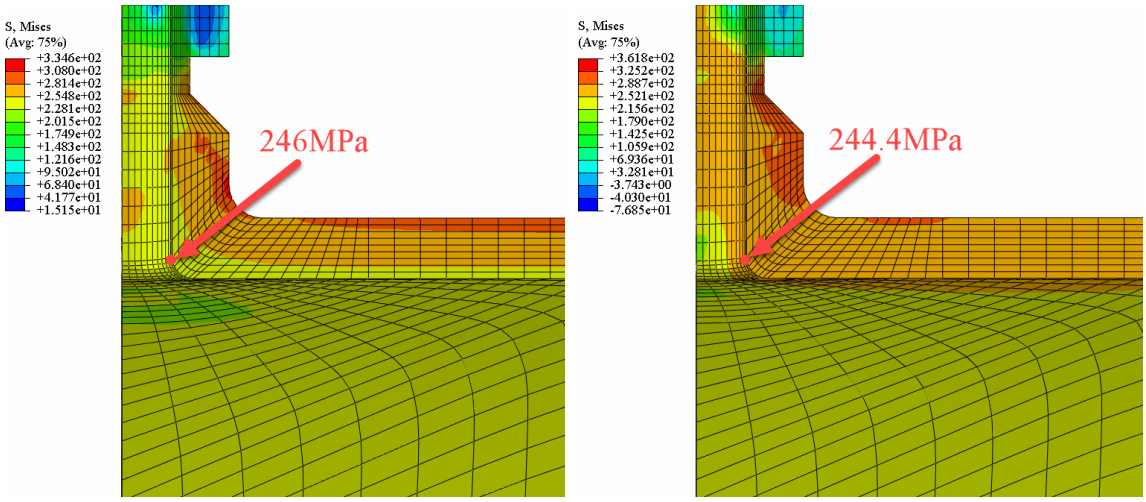

(a) (b)

Fig. 3.9. Stress distribution after creep dwell of 250,000 hours: (a) By ISS curve-based analysis; (b) By LMM creep rupture analysis

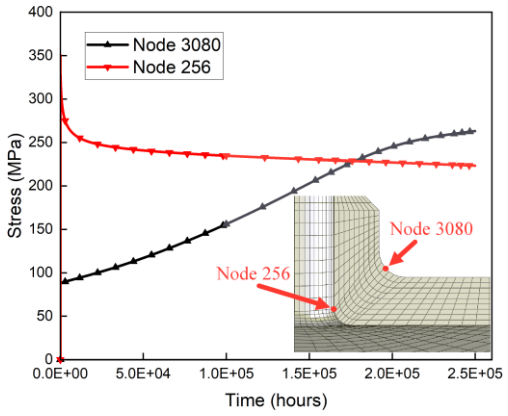

Fig. 3.10. Stress redistribution process by Omega model-based analysis

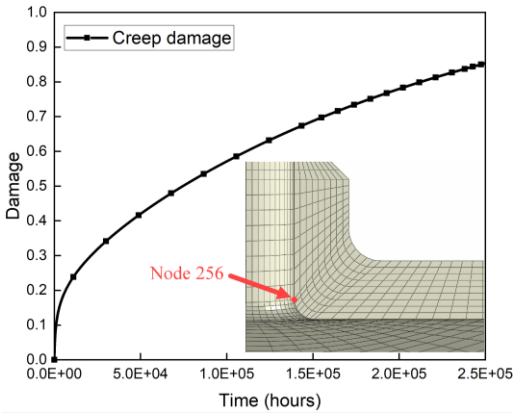

Fig. 3.11. Creep damage accumulation by Omega model-based analysis

On the other hand, as a time history analysis, the viscoplastic FEA with the Omega creep model generates detailed information on every step during the creep evolution, providing sufficient insight into stress relaxation and creep damage accumulation. After a short loading stage, the high-stress region induced by non-primary load begins to relax to a stable level. Simultaneously, in other regions, the relatively low stress increases gradually, leading to a stress redistribution which makes the local stress field at the transition region, connecting the main vessel and nozzle, tend to be more uniform, as shown in Fig. 3.10. This stress redistribution results from the attribution of the self-

equilibrating residual stress field that ensures an equilibrium with the external load. As the creep damage is controlled by the combination of stress level, working temperature and creep dwell, the critical location of creep damage may shift with the stress redistribution when the dwell time progresses, which is different from the case of fatigue-induced failure where the critical location normally keeps unchanged. During the tertiary creep stage, with the creep damage continuously cumulating (see Fig. 3.11), the creep strain rate starts to accelerate, leading to the subsequent creep crack initiation and propagation.

Table 3.3 compares the results of the creep rupture limit of the reactor under the predefined temperature field for 250,000 hours of dwell period. It can be seen that the creep rupture limit calculated by the Omega model-based analysis is lower (21.30 MPa, about 12% to 14% less than the other two methods) than the others which produce two close limit values, 24.95 MPa and 24.19 MPa, respectively. Essentially, the failure criterion of the Omega model-based creep assessment is dependent on the creep damage state variable (SDV 2 in Fig. 3.12) of one significant node that reaches nearly 1.0, which makes Equation (2.5) tend to diverge numerically. However, at the same time, the local materials surrounding the first failed node have not cumulated enough creep damage at all, which is observed from the creep damage distribution (around the inner corner of the nozzle) after 250,000 hours in Fig. 3.12. Therefore, the Omega model-based creep assessment produces a conservative result if the acceptable design load is determined based on the damage of a single node since this structure is able to withstand an additional load until the final rupture.

Exceptionally, if the interest is aimed at calculating the ultimate limit, the ABAQUS user subroutine USDFLD should be additionally employed to adjust Young's modulus at each damaged integration point along the specified path, so that the damaged elements are able to simulate the subsequent crack propagation from the initial crack tip. Moreover, in order to capture the crack propagation features, the element number along the potential fracture path should be refined with a large mesh density to alleviate the trouble of convergence difficulties during the sharp change in element stiffness. And, unavoidably, this poses an inevitable challenge for the computing resources, which, consequently, limits the application of this method only to the specimen structures stage at present instead of engineering structures.

Concerning the ISS curve-based approach and the LMM creep rupture analysis, the final creep rupture of the structure takes place once the material in a considerable region (see Fig. 3.9) meets the creep damage criterion, either the maximum isochronous stress (for the ISS curve-based method) or the revised creep rupture stress (for LMM creep rupture analysis). The creep rupture mechanism

calculated by these two methods is more consistent with the actual fracture failure, where the creep rupture region in the structure consists of a large number of fully creep damaged elements.

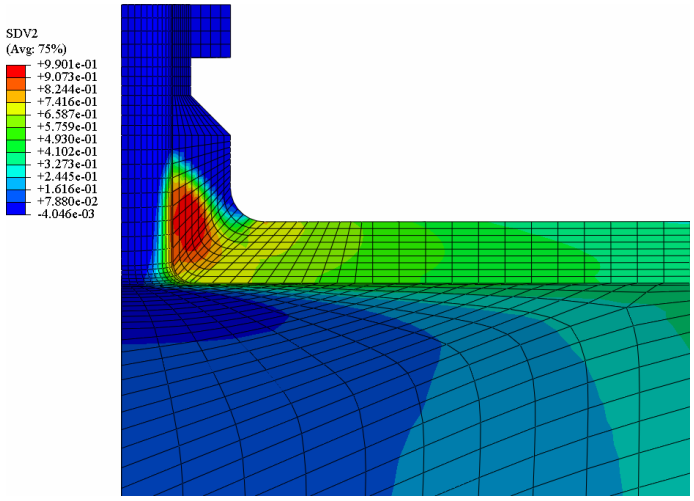

Fig. 3.12. Creep damage distribution after 250,000 hours by Omega model-based analysis

Table 3.3. Results of creep rupture limit load by three methods

Creep rupture analysis type	Creep rupture limit (MPa)	Difference of rupture limit (%)	Iterations	Difference of iterations (%)
LMM-based analysis	24.19	/	60	/
ISS curve-based analysis	24.95	3.1418	116	93
Omega model-based analysis	21.30	-11.9471	7218	11930

3.4.2 Discussion on computational efficiency

Besides conservativeness, computational efficiency is another obvious discrepancy between these methods that should be discussed. In Table 3.3, the number of iterations is considered as the total number of numerical iterations consumed in ABAQUS during the whole process of running

FEA programs. And the computational performances of different creep rupture analysis approaches are compared in Fig. 3.13. There is no doubt that the Omega model-based creep method consumes the most iterations, 7,218 times (in orange colour), among all three strategies, which is 120 times that of the LMM-based creep rupture analysis (in purple colour) and 62 times that of the ISS curve-based analysis (in green colour). Although this time history analysis has the capacity to simulate the exact evolution of each important result such as creep strain, creep damage and stress relaxation and redistribution over the creep dwelling period, this strategy appears redundant if the core problem of evaluation is to obtain the creep rupture limit as a design parameter for structures. Besides, when reaching the end of the tertiary creep stage depicted by CDM-based creep damage models, the creep strain rate in Equation (2.5) and creep strain soar rapidly even if an extremely tiny time increment is applied, which results in the difficulty in the convergence of the numerical calculation. Not to mention that subsequent fracture mechanics simulation may be required to solve the ultimate rupture load. Consequently, to prevent the FEA program from numerically diverging, the time increments have to be set as a series of tiny values, which causes a great consumption of computing resources. Facing a similar obstacle, the ISS curve-based inelastic approach employed the Newton-Raphson iteration scheme to solve non-linear problems so that when approaching the physical instability or encountering convergence difficulties, predicting the creep limit accurately needs a large number of equilibrium iterations (116 times in this case) in spite of being lower than the cost of Omega model-based analysis.

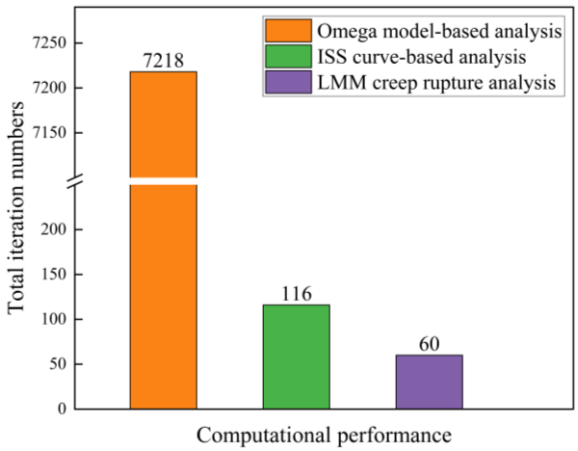

Fig. 3.13. Comparison of the computational efficiency of different creep rupture analyses

On the contrary, because of utilizing a more efficient iteration form, the LMM-based creep rupture analysis method performs a series of linear solutions to match the material's non-linear

behaviour based on the extended upper bound shakedown theory, which adopts a significantly lower number of iterations (consumed 60 times in this case) than the other two methods.

To summarize, although the Omega creep damage model is capable of providing detailed creep strain and creep damage information during the creep development process, it consumes too much computational resource during simulation. In addition, according to the API 579-1/ASME FFS-1[4] and ASME Boiler and Pressure Vessel Code Case 2605-3 [16], there are 10 related material parameters to depict the creep behaviour of the specified material. Besides, the failure threshold is only defined by the creep damage of one critical location, which finally produces acceptable but over-conservative load conditions. The ISS curve-based method needs the isochronous stress-strain curves data under a certain range of dwell periods and operating temperatures, which are derived from either long-term creep tests or the mathematical extrapolation [85] of short-time creep experiment data. However, when the Newton-Raphson iteration needs very tiny increments, its calculation process still faces the problem of difficulty in convergence. By contrast, with only one key parameter included, the revised yield stress, the LMM-based creep rupture analysis shows a more reasonable creep rupture limit for engineering design and evaluation than others. Moreover, by running a series of more robust and efficient linear algorithms, the LMM-based method costs the least amount of computing resources.

3.5 Creep rupture limit boundary of the hydrogenation reactor

In this section, the creep rupture limit boundary of the hydrogenation reactor with monotonic load conditions is built by the LMM creep rupture analysis procedure, and the effectiveness and accuracy of the proposed boundary are discussed by the CDM-based non-linear FEA.

3.5.1 Creep effect on limit boundary

Apart from calculating the creep rupture limit under specified load conditions, a more useful capability of the LMM creep rupture analysis is to construct the limit boundary including the mechanical load and thermal load. By selecting a series of load points sequentially in the load space (usually according to the ratios of different load combinations), the hydrogenation reactor's creep rupture limit boundary for 250,000 hours dwelling period (shown in solid red line) and the normal limit load boundaries (shown in black dash line) are constructed in Fig. 3.14. Here, the coordinates of the vertical and horizontal axes are normalised by the initial temperature condition $T_0 = 454$ °C and the limit pressure without any creep effect $P_0 = 38.52$ MPa, respectively.

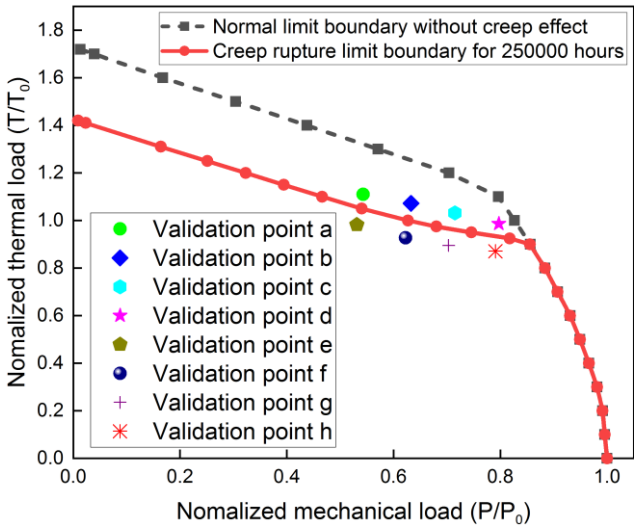

Fig. 3.14. Temperature-dependent normal limit load and creep rupture limit boundaries by LMM analysis

At the bifurcation location of two curves, a definite turning point divides the structural response into the high-temperature-dominated zone and mechanical load-dominated zone. Above this turning point, the failure mode is mainly influenced by the creep rupture under the high-temperature condition, and the acceptable mechanical load decreases gradually with the increasing thermal condition. In contrast, when below this turning point, the revised yield stress in the LMM creep rupture analysis algorithm is controlled by the material's yield stress. The creep-induced weakening effect reduces or disappears, and the excessive plastic deformation-induced failure mode takes over the dominant factor, leading to plastic instability or plastic collapse as the monotonic mechanical load approaches the limit on the boundaries.

Compared to the limit load boundary without the creep effect, the acceptable load domain shrinks inward dramatically under the elevated temperature, which means that the creep effect on the limit boundary appears only at the high-temperature zone above the turning point. This is because, under elevated temperature conditions, the revised yield stress is determined by the creep rupture stress which is much lower than the normal yield stress.

It is worth noting that normally, the effect of high-temperature conditions on structural failure is manifested in two forms: thermal stress and weakening of key material strength parameters. In this case, the thermal stress is secondary stress, which is self-balancing stress, and, hence, makes no contribution to the limit load. However, the weakening of material strength parameters under high-temperature conditions, including yield stress and creep rupture stress, is the significant factor

affecting the limit load. Consequently, this also results in the shape of the two limit curves in high-temperature regions. Even under extremely small mechanical loads, the limit curves are only close to the y-axis and have no intersection with the y-axis.

3.5.2 Verification strategy of creep rupture boundary

In order to further verify the effectiveness of the creep rupture boundary curve by LMM creep rupture analysis, validation work has been provided by Ref. [81], where the creep rupture stress functions as the standard yield stress during the step-by-step inelastic FEA. However, this method is only able to test the effectiveness of the extended LMM shakedown procedure with the revised yield stress employed, and it is not capable of directly verifying the creep rupture limit associated with a predefined dwell time.

Here, a new verification strategy for the creep rupture boundary is proposed to consider creep damage development. Firstly, the checkpoints are arranged according to the creep rupture boundary calculated by the LMM creep rupture analysis, where checkpoint A is just inside the creep rupture boundary, and checkpoint B is selected slightly above the boundary. Then, the conditions of checkpoints are applied to the FEA model to perform the detailed creep analysis with the Omega creep model. If the calculated creep rupture boundary is accurate, checkpoint A should produce a creep failure time larger than the predefined creep rupture time, whereas the creep failure time of checkpoint B should be less than the predefined time. The flowchart illustrates this verification strategy for creep rupture boundary, as shown in Fig. 3.15.

Four pairs of checkpoints are chosen in the load space at the following location: (a) (0.54292, 1.110), (b) (0.63278, 1.072), (c) (0.71504, 1.032), (d) (0.7973, 0.986), (e) (0.53128, 0.982), (f) (0.62265, 0.9275), (g) (0.70314, 0.895), (h) (0.79097, 0.871) in Fig. 3.14. All the condition points are determined according to the most commonly used operating temperature conditions of the hydrogenation reactor, ranging from 395 ℃ to 495 ℃ [86], among which checkpoints (a), (b), (c) and (d) are just above the creep rupture limit boundary, slightly outside the acceptable domain. While, accordingly, checkpoints (e), (f), (g) and (h) are selected inside the safe region near the boundary. Here, the detailed creep analysis is adopted to verify the accuracy of the creep rupture boundary under all the load conditions.

The verifications are listed in Table 3.4, and it can be seen that as the creep damage variable (output by ABAQUS SDV value) accumulates to the limit (the threshold of creep damage is equal to 1.0),

all load points outside the creep rupture limit boundary (including (a), (b), (c) and (d)) exhibit the creep rupture failure. The creep rupture time under these conditions is significantly less than the period (250,000 hours) which is prescribed by the corresponding creep rupture boundary.

Instead, when inside the acceptable regions, the creep behaviour of 250,000 hours of dwelling periods under each load condition satisfies the requirement of creep limit, and, at the same time, the creep damage variables at the predefined keypoint are lower than the threshold value (creep damage equals to 1.0), with their values 0.9827, 0.9842, 0.9881 and 0.9811, respectively (see detailed creep FEA results from Figs. 3.14 (e) to (h)). In other words, if the structure is subject to the load conditions determined by checkpoints (e), (f), (g) or (h), the maximum acceptable creep dwelling periods can be extended to a longer time, 267,012 hours, 272,531 hours, 262,311 hours and 268,630 hours, respectively. It is worth noting that all the checkpoints selected here are aimed at reflecting the response of the structure and accuracy of the boundary at the elevated working temperature, where the creep effect plays a more dominant role, hence avoiding the influence of plastic yield due to high mechanical load as much as possible.

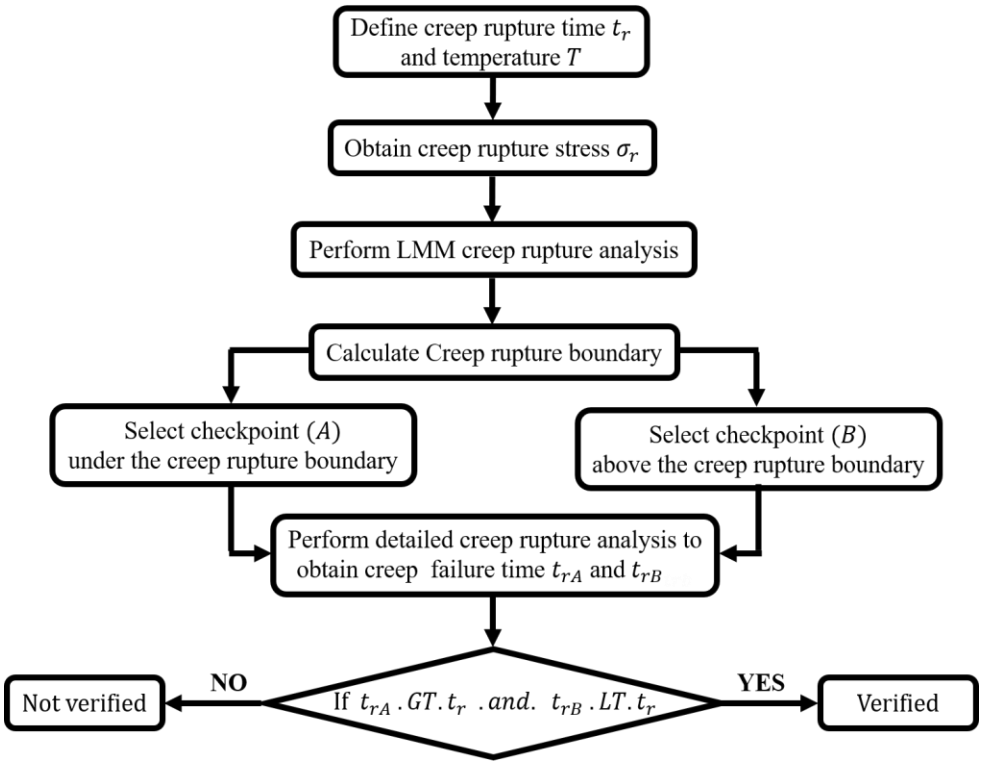

Fig. 3.15. Flowchart of verification strategy for creep rupture boundary

Table 3.4. Verification of the creep rupture boundary constructed by LMM creep rupture analysis

Checkpoint		Location	Maximum creep dwelling time (hours)
Outside	(a)	(0.54292, 1.110)	Up to 232675
	(b)	(0.63278, 1.072)	Up to 238164
	(c)	(0.71504, 1.032)	Up to 230922
	(d)	(0.79730, 0.986)	Up to 231981
Inside	(e)	(0.53128, 0.982)	Up to 267012
	(f)	(0.62265, 0.9275)	Up to 272531
	(g)	(0.70314, 0.895)	Up to 262311
	(h)	(0.79097, 0.871)	Up to 268630

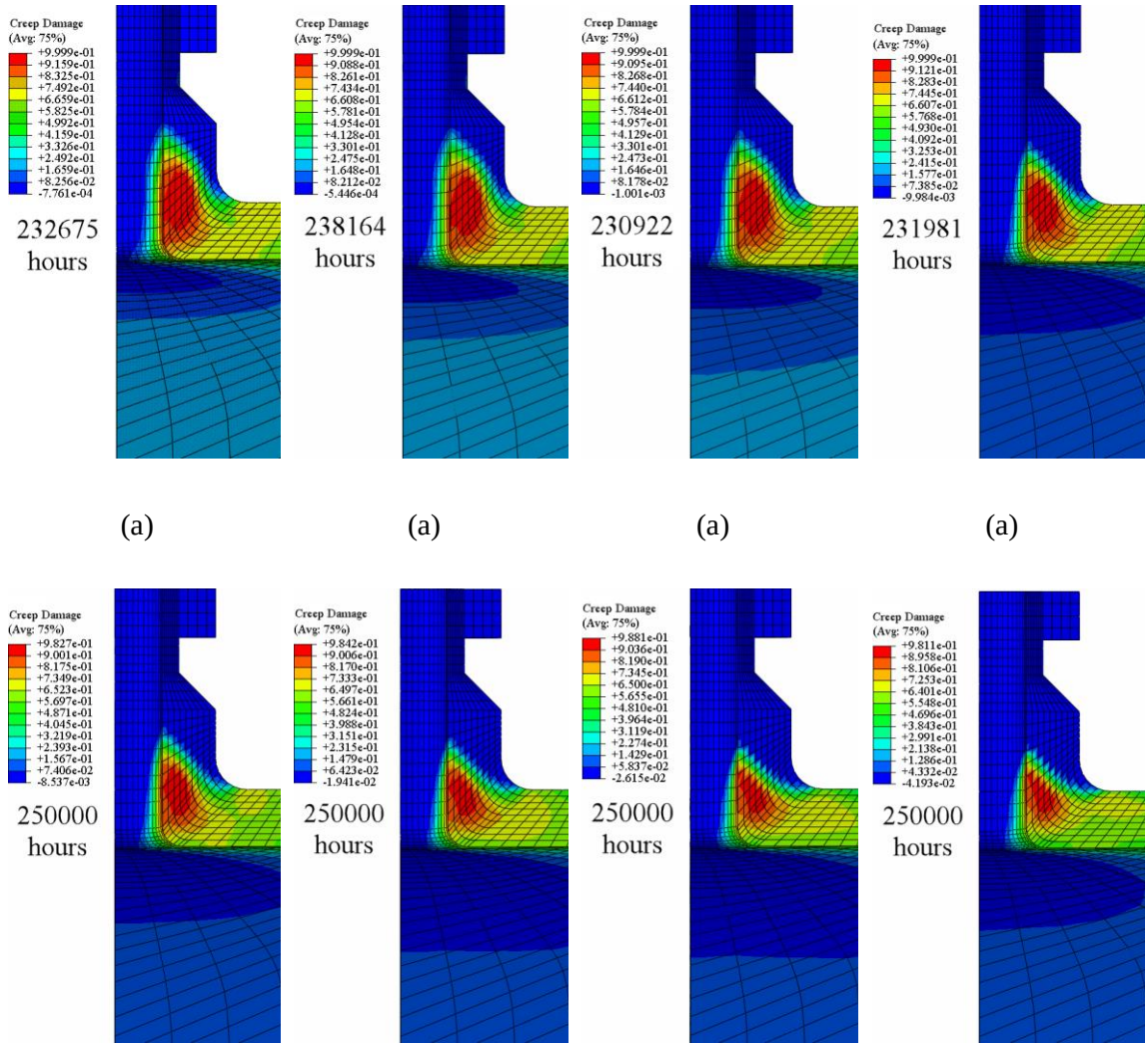

Fig. 3.16. Creep damage for verification cases: (a) creep damage under condition a; (b) creep damage under condition b; (c) creep damage under condition c; (d) creep damage under condition d; (e) creep damage under condition e; (f) creep damage under condition f; (g) creep damage under condition g; (h) creep damage under condition f; (g) creep damage under condition h

3.6 Further discussions of creep rupture assessment with cyclic load conditions

When extending the monotonic load condition to the cyclic one under a high-temperature environment, creep-fatigue interaction is viewed as a complicated failure behaviour by Refs. [87,

88]. Due to the severe combinations of mechanical and thermal loads, the cyclically enhanced creep and creep-enhanced plasticity interact simultaneously, leading to creep-fatigue damage accumulation. However, creep rupture is the first considered failure mode that should be avoided for equipment under high-temperature conditions.

Adopting the cyclic load path prescribed in Fig. 3.17, a cyclic creep rupture assessment is also able to be performed by the LMM-based creep rupture analysis where both mechanical load and thermal load conditions are assumed to be cyclic. Following the same strategy adopted when dealing with the monotonic loads, in Fig. 3.17, the black line represents the normal elastic shakedown boundary, while the cyclic creep limit boundary for 250,000 hours is presented by the red line, with an obvious inward contraction compared with the shakedown boundary.

Here, three typical failure mechanisms are distinguished by the different zones in terms of the limit boundaries of the cyclic load. The first one is when located outside the shakedown boundary, the hydrogenation reactor structure experiences the plastic ratcheting behaviour for the sake of excessive cyclic plastic deformation, with the plastic strain accumulating after every cycle.

Secondly, considering the load condition under the cyclic creep limit boundary, since the stress relaxation has fully developed to a steady state, all subsequent loading and unloading keep repeating elastically in every cycle, without any plastic behaviour. As a result, this structure shows a general shakedown phenomenon, and finally, the creep rupture failure occurs at the limit time specified by the corresponding boundary. The load condition point 1 is defined to exhibit this cyclic response by a step-by-step creep analysis, and the cyclic stress-strain curve in Fig. 3.18 verifies this mechanism. Although the plastic behaviour occurs during the first cycle, this cyclic load combination dominated by the primary load cannot generate continuous stress relaxation in the subsequent cycles, which is identical to the monotonic load case. That means under load condition 1 the cyclic loading behaviour makes no contribution to the final creep rupture failure.

The last failure mode is when the load condition moves into the intermediate region between the shakedown boundary and the cyclic creep limit boundary. Here, the response (that should have caused an elastic shakedown state similar to behaviour under condition 1 if there is no creep effect involved) changes to the creep effect-induced ratcheting or creep ratcheting [89, 90]. By validation result under load condition 2 (illustrated in Fig. 3.19), it can be observed that the increase of creep-induced inelastic strain makes the reverse plastic yield and elastoplastic unloading always exist after each creep dwell step. And this load condition pushes the unclosed stress-strain hysteresis

loops forward, keeping accumulating the cyclic inelastic strain cycle-by-cycle. In this response, the significant creep strain increment produced by the creep dwell period cannot be fully compensated by the reverse plastic strain during the unloading stage, which results in the open hysteresis loop. Compared with the second failure mode, the cyclic inelastic behaviour elevates the stress level at the start of each creep dwell period, making it much higher than the previous end of dwell stress, thereby strengthening the creep damage cyclically.

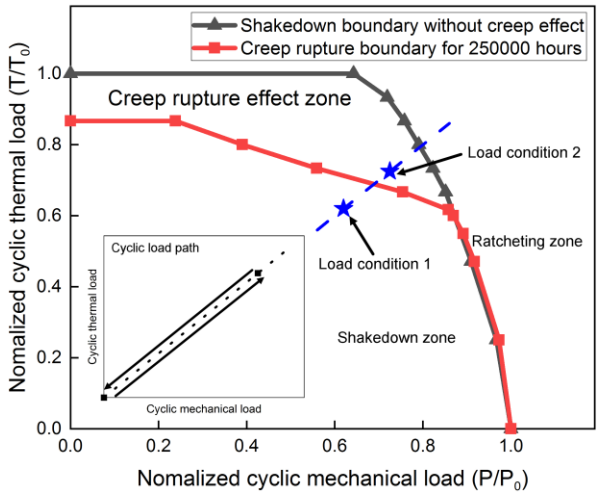

Fig. 3.17. Limit condition boundaries for cyclic load condition by LMM extended shakedown analysis

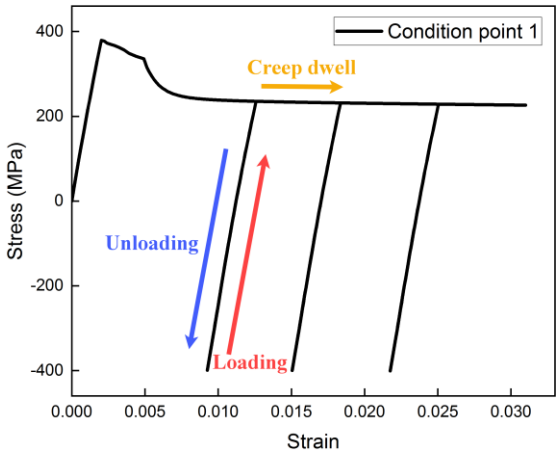

Fig. 3.18. Cyclic behaviour for load condition 1

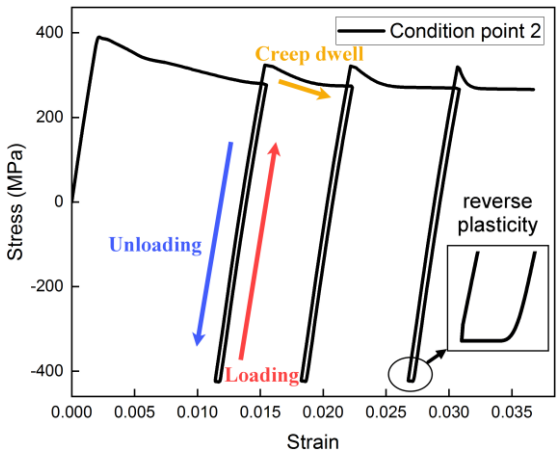

Fig. 3.19. Cyclic behaviour for load condition 2 (creep-induced ratcheting)

3.7 Conclusions

This chapter presents a detailed comparative investigation of creep rupture limit analysis techniques in engineering assessment based on the unified material data, including the ISS curves, the Omega creep damage model and the LMM creep rupture analysis. Three approaches are implemented by using ABAQUS with the user subroutines to assess the high-temperature pressure vessel component with creep rupture risk, providing a deep understanding of creep rupture failure mechanisms and comprehensive insight into creep rupture evaluation techniques from different views. The main conclusions of this study are as follows:

1. Although according to the ASME Boiler and Pressure Vessel Code Case 2605-3, the Omega creep damage model-based analysis can simulate the entire history of the creep damage evolution and predict the dangerous location, it seems time-consuming and conservative to determine creep rupture limit, since the initial damaged node is not suitable to indicate the creep rupture failure of the whole structure.

2. The proposed LMM creep rupture analysis is a concise and robust tool to address the creep rupture limit problem, providing a reasonable creep limit and clear creep rupture failure mechanism, which achieves a good balance between accuracy and efficiency.

3. In the engineering application, a creep rupture limit boundary for 250,000 hours dwelling period is given out by the LMM numerical scheme, where the acceptable domain is divided into two regions in terms of different failure mechanisms.

4. A numerical strategy is also proposed to verify the creep rupture boundary by the LMM creep rupture analysis, showing that this boundary can identify the acceptable domain in the load space composed of mechanical and thermal loads, which could be employed as a design and assessment tool for the high-temperature structures.

5. When evaluating more complicated cyclic load conditions, the LMM-based creep analysis also has the capability to scheme different failure regions, including general shakedown, plastic ratcheting and creep-induced ratcheting.

4 Effect of constraint on cyclic plastic behaviours of cracked bodies and the establishment of unified constraint correlation

4.1 Introduction

As an important factor that affects the stress and strain fields at the crack tip, constraint not only exists in the structures and affects the material fracture behaviour under monotonic loading, but also changes the cyclic plastic response of cracked structures (including ratcheting and low cycle fatigue (LCF)) under cyclic loading. Thus, it is significant to investigate the cyclic plastic response of the material and cracked structure considering the constraint effect.

Due to the high sensitivity of the crack tip to the cyclic structural responses [91], properly refined elements should be involved during discretizing cracked components, especially for the crack tip location [92] where the gradients of stress and strain are susceptible to the crack size. Hence, given the better balance between computational accuracy and efficiency, several numerical procedures were developed and devoted to addressing the ratcheting of a material or engineering structure with a crack. Chen et al. [93, 94] applied the LMM to study the effect of circular holes on the ratchet limit in a centre-cracked plate. Li et al. [95] analysed the ratchet limit of a pipe with an axisymmetric circumferential crack in a mismatched weld. Tong et al. [96] predicted the crack growth rate in a vacuum environment by including both ratcheting strain and accumulated inelastic strain near the crack tip. In addition to these main factors affecting the ratchet limit including cyclic load type, load level, crack location and size, the majority of current understanding attributed the influence of the crack on the ratcheting behaviour to the local highly discontinuous geometric effects and the related examinations mainly concentrated on the distribution rules and shape of the cyclic plastic zone [97, 98].

To reasonably carry out the structural integrity assessment containing defects, it is crucial to deal with the constraint effect in the detailed analysis of structural response, and hence, engineering standards [99-102] have incorporated the constraint effect into the analysis procedures. Several numerical investigations of the constraint effect on fatigue crack evaluation were reported by Refs. [103-105], which defined and utilized the constraint parameters to describe the underlying

influence of the constraint effect on the predictions of crack propagation life. Furthermore, the studies of constraint effect matching between the laboratory standard specimens and actual engineering components were explored, with specified applications to the steam turbine blade [106] and cracked pipeline [107] elaborated under monotonic load conditions.

However, the effect of constraint on the ratchet limit and alternating plasticity in different cracked specimens has not been studied clearly. And so far, there is no evidence to show whether there is a certain correlation between the constraint effect and the cyclic plastic response or whether there is a suitable constraint parameter that is able to characterise the influence of the constraint effect on the cyclic plastic response.

In this chapter, the first motivation is to investigate the effect of constraint conditions on the cyclic responses of cracked structures, including the reverse plasticity and ratcheting behaviour. And this analysis is aiming at establishing ratcheting boundaries for the cracked specimens as well as revealing the influence mechanisms of different constraint conditions. And the second purpose is to find an appropriate constraint effect parameter which has the capability to clearly depict the relationship between the ratchet limit and the strength of constraint and the relationship between the cyclic plastic strain range and the strength of constraint in terms of the cracked specimen. It is also intended to explore the potential of such a relationship in assessing cracked engineering structures. Last but not least, the third aim is to verify all the numerical processes which are applied in the virtual experiments when deriving the pertinent constraint parameter.

The structure of this chapter is outlined as follows. In Section 4.2, the numerical method, LMM procedures, to deal with the cyclic plastic responses is elaborated. Then, the selected experimental specimens, the laboratory compact tension (CT) and central-cracked tension (CCT) specimens with different in-plane and out-of-plane constraint conditions, are described in Section 4.3. And in Section 4.4, the interactive boundaries of ratcheting and constraint effect are constructed, with the mechanisms of the constraint effect on the ratchet limit and alternating plastic strain range in different cracked specimens analyzed comprehensively. Furthermore, the unified constraint parameter A_p is employed to reflect the strength of both in-plane and out-of-plane constraint conditions during ratcheting and alternating plasticity analyses. And the linear correlation between the parameter $\sqrt{A_p}$ and the cyclic plastic response of the cracked specimen is also derived. Next, a series of numerical verifications are presented in Section 4.5, where the effectiveness and accuracy of the proposed analysis strategy are demonstrated in detail. In the last section, the main conclusions of this study are summarized.

4.2 Numerical procedures for determination of cyclic plastic responses under the current LMM framework

4.2.1 Definition of cyclic load history

When an elastic-perfectly plastic (EPP) made structure is subjected to a general cyclic load, this condition can be decoupled into cyclic and constant components [108]. It can be assumed that a structure is subjected to a cyclic time-dependent surface load $F(x_i, t)$ applied on the part of the structure surface S_T. On the rest surface S_u, the displacement rate should be equal to zero. The process is considered over a full cycle from $t = 0$ to $t = \Delta t$. After decomposing the cyclic load condition into a cyclic part and a constant part [109], it can be represented by the following load:

$$F(x_i, t) = \lambda \bar{F}(x_i) + P(x_i, t) \tag{4.1}$$

here λ is a load parameter, $\bar{F}(x_i)$ is the constant load component and $P(x_i, t)$ is the cyclic part. The linear elastic stress corresponding to the time-dependent load condition is calculated by Equation (4.2):

$$\hat{\sigma}_{ij}(x_k, t) = \lambda \hat{\sigma}_{ij}^{\bar{F}} + \hat{\sigma}_{ij}^{\Delta}(x_k, t) \tag{4.2}$$

Here it can be seen that by changing the load parameter λ, the whole process during a full cycle can be taken into account.

4.2.2 Asymptotic cyclic solution

There are three components inside one typical response cycle: the elastic response which is a transient response accumulated up to the beginning of the cycle, and a residual component making contributes to the remaining change in the cycle [110]. The stress solution of the general cyclic load condition is comprised of the time-dependent and constant residual stress component, which is expressed by Equation (4.3):

$$\sigma_{ij}(x_k, t) = \hat{\sigma}_{ij}(x_k, t) + \bar{\rho}_{ij}(x_k) + \rho_{ij}^{r}(x_k, t) \tag{4.3}$$

where $\hat{\sigma}_{ij}$ is the elastic component, and $\bar{\rho}_{ij}$ is a constant stress field on equilibrium with a zero surface boundary condition state, corresponding to the residual stress field at the start and end of the cycle. And the time-dependent residual component over the cycle meets the condition:

$$\rho_{ij}^{r}(x_k, 0) = \rho_{ij}^{r}(x_k, \Delta t) = 0 \tag{4.4}$$

4.2.3 Minimum Theorem in Excess of Shakedown

The plastic strain is defined by a convex yield condition [108]:

$$f(\sigma_{ij}) \leq 0 \tag{4.5}$$

and the associated flow law is:

$$\dot{\varepsilon}_{ij}^{p} = \dot{\alpha}\frac{\partial f}{\partial \sigma_{ij}}, \qquad f = 0 \tag{4.6}$$

where $\dot{\alpha}$ is a plastic multiplier. And the maximum work principle should be:

$$(\sigma_{ij}^{c} - \sigma_{ij}^{*})\dot{\varepsilon}_{ij}^{c} \geq 0 \tag{4.7}$$

where σ_{ij}^{c} is the stress at yield state, $f(\sigma_{ij}^{c}) = 0$, associated with the flow law above, with the plastic strain rate $\dot{\varepsilon}_{ij}^{p} = \dot{\varepsilon}_{ij}^{c}$. And σ_{ij}^{*} represents any stress state that meets the yield condition, $f(\sigma_{ij}^{*}) \leq 0$.

Here a strain energy function [93] is defined as

$$I(\dot{\varepsilon}_{ij}^{c}, \lambda) = \int_{V}\int_{0}^{\Delta t}\left(\sigma_{ij}^{c} - \lambda\hat{\sigma}_{ij}^{\bar{F}} - \hat{\sigma}_{ij}^{\Delta}(x_k, t)\right)\dot{\varepsilon}_{ij}^{c}\,dt\,dV \tag{4.8}$$

where $\dot{\varepsilon}_{ij}^{c}$ is the kinematically admissible strain rate.

There also exists a load parameter so that

$$f\left(\lambda\hat{\sigma}_{ij}^{\bar{F}} + \hat{\sigma}_{ij}^{\Delta}(x_k, t) + \bar{\rho}_{ij}(x_k) + \rho_{ij}^{r}(x_k, t)\right) \leq 0 \tag{4.9}$$

and that

$$I(\dot{\varepsilon}_{ij}^{c}, \lambda) \geq I(\dot{\varepsilon}_{ij}^{s}, \lambda) \tag{4.10}$$

where $\dot{\varepsilon}_{ij}^{s}$ is the exact solution.

4.2.4 The calculations of time-dependent residual stress field and plastic strain range by DSCA procedure

The direct steady cyclic analysis (DSCA) proposed by Ref. [111] aims to analyze the time-dependent residual stress field and the corresponding plastic strain range due to the cyclic load condition. It can be assumed that in a deviatoric stress component space, the plastic strain occurs only at the load vertexes, which corresponds to *N* time points, $t_1, t_2, \dots, t_N$, in the cyclic load condition, leading to $\Delta\varepsilon_{ij}^{c} = \Sigma_{n=1}^{N}\Delta\varepsilon_{ij}^{n}$. Here $\Delta\varepsilon_{ij}^{n}$ is the increment of plastic strain in terms of time t_n. The strain energy function is approximated by the following equations:

$$I\left(\dot{\varepsilon}_{ij}^{c}, \lambda\right) = \sum_{n=1}^{N} I^{n} \tag{4.11}$$

$$I^{n}\left(\Delta\varepsilon_{ij}^{n}, \rho_{ij}(t_n)\right) = \int_{V}\left\{\sigma_{ij}^{n}\Delta\varepsilon_{ij}^{n} - \left(\hat{\sigma}_{ij}^{\Delta}(t_n) + \rho_{ij}(t_n)\right)\Delta\varepsilon_{ij}^{n}\right\}dV \tag{4.12}$$

where the strain increment is compatible and the residual stress field is equilibrium.

Considering that based on isotropic elastic properties and a von Mises yield condition, the shear modulus $\bar{\mu}_{ni}$ is defined linearly by matching conditions,

$$\sigma_y = 2\bar{\mu}_{ni}\bar{\varepsilon}\left(\Delta\varepsilon_{ij}^{ni}\right) \tag{4.13}$$

where σ_y is the Mises yield stress, and the initial estimation of $\Delta\varepsilon_{ij}^{n}$ is set to be equal to $\Delta\varepsilon_{ij}^{ni}$. The following linear equations can be solved :

$$\Delta\varepsilon_{ij}^{Tf'} = \frac{1}{2\mu}\Delta\rho_{ij}^{nf'} + \Delta\varepsilon_{ij}^{nf'}, \Delta\varepsilon_{kk}^{Tf} = \frac{1}{3K}\Delta\rho_{kk}^{nf} \tag{4.14}$$

$$\Delta\varepsilon_{ij}^{nf'} = \frac{1}{2\bar{\mu}_{ni}}\left\{\hat{\sigma}_{ij}^{\Delta}(t_n) + \rho_{ij}(t_{n-1}) + \Delta\rho_{ij}^{nf}\right\}' \tag{4.15}$$

where

$$\rho_{ij}(t_{n-1}) = \rho_{ij}(t_0) + \Delta\rho_{ij}^{1} + \Delta\rho_{ij}^{2} + \cdots + \Delta\rho_{ij}^{n-1}, \rho_{ij}(t_0) = \bar{\rho}_{ij} \tag{4.16}$$

It should be noted that the mark $'$ means the deviatoric component, and the subscript kk represents the hydrostatic component.

An efficient numerical iteration strategy is proposed to address the linear equations according to the flowchart in Fig. 4.1. At the first load point t_1, the iteration is to calculate the time-dependent residual stress field $\Delta\rho_{ij}^1$ corresponding to the elastic solution $\hat{\sigma}_{ij}^{\Delta}(t_1)$. $\Delta\rho_{ij_m}^n$ is considered as the time-dependent residual stress field for the nth load point during mth cycle, where $n = 1,2,\dots,N$ and $m = 1,2,\dots,M$. The time-dependent residual stress field for all load points at each cycle should be computed, and after satisfying the convergence, the sum of every time-dependent residual stress field at each load point should be equal to zero. At the same time, the constant residual stress field can be derived by

$$\bar{\rho}_{ij} = \sum_{n=1}^{N} \Delta\rho_{ij_1}^n + \sum_{n=1}^{N} \Delta\rho_{ij_2}^n + \cdots + \sum_{n=1}^{N} \Delta\rho_{ij_M}^n \tag{4.17}$$

Accordingly, the plastic strain amplitude for the load point n is evaluated by

$$\Delta\varepsilon_{ij}^P(t_n) = \frac{1}{2\bar{\mu}_n}\left(\hat{\sigma}_{ij}^{\Delta'}(t_n) + \rho_{ij}'(t_n)\right) \tag{4.18}$$

Then, at the end of each iteration, the subsequent yield strength $\sigma_0^m(t_n)$ at the load instance t_n associated with the current plastic strain is re-calculated if needed when the strain hardening model is involved in the material property. And the linear matching condition is able to be updated at the last step of each iteration process by

$$\bar{\mu}_{m+1}(t_n) = \bar{\mu}_m(t_n)\frac{\sigma_0^m(t_n)}{\bar{\sigma}\left(\hat{\sigma}_{ij}^{\Delta}(t_n) + \rho_{ij}^m(t_n)\right)} \tag{4.19}$$

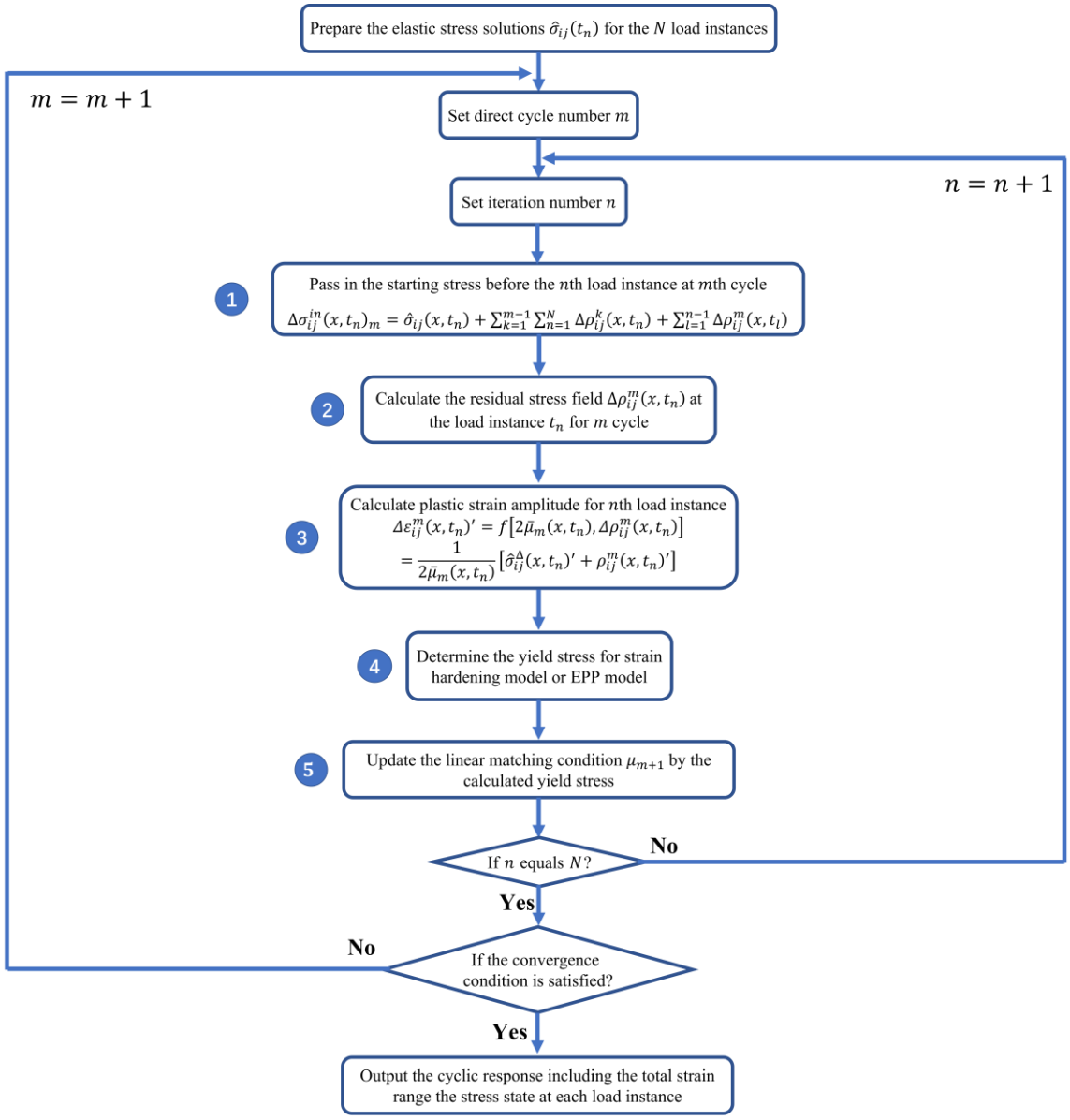

Fig. 4.1. Detailed iteration process of the DSCA procedure for cyclic plastic response calculation

4.2.5 Numerical procedure for ratchet limit calculation under the LMM framework

Under the LMM framework, the numerical procedure to calculate the ratchet limit contains two stages. In the first stage, the time-dependent residual stress related to the cyclic component of the load condition is acquired [109] by the DSCA procedure as shown in Section 4.2.4. Then, in the second stage, the ratchet limit multiplier can be accommodated by the established shakedown

analysis procedure [112] based on the upper bound shakedown theory in Equations (4.20) and (4.21), with the elastic stress field scaled by the changing residual stress calculated in the first stage.

$$\int_0^{\Delta t}\int_V \hat{\sigma}_{ij}\varepsilon_{ij}^{c}\,dtdV = \int_0^{\Delta t}\int_V \sigma_{ij}^{c}\varepsilon_{ij}^{c}\,dtdV \tag{4.20}$$

$$\hat{\sigma}_{ij} = \lambda\hat{\sigma}_{ij}^{\bar{F}} + \hat{\sigma}_{ij}^{\Delta}(x_k,t) + \rho_{ij}(x_k,t) \tag{4.21}$$

Given the von Mises yield condition and the associated flow rule, the strain energy associated with the yield state can be rewritten by

$$\int_0^{\Delta t}\int_V \sigma_{ij}^{c}\varepsilon_{ij}^{c}\,dtdV = \int_V^{N}\sum_{n=1}^{N}\sigma_{ij}^{c^n}\Delta\varepsilon_{ij}^{n}dV = \int_V\sum_{n=1}^{N}\sigma_y\bar{\varepsilon}\left(\Delta\varepsilon_{ij}^{n}\right)dV \tag{4.22}$$

where

$$\bar{\varepsilon}\left(\Delta\varepsilon_{ij}^{n}\right) = \sqrt{\frac{2}{3}\Delta\varepsilon_{ij}^{n}\Delta\varepsilon_{ij}^{n}} \tag{4.23}$$

Finally, the upper bound ratchet limit multiplier is expressed iteratively by a series of monotonically reducing upper bound ratcheting multipliers, defined by Equation (4.24), to predict the converged structural ratchet limit,

$$\lambda = \frac{\int_V \sum_{n=1}^{N}\sigma_y\bar{\varepsilon}\left(\Delta\varepsilon_{ij}^{n}\right)dV - \int_V\sum_{n=1}^{N}\left(\hat{\sigma}_{ij}^{\Delta}(t_n)+\rho_{ij}(t_n)\right)\Delta\varepsilon_{ij}^{n}dV}{\int_V \hat{\sigma}_{ij}^{\bar{F}}\left(\sum_{n=1}^{N}\Delta\varepsilon_{ij}^{n}\right)dV} \tag{4.24}$$

and the physical meaning of this load multiplier is the maximum capacity of the structure with a predefined cyclic load condition to withstand an additional constant load before ratcheting.

4.3 CT and CCT specimens with different constraint conditions

In this section, the virtual compact tension (CT) specimen and central-cracked tension (CCT) specimen are selected as the numerical models to investigate the influence of the constraint effect on the structural cyclic responses including the alternating plasticity and the ratcheting. The flowchart below displays the whole analysis procedure of the numerical strategies illustrated above.

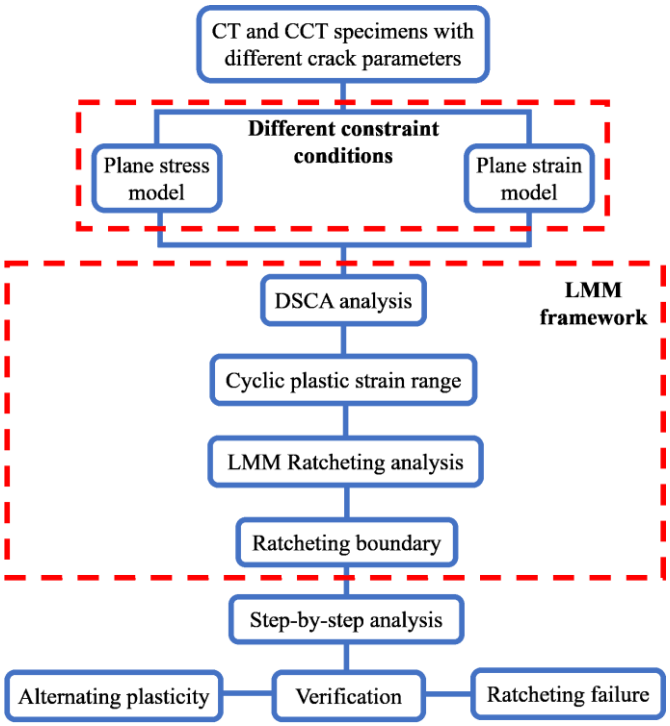

Fig. 4.2. Analysis strategy and application of the LMM DSCA and ratcheting analyses

4.3.1 Descriptions of CT and CCT specimens

Two sets of specimens containing compact tension (CT) specimen and central-cracked tension (CCT) specimen, with different loading configurations and geometrical features, are used in the subsequent finite element analysis (FEA), displayed in Fig. 4.3. To examine the in-plane constraint effect, four series of crack depths ratios denoted as $a/W = 0.1$, 0.3, 0.5 and 0.7 ($W = 32$ mm) are set for the CT and CCT specimens, reflecting the intensity of the constraint conditions, from low to high. On the other hand, plane stress and plane strain 2D conditions are employed respectively to distinguish the difference between out-of-plane constraint effects [113, 114], where the plane strain model provides the highest out-of-plane constraint condition for the cracked specimen, compared to the plane stress model with the lowest out-of-plane constraint condition.

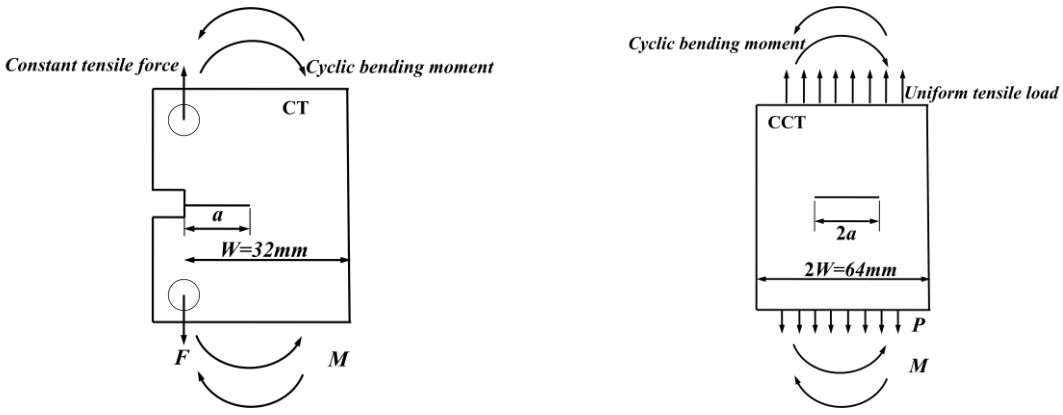

(a) (b)

Fig. 4.3. Loading configurations and geometries of the (a) CT specimen and (b) CCT specimen

4.3.2 Material property and FEA models

Both types of specimens are made of low alloy steel SA508 CL.3 which is widely used for pressure vessels in nuclear engineering [115, 116]. The cyclic behaviour of the material is described by the Ramberg-Osgood (R-O) model to provide the stress-strain relationship for the following FE analysis [117], and the cyclic response is approximated as follows,

$$\varepsilon_{ta} = \frac{\sigma_a}{\bar{E}} + \left(\frac{\sigma_a}{K}\right)^{\frac{1}{n}} \tag{4.25}$$

$$\bar{E} = \frac{3E}{2(1+\nu)} \tag{4.26}$$

where ε_{ta} is the total true strain amplitude, σ_a is the total stress amplitude, $\bar{E}$ is the multi-axial Young's modulus, $K = 660$ and $n = 0.116$ are the material parameters for the cyclic stress-strain curve model under room temperature, $E = 200$ GPa is the modulus of elasticity [84, 116, 118], and the Poisson's ratio ν is defined to be 0.3.

Since the 2D model can completely describe the in-plane constraint effect, and the plane strain and plane stress model are capable of maximising the difference between in-plane and out-of-plane constraint effect, the 8-node quadrilateral plane strain and plane stress elements with reduced integration CPE8R and CPS8R respectively are adopted to discretise the CT and CCT specimens in ABAQUS. Besides, around the crack tip, to reflect the highly complicated stress and strain fields

and the gradients of various physical quantities, a fine mesh configuration having a focused ring of elements surrounding the crack front is used with a small initial root radius (2 μm) at the crack tip (blunt tip) to enhance convergence of the nonlinear iterations, which is shown in Fig. 4.4 (in the red rectangle).

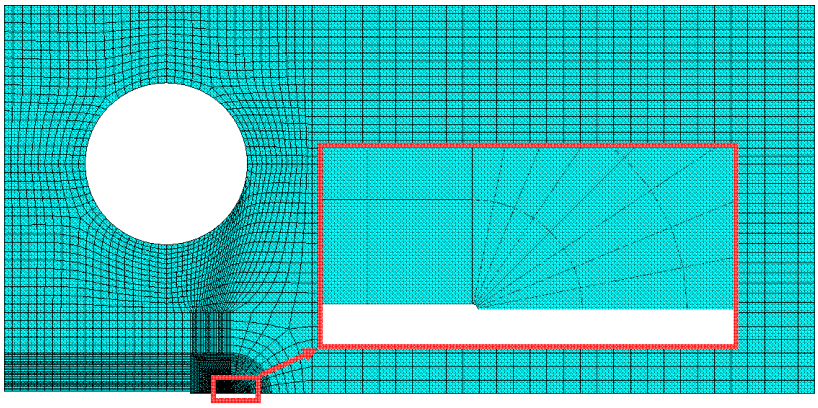

(a)

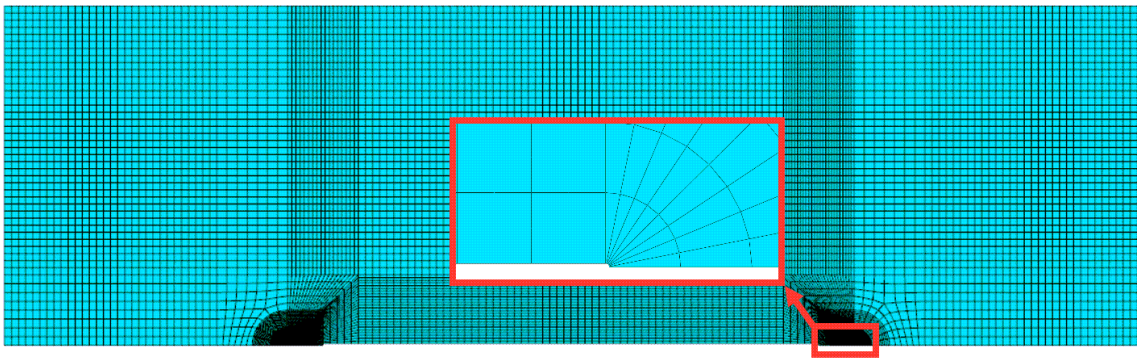

(b)

Fig. 4.4. FEA model and the feature of crack tip: (a) CT specimen and (b) CCT specimen

Due to the symmetry condition of the two types of specimens in the vertical direction, half models are created to save computing resources. For the CT specimen, a constant tensile force is applied on the left loading hole, and the CCT model is subjected to a constant tensile load which is exerted on the top surface. To simulate the effect of the cyclic bending moment history in Fig. 4.5, an equivalent cyclic linear distribution of stress is applied to the top boundary of each specimen. Moreover, the displacement at the symmetrical end of both models is constrained along the vertical direction, and another extra node is constrained in the horizontal direction to prevent rigid body displacement in each case. The spectrums of time-dependent loads in Fig. 4.5, depict the cyclic

modes of bending moment and tensile load, where all the reference loads are set to be one unit first, and then gradually scaled to the ratchet limit during the LMM ratcheting analysis.

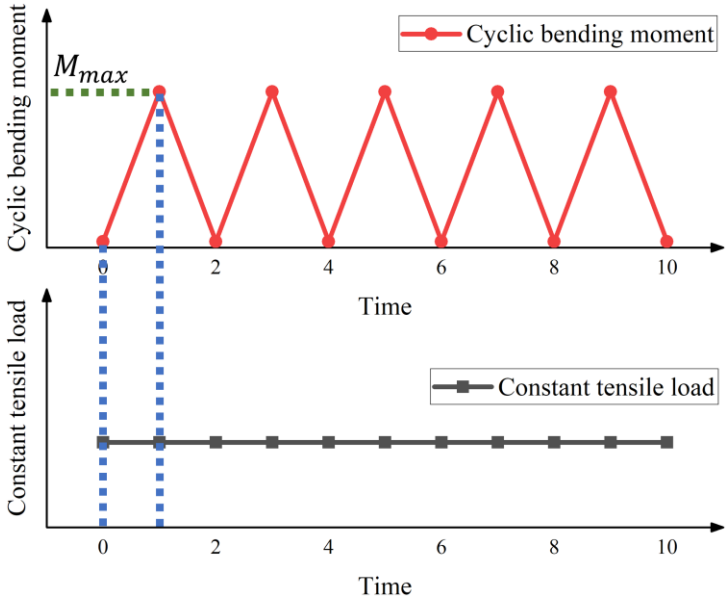

Fig. 4.5. Load spectrum of cyclic bending moment and constant tensile load

4.4 Effect of constraint on the ratchet limit and plastic strain range

The ratcheting boundary is capable of distinguishing different types of failure modes, including elastic shakedown, plastic shakedown or alternating plasticity and progressive plasticity or ratcheting behaviour. In this section, by repeatedly adopting the LMM ratcheting analysis at different levels of the cyclic load conditions, a series of ratchet limit boundaries of the provided load combinations are built for the CT and CCT specimens based on the presented LMM DSCA and ratcheting programs.

4.4.1 Ratcheting boundary of CT specimen with different constraint conditions

In the case of the CT specimen, the ratcheting boundaries under different constraint conditions are calculated by LMM ratcheting analysis considering a sequence of different cyclic bending moment levels, which are described in Fig. 4.6, where the horizontal and vertical axes represent the constant tensile force applied on the loading hole and the cyclic bending moment, respectively. It can be observed from both plane stress and plane strain CT specimens that, with the increasing in-plane constraint (a/W), the acceptable plastic shakedown region (including elastic and plastic

shakedown or alternating plasticity) is compressed inward continuously. That means, resulting from the enhancement of the in-plane constraint effect, the capacity of the structure against cyclic loads is severely weakened, which is similar to the effect of reducing the fracture resistance of the structure.

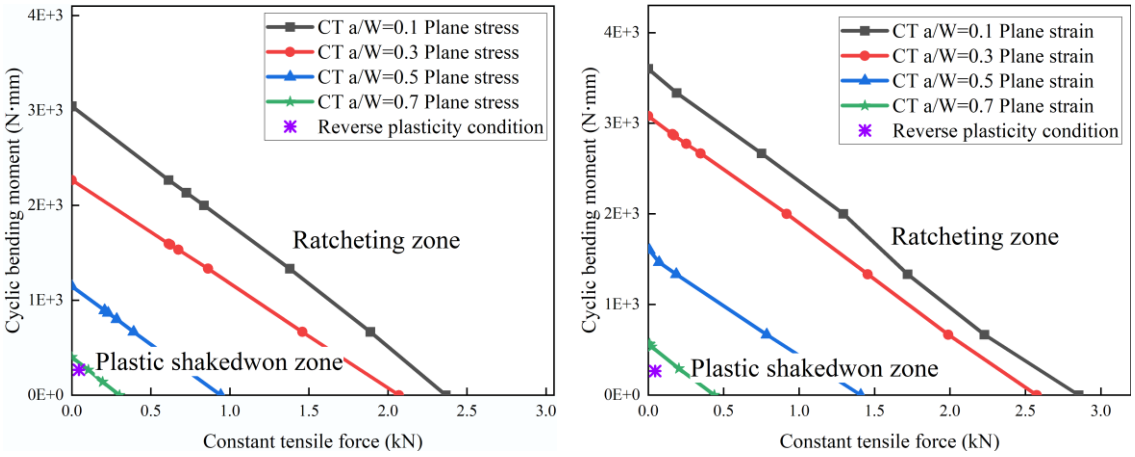

(a) (b)

Fig. 4.6. Ratcheting boundary of CT specimen: with (a) plane stress condition and (b) plane strain condition

Traditionally, there should be a linear relationship between the limit load of the structure and the effective cross-section. Conversely, as the dimension of the crack grows linearly, the limit capability of the structure that should have been linearly decreasing shows a nonlinear trend. Compared to the results of CT specimens with low constraint ($a/W = 0.1$ and $a/W = 0.3$), the ratcheting boundary shrinks inward more obviously, and the magnitude of change is also more significant in the CT specimens with high constraint ($a/W = 0.5$ and $a/W = 0.7$), which reflects that the higher constraint effect brings more remarkable change to the ratcheting boundary. In other words, the fluctuation of the ratchet limit is more sensitive under the high constraint effect, and, accordingly, the ratcheting boundary reduces more drastically and nonlinearly, which is caused by the complex response of the ratchet limit to the interaction of the high constraint effect and the reduction of the effective section.

Besides, in terms of out-of-plane constraint effects, by comparing plane stress and plane strain models with the same degree of in-plane constraint condition (a/W) and load conditions, it can be seen that the ratchet limit of the plane strain model is higher than that of the plane stress

model. Although the plane strain model corresponds to a higher out-of-plane constraint effect, considering that the ratchet limit is a measure of the overall capacity of the whole structure, the increase in thickness conceals the weakening by the high out-of-plane constraint effect, resulting in the ratchet limit greater than plane stress model.

4.4.2 Ratcheting boundary of CCT specimen with different constraint conditions

For the case of the CCT specimen, by employing the same numerical procedure to implement LMM ratcheting analysis, the ratcheting boundaries under different constraint conditions are constructed below in Fig. 4.7. Compared with the CT specimen mentioned above, a similar phenomenon can be noticed in both plane stress and plane strain models that the acceptable plastic shakedown region under each ratcheting boundary keeps remarkably shrinking as the in-plane constraint increases.

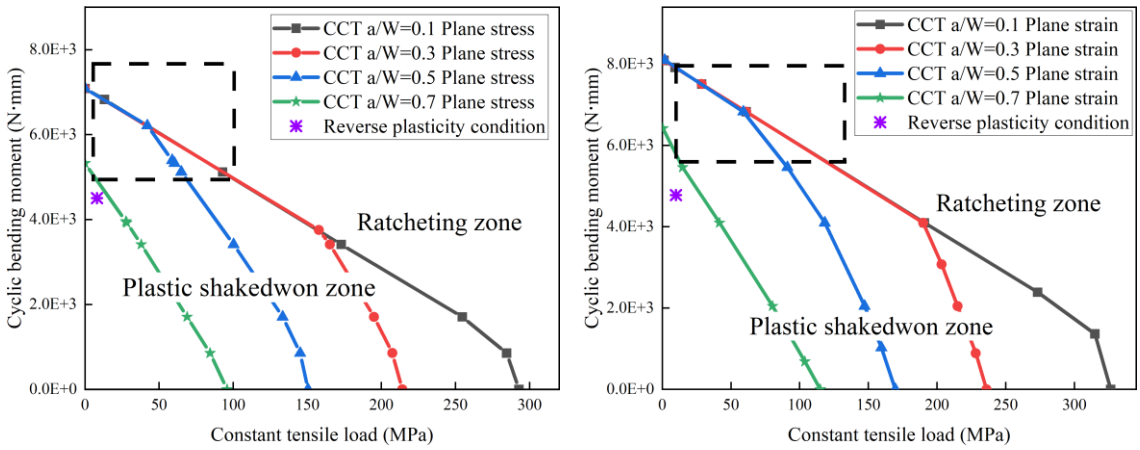

(a) (b)

Fig. 4.7. Ratcheting boundary of CCT specimen: with (a) plane stress condition and (b) plane strain condition

In addition, it is worth pointing out that although when the crack dimension (a/W) is between 0.1 and 0.5, these three ratcheting boundaries (the curves in black, red and blue) have a coincident segment in the interval of elevated cyclic bending moment level (inside the dotted rectangle), the ratcheting boundaries corresponding to crack sizes of 0.3 and 0.5 start to deviate from the ratcheting boundary with the lowest in-plane constraint ($a/W = 0.1$) successively. Forced by a stronger constraint effect in the CCT specimen, when considering the highest in-

plane constraint ($a/W = 0.7$), this ratcheting boundary (the curves presented in green) is completely separated from the previous three curves, where the value of reverse plasticity limit due to the cyclic bending moment is much lower than the previous three curves, which finally leads to the minimum plastic shakedown area.

Here it should be clarified that the constraint effect introduced by CCT specimens is weaker than that of CT specimens, hence the ratcheting boundaries of CCT specimens have a specific dense overlap area inside the dotted rectangles highlighted in Fig. 4.7, leading to a weaker separation of each boundary under the elevated cyclic bending moment level. However, the CT specimen, which symbolises a higher constraint effect, has a clearer degree of separation between each ratcheting boundary shown in Fig. 4.6. Hence, a general conclusion can be drawn that the ratcheting boundary of the cracked specimen is much more sensitive and vulnerable under the influence of high constraint effects.

Similarly, considering the out-of-plane constraint effect between CCT plane stress and plane strain models, the acceptable plastic shakedown regions (areas under the corresponding ratcheting boundaries in Fig. 4.7) of the plane strain model are much broader than that of the plane stress model, where the thickness is dominant in the comparative analysis. In other words, the out-of-plane constraint effect elevates the capability to resist ratcheting failure.

4.4.3 Unified correlation between constraint and the ratchet limit

In this study, the isoline of effective ratcheting strain $\varepsilon_{ratcheting} = 0.2$ ahead of the crack tip is used to calculate the A_{PEEQ}, where the effective ratcheting strain describes the net increment of the plastic strain after one entire load cycle (including one loading stage and one unloading stage), and A_{ref} is the reference area measured at the ratcheting state in the standard test with a standard CT plane strain model ($a/W = 0.5$).

The areas surrounded by the $\varepsilon_{ratcheting} = 0.2$ isolines are shown in Figs. 4.8 to 4.11. For each type of specimen, the ratcheting strain is calculated under the same level of cyclic bend moment, with the constant load located slightly outside the ratcheting boundaries in Figs. 4.6 and 4.7. This is intended to avoid the numerical error for which the ratcheting strain is too weak to identify due to the disturbance with the load condition point just located on the ratchet limit boundary, and, consequently, to maintain the conspicuous ratcheting level when demonstrating different constraint conditions.

As crack size a/W increases from 0.1 to 0.7, the in-plane constraint effect strengthens gradually, and, as a result, the areas (in red colour) surrounded by the $\varepsilon_{ratcheting} = 0.2$ isolines show a decreasing trend in both CT (see Figs. 4.8 and 4.9) and CCT (see Figs. 4.11 and 4.11) specimens. In addition, by comparing the areas surrounded by the $\varepsilon_{ratcheting} = 0.2$ isolines of plane stress and plane strain model under the same a/W level (e.g., comparing the results in Figs. 4.8 (a) and 4.9 (a), the results of plane strain models are much lower than those of plane stress models, where the strongest out-of-plane constraint condition of the plane strain model inhibits the development of ratcheting strain at the crack tip during the load combination outside the ratcheting boundary. Here, the plastic strain around the edge of the loading hole is generated by the contact stress between the supporting rollers and the inner surfaces of the loading hole during the movement of the rollers. However, as the loading hole is quite far from the crack tip, the ratcheting strain around the loading hole will not affect ratcheting results at the crack tip. Therefore, there is little impact of the ratcheting strain around the loading hole on the results in the thesis. Another noticeable difference is that due to the higher out-of-plane constraint level of plane strain models, relative to plane stress models, the shapes of areas of $\varepsilon_{ratcheting} = 0.2$ isolines of the plane strain model present a drop shape, which is more concentrated at the crack tip. However, in the plane stress model, the shapes of areas of $\varepsilon_{ratcheting} = 0.2$ isolines present a more widely distributed semi-ellipse.

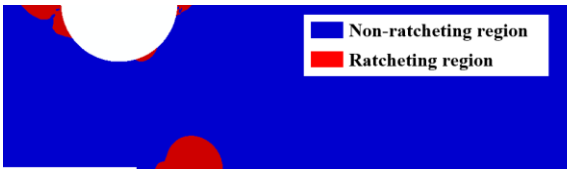

(a) $a/W = 0.1$

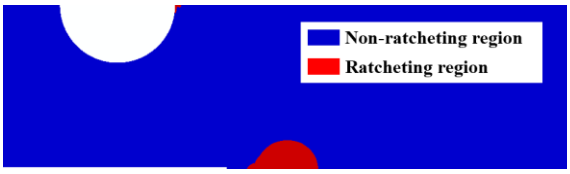

(b) $a/W = 0.3$

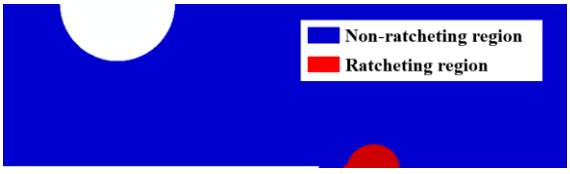

(c) $a/W = 0.5$

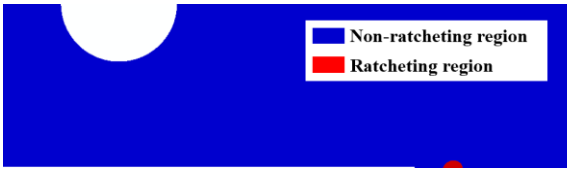

(d) $a/W = 0.7$

Fig. 4.8. Ratcheting strain contours of the CT plane stress model with different a/W

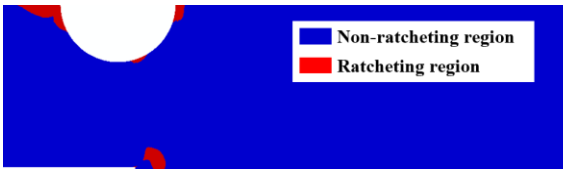

(a) $a/W = 0.1$

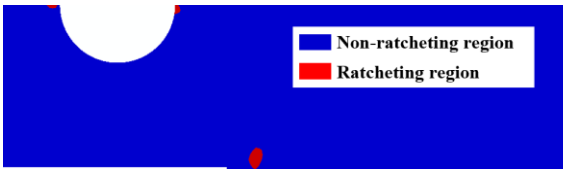

(b) $a/W = 0.3$

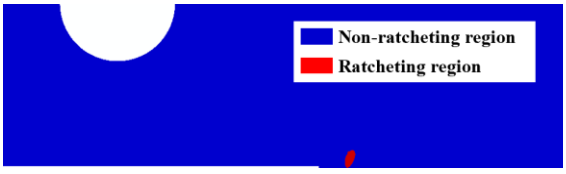

(c) $a/W = 0.5$

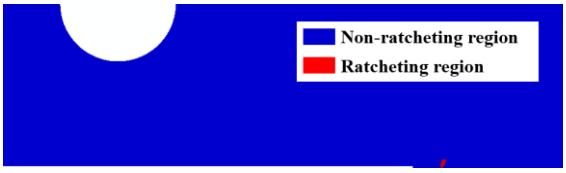

(d) $a/W = 0.7$

Fig. 4.9. Ratcheting strain contours of the CT plane strain model with different a/W

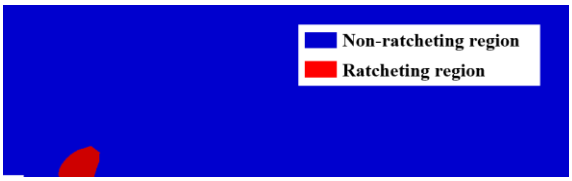

(a) $a/W = 0.1$

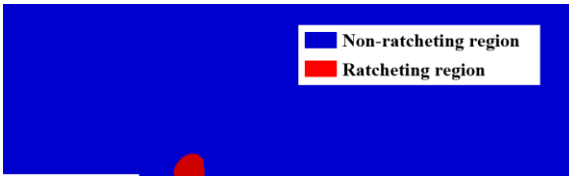

(b) $a/W = 0.3$

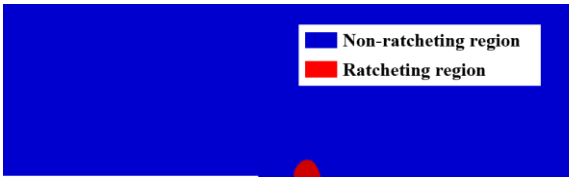

(c) $a/W = 0.5$

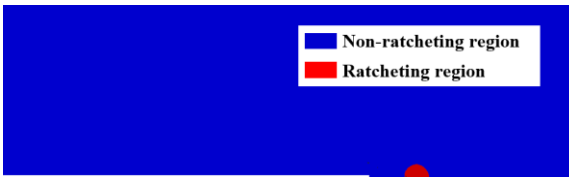

(d) $a/W = 0.7$

Fig. 4.10. Ratcheting strain contours of the CCT plane stress model with different a/W

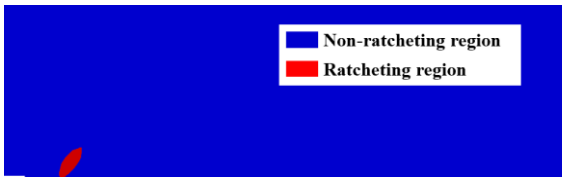

(a) $a/W = 0.1$

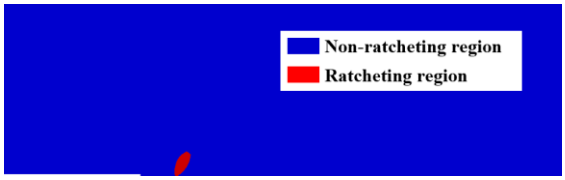

(b) $a/W = 0.3$

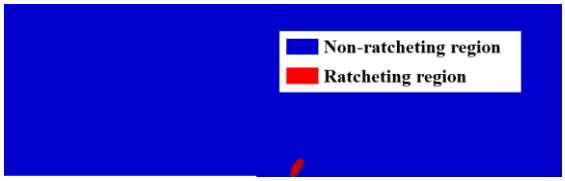

(c) $a/W = 0.5$

(d) $a/W = 0.7$

Fig. 4.11. Ratcheting strain contours of the CCT plane strain model with different a/W

Fig. 4.12 shows the unified constraint parameter A_p under different constraint conditions. It can be found that the unified constraint parameter A_p is also suitable for measuring the compound constraint effect of cracked specimens with cyclic loading conditions. Quite similar to the case of monotonic loading condition, as the constraint effect enhances (for the in-plane constraint condition, it refers to the increase of a/W crack dimension, and regarding the out-of-plane constraint condition, it means changing the thickness from plane stress to plane strain), the unified constraint parameter A_p reflects a negative correlation with the constraint condition. At the same time, a

lower level of A_p stands for a highly constrained condition, where only limited ratcheting strain develops, while a higher magnitude of A_p indicates a loss of constraint with a much broader ratcheting strain distribution around the crack tip region.

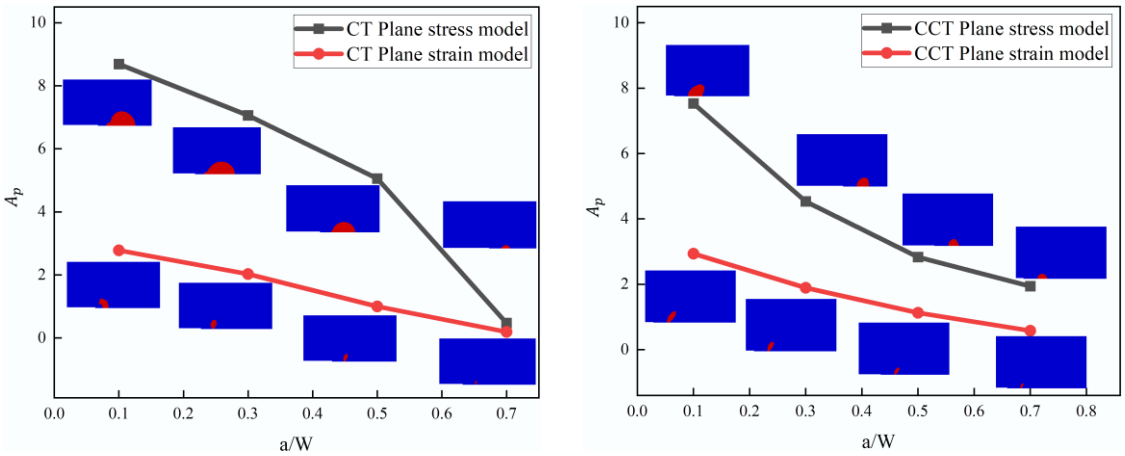

(a) (b)

Fig. 4.12. The unified constraint effect measurement of cracked specimens under different constraint conditions for (a) CT specimen and (b) CCT specimen

In addition, Fig. 4.13 further reveals that under the identical predefined level of cyclic bending moment, the ratchet limit of the cracked specimen and the unified constraint parameter $\sqrt{A_p}$ approximately show a salient linear correlation, reflecting the weakness of the ratchet limit due to the enhancement of the constraint effect.Although this linear relationship between the constraint parameter $\sqrt{A_p}$ and the ratchet limit is established by considering two extreme out-of-plane constraint states (i.e., the plane strain and plane stress states), for the actual 3D cracked structures, the data points should be on the correlation line. The correlation is very meaningful for the assessment of the ratchet limits of cracked structures in terms of different constraint conditions (including different in-plane, out-of-plane, and compound constraint conditions), where the constraint-related ratchet limit is able to be calculated through it directly.

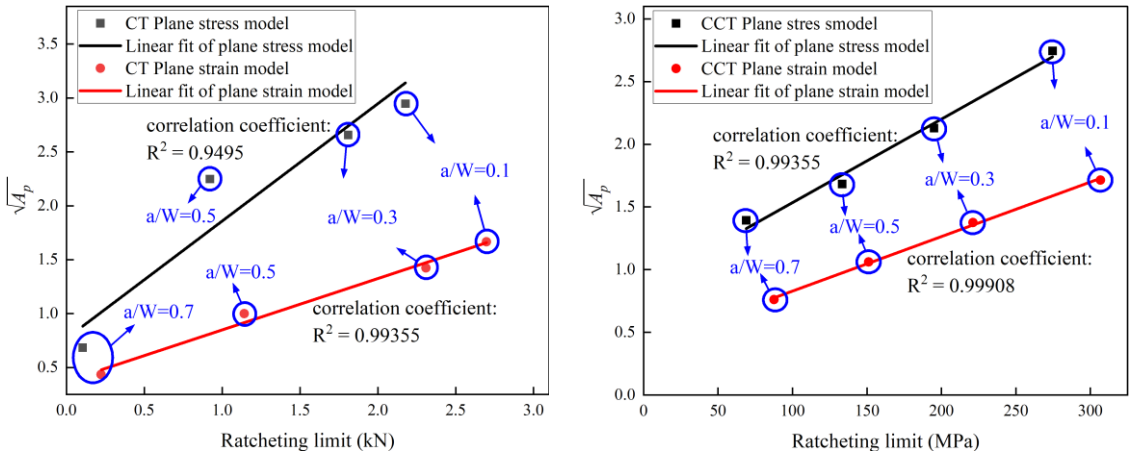

(a) (b)

Fig. 4.13. The general relationship between the unified constraint measurement $\sqrt{A_p}$ and the LMM ratchet limit under cyclic bending moment condition: (a) CT specimen and (b) CCT specimen

4.4.4 Effect of constraint on the plastic strain range and the unified correlation

Given that the structural low cycle fatigue failure and life are closely related to the amplitude of alternating plastic strain at the critical locations, it is meaningful to reveal the influence of the constraint effect in the cracked structure on the amplitude of alternating plastic strain. Therefore, based upon the established DSCA procedure under the LMM framework, two series of fatigue analyses for both CT and CCT specimens are implemented to acquire the convergent varying residual stress field and amplitude of alternating plastic strain range at the crack tip. Here, the load condition points are predefined to be lower than the values of the ratchet limit under both plane stress and plane strain conditions, which are displayed by the purple points in Figs. 4.6 and 4.7, slightly falling into the reverse plastic zone of specimens with $a/W = 0.7$.

Regardless of the CT or CCT specimen, with the in-plane constraint gradually strengthening, the amplitude of the alternating strain at the crack tip has an apparent upward trend, which is depicted by the two sets of closed stress-strain hysteretic curves in Figs. 4.14 and 4.15. Moreover, it is worth noting that there is a threshold of crack size at which the high constraint effect intervenes and intensively changes the cyclic strain range. For both specimens, when the a/W parameter is below 0.5, the increment of strain range for each size is almost uniform, while a surge of plastic strain range occurs with the crack parameter changing to 0.7 (see the green hysteresis loop in Figs.

4.14 and 4.15). However, the CCT specimen is not as sensitive to the constraint effect under the low in-plane constraint condition, which is reflected by the fact that when parameter a/W equals 0.1, and its cyclic strain range is still in a pure elastic state (see the short black dash curve in Fig. 4.15), resulting in much higher LCF life.

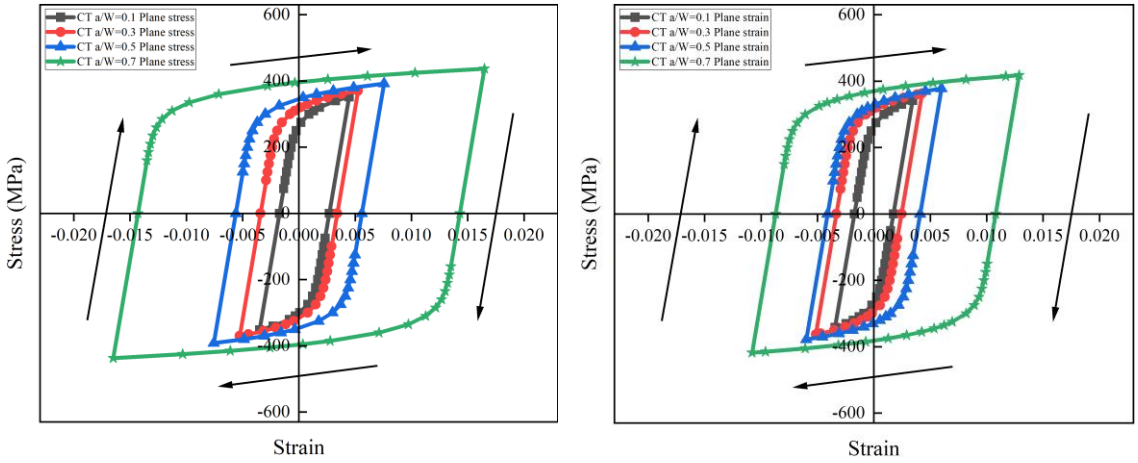

(a) (b)

Fig. 4.14. Saturated hysteresis loops of CT specimen under reverse plasticity condition: (a) under plane stress condition and (b) under plane strain condition

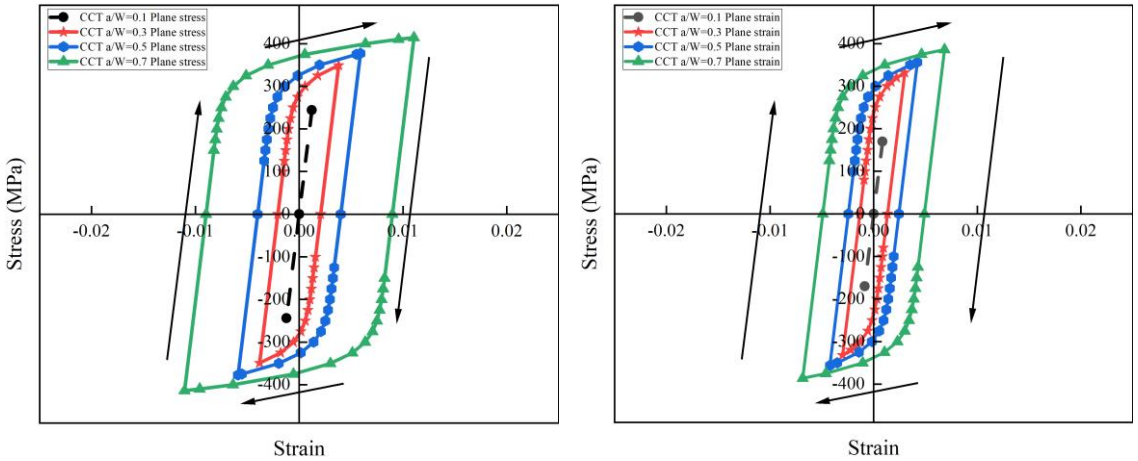

(a) (b)

Fig. 4.15. Saturated hysteresis loops of CCT specimen under reverse plasticity condition: (a) under plane stress condition and (b) under plane strain condition

The unified constraint parameter A_p is also adopted to further characterise the influence of the strength of constraint effect on the alternating plastic strain based on the DSCA results. There is a slight adjustment that since under the plastic shakedown load conditions, the local plastic region around the crack tip is not fully developed as in the ratcheting cases, the A_{PEEQ} to define the unified constraint parameter A_p is adjusted to the area surrounded by the alternating plastic strain isolines ahead of the crack tip. In this section, the alternating plastic strain range is selected to be 0.02 to determine the isolines ahead of the crack tip. In Fig. 4.16, there is a linear correlation between the unified constraint parameter $\sqrt{A_p}$ and the alternating plastic strain range at the crack tip, showing that as the compound constraint effect strengthens, the alternating plastic strain range increases linearly, which directly results in sharply reduced LCF life. Although there are only two extreme out-of-plane constraint states (i.e., the plane strain and plane stress states) exhibited here, the linear relationship line of specific 3D cracked structures should exist accordingly. This linear correlation is capable of functioning as the reduction coefficient for assessing the alternating plastic strain range and the LCF life of cracked structures once the constraint effect strength is calibrated according to the parameter A_p.

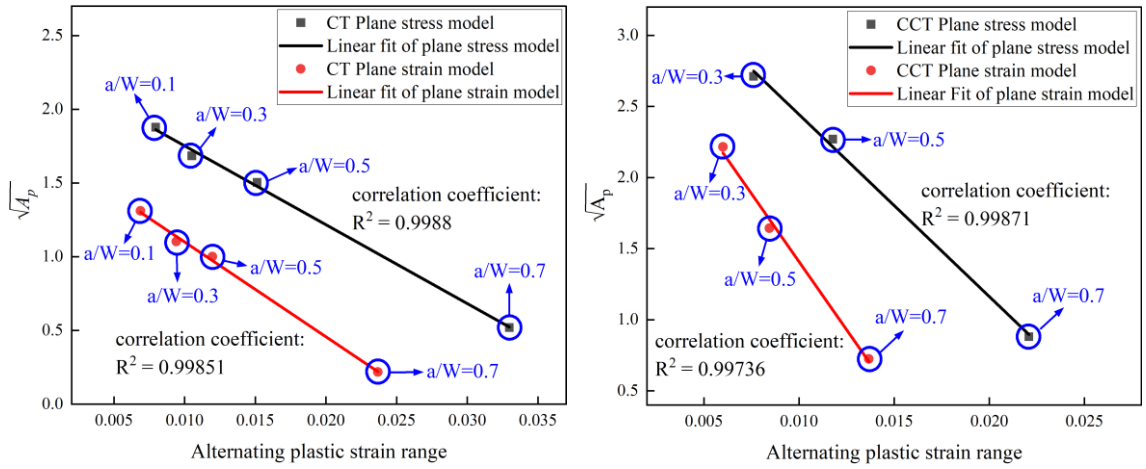

(a) (b)

Fig. 4.16. The general relationship between the unified constraint measurement $\sqrt{A_p}$ and the alternating plastic strain under cyclic bending moment condition: (a) CT specimen and (b) CCT specimen

4.5 Verifications and discussions

4.5.1 Strategy of validation

To verify the effectiveness of the ratcheting boundaries calculated by LMM ratcheting analysis, it is not necessary to verify all these ratcheting boundaries for all cases investigated, and we only need to verify the accuracy of ratcheting boundaries for some typical conditions. For this consideration, only the LMM ratcheting boundaries for both the CT specimen and CCT specimen with a/W=0.5 are verified. Two sets of virtual numerical tests are designed for both CT and CCT specimens by adopting the detailed ABAQUS non-linear analysis. The specimen whose crack size parameter a/W is equal to 0.5 is defined as the standard specimen and selected for validation purposes, with the same cyclic hardening material property (defined in Section 4.3.2) and BCs (illustrated by Fig. 4.3) adopted in the FEA model.

The multi-step FEA is implemented according to the load history in Fig. 4.5, where the maximum value of bending moment within the per load cycle and the constant value of the tensile load are determined by four pairs of condition points shown in the LMM ratcheting boundaries for standard CT and CCT specimens with $a/W = 0.5$ (see Fig. 17). The green and pink condition points inside the general ratcheting region represent the alternating plastic condition related to fatigue failure, while the blue and yellow points above the boundary prescribe the ratcheting condition (progressive plastic condition).

The criterion for verification is to witness a transition of dominated mechanism from the non-ratcheting to the ratcheting failure on both sides of the boundary. If the boundary is effective, there should exist a state of alternating plasticity with the load condition inside the boundary, and at the same time, under the load point outside the boundary, the ratcheting behaviour should be observed. To further decide the cyclic state during the load cycle progresses, the accumulation of time-dependent effective plastic strain is extracted from the key node at the crack tip, which is defined by the ABAQUS variable plastic strain magnitude PEMAG [119] (PEMAG=$\sqrt{\frac{2}{3}\varepsilon^{pl}:\varepsilon^{pl}}$, where ε^{pl} characterizes the plastic strain tensor). And the history of PEMAG is able to identify whether there is a ratcheting or non-ratcheting state for structures under cyclic load conditions.

4.5.2 Verification with CT specimen model

In the case of standard CT specimen, when the load combinations in Fig. 4.17 (a) are under the reverse plasticity condition, after the first load cycle (including loading and unloading

processes), the plastic strain continues to fluctuate, and the amplitude finally converges to a fixed amplitude, which is displayed by the blue curves of plastic strain histories in Fig. 4.18. From another two blue curves in Fig. 4.19, it can be observed that with the crack tip entering the plastic shakedown state, except for the first cycle, all the subsequent hysteresis loops always remain closed, and there is no net increment of plastic strain during this process.

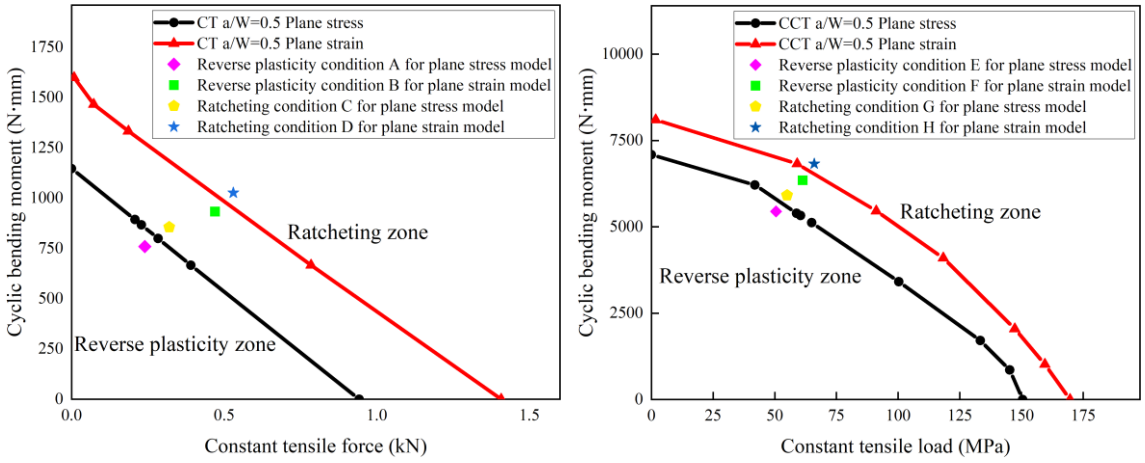

(a) (b)

Fig. 4.17. Load conditions for the verification of the LMM ratcheting boundaries: (a) Standard CT specimen (a/W=0.5) and (b) Standard CCT specimen (a/W=0.5)

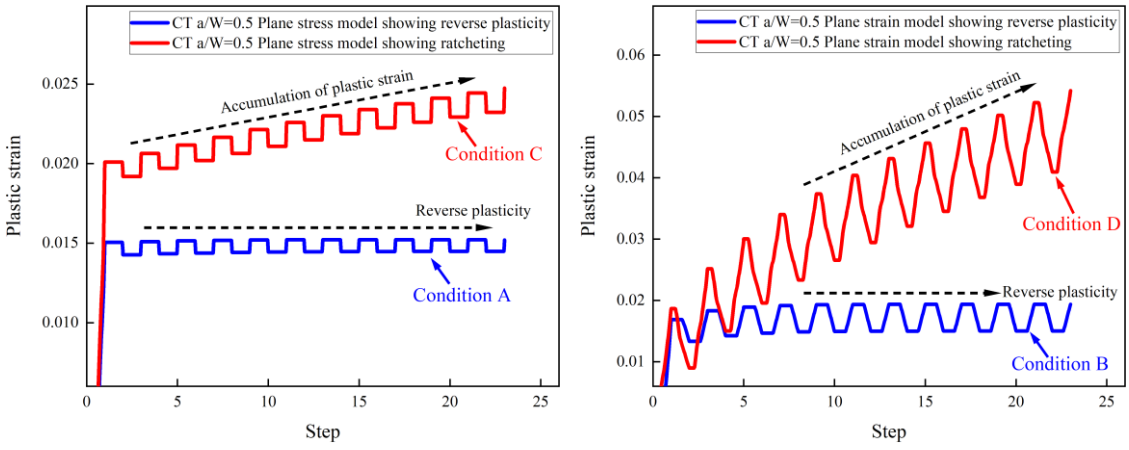

(a) (b)

Fig. 4.18. History of plastic strain magnitude at the crack tip: (a) standard CT specimen under plane stress condition and (b) standard CT specimen under plane strain condition

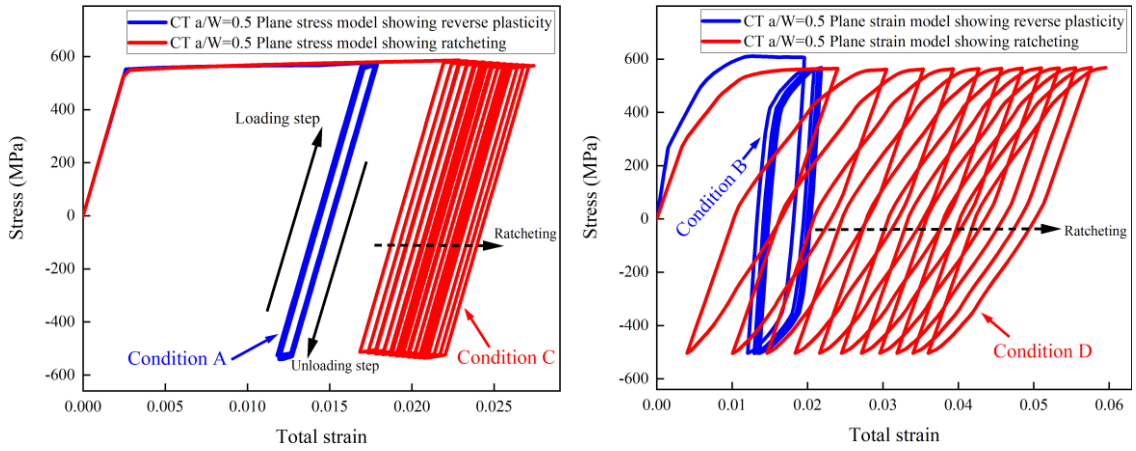

(a) (b)

Fig. 4.19. Cyclic stress-strain response at the crack tip: (a) standard CT specimen under plane stress condition and (b) standard CT specimen under plane strain condition

Instead, after the load condition points slightly rise to the ratcheting side, the net increase in cyclic plastic strain begins to occur, and it accumulates unstoppably during each cycle until progressive plastic collapse occurs. This process is described by the plastic strain history and stress-strain hysteresis curves shown in Figs. 4.18 (b) and 4.19 (b). Compared with the alternating plastic behaviour, the materials yield zone where progressive plastic strain occurs extends to a much broader range than the case of reverse plasticity condition, which is highly consistent with the failure mechanisms predicted by LMM ratcheting analysis.

4.5.3 Verification with CCT specimen model

To further explain the alternating plasticity at the crack tip of standard CCT specimen when the load condition points fall into the reverse plasticity zone in Fig. 4.17 (b), by tracking the histories of stress and strain at the crack tip, a series of converged cyclic plastic strain ranges (see Fig. 4.20) and closed hysteresis loops (see Fig. 4.21) can be observed clearly from the blue curves below. In addition, similar to the phenomenon of the CT specimen above, the plastic yield zone, as well as the cyclic plastic strain response, are generated only near the crack tip.

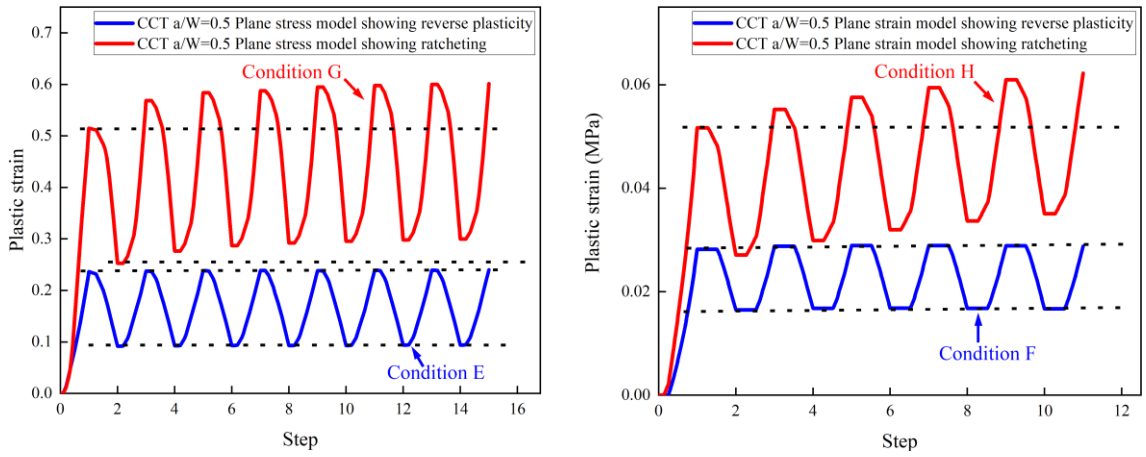

(a) (b)

Fig. 4.20. History of plastic strain magnitude at the crack tip: (a) standard CCT specimen under plane stress condition and (b) standard CCT specimen under plane strain condition

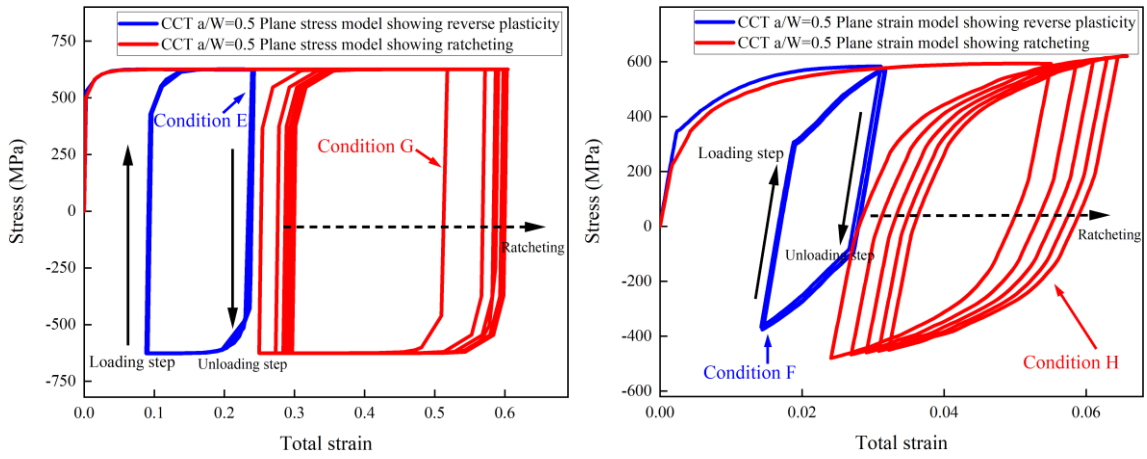

(a) (b)

Fig. 4.21. Cyclic stress-strain response at the crack tip: (a) standard CCT specimen under plane stress condition and (b) standard CCT specimen under plane strain condition

Compared to the standard CT case, the ratcheting strain at the standard CCT specimen crack tip develops more slowly when the load combinations lie slightly outside the ratcheting boundary, which is reflected by the ratcheting curves above in red colour, where the increment of cyclic plastic strain during every cycle accumulates gradually at a low speed. This fact also provides sufficient evidence for the predicted failure mode by the LMM ratcheting analysis.

4.6 Conclusions

In this chapter, with the constraint effect involved, cyclic plastic responses of the cracked structure are investigated by using the direct method. The constraint-related ratcheting boundary of the cracked specimen is well-built, and the influence of the constraint effect on the ratcheting boundary is clarified. In addition, the fracture mechanics constraint parameter Ap is generalized to measure the constraint-related alternating plasticity and ratcheting resistance.

The main conclusions of this chapter are as follows:

1. The high in-plane constraint effect keeps compressing the capacity of both CT and CCT specimens against ratcheting failure due to cyclic load conditions as the in-plane constraint increases. With regard to the out-of-plane constraint effect, the acceptable plastic shakedown regions in the plane strain model are larger than in the plane stress model since the out-of-plane constraint effect elevates the resistance of ratcheting failure.

2. The ratcheting boundary of the cracked specimen is much more vulnerable under the influence of the high in-plane constraint effect. And there is a significant nonlinear relationship between the weakening of the structural capacity against cyclic load conditions and the strengthening of in-plane constraint.

3. The unified constraint parameter A_p is employed to measure the strength of compound constraint under cyclic load conditions, showing that this unified constraint parameter is suitable for both monotonic and cyclic load conditions. And a salient linear relation between parameter $\sqrt{A_p}$ and cyclic plastic responses (including ratchet limit and alternating plasticity) of the cracked specimen is demonstrated, aiming at evaluating the ratchet limits and alternating plastic strain range (associated with LCF life) of cracked structures in terms of different constraint conditions.

4. As the load condition point falls into the reverse plasticity zone, there is a threshold of crack dimension at which the high constrain effect intervenes and intensively expands the amplitude of alternating plastic strain around the crack tip, leading to a sharp reduction in low cycle fatigue life.

5. The ratcheting and alternating plasticity behaviours of standard CT and CCT specimens, predicted by the LMM framework, are verified by a detailed step-by-step analysis. The load condition points located at both sides of the ratcheting boundary show different failure mechanisms, which are completely consistent with those obtained by LMM ratcheting analysis.

5 Direct method-based probabilistic shakedown analysis for the structure under multiple uncertain design conditions

5.1 Introduction

Solving probabilistic shakedown analysis requires an accurate but concise deterministic elastoplastic simulation procedure and an efficient reliability calculation strategy. Currently, there are two main schemes to address such a reliability problem and predict the failure probability. Firstly, a common approach is to directly combine the fundamental Monte Carlo Simulation (MCS) method [120-122] with the mature non-linear numerical analysis technologies [123, 124], and many variance reduction techniques are employed as well to reduce the repeated computational cost of the MCS process [125-127], especially for the cases where the acceptable failure probability is extremely small. With the direct MCS sampling adopted, there are more than 1 billion times repeated analyses needed to determine a tiny failure probability (usually less than 1×10^{-7}) for a high-reliability engineering component [128].

Another approach for improving the efficiency of MCS-based probabilistic analysis is finding an approximation of structural response, replacing the repeated and costly FEA calculations. Response surface method (RSM) is adopted in reliability analysis to describe the performance approximately in a certain range [129] or design space by means of a fitted first or second order polynomial when the relationship between the structural response and the input parameters cannot be expressed explicitly [130, 131] or the deterministic FEA calculation process is very time-consuming due to complicated nonlinearity [132]. Andrzej [133] provided a reliability-based design of a high-pressure chamber by integrating multiple technical approaches, including shakedown analysis procedure CYCLONE, RSM and MCS sampling method, with the cyclic inner pressure and radius treated as different kinds of random variables. As part of artificial intelligence, the neural network acts as the numerical substitution of running an FEA solver [134] during reliability analysis, where the neural network is trained by a database acquired from a set of analyses [135]. The underlying relationship between the shakedown boundary of a nozzle subjected to constant inner pressure and cyclic thermal load and design parameters was visualized through the neural network, with the probabilistic shakedown boundary also calculated [136]. Several

reliability analyses of elastoplastic structures were studied by Arnd [137] and Manolis [138, 139] based on a neural network-based strategy. Besides, the machine learning-based technique is also combined with reliability analysis [140], which connects the input design parameters to the structural behaviours.

First and Second Order Reliability Methods (FORM/SORM) [65] is a more effective analytical approach to performing reliability shakedown analysis, which depends on the gradient information of each random variable, and the process of solving the reliability index is implemented by a constrained non-linear minimization problem [141]. A stochastic FEA solution for elastoplastic material was studied by Liu [142], which focused on the uncertainties of material properties, and an iteration scheme for solving the reliability index according to advanced FORM was suggested by making use of the Taylor expansion of displacement. Augusti [143] introduced the randomness of strength and load conditions into the limit and shakedown analysis, and the probabilistic shakedown boundary was presented to discuss the impact of the uncertainty of input parameters on the deterministic structural limit load and shakedown behaviour. Chou [144] described a reliability shakedown analysis model to illustrate the residual deflection process of a 2-span continuous beam, where the uncertainty of load and resistance was included. Another shakedown analysis of plane frames under stochastic uncertainty was executed by Marti [145], and an explicit optimization problem was proposed to calculate the maximum load factors for reliability shakedown analysis. By combining the FORM and lower bound shakedown analysis program, Staat and Heitzer [146-148] developed a stochastic FEA procedure for reliability shakedown analysis that provides the gradient information from the deterministic shakedown problem simultaneously. Three cases including the central holed plate, pipe-junction and plate with mismatched weld and a crack were performed by this framework, with the numerical results verified by analytical analyses. Further, there were many improvements [149-151] applied to enhance the accuracy and efficiency of reliability shakedown analysis, where the mathematical programming algorithms of deterministic shakedown analyses in terms of upper bound theory, edge-based smoothed finite element method [152, 153] and the sequential quadratic programming iteration were incorporated in FORM reliability analysis. This framework was also extended to take the system reliability analysis based on multimode failure into consideration [154].

Therefore, the current key problem lies in that there are shortcomings of an accurate and concise deterministic shakedown analysis program that can conveniently but efficiently fit with the requirements of probabilistic analysis, so as to evaluate the reliability and failure probability during risk management. In this study, aiming at considering the uncertainty of the design parameters

during the shakedown evaluation, a novel strategy of probabilistic shakedown analysis under the pLMM framework is proposed based on the LMM shakedown procedure which nevertheless has been established and widely applied to deterministic engineering assessments but never involved in the probabilistic analysis approach before. And by this way, the risk of the non-shakedown state is able to be predicted by the physically based estimation model, where the efficient iteration is also employed to derive the reliability index. Moreover, seldom studies have dealt with the effect of randomness originating from loading fluctuation on the shakedown determination. In this work, the probabilistic shakedown boundary is well constructed, with the influence of the uncertain loading path on the reliability fully reflected.

This chapter is organized as follows. In Section 5.2, the pLMM framework for probabilistic shakedown analysis is proposed, with the whole calculation process elaborated in detail. Then, a benchmark of the holed plate is provided to illustrate the extensive applicability of the pLMM shakedown analysis. In Section 0, validations and further discussions are given out to demonstrate the effectiveness and accuracy of the probabilistic shakedown boundary. Finally, the main conclusions of this study are summarized briefly in the last section.

5.2 Probabilistic shakedown analysis under the pLMM framework

5.2.1 Determination of shakedown limit multiplier by LMM shakedown procedure

As the foundation of probabilistic shakedown analysis, the LMM shakedown analysis proposed by Ref. [112] is capable of fully reflecting the structural shakedown limit at the physical level, with a good balance between high accuracy, efficiency and conciseness guaranteed at the same time. The adopted numerical procedure to calculate the shakedown multiplier is similar to the description in 3.2, but without the revised yield stress substituting the material yield stress.

This program commences with the weighed elastic stress input, and the linear matching condition is applied iteratively based on the constant residual stress and plastic strain increment, with a series of linear equations solved. By repeating the steps displayed in Fig. 5.1, the monotonically decreasing shakedown multipliers are given out until the iteration converges to a stable result.

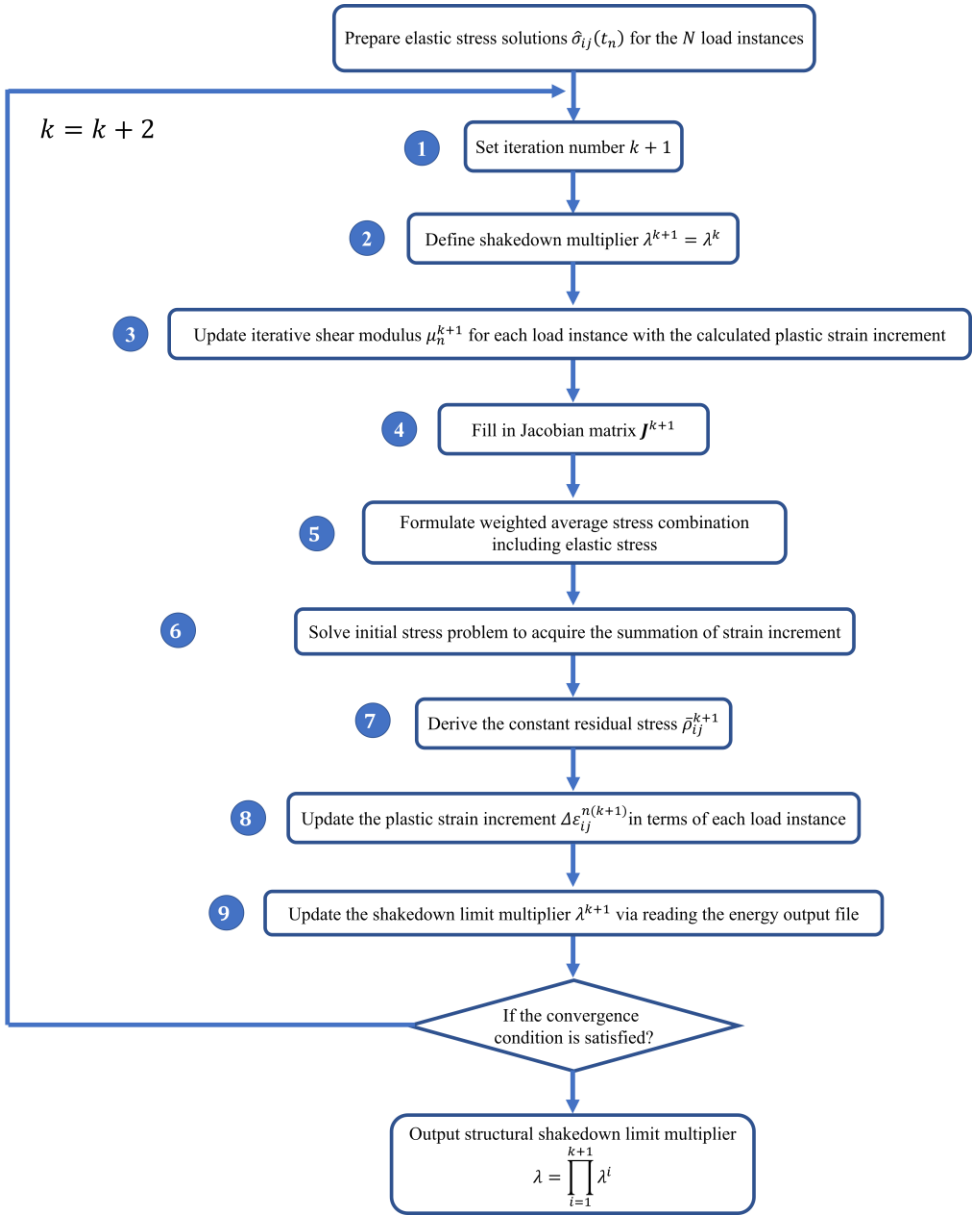

Fig. 5.1. Program for structural shakedown limit calculation by LMM shakedown procedure

5.2.2 Establishment of the structural probabilistic shakedown boundary

The structural probabilistic shakedown boundary is an effective way to visualize how and where the shakedown boundary is affected by the uncertainty of the design parameters. During this process, the sensitivity analysis result is also acquired by the design of experiments (DOE), providing the essential information on the importance sequence of each input factor. The probabilistic shakedown boundary under a certain load ratio can be constructed by implementing a

series of MCS samplings to simulate the statistical distribution of the LMM shakedown multipliers (see Fig. 5.2), where different load ratios are defined by the ratio of Load 2 to Load 1 as shown in Fig. 5.3.

Here, each probabilistic shakedown boundary envelop gives out a specific statistical significance that when incorporating the uncertainty of the design parameters, the structural shakedown boundary appears with a certain probability (e.g. 30% with the red curve) inside each domain surrounded by the corresponding boundary (e.g. the load region under the red curve in Fig. 5.3). In other words, the applied load condition on the farther boundary corresponds to a less survival probability and a greater risk of non-shakedown failure.

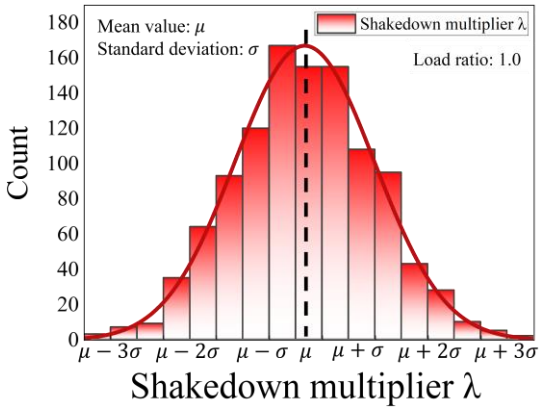

Fig. 5.2. Probabilistic distribution of shakedown multiplier λ under certain load ratio

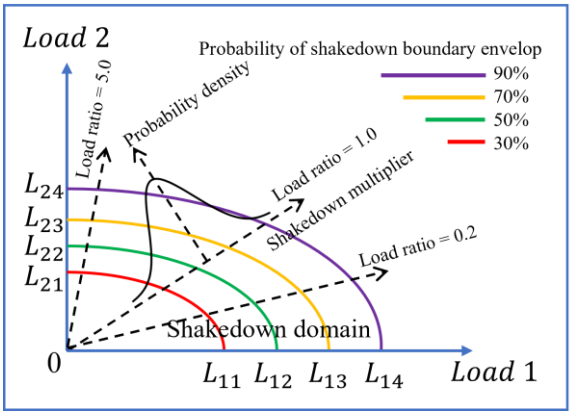

Fig. 5.3. Probabilistic shakedown boundary and shakedown envelop with different probability

5.2.3 Shakedown limit state indicator function (SLSIF)

A concise governing function, the shakedown limit state indicator function (SLSIF), is established by Equation (5.1) under the pLMM framework. The shakedown multiplier λ_{UB_LIMIT} calculated during each deterministic analysis is utilized to measure whether the structural response satisfies the shakedown condition or not under cyclic loading conditions. Hence, the performance function and limit state is constructed for the reliability analysis below.

With all the uncertainty of R and S involved in the SLSIF, the LMM shakedown multiplier, $\lambda(\boldsymbol{X})$, acts as a clear indicator to point out the relative location of the load condition to the probabilistic shakedown boundary. Specifically, when the multiplier is equal to 1, it implies that

the applied reference load condition lies on the shakedown boundary. If the multiplier is less than 1, that means the reference load condition fluctuates to a higher level beyond the boundary or the structural resistance deteriorates due to unexpected circumstances (i.e., the current case works outside the shakedown boundary, the shakedown multiplier is a multiple by which the load level needs to be scaled down.). On the other hand, for an acceptable case, the shakedown multiplier should be larger than the threshold value ($\lambda = 1$), which represents the safety redundancy between the working load and the shakedown boundary.

$$G(\boldsymbol{X}) = \lambda(\boldsymbol{X}) - 1 \begin{cases} < 0, \text{Outside the shakedown boundary (Failed)} \\ = 0, \text{On the shakedown boundary (Limit state)} \\ > 0, \text{Under the shakedown boundary (Safe)} \end{cases} \tag{5.1}$$

5.2.4 Probabilistic shakedown analysis procedure under the pLMM framework

The iteration of reliability analysis starts with the initial estimations of random variables, which are usually set as the mean values of random variables. Different from the traditional non-linear approach where the shakedown limit is dependent on the non-convergent result of a huge number of incremental FEA analyses, in each iteration, this direct method-based procedure converges to the exact shakedown limit regarding the EPP material model more efficiently via the upper bound solutions. Hence, it is more accessible to automatically integrate the process of calculating performance function and its gradient information into one framework, which is illustrated by the flow chart in Fig. 5.4 below.

The reliability analysis is implemented by adopting software ABAQUS and Isight shown in Fig. 5.5. At the beginning, the Python file is generated by the ABAQUS, which contains the FEA model as well as the design variables determined by Isight at the start of each iteration. Next, the LMM plugin edits this Python code to create the shakedown analysis procedure. With the input file passed into the FEA solver, a series of LMM linear equations are solved to acquire the shakedown multiplier and the gradient of SLSIF, which are input into the subsequent optimum algorithms of FORM. According to the convergency condition of reliability analysis, the reliability index and failure probability can be calculated, otherwise, another round of calculation will be launched.

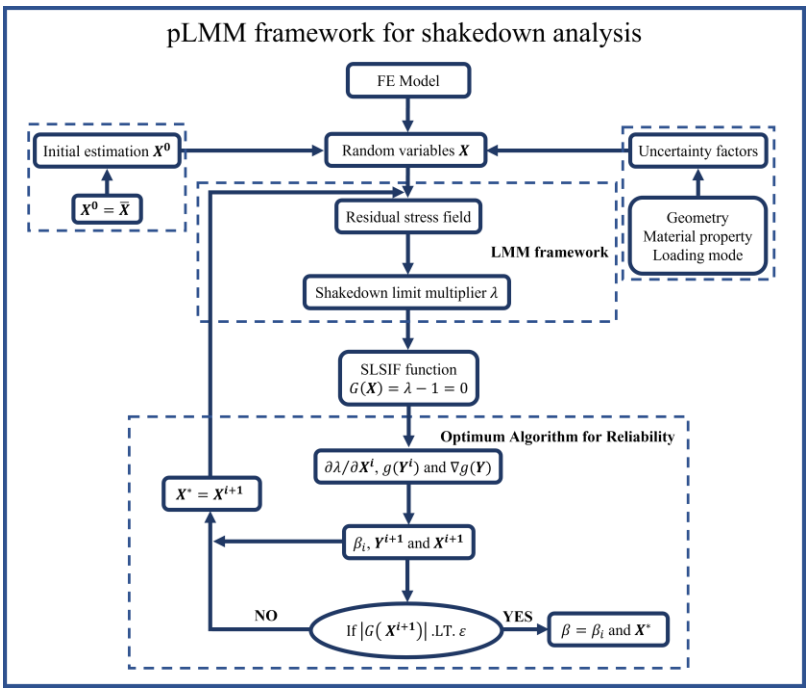

Fig. 5.4. Iteration process of pLMM shakedown analysis

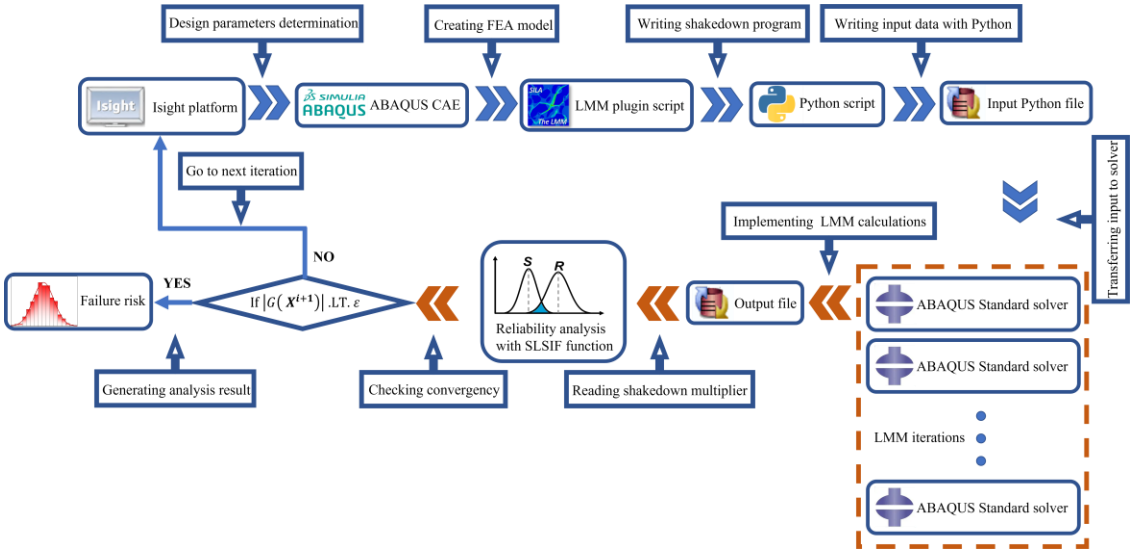

Fig. 5.5. Flow chart of pLMM framework configuration for shakedown analysis

5.3 Benchmark of probabilistic shakedown analysis by pLMM framework

A central holed plate with a salient stress concentration is selected as a simplified structure, which is commonly used in the nuclear, aerospace and petroleum industries, to present the comprehensive applicability of the proposed probabilistic shakedown analysis.

5.3.1 Description of deterministic FEA model

The 20-node quadratic brick element C3D20R with reduced integration technology is utilized to discretize the holed plate displayed in Fig. 5.6, where the ratio between the hole diameter D and the length L of the plate is 0.2, and the ratio between the depth d of the plate and the length L is equal to 0.05. Based on the mesh convergence study, the total element number and minimum element size are determined to be 721 and 1.25 mm, respectively. The Young's modulus E and the Poisson's ratio ν of the elastic-perfect plastic material are assumed to be 2×10^5 MPa and 0.3 respectively, and the yield strength σ_y is defined to be 200 MPa.

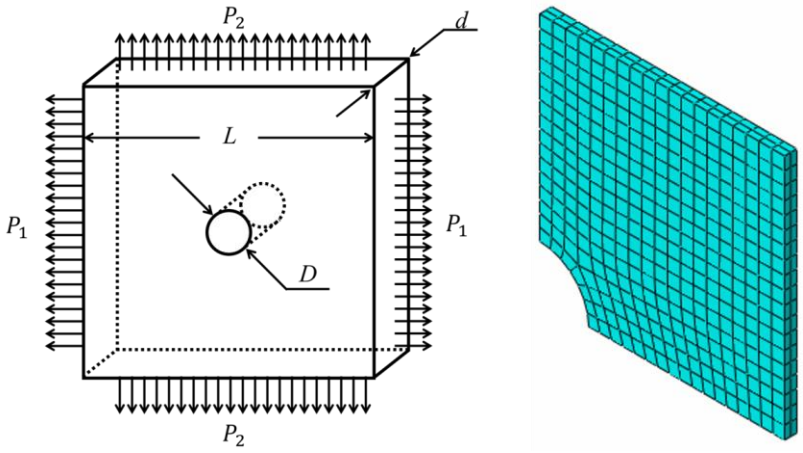

Fig. 5.6. Geometry and the FE model of the central holed plate

The shakedown analysis is based on the biaxial tensile load state shown in Fig. 5.6, and two predefined loading histories of the cyclic tensile load are presented in Fig. 5.7. Regarding loading path 1, the horizontal tensile load P_1 is a constant uniform load, with P_2, a cyclic uniform load, acting along the vertical axis, and for loading path 2, both are variable loads. The cyclic patterns of time-dependent load conditions are depicted in Fig. 5.8, with a typical load cycle determined from t_1 to t_5. It is worth noting that under the LMM shakedown analysis, both load conditions are defined as reference load, which is usually set to one unit, 1 MPa. In addition, to save the computing resource, the FEA model is simplified by a 3D quarter model, with the symmetric boundary conditions applied on the symmetric surfaces.

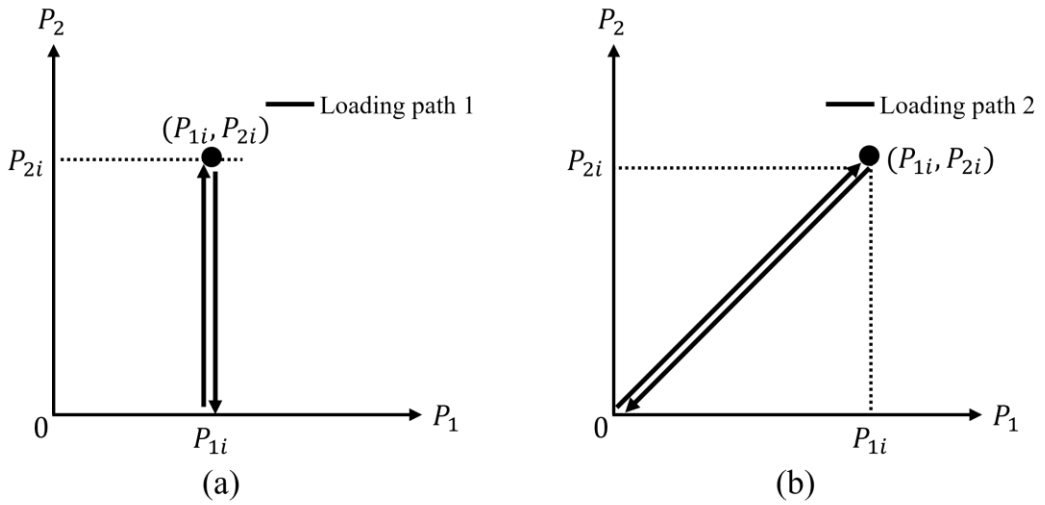

Fig. 5.7. Loading paths for shakedown analysis: (a) loading path 1 with one cyclic tensile load and (b) loading path 2 with two cyclic tensile loads

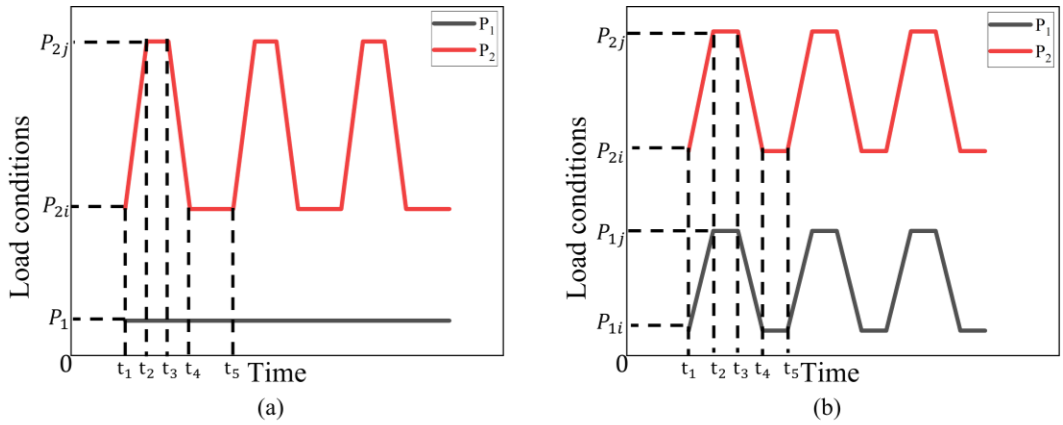

Fig. 5.8. Cyclic pattern of time-dependent load conditions: (a) loading path 1 and (b) loading path 2

5.3.2 Random variables involved in the probabilistic shakedown analysis

The probabilistic numerical cases with different loading paths are investigated by the pLMM framework, where both the hole diameter D and the material yield strength σ_y are set to be essential random variables, following the normal distribution. Besides, another more complex random variable, the influence of load fluctuation ΔP (shown in Fig. 5.9) is set to illustrate the effect of uncertain cyclic load mode on the structural shakedown limit. That is capable of accounting for the inevitable fluctuation of working load around the peak or average value of

engineering components (e.g. the fluctuation of the inner pressure of pressure vessels and pipes), as displayed by the time-dependent loading conditions in Fig. 5.10. This micro-cyclic load condition around the load P_1 (represented by the shadow regions) is added to the original one compared to the loading paths in Fig. 5.8. All the random variables are assumed to be mutually independent, and the statistical information is listed in Table 5.1.

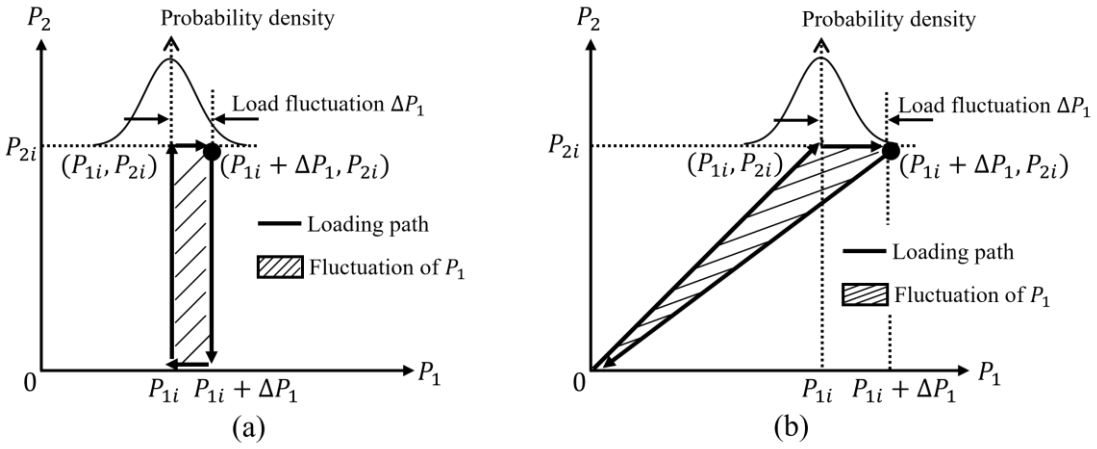

Fig. 5.9. Loading paths of the cyclic load for probabilistic shakedown analysis: (a) loading path $1'$ with one cyclic tensile load and (b) loading path $2'$ with two cyclic tensile loads

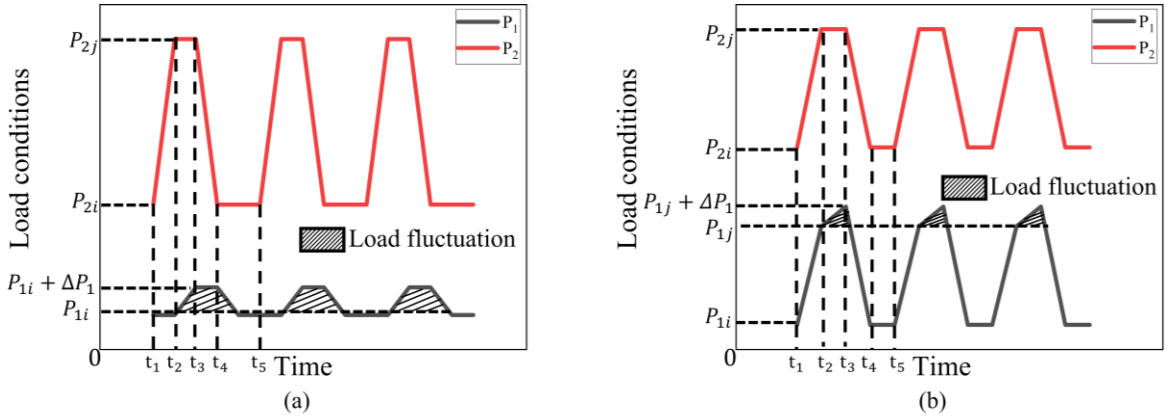

Fig. 5.10. Cyclic pattern of time-dependent load conditions: (a) loading path $1'$ and (b) loading path $2'$

Table 5.1. Statistical information of the random variables for probabilistic shakedown analysis

Random variable	Mean value	Standard deviation	Distribution
D (mm)	20	10% of $\bar{D}$	Normal
σ_y (MPa)	200	5% of $\bar{\sigma}_y$	Normal
ΔP_1 (MPa)	0	10% of the reference load $\bar{P}_1$	Normal

The reference load refers to the load condition applied to the FEA model during the LMM shakedown analysis, which is usually set to 1 MPa in this benchmark.

5.3.3 Establishment of the probabilistic shakedown boundary by the pLMM framework

The probabilistic shakedown boundaries of holed plate considering various random variables under different loading paths are plotted in Figs. 5.11 and 5.12, where the load ratios are denoted by P_2/P_1. Figs. 5.11 (a) and 5.12 (a) show the probabilistic shakedown boundaries regarding the uncertain geometric dimension and material yield strength, whereas Figs. 5.11 (b) and 5.12 (b) display the influences of an additional load fluctuation ΔP_1 on the probabilistic shakedown boundaries. Driven by the uncertainties of design parameters, the probabilistic shakedown assessment diagram is constructed by a series of random variables λ_i, and the shakedown boundary occurs stochastically inside the envelope surrounded by a certain curve with corresponding probability. Given a specified load point located on one of the probabilistic shakedown boundaries, the failure risk is defined according to the probability of the corresponding boundary. It is worth noting that with the load fluctuation ΔP_1 included, the probabilistic shakedown boundaries representing the same probability are dramatically compressed inward. For instance, In Figs. 5.11 (b) and 5.12 (b), it can be seen that the orange short dash curves are the 50% probability shakedown boundaries without uncertain load fluctuation, respectively, which cover most of the shakedown load regions for the cases with additional random variables. That means that when satisfying the same acceptable shakedown probability, the shakedown limit is restricted to a smaller load domain.

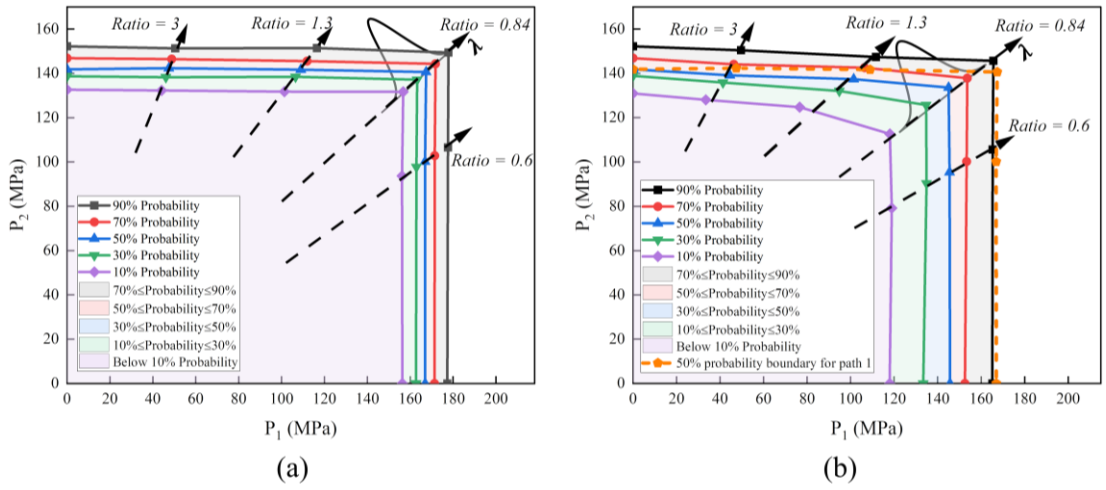

Fig. 5.11. Probabilistic shakedown boundaries of the central holed plate under loading paths 1 and $1'$ considering random variables: (a) D and σ_y and (b) D, σ_y and ΔP_1

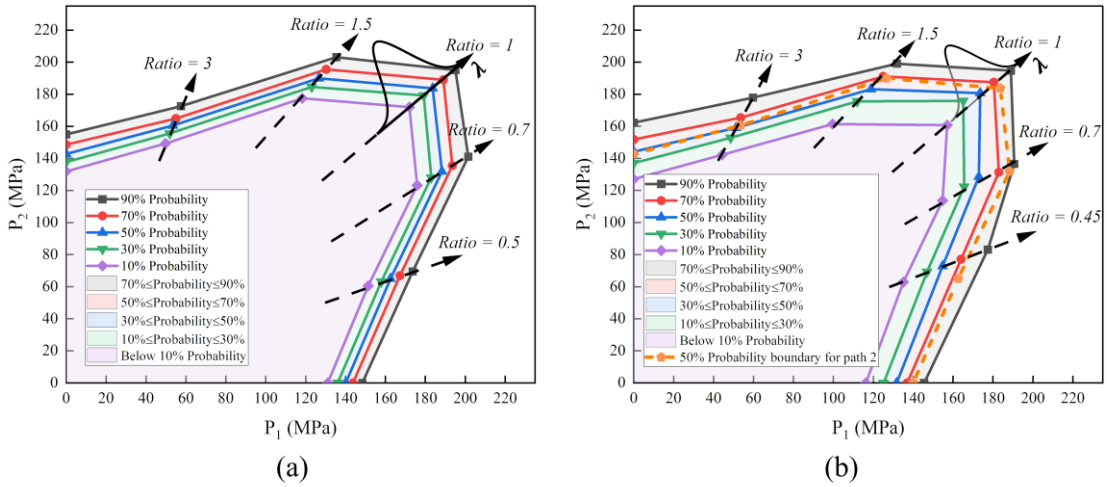

Fig. 5.12. Probabilistic shakedown boundaries of the central holed plate under loading paths 2 and $2'$ considering random variables: (a) D and σ_y and (b) D, σ_y and ΔP_1

In addition, the load fluctuation ΔP_1 also affects the dispersion of the boundary distribution, which is reflected by the below statistical distribution of the shakedown multiplier for different load ratios, where the relative frequency is defined by the fraction of the number of occurrences for a certain value to the total number of outcomes. Under the effect of load fluctuations, there is a more significant dispersion between each boundary, as the statistical standard deviations of the shakedown multipliers (see Figs. 5.14 and 5.16) are much larger than that of the cases in Figs. 5.13 and 5.15, respectively, where the uncertainties only exist in terms of geometric dimensions and

material properties. As compared in Fig. 5.17, this phenomenon is more conspicuous in the cases with lower load ratios (lower than 1.0 for both cases), where failure mode is dominated mainly by the instantaneous collapse. For example, in Fig. 5.11 (b), the sensitivities of the shakedown boundaries to load fluctuation ΔP_1 are not consistent between each side of load ratios 0.84 because of different failure mechanisms, since the alternating plasticity limit controls the domain near the y-axis, while the limit load dominates the area close to the x-axis.

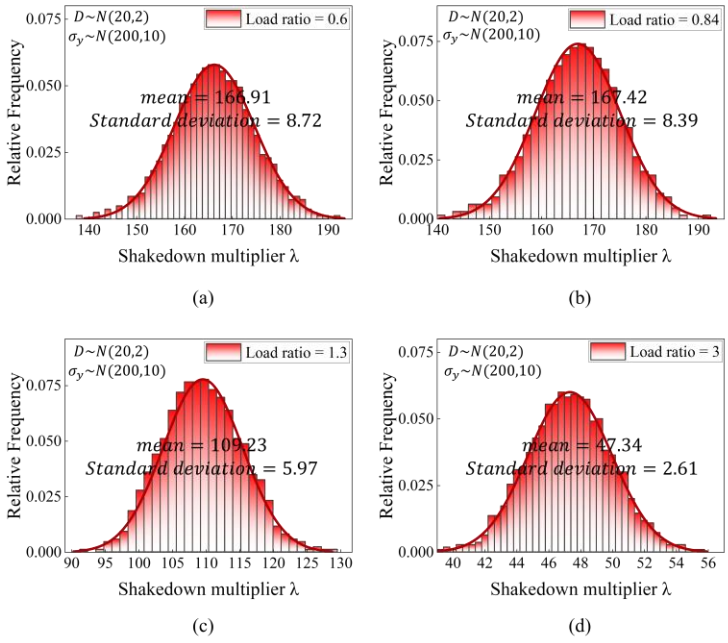

Fig. 5.13. Probabilistic distribution of shakedown multiplier under loading path 1 with random variables of D and σ_y under different load ratios: (a) ratio=0.6; (b) ratio=0.84; (c) ratio=1.3 and (d) ratio=3

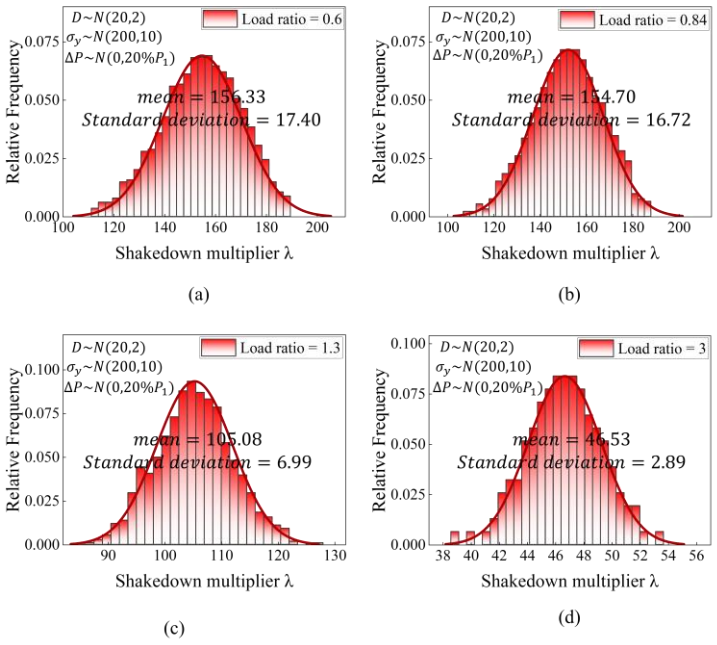

Fig. 5.14. Probabilistic distribution of shakedown multiplier under loading path $1'$ with random variables of D, σ_y and ΔP_1 under different load ratios: (a) ratio=0.6; (b) ratio=0.84; (c) ratio=1.3 and (d) ratio=3

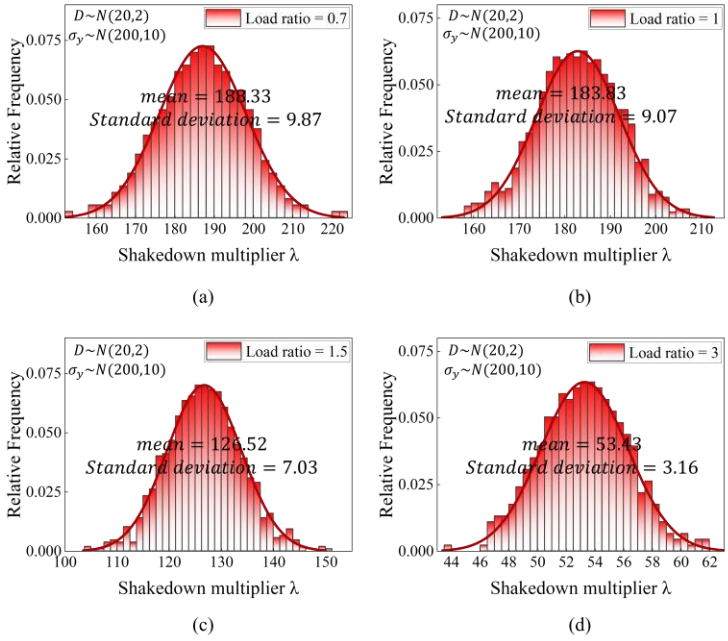

Fig. 5.15. Probabilistic distribution of shakedown multiplier under loading path 2 with random variables of D and σ_y under different load ratios: (a) ratio=0.7; (b) ratio=1; (c) ratio=1.5 and (d) ratio=3

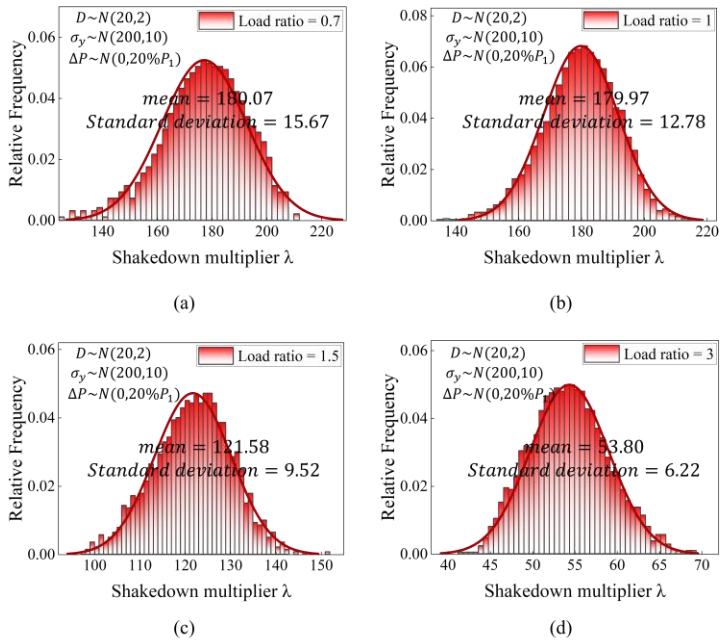

Fig. 5.16. Probabilistic distribution of shakedown multiplier under loading path $2'$ with random variables of D, σ_y and ΔP_1 under different load ratios: (a) ratio=0.7; (b) ratio=1; (c) ratio=1.5 and (d) ratio=3

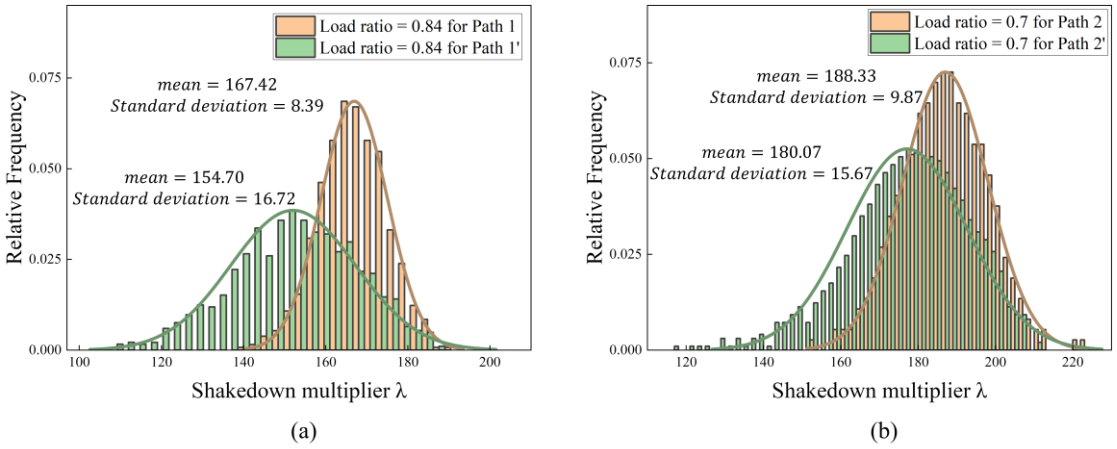

Fig. 5.17. Comparison of the standard deviations of shakedown multipliers between different random variables considerations: (a) comparison between load pathing 1 and $1'$; (b) comparison between load pathing 2 and $2'$

5.3.4 Reliability analysis by pLMM considering uncertain cyclic loading pattern

Considering the failure against the shakedown condition, the performance function is defined by SLSIF in Equation (5.1). And the gradient vector of the performance function is provided during each iteration by calculating the convergent numerical partial derivatives of random variables at the current design point. Besides the diameter and the yield strength, the load conditions are also considered as random variables to fully reflect the applicability of the proposed reliability analysis method. There are two sets of reliability analyses performed in this section. For the first set, aiming at demonstrating the effect of uncertain geometric dimension and material property on the structural reliability of the shakedown state, load points 1 and 2 are selected at the vertices of deterministic boundary curves in Fig. 5.18. As the uncertainty extends to cover load conditions, the load level is reduced for the rest of the reliability analyses, dropping from deterministic boundaries to the inner domain (load points 3 and 4) to give out plausible results.

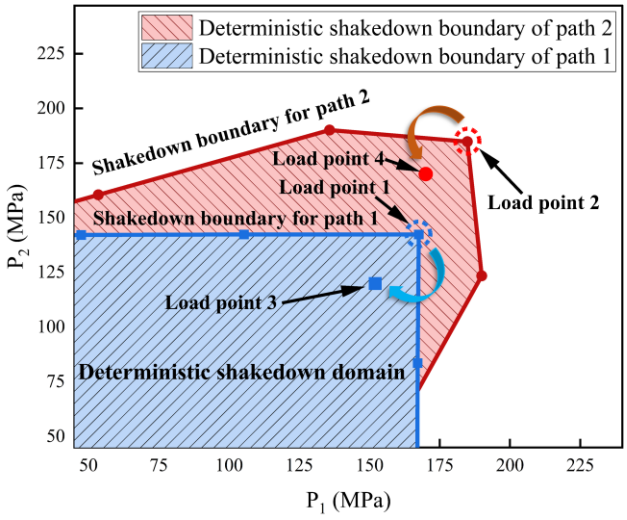

Fig. 5.18. Deterministic shakedown boundaries of different loading paths and the load conditions for reliability analyses

The results of reliability analysis with different combinations of random variables are compared in Table 5.2, where the path reference number is defined in Figs. 5.7 and 5.9. For both paths 1 and 2, due to the uncertainties of geometric dimension and material property, even though the load conditions (points 1 and 2 in Fig. 5.18) are located on the deterministic shakedown boundaries, the results of survival probability are still much lower than 100%, which are 70.45% and 70.18%, respectively. To improve structural reliability, the load conditions are reduced, moving down to points 3 and 4 for paths 1 and 2, where the structural failure probabilities decrease to 4.03%

and 3.30%. When the load P_1 is set to a random variable following the normal distribution in Table 5.1, the structural reliability indexes further decline to lower levels, leading to much higher non-shakedown failure risks compared with the previous results of deterministic load conditions.

With the additional random variable ΔP_1 incorporated, paths 1 and 2 are viewed as exceptional cases of path $1'$ and $2'$, where the load fluctuation of P_1 affects the structural reliability by changing not only the applied load magnitude but the cyclic loading mode. According to the previous section, under paths $1'$ and $2'$, the random fluctuation ΔP_1 significantly influences the shakedown boundary determination and the dispersion, which, as shown in Fig. 5.19, finally lowers the structural reliability of loading paths 1 and 2. Furthermore, in Fig. 5.20, as the dispersion degree (depicted by the coefficient of variation) of the random load fluctuation raises, the reliability indexes of the structure deteriorated sharply under the CV levels covering the most frequently used range (from 0.1 to 0.3), resulting in a lower shakedown probability, no matter which loading path is considered.

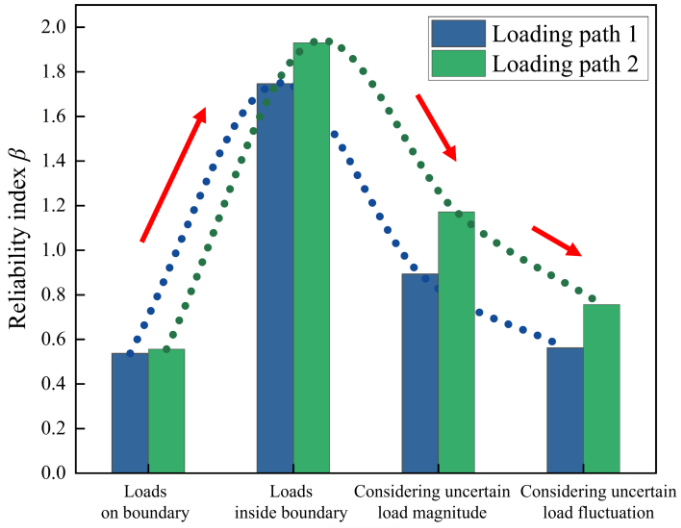

Fig. 5.19. . Reliability index of the holed plate predicted by pLMM with multiple combinations of random variables

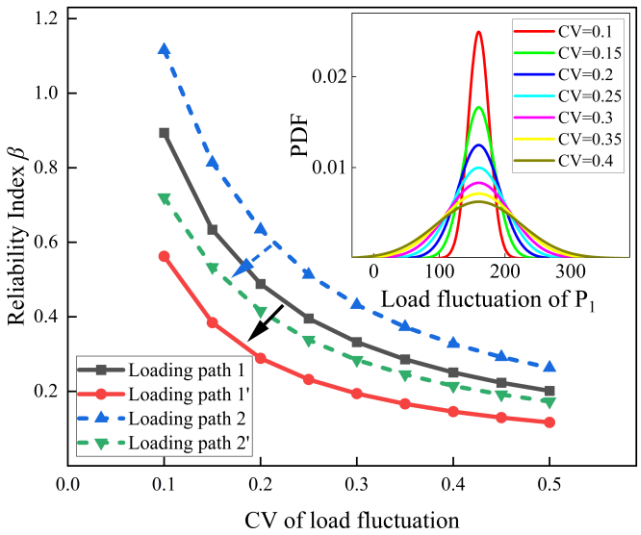

Fig. 5.20. Influence of load fluctuation ΔP_1 on structural reliability under different cyclic loading paths

Table 5.2. Results of reliability analysis and failure probability with different random variables involved

Path reference	Load point	Random variables	Failure Probability P_f	
			pLMM	MCS
1	1	D and σ_y	0.29545	0.29909
	3	D and σ_y	0.04034	0.04296
	3	D, σ_y and P_1	0.18572	0.19733
$1'$	3	D, σ_y and fluctuation ΔP_1	0.28688	0.29473
2	2	D and σ_y	0.29816	0.31462
	4	D and σ_y	0.03299	0.03344
	4	D, σ_y and P_1	0.13221	0.13391
$2'$	4	D, σ_y and fluctuation ΔP_1	0.23561	0.24307

The failure probabilities of non-shakedown by pLMM are also compared with the direct MCS, with all random variables (including geometric dimension, material property and boundary condition) keeping the identical settings with Section 5.3.2. And the MCS convergency is guaranteed by the pertinent requirement [155], where the gross sampling times N (set as 3,000 times in this case) is determined according to Equation (5.2). The verifications are also shown in Table 5.2, and it can be observed that the results of the proposed probabilistic shakedown analysis are consistent with the exact solutions provided by MCS, with the relative error controlled within an acceptable range.

$$N > \frac{100}{P_f} \tag{5.2}$$

5.4 Validations and discussions

5.4.1 Validation strategy for the pLMM-based shakedown analysis

Driven by the conjunction of the MCS sampling and the direct non-linear FEA, the validation scheme is set to verify the effectiveness and accuracy of the proposed probabilistic shakedown analysis. As demonstrated in Fig. 5.21, the stochastic non-linear FEA model for verification consists of two parts. Firstly, according to the pLMM shakedown boundary acquired in Section 5.3.3, the verification load is selected on each boundary curve, which depicts the probabilistic shakedown limit. This load combination indicates the failure risk for which the load may cause the non-shakedown state due to exceeding the selected boundary. And based on the statistical distribution of design parameters, random variables are processed by MCS to acquire enough data points. Secondly, all the MCS-derived input data are transferred into the same non-linear FEA model with Section 5.3, formulating the stochastic FEA model to perform the step-by-step examination and evaluate the cyclic response of structural plastic strain at critical locations. In this verification, the edge of the hole (pointed out in the red circles in Figs. 5.22 and 5.23, where the cyclic plastic strain is more significant) is examined to find out whether the structure satisfies the shakedown state.

Here, the equivalent plastic strain (PEEQ) history is tracked to recognize different structural responses. If there is no progressive plastic strain taking place and the structure shows elastic behaviour after the first limited number of loadings and unloadings, it means the shakedown state is satisfied, as shown in Figs. 5.22 (a) and 5.23 (a). The black curves in Figs. 5.24 and 5.25 reflect the shakedown responses of the central holed plate under uncertain design conditions, where the time-dependent PEEQ stops accumulating after a few cycles at the beginning. On the contrary, alternating or progressive plastic strain is depicted by the red curves for which the structure response violates the shakedown condition, resulting in alternating plasticity or ratcheting mechanism (see the trends in Figs. 5.22 (b) and 5.23 (b). Here, the red curves in Figs. 5.24 (b) and 5.25 (b) also capture the effect of load fluctuations on the cyclic response of the central holed plate (see the blue ellipses in dotted lines). Consequently, when the non-shakedown state occurs, this random variable introduces an additional uncertain incremental plastic strain to the structural

response compared with the cases in the red lines of Figs. 5.24 (a) and 5.25 (a), leading to the lower shakedown limit as discussed in Section 5.3.3.

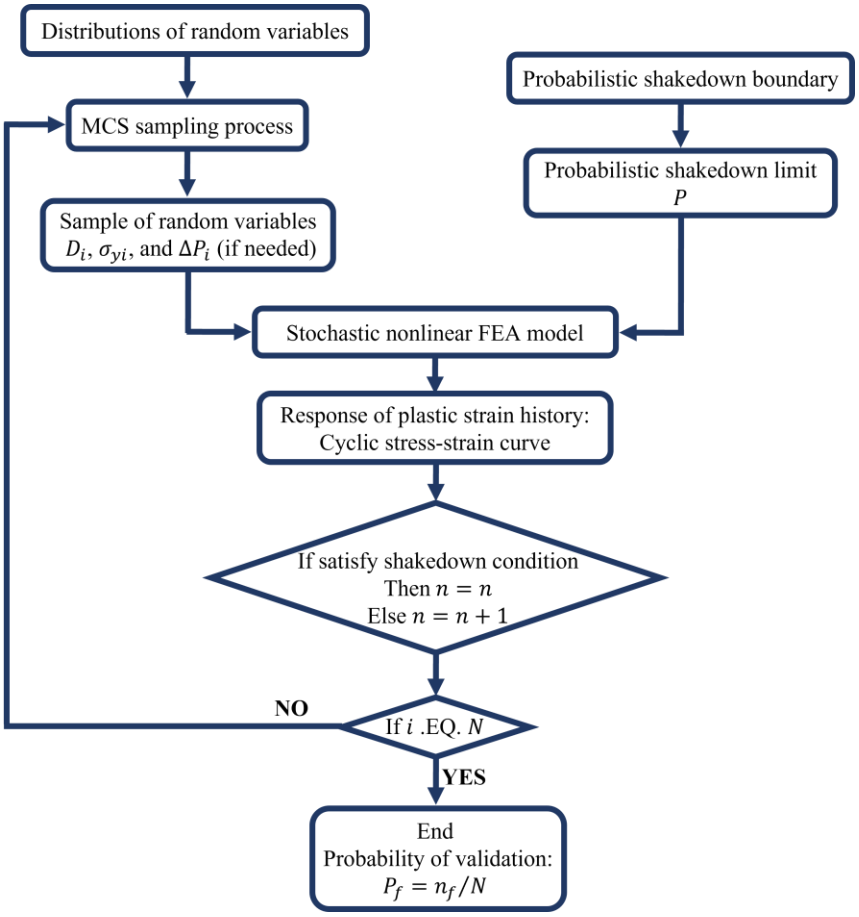

Fig. 5.21. MCS-based validation strategy for the pLMM shakedown boundary

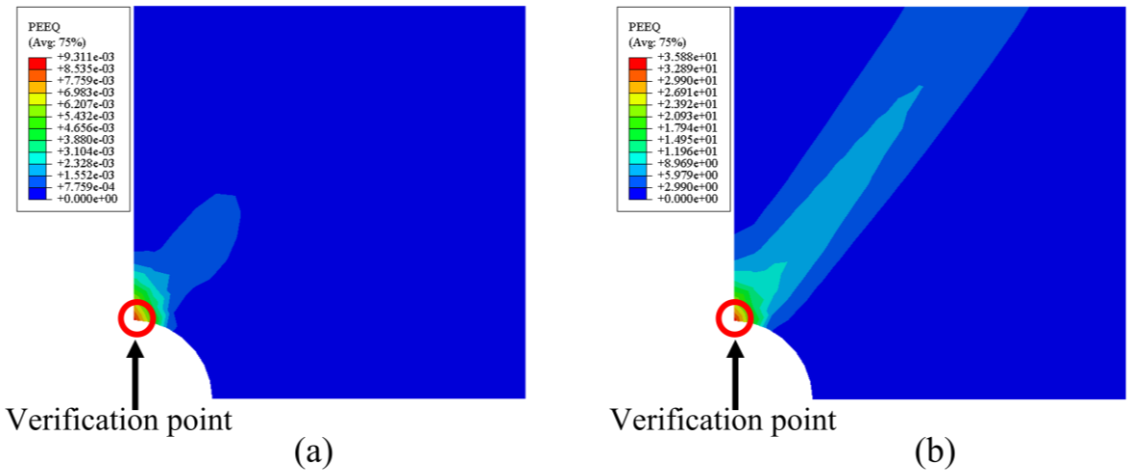

Fig. 5.22. Distribution of equivalent plastic strain field for loading paths 1 and $1'$: (a) under the shakedown mechanism and (b) under the ratcheting mechanism

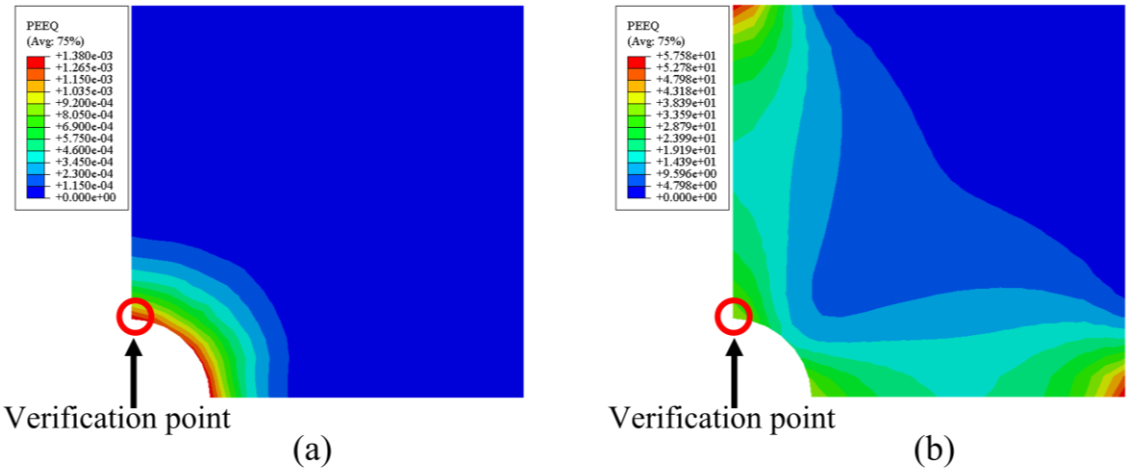

Fig. 5.23. Distribution of equivalent plastic strain field for loading paths 2 and $2'$: (a) under the shakedown mechanism and (b) under the ratcheting mechanism

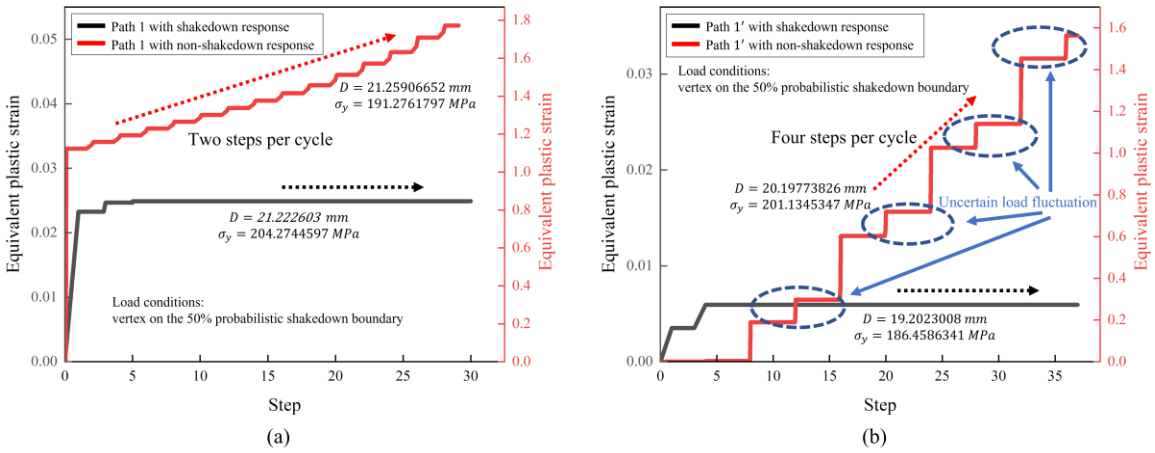

Fig. 5.24. Uncertain structural responses of the central holed plate at the verification point under different loading paths: (a) under loading paths 1 and (b) under loading path 1′ with additional uncertain load fluctuation

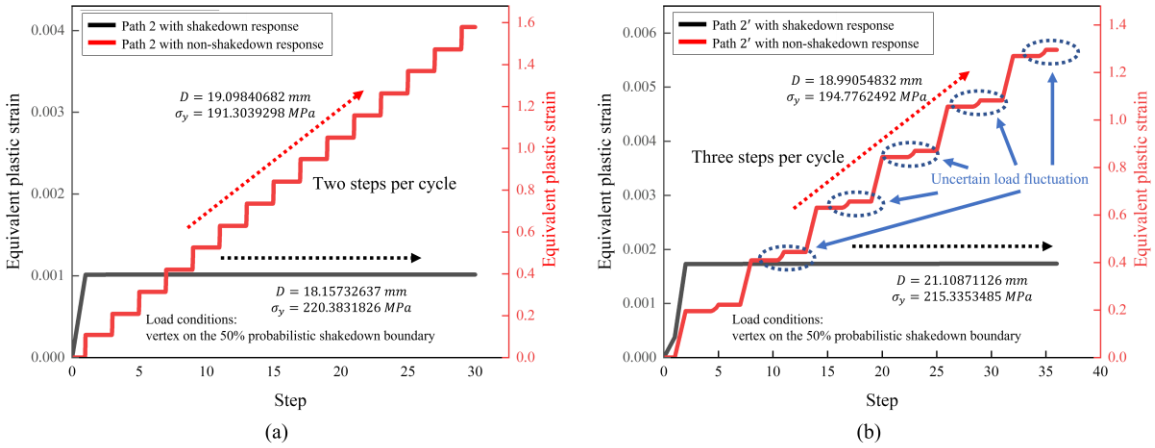

Fig. 5.25. Uncertain structural responses of the central holed plate at the verification point under different loading paths: (a) under loading paths 2 and (b) under loading path 2′ with additional uncertain load fluctuation

After finishing the whole MCS sampling with a step-by-step simulations process, by counting the total number of non-shakedown cases, the failure probability for verification is given by Equation (5.3):

$$P_f = \frac{1}{N}\sum_{i=1}^{N} I_f[G(\boldsymbol{X}_i)] = \frac{n_f}{N}$$

$$I_f[G(\boldsymbol{X}_i)] = \begin{cases} 0, & \text{shakedown state (safe case)} \\ 1, & \text{non} - \text{shakedown state (failed case)} \end{cases} \tag{5.3}$$

where n_f is the aggregate of failed cases due to non-shakedown, and N denotes the total times of MCS samplings that meet the prerequisite in Equation (5.2); I_f is the indicator function of failed cases due to a non-shakedown state.

5.4.2 Validation for the probabilistic shakedown boundary

For each loading path predefined in Figs. 5.7 and 5.9, a series of load conditions are chosen at the corner vertexes of the probabilistic shakedown boundary (see Figs. 5.11 and 5.12) along with a certain loading ratio of P_2/P_1, where the loading ratio is equal to 0.84 for paths 1 and 2, and 1.0 for paths $1'$ and $2'$. And the failure risk of non-shakedown is calculated by MCS with enough samplings, considering the uncertain structural design parameters (including geometric dimension, material yield strength and load fluctuation). The verification with MCS of the probabilistic shakedown boundary is listed and compared in Table 5.3, with the relative error defined by $\left(\left|P_{fLMM} - P_{fMC}\right|/P_{fMC}\right) \times 100\%$. In the verification of stochastic nonlinear FEA, several non-shakedown failure probabilities are predicted, which are quite aligned with that calibrated by the pLMM shakedown boundaries, and the maximum relative error does not exceed 20%, occurring only under the failure probability of 0.1. That means the pLMM shakedown analysis is able to provide accurate failure probability but avoid the heavy and complex trial-and-error process during Newton-Raphson iterations to derive the shakedown limit.

Table 5.3. MCS verification of the probabilistic shakedown boundary by pLMM shakedown procedure

Path reference number	Condition (P_1, P_2) (MPa)	P_f by pLMM calculation	P_f by MCS verification	Relative error (%)
1	(155,130)	0.1	0.1257	20.454
	(163,137)	0.3	0.3109	3.508
	(167,140)	0.5	0.5094	1.859
	(172,144)	0.7	0.7127	1.785
	(178,149)	0.9	0.9176	1.923
$1'$	(118,112)	0.1	0.1203	16.913
	(134,125)	0.3	0.3191	6.010
	(145,133)	0.5	0.5171	3.323
	(153,138)	0.7	0.7251	3.470
	(165,145)	0.9	0.9167	1.827
2	(170,170)	0.1	0.1152	13.265
	(179, 179)	0.3	0.3115	3.716
	(183,183)	0.5	0.5060	1.202
	(189,189)	0.7	0.7169	2.368
	(195,195)	0.9	0.9152	1.670
	(157,160)	0.1	0.1191	16.041

	(165,176)	0.3	0.3169	5.347
	(173,181)	0.5	0.5310	5.845
2′				
	(180,187)	0.7	0.7221	3.061
	(189,195)	0.9	0.9149	1.634

5.5 Conclusions

This chapter presents a novel strategy of probabilistic shakedown analysis under the pLMM framework, where multiple uncertainties of the design parameters are taken into consideration. With the shakedown multiplier calculated by the direct method, a concise limit state function, the shakedown limit state indicator function (SLSIF), is established, making the efficient reliability analysis for shakedown behaviour available. Besides, the uncertainty due to the loading fluctuation is considered to account for complicated loading conditions in the benchmark and validations.

The main conclusions of this study are as follows:

1. The pLMM framework for probabilistic shakedown analysis is proposed with the physically-based estimation model and the highly efficient iteration form to predict the failure risk against the non-shakedown state, which is conducive to improving the design robustness under cyclic load conditions.

2. With the benchmark of the holed plate investigated, the probabilistic shakedown boundary and reliability index are provided considering different combinations of random variables.

3. The influence of uncertainty from loading fluctuation is also emphasized and clarified in detail, and the influence on the structural reliability level is demonstrated clearly.

4. The validation plan with direct MCS is also elaborated to verify the effectiveness of the probabilistic shakedown boundary by the pLMM, which reveals that the proposed pLMM shakedown analysis provides an accurate probabilistic shakedown limit and the related failure risk.

6 Physics-based neural network for probabilistic low cycle fatigue and ratcheting assessments of pressurized elbow pipe component

6.1 Introduction

As a frequently used component in nuclear and aerospace engineering, the structure of elbow pipe faces two concerned failure modes under cyclic thermo-mechanical loads: Low Cycle Fatigue (LCF) and ratcheting, leading to LCF crack initiation and accumulative plastic strain, respectively. A wide variety of experimental investigations of the pipeline structures revealed the importance of failure analysis for LCF [156, 157] and ratcheting behaviours [158, 159], delivering a large amount of relevant failure data [160, 161]. To predict the LCF life, Takahashi [162] investigated the elbow pipe with cyclic bending moment through experiments and Finite Element Analysis (FEA), with the location of crack initiation and crack growth direction estimated considering the local thinning effect. Zheng et al. [163] utilized the Direct Steady Cyclic Analysis (DSCA) under the Linear Matching Method (LMM) [164] to simulate the cyclic plastic response of the pressurized pipe, where different constitutive models are adopted to illustrate the strain hardening effect on the structural LCF life. When addressing the ratcheting analysis of pipe components, various material hardening laws have been applied to explore the response of ratcheting strain [165, 166]. Liu et al. [167] reported several ratcheting behaviours of elbow pipe by numerical simulations with the Chen-Jiao-Kim (CJK) model, during which the influence of loading paths on the ratcheting strain was illustrated, and the Ahmadzadeh-Varvani (A-V) [168] hardening rule showed wide effectiveness as well. To further improve the efficiency, Chen extended the LMM shakedown algorithms to calculate the ratcheting boundary [169] under mechanical and thermal load combinations [93].

Although numerous research efforts were made toward evaluating LCF life and ratcheting behaviour of pipe components, the aforementioned deterministic analyses still lack uncertainty considered and ignore statistical information about output in the assessment schemes. Therefore, pertinent attempts to deal with the randomness of fatigue life by probabilistic analysis methodology [170] have been developed to fulfil the reliability-based design, with the underlying uncertainty of design parameters reflected. The prototype was a simple combination of probabilistic analysis tools and evaluation functions of fatigue life. In Refs. [171, 172], the failure probability of elbow pipe

was examined by FORM and verified by MCS. To save computational resources, the reduced-order model was needed during repeated MC. For instance, RSM, with the polynomial formula and least-squares regression, has been adopted to estimate fatigue life [173, 174]. Another universal modelling tool, the artificial neural network was also employed in reliability-based fatigue assessments. It connects the deterministic model and probabilistic calculation, providing a high-quality approximation of LCF life [175]. Durodola [176] applied the feedforward backpropagation Multi-Layer Perceptron (MLP) neural network to perform the probabilistic fatigue analysis, and the dynamic Bayesian network was proved to be able to derive the probabilistic fatigue damage of subsea pipe [177]. In addition, the neural network-based probabilistic density function of fatigue life was introduced in Ref. [178] and recently extended by Ma [179] and Mortazavi [180] to address the fatigue crack growth problem with small experimental data available. Among sorts of neural network techniques, the Elliptical Basis Function (EBF) neural network has shown the comprehensive capability to produce a reliable surrogate model, covering a huge number of engineering disciplines [181, 182].

Currently, unsolved challenges still exist that as the fundamental of the probabilistic analysis framework, there are limited general engineering LCF and ratcheting procedures integrated with the neural network techniques, where the feasible balance of efficiency and accuracy is achieved during the training and predicting. This study focuses on proposing unified probabilistic fatigue and ratcheting analyses with multiple uncertainties of design parameters considered, by which the statistical information of key output and the reliability-centred assessment diagram are acquired for structural risk management.

The rest of this chapter is organized below: In Section 6.2, the probabilistic Liner Matching Method (pLMM) framework for probabilistic fatigue and ratcheting analyses is proposed, where the surrogate modelling strategy with the Linear Matching Method-driven neural network (LDNN) is established to predict the key structural responses. Following, the benchmark of elbow pipe bend is investigated in Sections 6.3 and 6.4 to illustrate the extensive applicability of the proposed pLMM, with the probabilistic assessment curves for LCF and ratcheting failures constructed. In Section 6.5, the Unified Limit State Indicator (ULSI) is adopted to build the reliability-based evaluation diagrams. In the last section, the main conclusions of this study are given out.

6.2 Probabilistic Linear Matching Method (pLMM) framework for LCF and ratcheting analyses

The probabilistic Linear Matching Method (pLMM) framework is developed to conduct the structure-level probabilistic analysis and reliability-based design in terms of cyclic plastic failures, where the Linear Matching Method-driven neural network (LDNN) surrogate model is proposed to efficiently predict the LCF lifetime and ratchet limit.

6.2.1 Probabilistic Linear Matching Method (pLMM) framework for LCF and ratcheting analyses

As the foundation of the probabilistic structural integrity assessment, the efficient LCF and ratcheting analysis procedures play a vital role in the mathematical modelling of structural responses due to cyclic loadings. Here, a two-step strategy (including LMM DSCA and ratcheting analysis procedures [183]) developed by Ref. [110] is responsible for generating reliable datasets for the subsequent training, testing and validating of the surrogate models. In the first step, the residual stress history and the associated plastic strain range are calculated by DSCA to determine the LCF life, $L_f = L_f(\Delta\varepsilon)$, considering the material fatigue data. And the ratchet limit multiplier, $\lambda_{ratcheting}$, is solved according to the extended upper bound shakedown theorem in the second step.

Under the pLMM framework, the LDNN, a feedforward neural network [73], is built and employed as the MLP for modelling and prediction. Based on the universal approximation theorem [74], the rationality and effectiveness of the three-layer neural network have been proved by Ref. [75], and the general structure contains three layers [184]: the input layer, the hidden layer and the output layer. The data flow commences with the design input vector passed in through the input layer to the hidden layer, and in the middle layer, the EBF [185] existing in each neuron acts as the activation function, leading to non-linear mapping. Usually, the number of neurons used in the hidden layer depends on the size of the training data set for a certain type of analysis, and it should be guaranteed to be larger than the dimensionality of the input vector being processed. Then, with the summation of the weighted input and bias, the output layer generates the final predictions.

Adopting the non-linear activation functions in the hidden layer, the interpolating function is formulated for implementing LCF lifetime and ratchet limit modelling, which is written in the following forms,

$$L_f(\boldsymbol{x}) = \sum_{i=1}^{N} \alpha_i \phi_i(\boldsymbol{x}) + \alpha_{N+1}, \text{ for LCF lifetime modelling} \tag{6.1}$$

$$\lambda_{ratcheting}(\boldsymbol{x}) = \sum_{i=1}^{N} \alpha_i \phi_i(\boldsymbol{x}) + \alpha_{N+1}, \text{ for ratchet limit modelling} \quad (6.2)$$

where $\phi_i(\boldsymbol{x})$ is the basis function of EBF, α_i and α_{N+1} are the weight and bias terms, respectively, and the L_f and $\lambda_{ratcheting}$ represent the approximations of LCF life and ratchet limit multiplier. It is worth noting that the input variable of the activation function is the Mahalanobis distance vector [186] determined by Equation (6.3),

$$\|\boldsymbol{x} - \boldsymbol{x_i}\|_m^2 = (\boldsymbol{x} - \boldsymbol{x_i})^T \boldsymbol{S}^{-1} (\boldsymbol{x} - \boldsymbol{x_i}) \quad (6.3)$$

where the covariance matrix $\boldsymbol{C}$ controlling the quality of surrogate modelling is given by Equation (6.4) and the $\boldsymbol{\mu}$ is the centre of known data.

$$\boldsymbol{C} \approx \frac{1}{N} \sum_{i=1}^{N} (\boldsymbol{x_i} - \boldsymbol{\mu})(\boldsymbol{x_i} - \boldsymbol{\mu})^T \quad (6.4)$$

6.2.2 Configuration of LDNN-based probabilistic LCF and ratcheting analyses

The working flow of LDNN-based probabilistic LCF and ratcheting analyses under the pLMM framework is illustrated by the flowchart in Fig. 6.1, including three main stages.

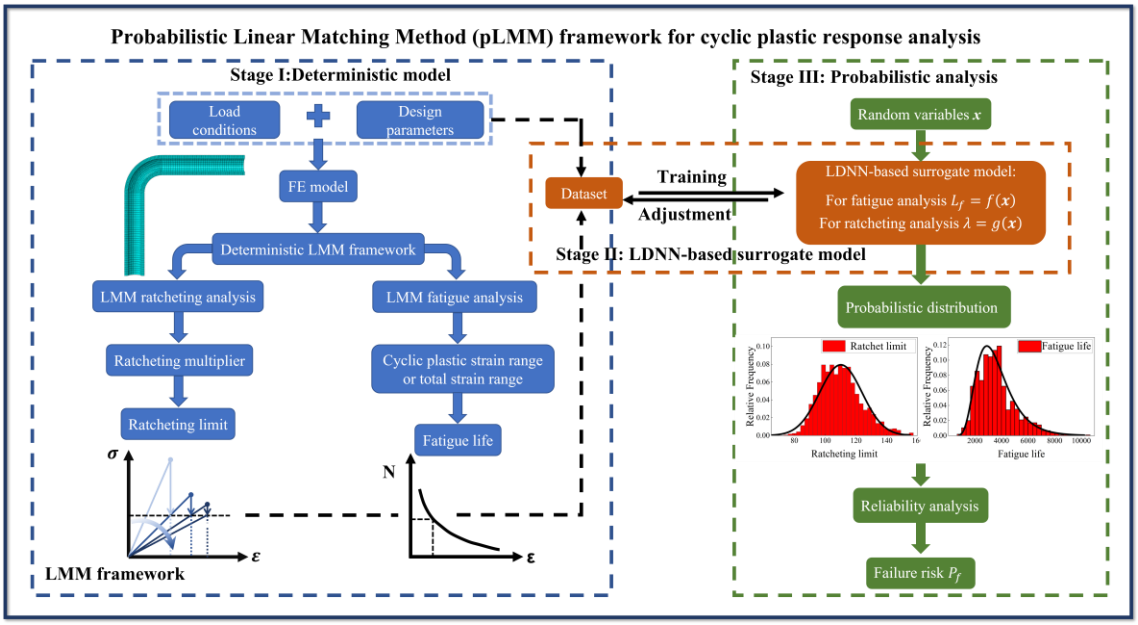

Fig. 6.1. Flowchart of probabilistic LCF and ratcheting analyses under the pLMM framework

- Stage 1. Running the deterministic LMM procedure to prepare the training dataset;

- Stage 2. Establishing the LDNN through a series of training, testing and validating steps;

- Stage 3. Performing the probabilistic LCF or ratcheting analysis with surrogate models to predict the distribution of key output and the failure probability. As the core element of the pLMM, the LDNN surrogate model connects the deterministic analysis and the probabilistic analysis, which is dedicated to providing precise mapping from input parameters to output.

The pLMM LCF and ratcheting analyses are implemented by using the conjunction of ABAQUS and Isight, and the computational configuration is briefly exhibited in Fig. 6.2. In the first step, the LDNN is trained with a given dataset, enabling it to recognize the known data. As illustrated in the blue dotted rectangle, to prepare the physics-based dataset for the training of LDNN, the Latin Hypercube Sampling (LHS) technique is adopted to generate a series of design condition sets within the design space, including the geometric dimensions, the material properties and the load conditions. Then, these sets of design conditions are processed by the LMM Plugin program to derive the LCF life and ratchet limit multiplier accordingly (see Appendix B). Hence, the weights parameters and the bias term for the LDNN surrogate model are able to be calculated simultaneously by solving the training algorithms [187] from Equations (6.5) to (6.9), which is implemented according to Appendix C.

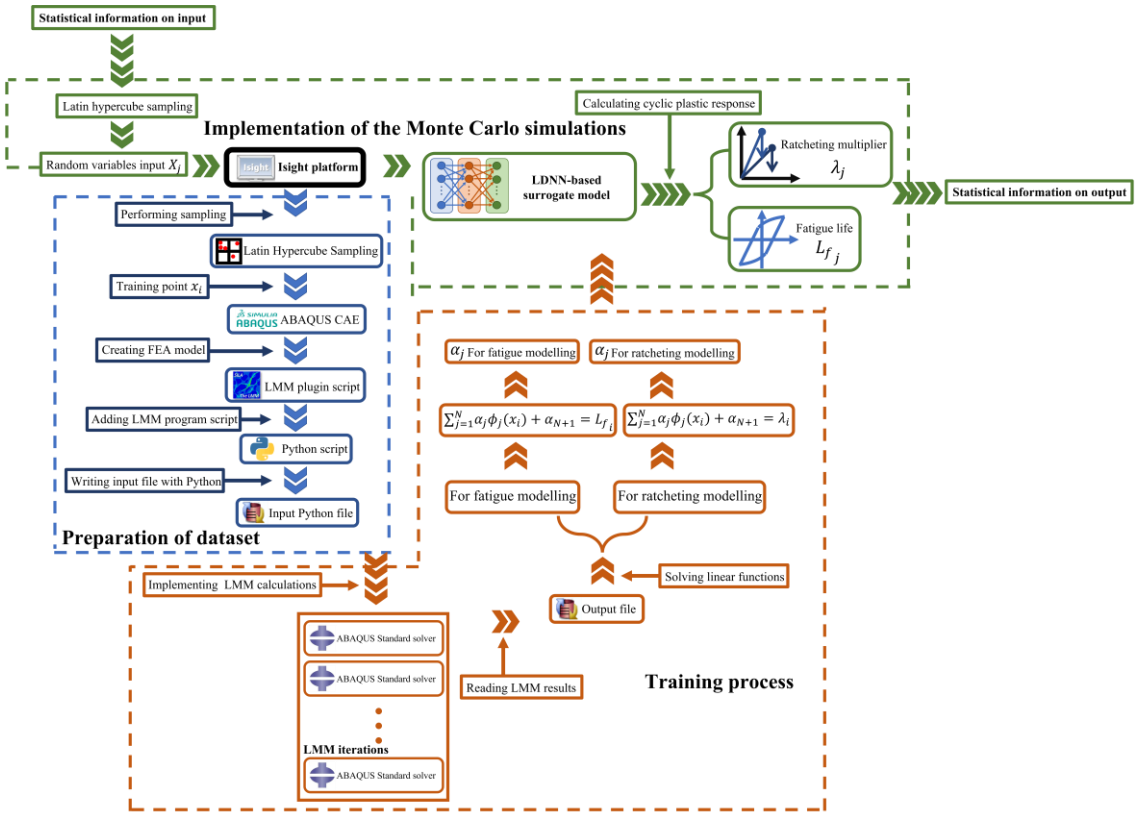

Fig. 6.2. Configuration of pLMM framework for probabilistic LCF and ratcheting analyses

$$\sum_{j=1}^{N}\alpha_j\phi_j(\boldsymbol{x_i})+\alpha_{N+1}=\begin{cases}L_{f_i}(\boldsymbol{x_i}), & \text{for fatigue analysis}\\ \lambda_{ratcheting_i}(\boldsymbol{x_i}), & \text{for ratcheting analysis}\end{cases} \tag{6.5}$$

$$i=1,2,\dots,N$$

$$\sum_{j=1}^{N}\alpha_j=0 \tag{6.6}$$

Here, the coefficients matrix of the above linear equations system is introduced below,

$$\boldsymbol{H}=\begin{bmatrix}\boldsymbol{G} & \boldsymbol{p}\\ \boldsymbol{p}^T & \boldsymbol{0}\end{bmatrix} \tag{6.7}$$

where the $\boldsymbol{p}=\begin{bmatrix}1\\1\\\vdots\\1\end{bmatrix}$ and $\boldsymbol{G}=\begin{bmatrix}\phi_1(\boldsymbol{x_1}) & \phi_2(\boldsymbol{x_1}) & \cdots & \phi_N(\boldsymbol{x_1})\\ \phi_1(\boldsymbol{x_2}) & \phi_2(\boldsymbol{x_2}) & \cdots & \phi_N(\boldsymbol{x_2})\\ \vdots & & \ddots & \vdots\\ \phi_1(\boldsymbol{x_N}) & \phi_2(\boldsymbol{x_N}) & \cdots & \phi_N(\boldsymbol{x_N})\end{bmatrix}$

This linear equations system is able to be expressed by matrix form, and consequently, the weights matrix is acquired by solving Equations (6.8) and (6.9),

$$\boldsymbol{H\alpha = y} \tag{6.8}$$

$$\boldsymbol{\alpha = H^{-1}y} \tag{6.9}$$

where the output matrix y, including LCF life or the ratchet limit multiplier, is predicted by the LMM procedure in terms of the associated input parameters. To further improve the fitting quality in the second stage (in Fig. 6.1), the coefficients of weights and biases are adjusted iteratively based on the error analyses, and the more pertinent surrogate relationship is determined to estimate the LCF life and ratchet limit multiplier accurately. Finally, as the input parameters with significant impact are identified by the sensitivity analysis, the selected random variables with the predefined statistical features (e.g., statistical distribution type, mean value, and standard deviation) are passed into the probabilistic analysis framework through the built LDNN-based surrogate model, instead of the traditional FEA solver, to predict the distributions of key results and the failure risk regarding structural cyclic plastic response by MCS (see Appendixes D and E).

6.3 Probabilistic LCF analysis for elbow pipe bend component

There are considerable fatigue failure cases of elbow pipe bends reported in nuclear, aerospace and chemical engineering, where the uncertain design and operating conditions tend to be non-negligible. Here, a benchmark of such a structure is investigated to illustrate the applicability of the proposed probabilistic LCF assessment.

6.3.1 Description of the FEA model

As displayed in Fig. 6.3, the structure of the elbow pipe is characterized by the dimensions in Table 6.1, where the parameters R_O, t_n, R and L denote the outer radius of elbow pipe, nominal pipe wall thickness, bending radius and straight length, respectively. Besides, the bending characteristic, h, is defined as $Rt/{r_m}^2$, where r_m refers to the nominal mean radius of the pipe. The FEA model is discretized by ABAQUS, with the 20-node quadratic brick element C3D20R adopted, which keeps a good balance of numerical precision and computational efficiency by reduced integration technology. And inside the black dotted box, the elbow zone is refined so as to satisfy the requirements of mesh convergence and to capture the prominent stress gradient around

this local region, with 7,680 elements created in total. It is also assumed that the small deformation theory is adopted in the subsequent non-linear analysis concerning LCF and ratcheting behaviour.

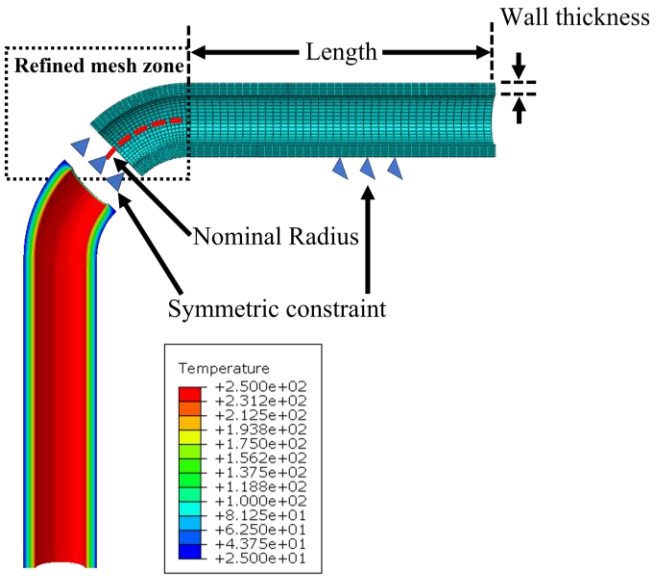

Fig. 6.3. Geometry dimensions and FEA model of the elbow pipe bend with BCs

Table 6.1. Geometry dimensions of the selected elbow pipe bend

Outer radius R_O (mm)	Wall thickness t_n (mm)	Bending radius R (mm)	Length L (mm)	Bending characteristic h
180	60	500	1500	1.33

6.3.2 Material properties and boundary conditions (BCs)

The elbow pipe bend is made of austenitic stainless steel 316L, due to the superior corrosion resistance in the high-temperature environment [188], and the temperature-dependent material properties are provided [6] in Table 6.2, including Young's modulus E, Poisson's ratio ν, the average coefficient of linear thermal expansion α_m and thermal conductivity k. In addition, the temperature-dependent cyclic stress-strain relationship is described by Ramberg-Osgood (R-O) form derived from Appendix A3.3S of Ref. [6], where ε_{ta} is the total true strain amplitude, σ_a is

the total true stress amplitude, $\bar{E}$ is the multi-axial Young's modulus, and K and n are the strength coefficient and plastic hardening parameters controlling the cyclic responses. For the purpose of fatigue life determination, the relationship between the maximum acceptable cyclic strain range and the LCF life considering various temperature conditions is depicted in Fig. 6.4.

Table 6.2. Temperature-dependent material properties of 316L stainless steel

Temperature (℃)	20	100	200	300	400
Young's modulus E (10^3MPa)	200	193	185	176	168
Poisson's ratio ν			0.3		
Coefficient of thermal expansion α_m (10^{-6}/ ℃)	15.3	15.9	16.6	17.2	17.8
Thermal conductivity k (W/mm · K)	0.01428	0.01548	0.01698	0.01849	0.01999
K (MPa)	2286	2082	1860	1650	1650
n	0.351	0.339	0.325	0.31	0.31

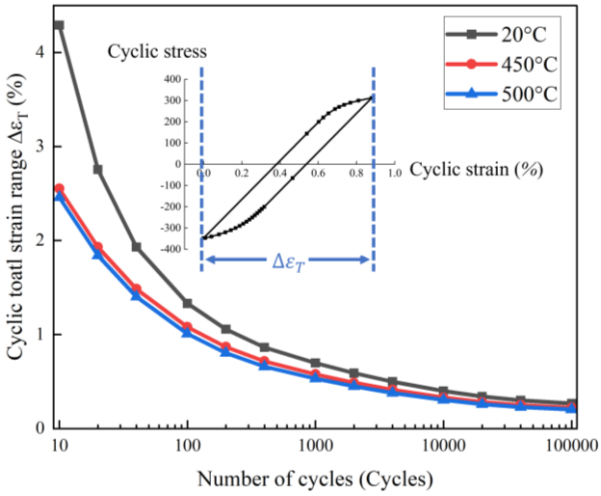

Fig. 6.4. Relationship between the maximum acceptable cyclic strain range and the fatigue life under different temperature conditions [6]

The quarter model of the elbow pipe bend is created with the symmetric BCs exerted on the symmetric surfaces, as shown in Fig. 6.3. On the inner surfaces lies the inner pressure, with an equivalent tensile load applied and plane condition on the free end of the straight pipe to satisfy the closed end condition. And along the wall thickness of the elbow pipe, there exists the salient temperature difference displayed in Fig. 6.3, which is obtained by the steady-state thermal analysis with prescribed temperatures on the inside and outside surfaces. As predefined in Fig. 6.5, there are two typical loading paths considered concerning the working circumstances of the elbow pipe bend: the first path is comprised of constant inner pressure and cyclic temperature difference, while path 2 is the combination of both cyclic loading conditions. It should be clarified that when configuring the LMM ratcheting analysis, the reference temperature difference is defined by the inner surface temperature of 250 ℃ and outer surface temperature of 25 ℃, with the reference inner pressure usually set to 1 unit (1 MPa for this case), by which the ratchet limit is approached by scaling the reference loading conditions iteratively.

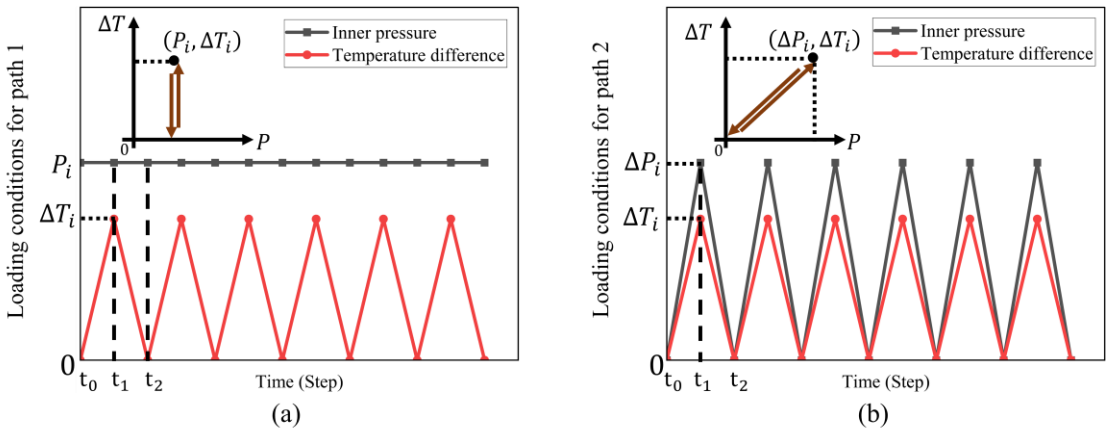

Fig. 6.5. Loading condition combinations with different paths: (a) constant inner pressure and cyclic temperature difference and (b) cyclic inner pressure and temperature difference

6.3.3 Deterministic ratchet limit boundary and reverse plasticity region

By means of the deterministic LMM procedures, the limit boundaries of the elbow pipe bend are established in Fig. 6.6, in terms of two predefined cyclic loading patterns. The black curve describes the ratcheting boundary of loading path 1 and the red boundary is related to loading path 2, by which the structural responses are divided into two different sections: the ratcheting region and the reverse plasticity region. Here, the horizontal and vertical coordinates are normalized by the limit load of the elbow pipe bend, 112.4 MPa, and the applied reference temperature difference, 225 ℃, respectively. It is assumed that in the subsequent probabilistic analyses, the maximum normalized temperature difference is limited to a level lower than 1.8, which refers to the potential maximum inner temperature not exceeding 450 ℃, without significant creep-fatigue interaction due to the high-temperature environment included.

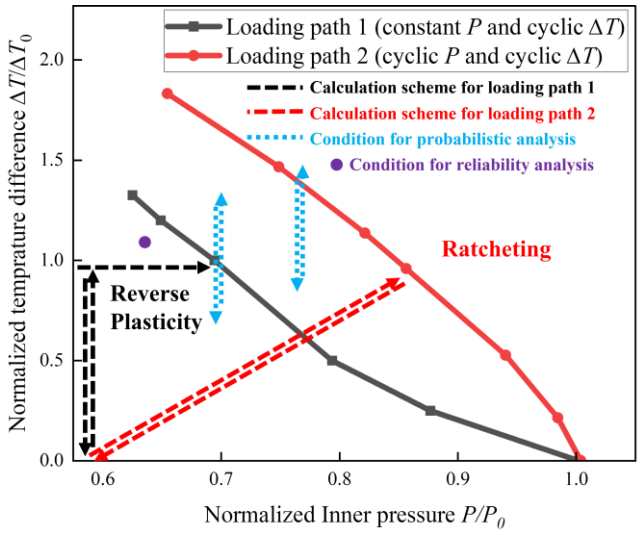

Fig. 6.6. Ratcheting boundary and reverse plasticity region of the elbow pipe bend under different cyclic loading paths

6.3.4 LDNN-based modelling of structural LCF life

The sensitivity analysis result visualizes the significance of related parameters by quantifying the effect of each input x on LCF life L_f, where the input parameters include cyclic plastic material properties K and n, geometric dimension (nominal thickness t_n), maximum inner pressure P (constant pressure for loading path 1 and cyclic pressure for loading path 2) and maximum cyclic temperature difference ΔT. Here, the LCF life of the elbow pipe is determined by the maximum cyclic plastic strain range at the geometrically discontinuous location, the inner flank of the transition area between two straight segments, which is pointed out by the red dotted line in Fig. 6.7, and to capture the mechanism of reverse plasticity, the negative sign of the equivalent stress expresses the stress state of the unloading step is opposite to that during the loading process.

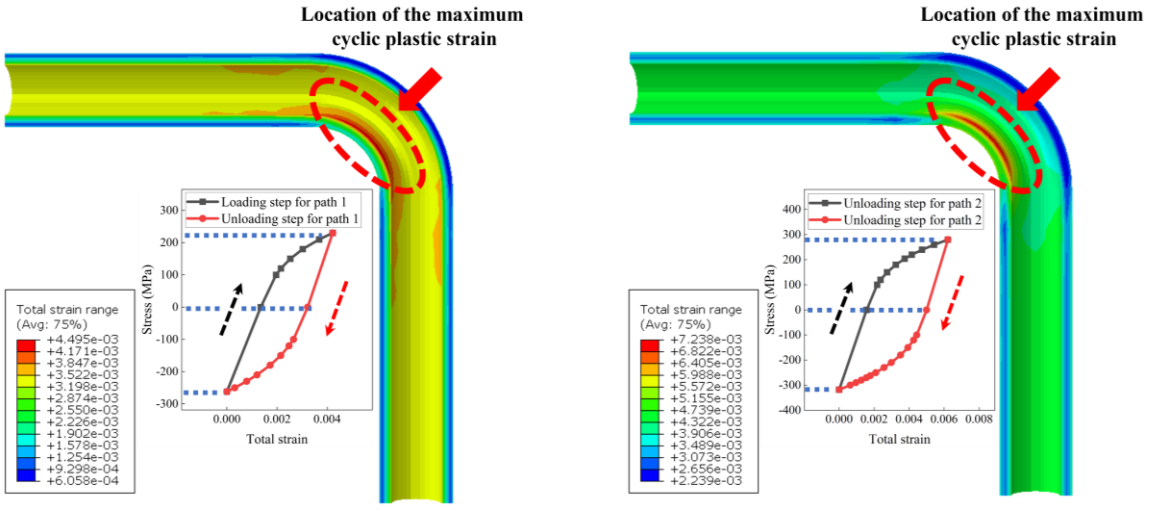

(a) (b)

Fig. 6.7. Failure mechanisms and cyclic plastic strain range of elbow pipe bend for LCF life determination at critical location: (a) under loading path 1 and (b) under loading path 2

The sensitivity analysis considers each input parameter as a random variable that follows the statistical assumption listed in Table 6.3, and the Design of the Experiment (DOE) employs the LHS to generate the design matrix which covers the scope of ± 3 of its standard deviation σ (in terms of 99.7% probability region) from the mean value. Figs. 6.8 (a) and (b) firstly indicate that no matter which cyclic loading pattern is selected, concerning the LCF life L_f of elbow pipe bend, the cyclic temperature difference and the cyclic strain hardening exponent n play the most remarkable role, showing negative correlations with the output. The detailed relationship between the $\Delta T/\Delta T_0$, n and L_f is visualized by the 3D response surfaces of fatigue life in Figs. 6.8 (c) and (d). It can be found that the most significant parameter range affecting fatigue life is largely concentrated in the place where the normalized temperature difference is around 1.0 (i.e., $250\ ℃$ applied on the inner surface and $25\ ℃$ on the outer).

Besides, the material cyclic strength coefficient K and the structural nominal thickness t_n also have an inferior positive impact on the LCF life L_f. With respect to inner pressure, there appears a certain negative effect on the determination of LCF life. As the adopted load combinations in this sensitivity study are selected quite close to the structural ratcheting boundary (shown in Fig. 6.6) to deliver a comprehensive analysis, consequently, the strength of the cyclic plastic strain range under loading path 1 is also affected by the interaction between the alternating

plasticity and the ratcheting effect. In such a case, once the constant inner pressure tends to approach and further exceed the ratcheting boundary, the additional ratcheting strain per cycle is needed to be taken into account during the measurement of the enhanced cyclic response and the subsequent evaluation for LCF life.

Table 6.3. Statistical information of the random variables for probabilistic analysis

Random variable	Mean value	Coefficient of variation	Distribution
Material parameter K	1650		
Material parameter n	0.31	0.05	
Nominal thickness t_n (mm)	60		Normal
Normalized inner pressure P/P_0	0.625		
Normalized temperature difference $\Delta T/\Delta T_0$	1.2	0.1	

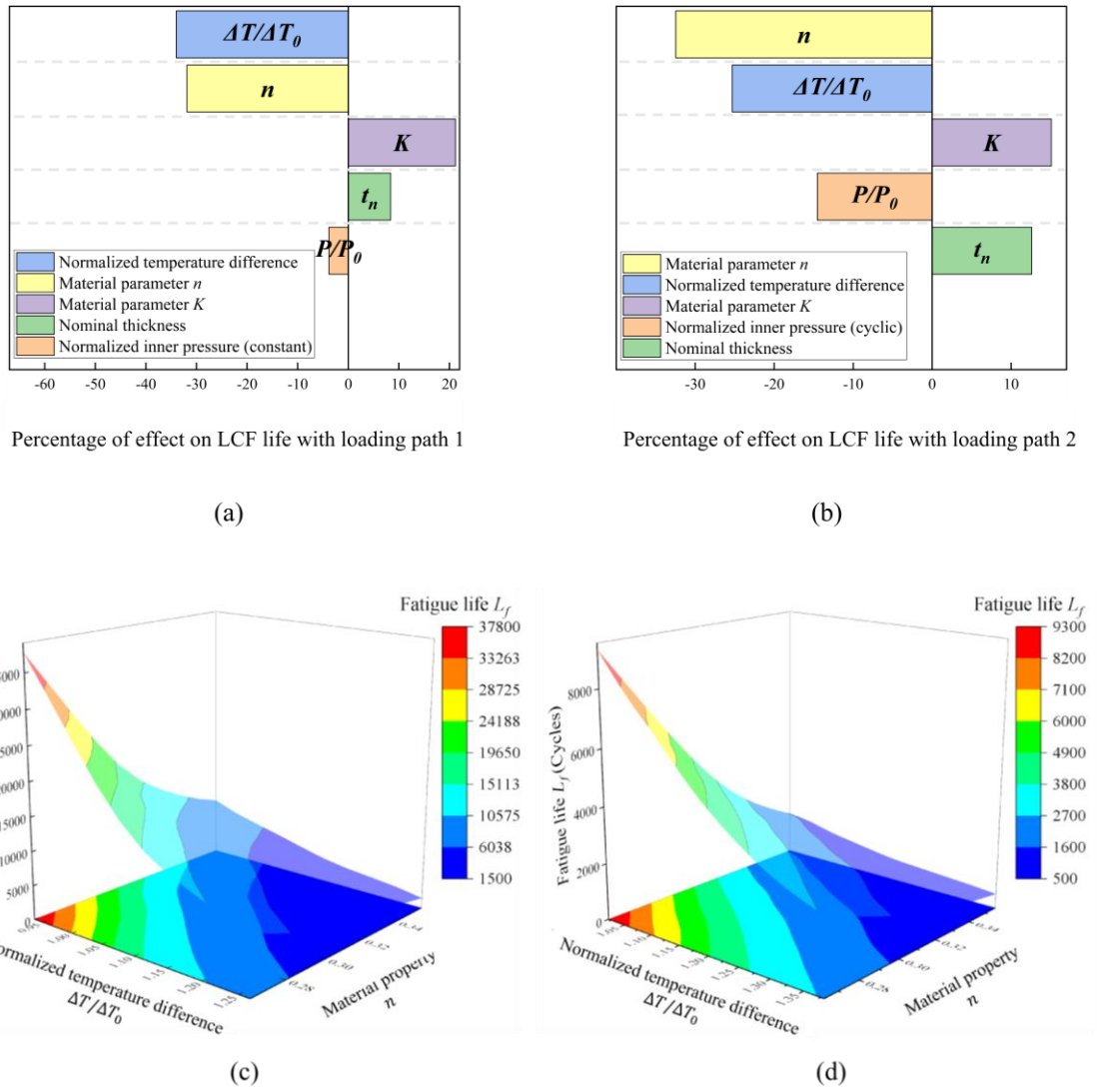

Fig. 6.8. Sensitivity analysis for LCF life of the elbow pipe bend: (a) sensitivity of each design parameter for loading path 1; (b) sensitivity of each design parameter for loading path 2; (c) response surface of LCF life under loading path 1 and (d) response surface of LCF life under loading path 2

The training process is implemented by solving the linear equations system in Equation (6.8), with several pairs of data including given input (selected by LHS to cover the same range in the sensitivity analysis) and corresponding output (provided by the LMM DSCA procedure) arranged. During this process, the bias and weight terms of the 200 neuron pathways are calibrated first and then adjusted through a series of validation iterations to minimize the squared fitting errors, and finally to enhance the prediction accuracy. Fig. 6.9 exhibits the fitting quality and error analysis by comparing LCF life derived by LMM DSCA and the prediction of LDNN, and for both cases, there

is an acceptable consistency ($R^2 \geq 0.99$) between the predicted values and the given solutions of LMM fatigue analyses, with all the test data lying within the ± 1.4 scatter band.

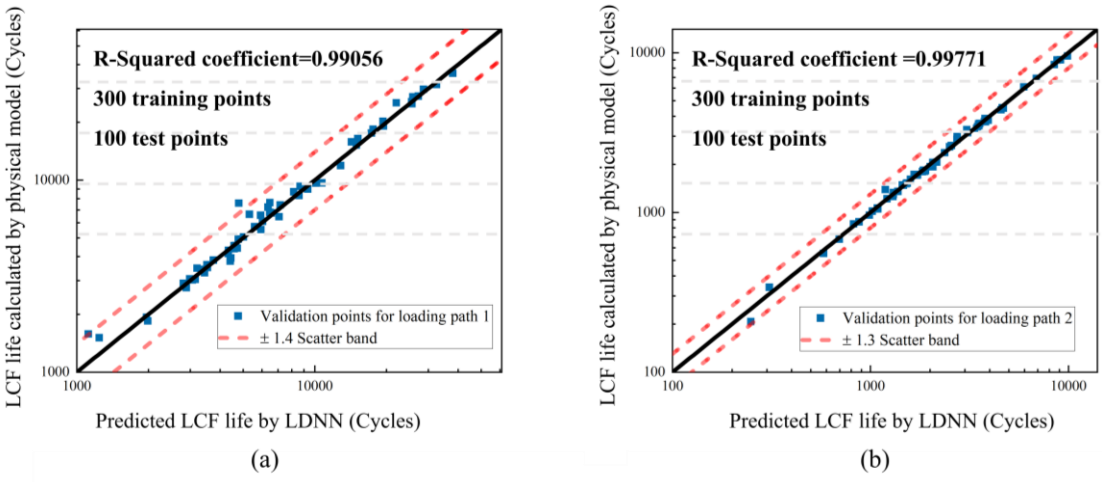

Fig. 6.9. Fitting quality of the prediction with the LDNN method: (a) for cyclic loading path 1 and (b) for cyclic loading path 2

6.3.5 Probabilistic LCF assessment boundary for elbow pipe bend

The statistical distribution of the elbow pipe LCF life, visualized by the 3D plots in Fig. 6.10, is investigated employing the LDNN-based surrogate model, where the load combinations mainly pertain within the alternating plasticity domain in Fig. 6.6. During the MCS, the statistical parameters, including the mean and standard deviation, are checked by the convergence criterion to maintain enough gross sampling numbers generated. It can be observed from Fig. 6.10 (a) that for loading path 1, under the existence of random variables including material property parameters (K and n), pipe thickness and the inner pressure, the LCF life of elbow pipe bend tends to show the Lognormal distribution. The mean value of LCF life keeps reducing and the dispersion appears more obvious as the level of cyclic temperature difference declines. On the other hand, when operating with loading path 2 (both inner pressure and temperature difference are cyclic), it is more proper to describe the trend of LCF life by the Weibull distribution, and such two cyclic conditions make the mean LCF life disperse more concentrated in a narrow lifetime range from 1,000 to 8,000 cycles, which, among all the cyclic temperature difference levels, shift more slightly than in the case of loading path 1. However, under $\Delta T/\Delta T_0$ ranging from 0.8 to 1.3, the LCF life distribution is more sparse in terms of the feature of the Weibull distribution compared with the Lognormal

distribution in the results of loading path 1. Detailed distribution parameters for these two sets are also listed in Table 6.4

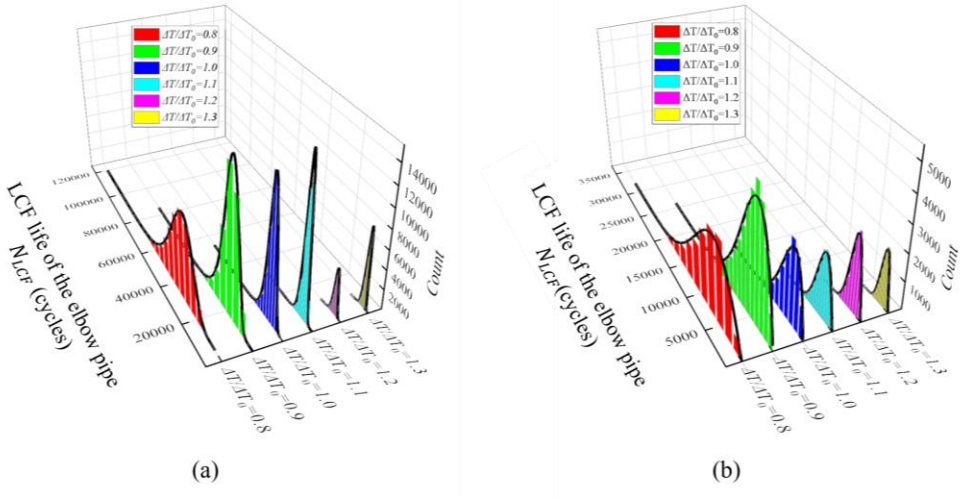

Fig. 6.10. Statistical distribution of LCF life under different normalized cyclic temperature difference levels: (a) with loading path 1 and (b) with loading path 2

Table 6.4. Statistical distribution of LCF life under normalized cyclic temperature differences with two different loading paths

Loading path	$\Delta T/\Delta T_0$	Statistical distribution of LCF life
1	0.8	$N_{LCF} \sim Lognormal(10.428,\ 0.3090)$
	0.9	$N_{LCF} \sim Lognormal(9.736,\ 0.3396)$
	1.0	$N_{LCF} \sim Lognormal(9.108,\ 0.3202)$
	1.1	$N_{LCF} \sim Lognormal(8.704,\ 0.2817)$
	1.2	$N_{LCF} \sim Lognormal(8.289,\ 0.2931)$
	1.3	$N_{LCF} \sim Lognormal(7.943,\ 0.3004)$
2	0.8	$N_{LCF} \sim Weibull\ (9282.420, 1.9340)$
	0.9	$N_{LCF} \sim Weibull\ (5832.022, 1.7249)$
	1.0	$N_{LCF} \sim Weibull\ (3741.487, 1.7164)$
	1.1	$N_{LCF} \sim Weibull\ (2606.012, 1.9965)$
	1.2	$N_{LCF} \sim Weibull\ (1947.245, 2.1429)$
	1.3	$N_{LCF} \sim Weibull\ (1404.174, 2.3017)$

Similar to the material probabilistic S-N (P-S-N) curves, the probabilistic LCF assessment boundary for elbow pipe bend is established by connecting a series of probabilistic LCF life within the same survival probability, as plotted in Fig. 6.11. Here, the green colour represents the relationship between the median LCF life and different levels of normalized cyclic temperature difference. With the additional cyclic inner pressure applied, the probabilistic LCF assessment boundary of loading path 2 possesses a much lower acceptable lifetime range than that of loading path 1. It is critical that for the most conservative boundary with 99% survival probability, the LCF life with loading path 1 distributes from 1,000 cycles to 11,000 cycles, while the lifespan of loading

path 2 sharply reduces to within only 1,000 cycles due to the combination of cyclic mechanical and thermal conditions. Besides, similar to the circumstance of probabilistic LCF life, there is a more decentralized characteristic of each LCF assessment boundary when considering loading path 2, especially in the domain with high survival probability, which results in the fragile reliability of the elbow pipe component because of the interaction of the thermomechanical fatigue mechanism. That means when addressing the risk management with a combination of cyclic mechanical and thermal loading conditions, more redundant design safety parameters should be considered for not only directly weakening the survival probability range but also enlarging the dispersion degree of the fatigue boundary cluster.

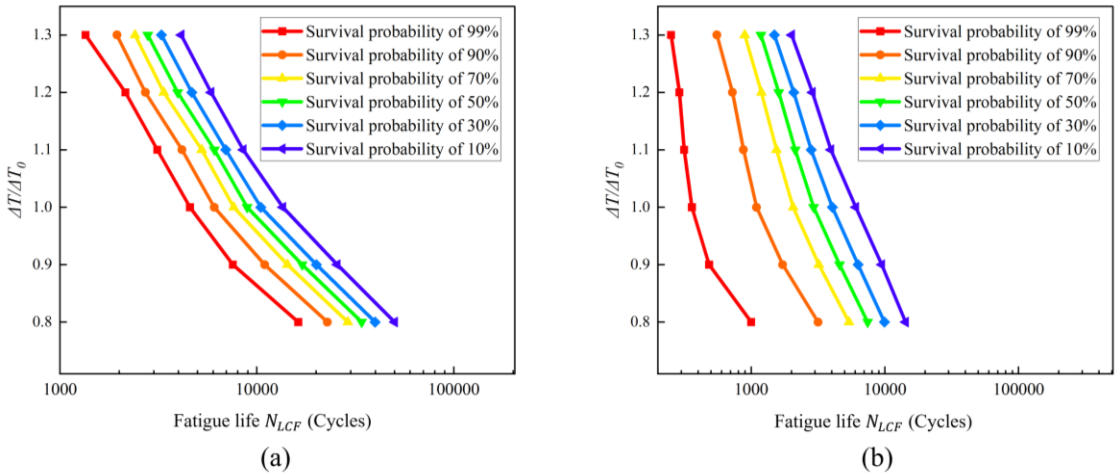

Fig. 6.11. Probabilistic LCF assessment boundary for elbow pipe bend under (a) cyclic loading path 1 and (b) cyclic loading path 2

6.4 Probabilistic ratcheting analysis for elbow pipe bend component

The probabilistic ratcheting modelling and analysis mainly focus on loading path 1(see Fig. 6.5 (a)), which is comprised of the constant inner pressure and time-dependent cyclic temperature difference throughout the wall section. The ratchet limit multiplier calculated by LMM ratcheting analysis is defined as the indicator of the structural state against cyclic loading conditions, pointing out whether the component under certain design parameters exceeds the ratcheting boundary or not. When the loading conditions are beyond the ratchet limit, it can be observed that in Fig. 6.12, the cyclic response at the inner flank of the elbow pipe presents significant accumulative plastic strain every cycle, reflecting structural ratcheting behaviour and finally leading to the progressive plastic

collapse. It should be clarified the structural ratchet limit is defined as the acceptable constant inner pressure in addition to the cyclic temperature difference.

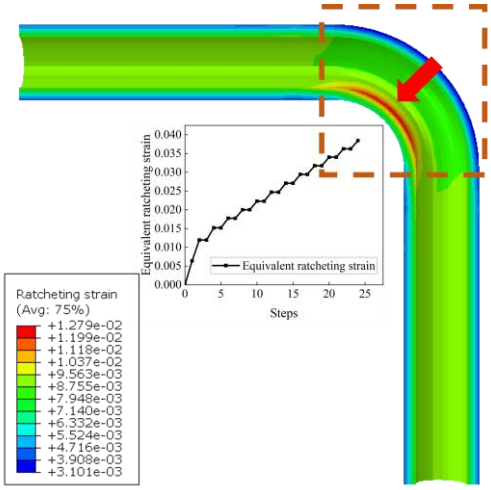

Fig. 6.12. Accumulative ratcheting strain per cycle during the steady state stage and the ratcheting state evolution at the critical location of elbow pipe bend

6.4.1 LDNN-based modelling of structural ratchet limit

The sensitivity of the input parameters to the ratchet limit multiplier is quantified in Fig. 6.13 (a), and it can be seen that different from the LCF analysis cases in the previous section, the most vital parameter is the nominal thickness. This is because the ratcheting failure considers the progressive plastic strain-induced collapse occurring among the whole structure or section, whereas the LCF failure focuses on the fatigue crack initiation at the local critical region. Following is the cyclic strain hardening exponent n playing a predominant positive role in both LCF and ratcheting analyses, and it should be dealt with carefully for structures with cyclic plastic behaviours induced failure modes. However, compared to the obvious non-linear influence on the LCF life in Figs. 6.8 (c) and (d), there is a linear relationship (see the response surface plotted in Fig. 6.13 (b)) appearing between the material parameter n and the ratchet limit. Besides, another material cyclic strength parameter K shows a negative relation to the ratchet limit multiplier, which, in contrast, exhibits a positive effect on LCF analyses. For the loading conditions, there is an opposite trend to the cases of LCF life evaluations in that the inner pressure makes much more contribution than the cyclic temperature difference.

The fitting quality and error analysis of the surrogate model of ratchet limit with LDNN (with 160 neurons set in the hidden layer) is revealed in Fig. 6.14, with all the training points located with the ± 3 MPa scatter band. Here much fewer training data are involved to meet the requirement of the R-Squared coefficient (≥ 0.99) in the training process due to the less non-linear effect of the input parameters on the ratchet limit.

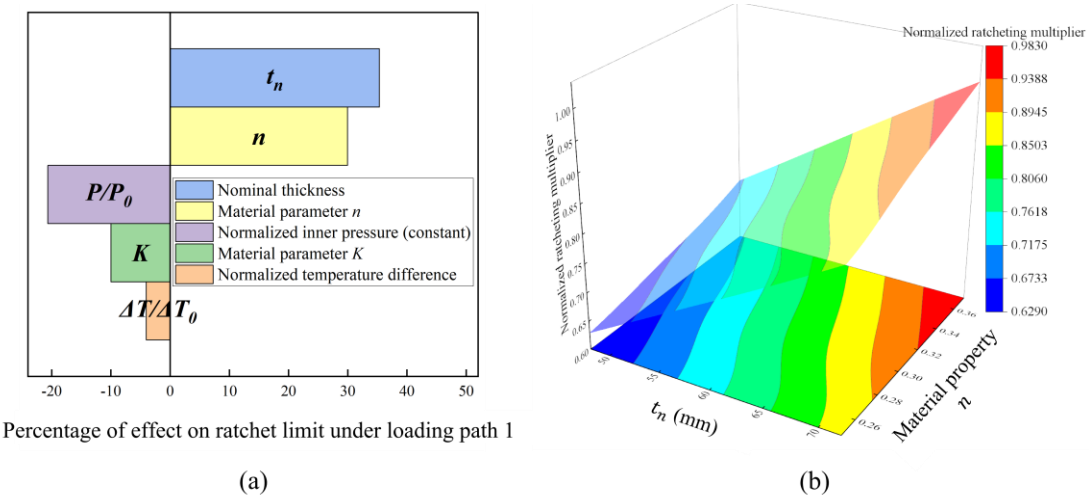

Fig. 6.13. Sensitivity analysis for LMM ratchet limit under constant inner pressure and cyclic temperature difference: (a) sensitivity of each design parameter of elbow pipe; (b) response surface of ratchet limit multiplier of elbow pipe

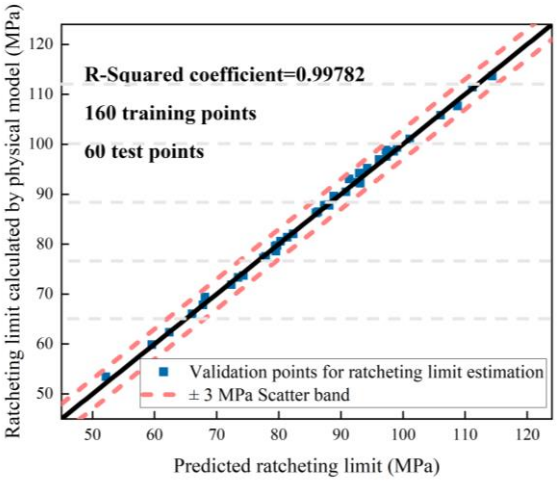

Fig. 6.14. Fitting quality by comparison of LMM ratchet limit and prediction of LDNN modelling

6.4.2 Probabilistic ratcheting boundary for elbow pipe bend

The probabilistic ratchet limit of the elbow pipe bend is estimated by the LDNN-based surrogate model and MCS sampling in terms of the random variables set in Table 6.3, with the 3D statistical distribution curves plotted in Fig. 6.15. Definitely different from the distribution types (Lognormal and Weibull) to depict the probabilistic LCF life, here the probabilistic ratchet limit considering the random variables (including nominal thickness and material property parameters K and n) obey the Normal distribution, with the detailed statistical information provided in Table 6.5. As the level of cyclic temperature difference gradually increases, the mean values of the ratchet limit decrease from 79.04 MPa to 69.42 MPa, whereas the standard deviations, accounting for the dispersion degree of the random variable, reduce slightly and remain stable at high-temperature conditions (for the cases where the normalized temperature difference ranges from 1.1 to 1.3).

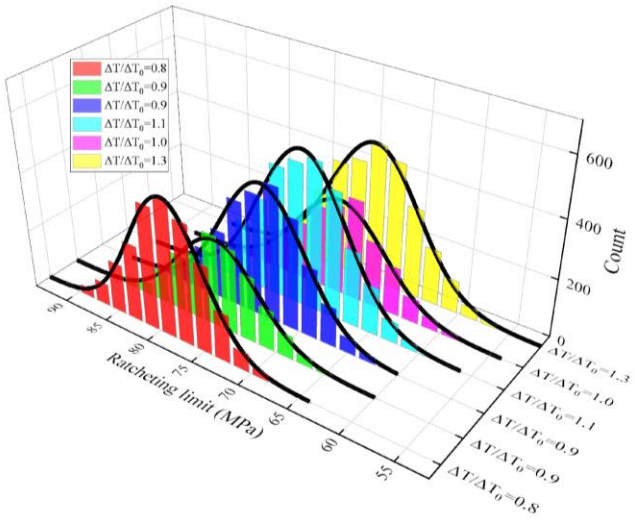

Fig. 6.15. Statistical distribution of ratchet limit under constant inner pressure and cyclic temperature difference with different levels of normalized cyclic temperature difference

By connecting the ratchet limits (under different temperature differences) with the same probability, the probabilistic ratcheting assessment curves are displayed in Fig. 6.16, calibrating different survival probabilities against ratcheting failure. When uncertain parameters are involved in the design process, the allowable operating ratchet limit is able to be selected, with an acceptable failure risk predefined according to different applications. On the other hand, if aiming at assessing certain loading conditions, the proposed probabilistic ratcheting assessment curves are capable of estimating the underlying failure probability to achieve better risk management.

Table 6.5. Statistical distribution of ratchet limit under constant inner pressure and normalized cyclic temperature differences

Loading path	$\Delta T/\Delta T_0$	Statistical distribution of ratchet limit
1	0.8	$N{\sim}Normal(79.038,\ 4.1221)$
	0.9	$N{\sim}Normal(76.446,\ 4.4509)$
	1.0	$N{\sim}Normal(74.162,\ 4.5644)$
	1.1	$N{\sim}Normal(72.389,\ 4.6676)$
	1.2	$N{\sim}Normal(70.713,\ 4.7538)$
	1.3	$N{\sim}Normal(69.416,\ 4.7425)$

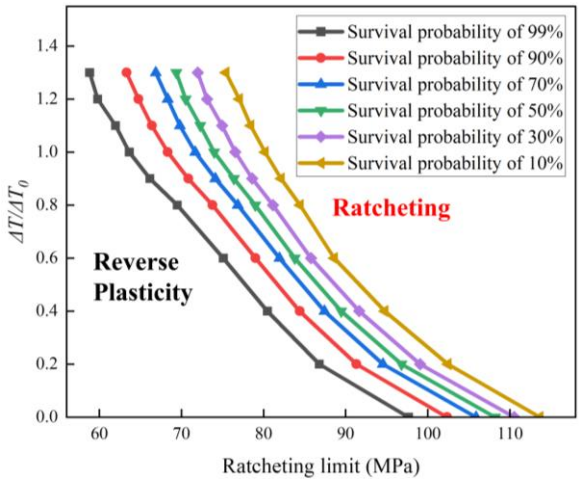

Fig. 6.16. Probabilistic ratchet limit boundary of the elbow pipe bend with different levels of normalized cyclic temperature difference

6.5 Reliability analyses for LCF and ratcheting failure modes

6.5.1 Limit state definitions by pLMM multiplier

Under the pLMM framework, the unified limit state indicator (ULSI) function is proposed to simplify the reliability analysis with a concise form by Equation (6.10)

$$G(\boldsymbol{X}) = \lambda(\boldsymbol{X}) - 1$$

$$= \begin{cases} \lambda_{LCF}(\boldsymbol{X}) - 1 = \dfrac{L_f(\boldsymbol{X})}{L_{design}} - 1, \text{for probabilistic LCF life assessment} \\ \lambda_{ratcheting}(\boldsymbol{X}) - 1, \text{for probabilistic ratcheting analysis} \end{cases} \tag{6.10}$$

The LCF multiplier λ_{LCF} in the ULSI function is expressed by the proportion of the predicted structural lifetime to the design life to satisfy the operation requirement (which is predefined as 2,000 cycles in this reliability analysis for the elbow pipe bend). Concerning the probabilistic ratcheting analysis, the ratcheting multiplier $\lambda_{ratcheting}$ is directly generated by the LMM ratcheting procedure, which refers to the amplification factor from the current load level to the ratchet limit when $\lambda_{ratcheting} > 1.0$.

6.5.2 Reliability analysis and reliability-centred evaluation diagram by LDNN surrogate model

Based on the deterministic ratcheting boundary, the load combination located in the reverse plasticity region (in purple colour) is reinvestigated by reliability analysis with the *R-S* model illustrated in Section 5.2.3, where the design parameters are set as random variables following the distributions in Table 6.3. To verify the effectiveness of the pLMM framework, there are two comparison sets employed. The first one is carried out by the RSM, with the quartic order polynomial applied to fit the least-squares regression of the LCF life and the ratchet limit, and the training process is based on the same dataset applied to constructing the LDNN. Another is the step-by-step elastoplastic analysis, during which the material properties adopted are consistent with the setting defined in Section 6.3.2, where the same constitutive model and the hardening law are involved in numerical simulations. There are 100 analysis cycles recorded in total, to investigate the structural cyclic response at the critical location of the elbow pipe bend (at the inner flank), and the LCF life and ratcheting state are determined by either the calculated cyclic strain range or the positive accumulative plastic strain, respectively. The final failure probability regarding a certain cyclic plastic response is calculated via the MCS.

The reliability analysis results of the proposed LDNN surrogate model and the RSM-based method are shown in Table 6.6 with the failure probability compared to the detailed MCS. It can be observed in Fig. 6.17 that with the lowest training points involved, the failure probability of the proposed LDNN-based approach is much closer to validation than the RSM-based method for the probabilistic fatigue and ratcheting evaluations. The error generated by the RSM-based method is mainly caused by insufficient training data, which means to guarantee adequate estimation quality, much more training points should be prepared and input during the fitting process of the RSM model.

Table 6.6. Results of reliability analyses for LCF and ratcheting failures by LDNN surrogate model, RSM model and MCS validation

Analysis type	LDNN-based method			RSM-based method			Verification of MCS with elastoplastic analysis	
	P_f	N_{LDNN}	R^2	P_f	N_{RSM}	R^2	P_f	N_{MCS}
LCF for path1	0.10483	120	0.98	0.10797	250	0.95	0.08190	4452
LCF for path 2	0.56656	150	0.99	0.57970	250	0.94	0.54320	3675
Ratcheting for path 1	0.66350	100	0.99	0.68024	220	0.98	0.66794	4351

Noting that N_{LDNN} and N_{RSM} indicate the gross number of data points used in the training processes of the LDNN and RSM models, respectively, and N_{MCS} refers to the total number of elastoplastic simulations during MSC.

Besides, concerning the applications with a high-reliability requirement (i.e., needs for low failure risk, especially for nuclear components), the direct MCS working with non-linear FEA

simulation may not be acceptable because of the huge computational resource consumed (4,452, 3,675 and 4,351 times for non-linear FEA analyses in the validation set). Hence, to give out the precise failure probability in practical engineering applications, employing an appropriate surrogate modelling strategy is inevitable.

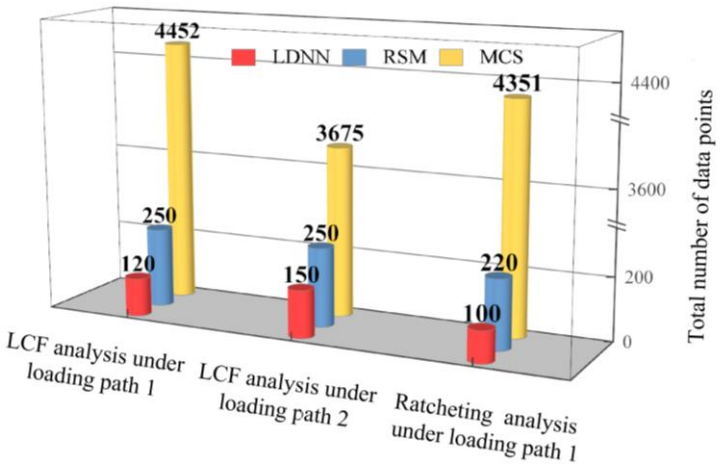

Fig. 6.17. Comparison of the computational efficiency of each probabilistic analysis strategy

It is worth noting that under loading path 2, the combination of cyclic internal pressure and temperature difference broadens the alternating plastic load region to a certain extent (from the black curve to the red one in Fig. 6.6). However, when considering the same loading amplitude with path 1, it cannot be ignored that the additional cyclic inner pressure greatly weakens the reliability, making the elbow pipe structure more vulnerable. This is also reflected by the reliability-centred evaluation diagram in terms of the required LCF lifetime in Fig. 6.18, where the gap in blue depicts the negative influence of the extra cyclic inner pressure on the structural reliability. Concerning the high-reliability requirements (reliability not less than 0.99), the acceptable LCF life N_{P_2} (250 cycles) of loading path 2 is only a quarter of the lifetime N_{P_1} (1,000 cycles) under the first loading path.

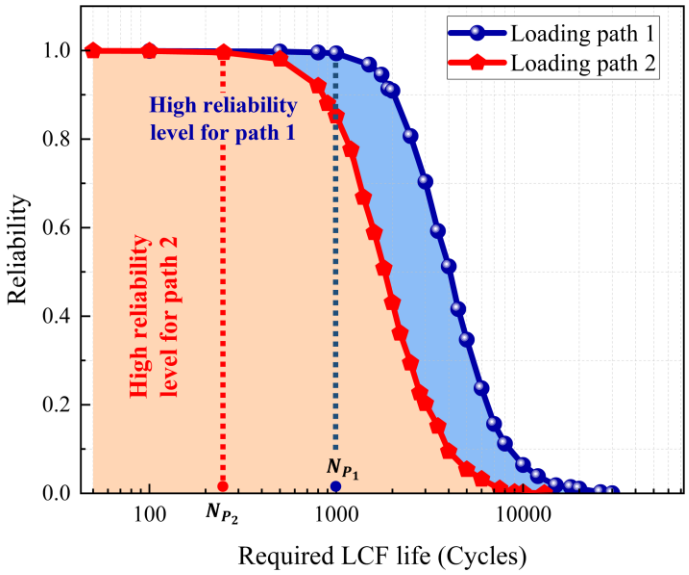

Fig. 6.18. Reliability-centred evaluation curves in terms of the required LCF life of elbow pipe bend under different loading paths

The reliability-centred ratcheting assessment diagram for the elbow pipe bend is also schemed by the proposed LDNN surrogate model and exhibited in Fig. 6.19 to quantitatively measure the structural reliability level. In the load space composed of the mean value of cyclic temperature difference and the mean value of constant inner pressure, there are two commonly used reliability levels calibrated for different design purposes: the high-reliability demand (more than 0.99 in dark red) for crucial infrastructure and the medium requirement (more than 0.95) related to general appliance.

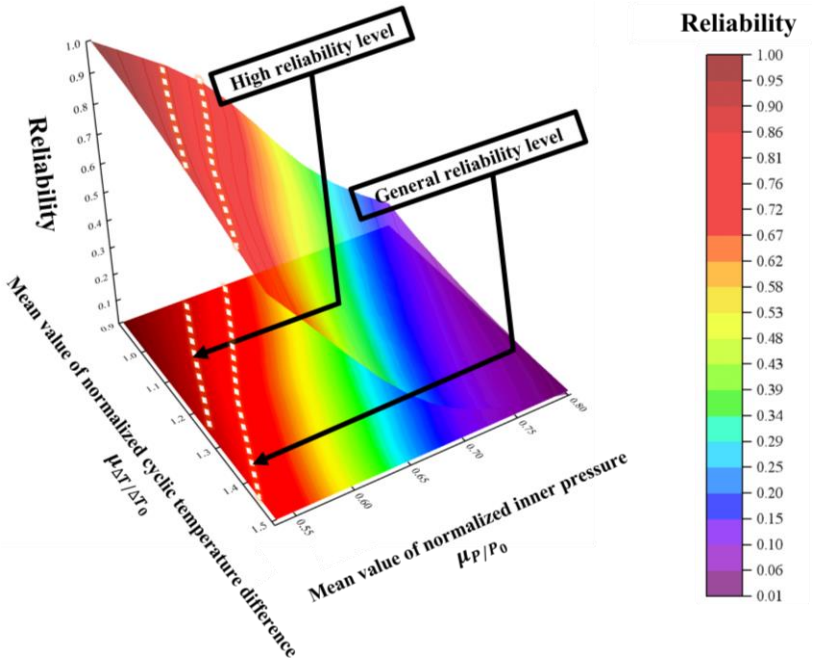

Fig. 6.19. Reliability-centred ratcheting assessment diagram for the elbow pipe bend under different reliability levels

6.6 Conclusions

In this chapter, a unified pLMM framework for probabilistic structural integrity assessment is proposed with the physics-based LDNN surrogate model in terms of structural LCF life and ratchet limit. The detailed benchmark of elbow pipe bend subjected to thermo-mechanical loads is elaborated to demonstrate the comprehensive applicability of the pLMM, which exhibits a good balance between computational efficiency and accuracy, and could be further adopted to substitute the conservative safety factors for reliability-centred design and evaluation. The main conclusions are summarized below:

1. To implement the probabilistic analysis of cyclic plastic behaviours, the physics-based LDNN surrogate model is constructed for the first time and well-trained with the direct method-derived database.

2. The sensitivity of design parameters to LCF life and ratchet limit of elbow pipe is identified, and a series of probabilistic LCF assessment boundaries and ratchet limit boundaries for thermo-

mechanical loading conditions are established, with the random variables of LCF life and ratchet limit quantitatively described by appropriate statistical distributions.

3. The general ULSI is formulated under the pLMM framework to define the limit states of structural cyclic plastic responses. Compared with the traditional RSM, the pLMM reliability analysis of the elbow pipe shows less dependency on training data but gives out failure probability quite closer to the validation of direct MCS with elastoplastic analysis.

4. With several reliability levels calibrated for different applications, the reliability-centred evaluation diagrams for the elbow pipe regarding the design LCF lifetime and structural ratchet limit are also built. This assessment strategy is conducive to providing fundamental technical support for risk management of critical infrastructures against LCF and ratcheting failures.

7 Physics-based probabilistic assessment of creep-fatigue failure for pressurized components by extended Direct Steady Cycle Analysis-driven neural network

7.1 Introduction

The deterministic creep-fatigue analysis largely focuses on an idealized estimation, but, inevitably, the randomness originating from the design parameters (i.e., geometric dimensions, material properties, environmental factors and operating conditions, not to mention the material ageing problems) poses a huge challenge to maintaining the structure safety. Traditionally, the safety factor according to the different applications or the expert experience is frequently set to account for the comprehensive uncertainty, which sometimes leads to over-conservative design schemes due to the absence of statistical information on key structural responses. Hence, it is imperative to have a deep understanding of statistical distributions of the creep-fatigue lifetime and to reasonably describe the failure probability during the engineering design and risk management against the creep-fatigue failure.

To tackle such a problem, combining the repeated Monte Carlo Simulation (MCS) with the deterministic model of creep-fatigue life is the elementary scheme to implement creep-fatigue analysis from a probabilistic perspective. However, suffering from the computational burden of the direct MCS, especially for the cases requiring high reliability, this methodology is limited to the study of simple specimens [189]. Making use of the First Order and Second Order Reliability Methods (FORM/SORM) in the probabilistic fatigue analysis [190, 191] and creep-fatigue analysis [192, 193] is an effective approach to improve the calculation efficiency when deriving the failure probability and reliability index. As a semi-analytical solution, the disadvantage is that for a highly strong non-linear limit state hyper-surface, the approximation of failure probability may deviate greatly from the actual values, and thus, detailed MSC-based validations are still necessary to check the effectiveness.

In contrast, the Three-Term Reference Damage Model (3T-RDM) was developed [194] based on the R5 high-temperature assessment procedure, which simplified the deterministic creep-fatigue

evaluation for subsequent estimation of crack initiation risk. And in Ref. [195], to investigate the probabilistic creep-fatigue life distribution of superalloy GH720Li under elevated temperature, an life prediction model was built based on the applied mechanical work density (AMWD) function, with the values of several key material parameters calibrated and recommended by the experimental data.

Alternatively, the data-driven modelling technique is beneficial to avoiding directly processing the complicated failure mechanisms, with the high-quality surrogate model constructed through the training process. It is reported that combining the fatigue damage model and machine learning (ML) is conducive to significantly elevating the efficiency of large-scale life prediction [196]. By adopting the Response Surface Method (RSM) [197], the uncertainty of geometric dimension, material properties and operating conditions were taken into consideration for the creep-fatigue remaining life management. Aiming to further improve the accuracy and efficiency of creep-fatigue life estimation, the multi-layer and multi-response modelling techniques are beneficial to handling complicated interactive failure behaviour. Song [198] applied the Kriging surrogate model to evaluate the probabilistic creep-fatigue life of nickel-based superalloy, where the assessment was decomposed into three stages: the stress and strain simulations, damage calculation and the collaborative probabilistic analysis. Another similar application was reported by Ref. [199]. Aiming at removing the limitation of the modelling approaches, the artificial neural network (ANN) is another practical way due to its strong generalization ability to fit the complex relationship between input and output, which has been utilized before to model the fatigue life of S420MC steel [175] and SAE 8620 steel [178]. Three types of neural networks to predict the creep-fatigue life of 316 stainless steel was employed and compared by Zhang [200], and the results showed that the physics-informed neural network is capable of providing the creep-fatigue life approximation with better fitting quality. Another prediction approach of probabilistic creep-fatigue life was applied to low-alloy steel 42CrMo4 specimen [201], and the damage model derived by the long short-term memory network and gated recurrent unit neural network was proved to be suitable for creep-fatigue life estimation.

To extend the applicability of probabilistic creep-fatigue analysis, the probabilistic creep-fatigue damage assessment diagram of Inconel 718 alloy was established for design purposes by Gu et al. [202]. Under this analysis framework, a small sample size expansion method was adopted to generate reliable statistic features of uncertain material parameters for the creep-fatigue life evaluation model, the SEDE. Another structure-level study was reported in Ref. [203], the creep-fatigue failure probability of the turbine disk was predicted based on the response at the constant

hotspot. And the criterion of constructing the limit state function (LSF) for reliability analysis was discussed comprehensively, where the load-life model, strength-damage model and modelling with non-linear creep-fatigue interaction were compared in depth. Furthermore, to avoid the shortcoming of the evaluation based on a single hot spot, the zone-based method for probabilistic fatigue analysis was also established by Wang [204], which was utilized to measure the uncertain influence on the LCF life of the turbine disk and calculate the jointing failure probability.

Therefore, the superior probabilistic creep-fatigue analysis framework should meet three requirements at three different levels:

Level 1. Reliable structural creep-fatigue evaluation approach with a good balance between computational accuracy and efficiency.

Level 2. Applicable approximation modelling technology that can capture the complicated nonlinear relationship between the input and output, without depending on the detailed step-by-step creep-fatigue FEA program.

Level 3. Acceptable probabilistic analysis strategy for engineering applications to provide statistical information on the key responses and the failure risk due to creep-fatigue failure.

To further accommodate such requirements, the probabilistic Linear Matching Method framework for creep-fatigue analysis is proposed, where the eDSCA-driven neural network (EDDNN) is built to generate the surrogate model for lifetime prediction. This strategy of probabilistic creep-fatigue analysis provides a feasible way to acquire statistical information on creep-fatigue damage and the life of engineering components, as well as the structural failure probability under uncertain design or operating conditions.

The rest sections of this chapter are structured as follows. In Section 7.2, the probabilistic analysis strategy for creep-fatigue interaction evaluation is elaborated in detail, where the extended DSCA-driven neural network (EDDNN) is constructed. Then, the applicability is exhibited in Section 7.3 through two practical engineering benchmarks: the first benchmark, the probabilistic creep-fatigue analysis of the elbow pipe component, is concentrated on the circumstance dominated by fatigue damage; instead, the typical creep damage-controlled case is illustrated in Section 7.4 by the probabilistic creep-fatigue analysis of the hydrogenation reactor. The reliability-based safety factor (RBSF) determination under pLMM framework is introduced in Section 7.5, with the discussion on the enhanced data classification scheme for the randomness in creep damage-

dominated assessment presented in Section 7.6. Finally, the main conclusions are summarized and given out in Section 7.7.

7.2 Creep-fatigue modelling by probabilistic Linear Matching Method (pLMM) framework

Deterministic modelling of structural response considering creep-fatigue behaviour at critical locations is fundamental to the probabilistic analysis, and its robustness plays a crucial role in reliability-based design and evaluation. Due to the excellent computational efficiency and accuracy, the extended Direct Steady Cyclic Analysis (eDSCA) procedure is chosen to build the probabilistic analysis framework, providing the data of structural responses for the training of the neural network.

7.2.1 Establishment of structural cyclic responses regarding creep-fatigue interaction by eDSCA procedure

The numerical implementation of the eDSCA procedure is demonstrated below. It is assumed that there are time-dependent thermal conditions $\lambda_\theta \theta(t)$ and surface loads $\lambda_p P(t)$ applied on the component, with the boundary conditions (BCs) $u = 0$ constraining the rest part of the body. Within each cyclic period $0 \le t \le \Delta t$, the linear elastic history is expressed by the load multipliers λ_θ and λ_p,

$$\hat{\sigma}_{ij}(t) = \lambda_\theta \hat{\sigma}^{\theta}_{ij}(t) + \lambda_p \hat{\sigma}^{p}_{ij}(t) \tag{7.1}$$

where, $\hat{\sigma}^{\theta}_{ij}(t)$ and $\hat{\sigma}^{p}_{ij}(t)$ are the elastic stress induced by the thermal conditions $\theta(t)$ and the surface loads $P(t)$.

According to Equation (7.2), the general stress solution is further de-coupled into three components: elastic stress $\hat{\sigma}_{ij}$, time-dependent residual stress $\rho_{ij}(t)$ and time-independent residual stress $\bar{\rho}_{ij}$.

$$\sigma_{ij}(t) = \hat{\sigma}_{ij}(t) + \bar{\rho}_{ij} + \rho_{ij}(t) \tag{7.2}$$

Here, the time-dependent residual stress $\rho_{ij}(t)$ equals zero when the load cycle starts and ends, making the cyclic stress and strain rate asymptote to the cyclic state.

The eDSCA procedure evaluates the structural steady cyclic response including plastic behaviour and creep effect by solving a series of linear equations, by which the cyclic plastic strain and creep strain increment are determined iteratively by means of the calculation process in Fig. 7.1.

Considering each iteration cycle $m = 1, 2, 3, \cdots, M$, under a certain iteration cycle lie several load time points t_n, where $n = 1, 2, 3, \cdots, N$. For the calculation of nth load time point under mth cycle, the iteration starts with constructing the input stress field $\Delta\sigma_{ij}^{in}$ at each material point by Equation (7.3), including the elastic solution of t_n and the accumulation of the previous residual stress.

$$\Delta\sigma_{ij}^{in}(x, t_n)_m = \Delta\hat{\sigma}_{ij}(x, t_n) + \sum_{k=1}^{m-1}\sum_{n=1}^{N} \Delta\rho_{ij}^{k}(x, t_n) + \sum_{l=1}^{n-1} \Delta\rho_{ij}^{m}(x, t_l) \tag{7.3}$$

Next, Equation (7.4) is what is known as an initial stress problem, where, $\boldsymbol{B}$ and $\boldsymbol{K}$ represent the strain-displacement matrix and stiffness matrix, and $\Delta\boldsymbol{u}$ is the displacement increment related to the initial stress distribution and calculated by the FEA solver.

$$\boldsymbol{K}\Delta\boldsymbol{u}^{m}(t_n) = -\int_{V} \boldsymbol{B}\,\Delta\boldsymbol{\sigma}^{in}(t_n)_m dV \tag{7.4}$$

In such problems, there is a body under zero external load and we introduce an internal distribution of incompatible strain which then induce a residual stress field derived from Equation (7.5) with the Jacobian matrix $\boldsymbol{J}^{m}(t_n)$ defined in ABAQUS UMAT.

$$\Delta\boldsymbol{\rho}^{m}(t_n) = \boldsymbol{J}^{m}(t_n)\boldsymbol{B}\Delta\boldsymbol{u}^{m}(t_n) - \Delta\boldsymbol{\sigma}^{in}(t_n)_m \tag{7.5}$$

Once the accumulated residual stress for t_n is determined by the summation of the previous history in Equation (7.6), to further evaluate the inelastic strain increment, there are two different numerical schemes provided.

$$\rho_{ij}^{m}(x, t_n) = \sum_{k=1}^{m-1}\sum_{n=1}^{N} \Delta\rho_{ij}^{k}(x, t_l) + \sum_{n=1}^{n} \Delta\rho_{ij}^{m}(x, t_l) \tag{7.6}$$

Scheme 1. Plastic strain increment calculation

Regarding the step to predict the plastic behaviour, the plastic strain increment is given by Equation (7.7),

$$\begin{aligned}\left[\Delta\varepsilon_{ij}^{m}(x,t_n)\right]' &= f\left[2\bar{\mu}_m(x,t_n),\Delta\rho_{ij}^{m}(x,t_n)\right] \\ &= \frac{1}{2\bar{\mu}_m(x,t_n)}\left[\hat{\sigma}_{ij}(x,t_n)' + \rho_{ij}^{m}(x,t_n)'\right]\end{aligned} \tag{7.7}$$

where $\bar{\mu}_m$ stands for the shear modulus that is read in at the start of this iteration procedure, and the mark $(')$ specifies the deviatoric component of each variable.

Scheme 2. Creep strain increment calculation

For the purpose to consider the creep during the dwell, the creep strain increment is addressed below by adopting the time-hardening constitutive law and the concept of elastic follow-up during the stress relaxation.

$$\Delta\bar{\varepsilon}_c = \frac{A(n^*-1)\Delta t^{m^*+1}(\bar{\sigma}_s - \bar{\sigma}_c)}{\left(\frac{1}{\bar{\sigma}_c^{n^*-1}} - \frac{1}{\bar{\sigma}_s^{n^*-1}}\right)(m^*+1)} \tag{7.8}$$

Here A, n^* and m^* are the creep parameters according to the creep rule $\dot{\bar{\varepsilon}}_c = A^*\bar{\sigma}^{n*}t^{m*}$. The creep flow stress $\bar{\sigma}_c$ is defined by adding the creep effect-induced residual stress to the creep stress at the start of the dwell period.

$$\bar{\sigma}_c(x,t_n) = \bar{\sigma}\left[\left(\sigma_{sij}(x,t_n) + \Delta\rho_{cij}(x,t_n)\right)\right] \tag{7.9}$$

Before completing the iteration, the creep flow stress is updated by the generated value in Equation (7.10), and a new linear matching condition is also established by Equation (7.11), where the σ_0^m is either the plastic yield stress for plastic behaviour calculation or the creep flow stress with the creep effect involved, and $\bar{\varepsilon}^F$ is the creep strain rate at the end of dwell. Hence, the evaluations of creep-fatigue damage and life are carried out according to the methodology introduced in Section 2.2.3.2.

$$\bar{\sigma}_c^m = f\left[\Delta\bar{\varepsilon}_c^m, \Delta\rho_{ij}^m(x,t_n)\right] = \left(\frac{\bar{\varepsilon}^F}{A^*\Delta t^{m^*}}\right)^{\frac{1}{n^*}} \tag{7.10}$$

$$\bar{\mu}_{m+1}(t_n) = \bar{\mu}_m(t_n)\frac{\sigma_0^m(t_n)}{\bar{\sigma}\left(\hat{\sigma}_{ij}(t_n) + \rho_{ij}^m(t_n)\right)} \tag{7.11}$$

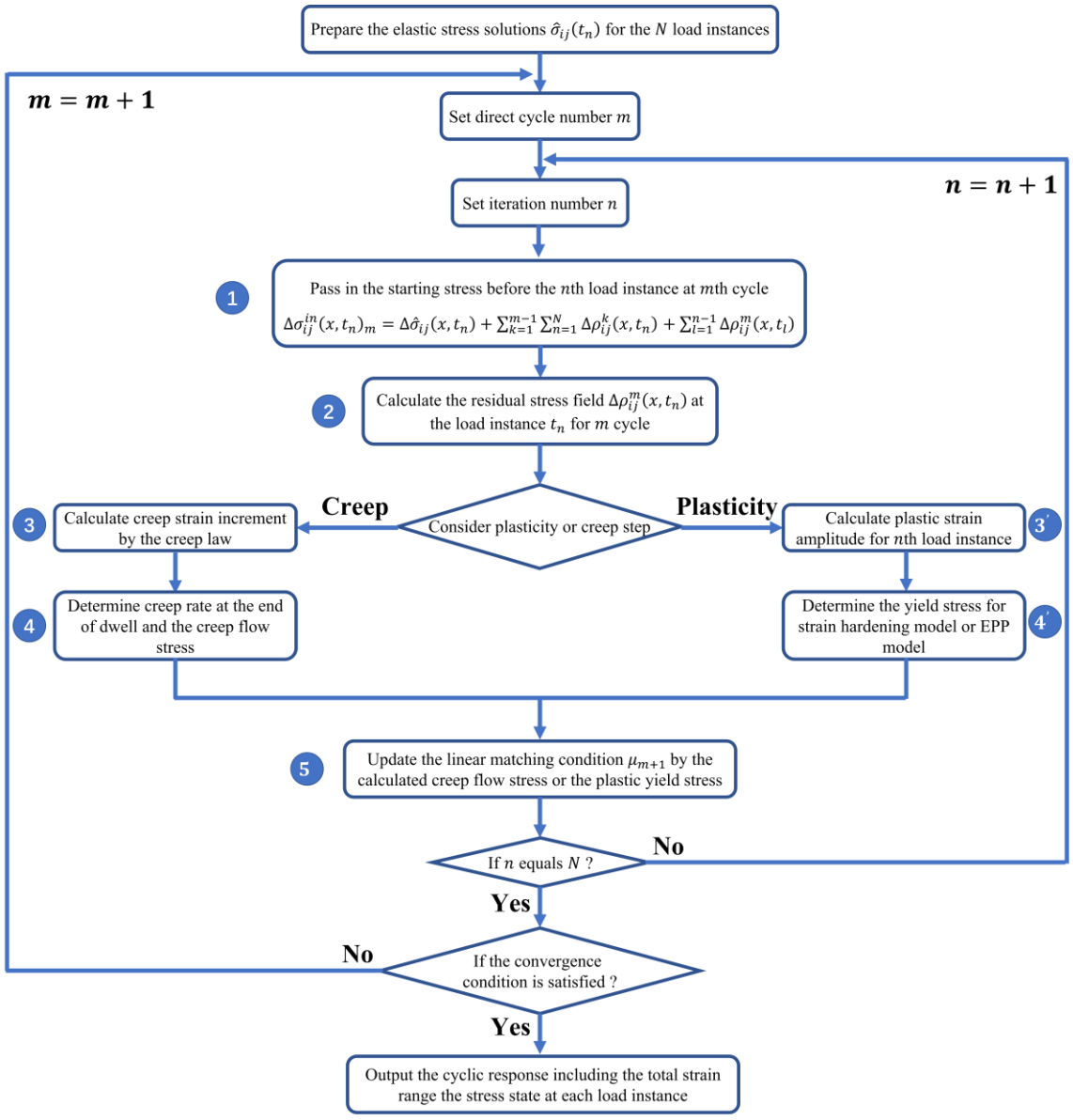

Fig. 7.1. Numerical iteration of LMM eDSCA procedure for creep-fatigue evaluation

7.2.2 Structure of extended DSCA-driven neural network (EDDNN)

The extended DSCA-driven neural network (EDDNN) is constructed by the feedforward neural network functioning as the multi-layer perceptron (MLP) for approximation modelling and

prediction. The commonly used neural network contains the input layer, the hidden layer and the output layer, as exhibited in Fig. 7.2. Initially, the weighted input vector x was summed through the input layer and passed to the hidden layer. Then, the activation function existing in each neuron performs non-linear mapping which is dependent on the summation of input with weights and bias. Finally, the relationship between the input x and the output y is expressed implicitly. Specifically, when considering the perceptual process through a single neuron node in Fig. 7.3, the input vector is mapped non-linearly through the neuron with Elliptical Basis Functions (EBF), where the Mahalanobis distance is adopted to depict the distance from the input vector to the centre vector for a certain neuron.

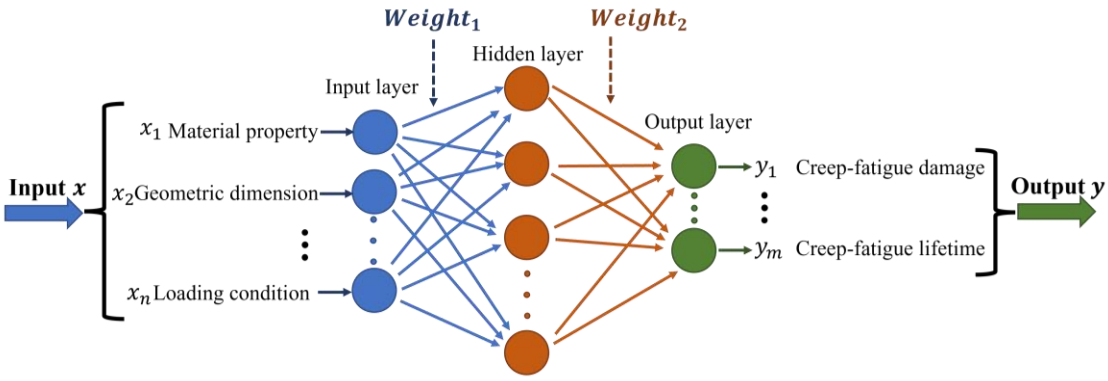

Fig. 7.2. Detailed structure of the three-layer neural network for creep-fatigue damage and lifetime estimations

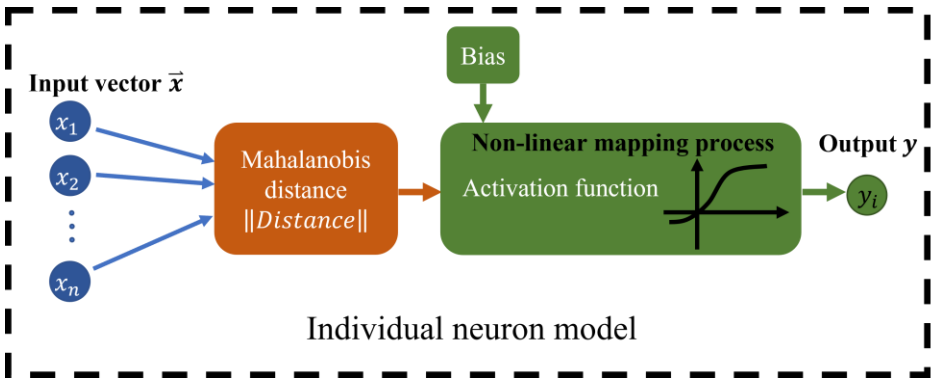

Fig. 7.3. Perceptron process with non-linear activation function

The basic interpolating functions of creep-fatigue damage D and lifetime L are comprised of the summation of weighted activation function values and the according bias terms, which are depicted by the basis functions of EBF of $\phi_i(\boldsymbol{x})$ and $\varphi_i(\boldsymbol{x})$,

$$D(\boldsymbol{x}) = \sum_{i=1}^{N} \alpha_i \phi_i(\boldsymbol{x}) + \alpha_{N+1} \tag{7.12}$$

$$L(\boldsymbol{x}) = \sum_{i=1}^{N} \beta_i \varphi_i(\boldsymbol{x}) + \beta_{N+1} \tag{7.13}$$

where α_i and β_i are the weights and α_{N+1} and β_{N+1} are the bias terms, respectively.

7.2.3 Configuration of surrogate model-based probabilistic creep-fatigue analysis

The probabilistic creep-fatigue analysis is implemented by using the conjunction of ABAQUS and Isight, and the core computational configuration of the extended DSCA-driven neural network (EDDNN) is formulated in Fig. 7.4 with three different stages. To recognize the known data, firstly, the EDDNN is trained with a given database. It contains a series of random combinations of input data points produced in the design space by the Latin Hypercube Sampling (LHS) technique, which is then processed by the LMM Plugin program to derive the creep-fatigue damage and life accordingly. Hence, the prerequisites for building the EDDNN-based surrogate model, including the weights parameters and the bias term, can be calculated simultaneously by solving the combination of linear equations:

$$\sum_{j=1}^{N} \alpha_j \phi_j(\boldsymbol{x_i}) + \alpha_{N+1} = \begin{cases} D_i(\boldsymbol{x_i}), \text{for creep} - \text{fatigue damage evaluation} \\ L_i(\boldsymbol{x_i}), \text{for creep} - \text{fatigue lifetime evaluation} \end{cases} \tag{7.14}$$

$$i = 1,2,\dots,N$$

$$\sum_{j=1}^{N} \alpha_j = 0 \tag{7.15}$$

The output matrix y of creep-fatigue damage or lifetime is predefined by the LMM procedure in terms of the input parameters covering structural design conditions. Consequently, the linear equations system is able to be solved by the same procedure described in Section 6.2 to get the weights matrix.

Next, to further improve the fitting quality in the second stage, the coefficients of weights and biases are adjusted iteratively based on the error analyses, and the more pertinent surrogate relationship is determined. Finally, as the input parameters with significant impact are identified

by the sensitivity analysis, the selected random variables with the predefined statistical features (e.g., statistical distribution type, mean value, and standard deviation) are passed into the built EDDNN-based surrogate model, instead of the traditional non-linear FEA solver, to simulate the distributions of key responses and predict the failure risk by MCS.

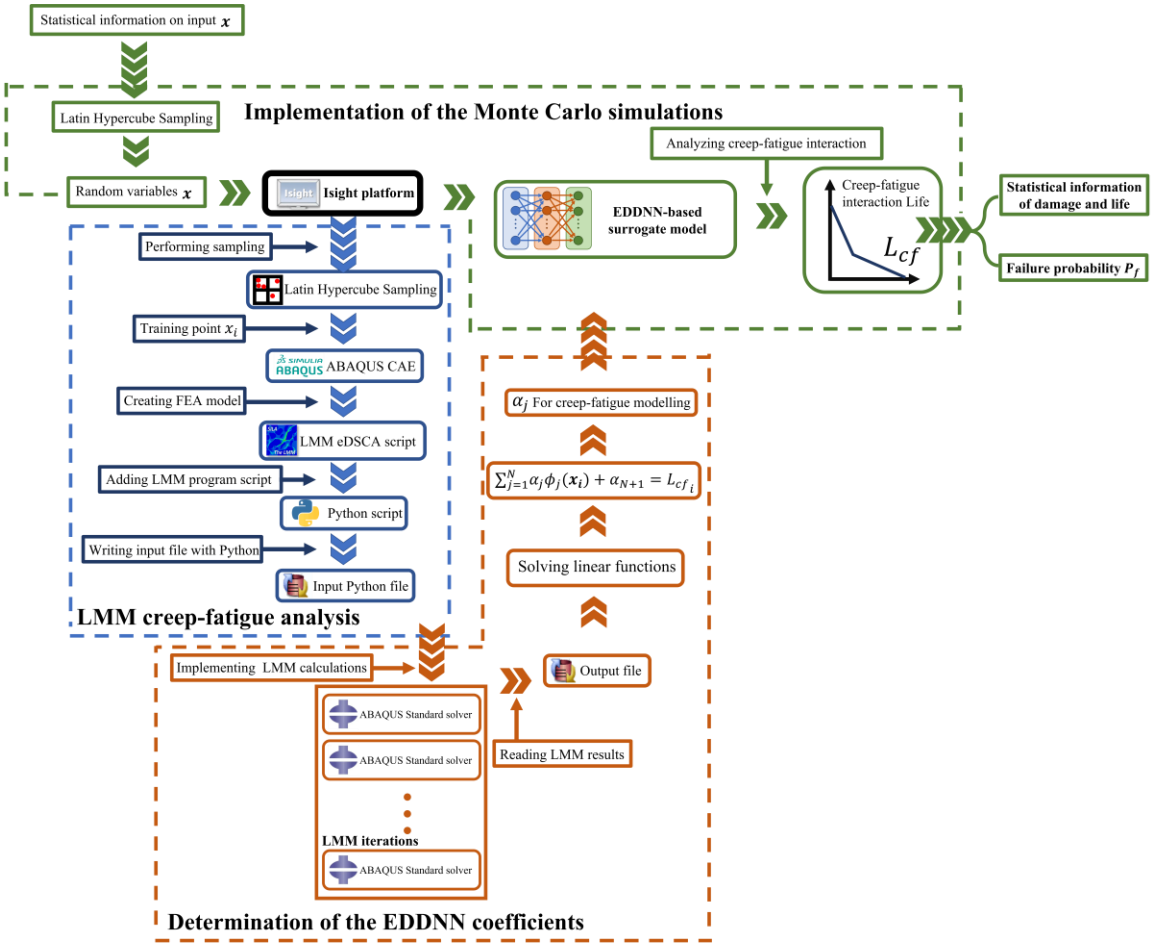

Fig. 7.4. Configuration of EDDNN under pLMM framework for probabilistic creep-fatigue assessment

7.3 Probabilistic creep-fatigue analysis with fatigue damage-dominated case

The first numerical case study is designed to illustrate the probabilistic creep-fatigue analysis dominated by fatigue failure, where the assessment of the elbow pipe component is considered under several uncertain design parameters.

7.3.1 Model description of the elbow pipe structure

The geometric dimensions are exhibited in Fig. 7.5 (a), where the parameters R_O, t_n, R and L denote the outer radius of the pipe, nominal pipe wall thickness, bending radius and straight length, respectively. Another bending characteristic of the elbow pipe, h, is defined as $Rt/{r_m}^2$, where r_m refers to the mean radius of the straight pipe. The FEA model is discretized and generated by ABAQUS, with the 20-node quadratic brick element C3D20R adopted to keep the balance of numerical precision and computational efficiency by the reduced integration technology included. And the elements of the elbow zone are refined, which meet the requirements of mesh convergence and capture the prominent stress and strain gradients around the local region, with 4,760 elements created in total.

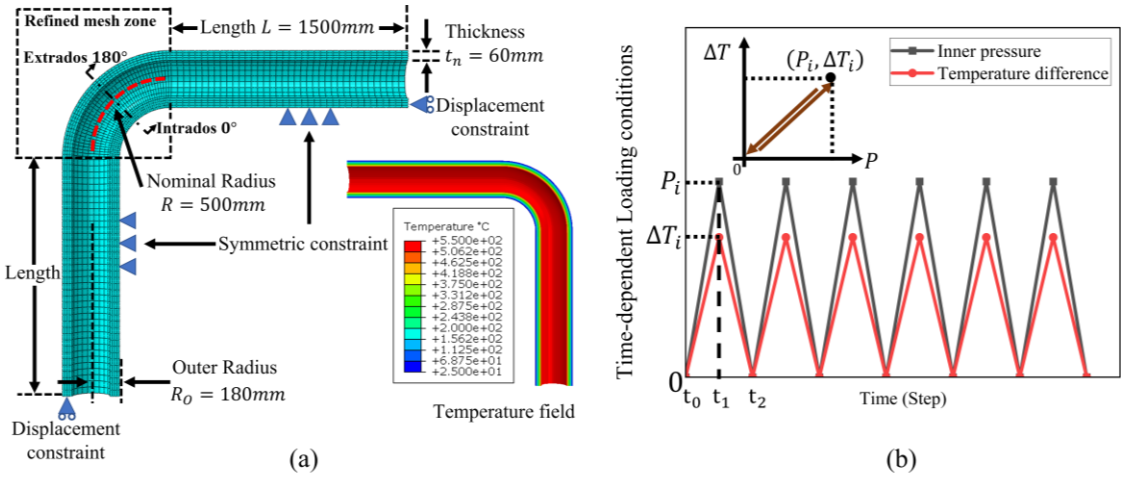

Fig. 7.5. Descriptions of: (a) the geometry and FEA model of the elbow pipe bend component; (b) the time-dependent loading conditions

The elbow pipe bend is made of austenitic stainless steel, 316L, due to the superior corrosion resistance in the high-temperature environment [188], and the material properties at high-temperature are provided in Table 7.1, where the cyclic yield strength $R_{p0.2}(T)$ is determined according to 0.2% proof stress from the cyclic steady-state stress-strain curves taken from Ref. [6]. To depict the creep behaviour, the Norton law has been adopted to consider the secondary creep regime, where the related material parameters are given out including the power law multiplier A and stress order n. The fatigue property to describe the relationship between the fatigue life and the cyclic total strain range is displayed in Fig. 7.6, given various temperature conditions [3, 6].

And the total damage is able to be predicted by the bilinear creep-fatigue interaction diagram in Fig. 7.7, with the X-axis and Y-axis meaning the fatigue damage and creep damage, respectively.

Table 7.1. Material properties of 316L stainless steel under operating temperature [6] and the geometric dimension

Parameter type	Design parameter		Mean value μ	Distribution type	Coefficient of variation CV
Material property	Young's modulus E $(10^3\mathrm{MPa})$		159	Constant	–
	Poisson's ratio ν		0.3	Constant	–
	Thermal conductivity k $(\mathrm{W/mm\cdot ℃})$	Based on 500 ℃	0.02149	Constant	–
	Coefficient of thermal expansion α_m $(10^{-6}/$ ℃$)$		18.3	Constant	–
	$R_{p0.2}(T)$ (MPa)		240	Normal	0.1
Creep strain rate parameters	A^*		46333.8	Normal	0.1
	Q (J/mol)		330000	Normal	0.1
	R [J/(mol · K)]		8.314	Constant	–
	n		6.1	Normal	0.1
Geometric dimension	Nominal thickness t_n (mm)		60	Normal	0.1

Noting that the creep strain rate is calculated by the Arrhenius temperature dependency relationship $\dot{\varepsilon}_{cr} = A^*\sigma^n t^m \exp\left(\frac{-Q}{RT}\right)$, where Q is the activation energy and R is the universal gas constant

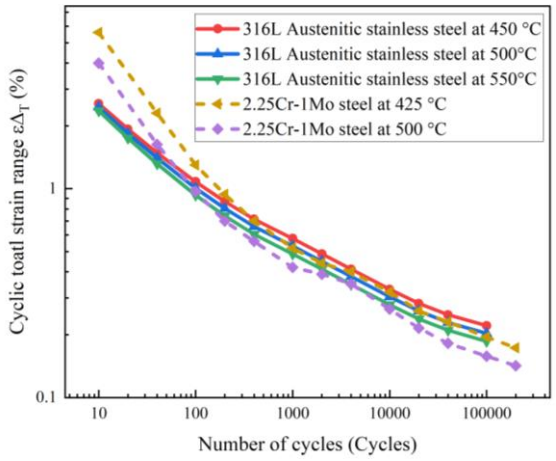

Fig. 7.6. Temperature-dependent fatigue curves of different materials

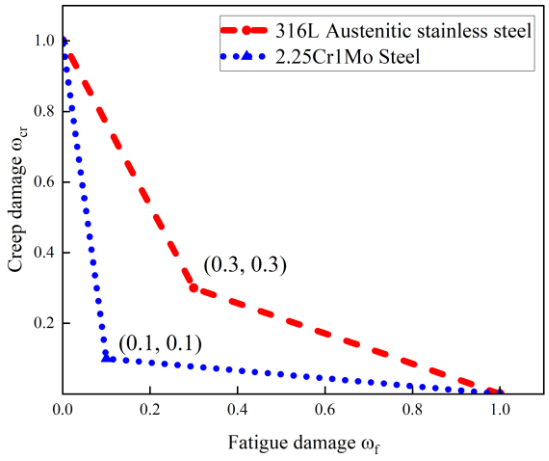

Fig. 7.7. Creep-fatigue damage envelope of different materials

The half geometry model of the elbow pipe bend is constrained with the symmetric BCs exerted on the symmetric surfaces, and the displacement constraints are also applied along with the horizontal and vertical directions at each end of the elbow pipe. On the inner surfaces lie the cyclic inner pressure, and between the inner and outer surfaces of the pipe wall, there exists the cyclic temperature difference, both of which are defined in Table 7.2, with the loading history predefined in Fig. 7.5 (b).

Table 7.2. Load conditions of the elbow component for the probabilistic creep-fatigue analysis

Parameter type	Design parameter	Mean value μ	Distribution type	Coefficient of variation CV
Loading conditions	Maximum cyclic inner pressure P (MPa)	65	Normal	0.1
	Maximum cyclic temperature difference ΔT (℃)	550	Normal	0.1
	Creep dwell time t (hours)	8760	Normal	0.1

7.3.2 Identification of fatigue-dominated failure mode of the elbow pipe bend under cyclic thermo-mechanical load conditions

Under the mean values of the design parameters, the typical failure mechanism of the elbow pipe component is dominated by the fatigue failure plotted in Fig. 7.8. It can be observed that due to the effect of geometric discontinuity at the elbow location, here, the inner surface of the intrados exhibits the maximum strength of fatigue damage and creep damage simultaneously. The critical fatigue damage arises from the cyclic coupling stress generated by thermal stress and internal pressure-induced mechanical stress. By contrast, the significant creep damage is attributed to the combination of the elevated working temperature and the high-stress level to which the temperature-dependent material creep properties and the creep strain evolution are extremely sensitive. In this case, although the location of maximum fatigue damage coincides with that of creep damage, according to Fig. 7.8 (d), the creep damage developed per cycle is two orders of magnitude weaker than that of fatigue damage.

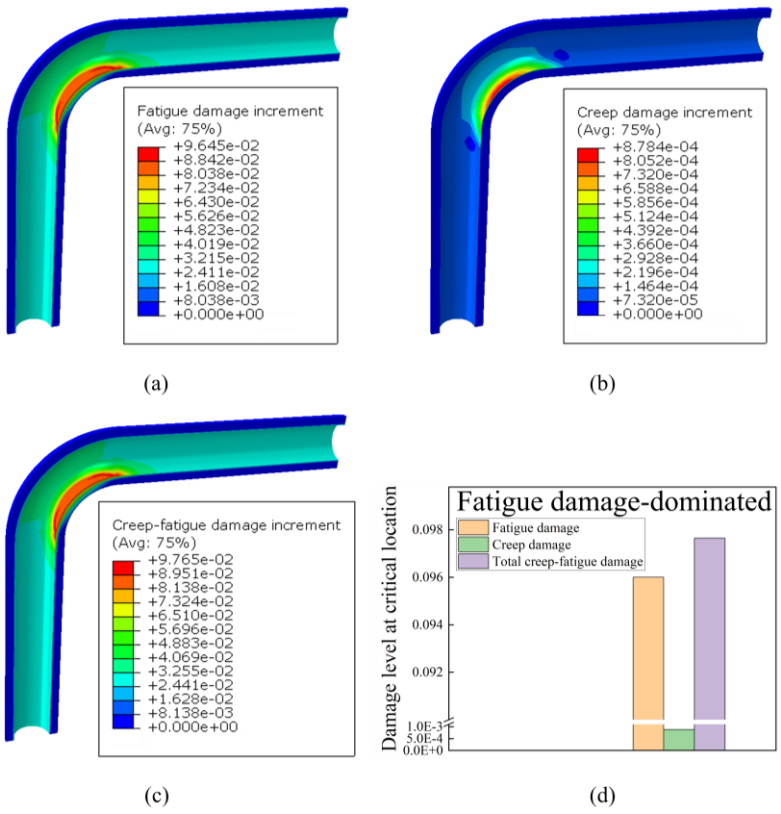

Fig. 7.8. Distributions of damage increment per cycle of the elbow pipe under the mean values of the design conditions: (a) fatigue damage increment; (b) creep damage increment; (c) creep-fatigue damage increment

7.3.3 Statistical distributions of structural creep-fatigue damage and lifetime

For the probabilistic creep-fatigue analysis of the elbow pipe component, the randomness of the design parameters covers the material plastic yield strength, the material creep property, the geometric dimension and the cyclic loading conditions, and the related statistical information of these random variables is listed in Tables 7.1 and 7.2. The sensitivity analysis recognizes the importance of the input parameters on the structural creep-fatigue lifetime. As shown in Fig. 7.9, the cyclic load conditions play the most significant role in the creep-fatigue life, and with the peak values of the inner temperature and pressure increasing, the cyclic plasticity is enhanced for which the creep-fatigue life drops sharply. Instead, as the cyclic yield strength and the nominal pipe thickness raise, the cyclic strain range is weakened at the elbow region, hence, improving the structural resistance of LCF. Given the controlling mechanism of alternating plasticity, the material creep parameters and the creep dwell time make very limited contributions to the creep-fatigue life.

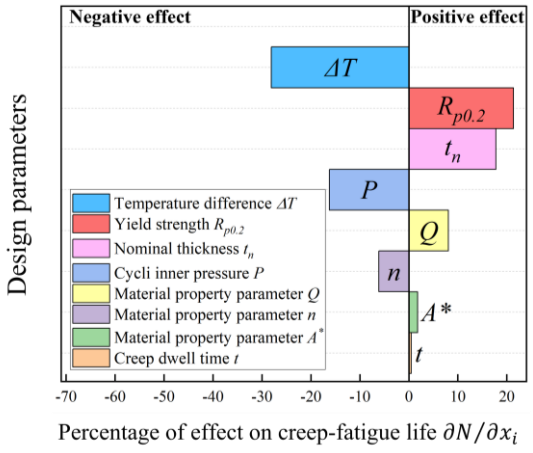

Fig. 7.9. Sensitivity of the design parameters on creep-fatigue life of the elbow pipe

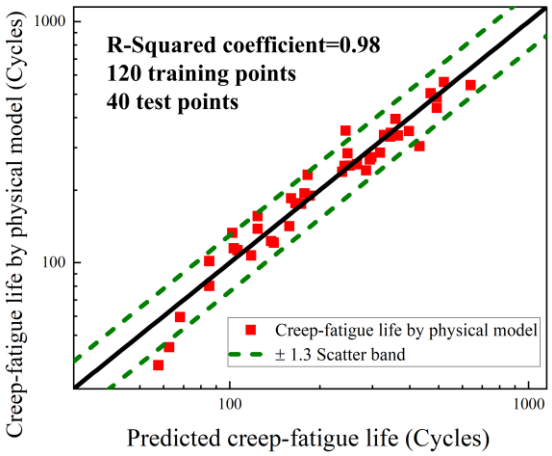

Fig. 7.10. Fitting quality of the EDDNN for creep-fatigue life estimation of the elbow pipe

In addition, the training process of this benchmark consumes 120 training points to acquire the relationship between the input and the creep-fatigue response, where the fitting quality of the EDDNN approach is demonstrated by comparing the results from the physical model versus the predicted values in Fig. 7.10. Within the creep-fatigue life ranging from 100 to 1,000 cycles, all the 40 validation points lie in the zone of the ± 1.3 scattering band, with the R-squared coefficient equal to 0.98.

Considering the uncertainty in design parameters, the proposed probabilistic analysis framework of creep-fatigue analysis for the elbow pipe bend quantifies the statistical distributions of the creep-fatigue damage and lifetime, as well as the estimation of the statistical parameters, as plotted in Fig. 7.11. By the converged MCS, both the creep-fatigue damage and the lifetime approximately follow the log-normal distribution, with the logarithmic mean value and the logarithmic standard deviation also fitted, and such distribution features display a distinctive trend of the LCF-dominated failure mechanism [204, 205].

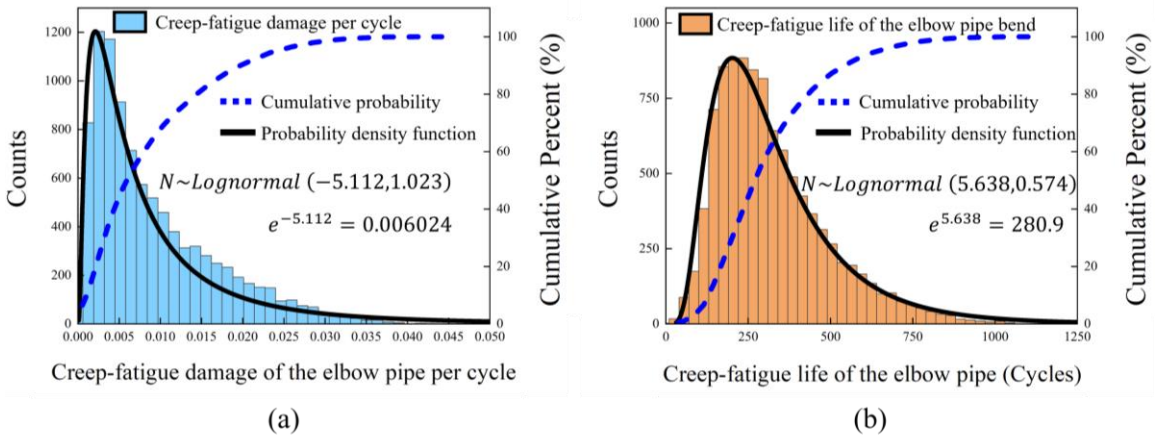

Fig. 7.11. Statistical distribution of the predicted creep-fatigue responses: (a) creep-fatigue damage per cycle of the elbow pipe; (b) creep-fatigue life of the elbow pipe

By adopting the structural resistance and the loading conditions model, the structural failure probability is able to be expressed by the performance function $G(\boldsymbol{X})$ in Equation (7.16), where $\boldsymbol{X}$ is an n-dimensional vector $\boldsymbol{X} = (x_1, x_1, \dots, x_n)$, including all the random variables, which are defined to consider the uncertain design conditions. Thus, in Equations (7.17) and (7.18), structural reliability refers to the survival probability for which the stochastic creep-fatigue life safely exceeds the level required by the actual design purpose. Based on the selected critical location in terms of the maximum creep-fatigue damage at the elbow region, Fig. 7.12 visualizes the structural reliability and the failure probability versus the minimum creep-fatigue life for design purposes [174], by which once the required creep-fatigue life is assigned, the reliability and the related failure probability are able to be acquired through such curves. Furthermore, for a specified reliability consideration, this relationship is capable of directly calibrating the maximum acceptable number of creep-fatigue cycles, by which three different reliability grades are identified in terms of the importance of application.

$$G(\boldsymbol{X}) = N(\boldsymbol{X}) - N_0 \tag{7.16}$$

$$P_f = P[G(\boldsymbol{X}) < 0] = P[N(\boldsymbol{X}) - N_0] \tag{7.17}$$

$$R = 1 - P_f \tag{7.18}$$

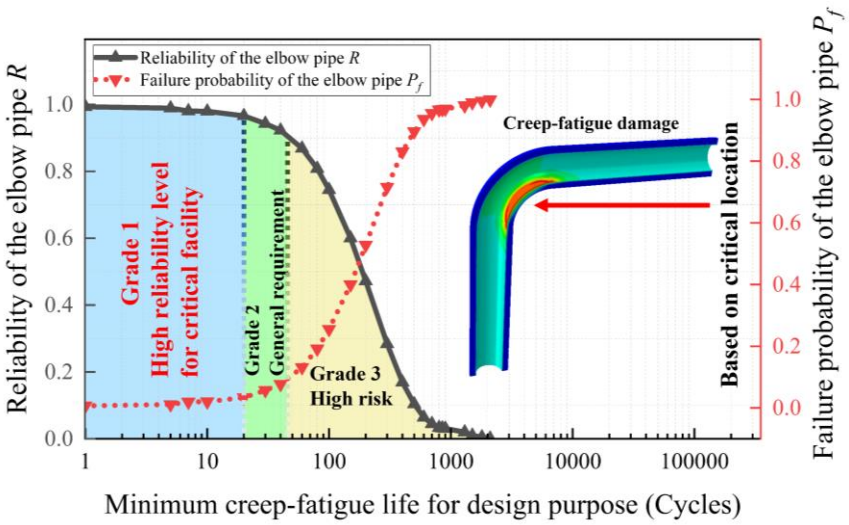

Fig. 7.12. Structural reliability and the failure probability of the elbow pipe versus the minimum creep-fatigue life for design purposes

7.4 Probabilistic creep-fatigue analysis with creep damage-dominated failure mechanism

In the second benchmark, the hydrogenation reactor component with a noticeable high-temperature gradient zone at the support structure is selected and evaluated considering the uncertainty of design conditions, with the predominant creep damage mechanism clarified in the probabilistic assessment.

7.4.1 Outline of the hydrogenation reactor model

As the extensively used core operation unit in petrochemical industries, the hydrogenation reactor is inevitably exposed to severe environments with elevated temperatures, complicated stress states, frequent load cycles and long dwell periods [206]. To meet the operating requirements, a forging component, the bottom ring shell with the integrated support [207], is often uniquely designed around the lower head, which often results in creep-fatigue damage at this susceptible location under cyclic thermos-mechanical load conditions.

The geometric structure of the hydrogenation reactor for creep-fatigue assessment is shown in Fig. 7.13, which is constructed with five individual components, including the main vessel, H-shape forging, spherical lower head with nozzle, support and insulation layer. It is worth noting that between the main vessel and the support side, there is an annular air chamber set especially so as to relieve the marked effect of temperature difference which, accordingly, produces high temperature-dependent stress. The geometric dimensions are listed in Table 7.3.

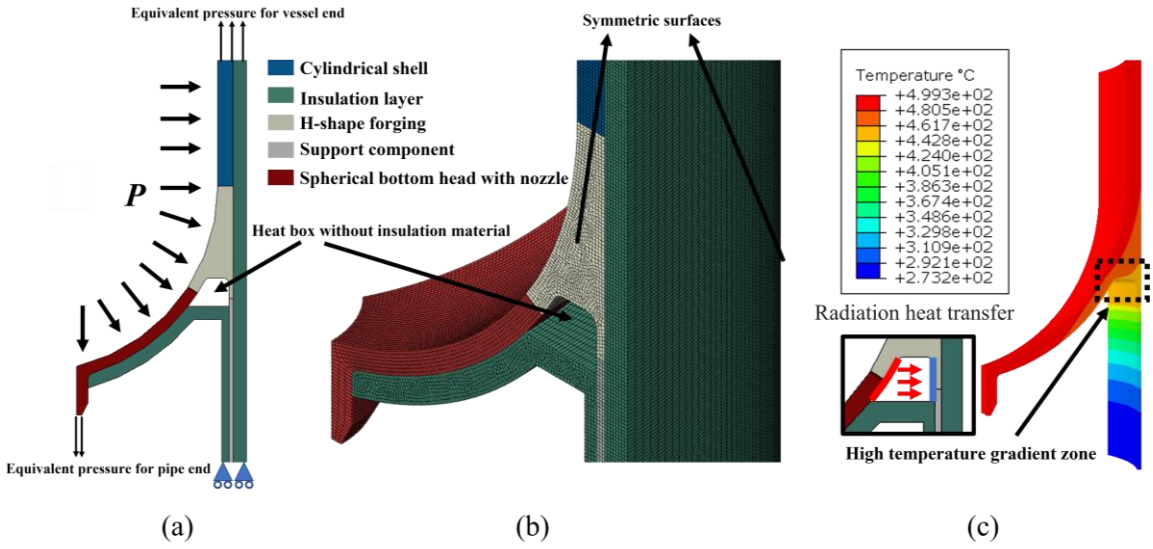

Fig. 7.13. Configuration of the hydrogenation reactor model for creep-fatigue analysis: (a) the geometry model; (a) the FEA model; (c) the distribution of reference temperature difference along the thickness direction

Table 7.3. Geometric dimension of the hydrogenation reactor

Parameter type	Design parameter	Mean value μ	Distribution type	Coefficient of variation CV
Geometric dimension	Nominal thickness of the main vessel t_{n1} (mm)	85	Normal	0.1
	Nominal thickness of the lower head t_{n2} (mm)	50	Normal	0.1
	Nominal height of air chamber h_n (mm)	130	Normal	0.1

The candidate material for constructing the hydrogenation reactor is selected as 2.25Cr1Mo steel, the most commonly used chromium–molybdenum steel for building high-temperature pressure vessels. The detailed material properties are given out in Table 7.4. To derive the temperature field for the subsequent creep-fatigue analysis, the inner surface of the vessel and the outer surface of the insulation layer are subjected to the convection heat transfer conditions, and at the same time, the radiation heat transfer is also well considered between both sides of the H-shape forging. Detailed conditions for the thermal analysis are provided in Table 7.5. Especially, due to the uncertainty of the radiation process between the vessel side and the support, the random variable of the emissivity is set, which affects the strength of the heat transfer inside this region.

Table 7.4. Material properties and creep strain rate parameters of 2.25Cr1Mo steel under operating temperature [84, 208]

Parameter type	Design parameter		Mean value μ	Distribution type	Coefficient of variation CV
Material property	Young's modulus E (10^3MPa)		175	Constant	–
	Poisson's ratio ν		0.3	Constant	–
	Thermal conductivity k $(\text{W/mm}\cdot\text{℃})$		0.02149	Constant	–
	Coefficient of thermal expansion α_m $(10^{-6}/\,\text{℃})$	Based on 500 ℃	33.7	Constant	–
	Density ρ (tone/mm^3)		$7.85\text{E}10^{-9}$	Constant	–
	Specific heat C_p $[\text{mm}^2/(\text{s}^2\cdot\text{K})]$		$6.4\text{E}10^{9}$	Constant	–
	$R_{p0.2}(T)$ (MPa)		312	Normal	0.1
Creep strain rate parameters	A^*		2.32E-31	Normal	0.1
	n		11.34	Normal	0.1
Noting that the creep strain rate is calculated by the Norton creep relationship $\dot{\varepsilon}_{cr} = A^*\sigma^n$					

Table 7.5. Material property and conditions for the thermal analysis

Parameter type	Design parameter	Mean value μ	Distribution type	Coefficient of variation CV
Material property of insulation	Thermal conductivity k $(\mathrm{W/mm \cdot ℃})$	175	Constant	−
Emissivity	ε	0.6	Normal	0.1
Convection coefficient at the inner surface	h_1 $(\mathrm{W/mm^2 \cdot ℃})$	1.2E-3	Constant	−
Convection coefficient at the outer surface	h_2 $(\mathrm{W/mm^2 \cdot ℃})$	1.2E-5	Constant	−

A quarter geometry model of the reactor structure is created and exhibited in Fig. 7.13, with symmetric BCs applied on the symmetric surfaces, and the movement along the vertical direction is also constrained. According to Table 7.6, the reactor structure suffers the cyclic inner pressure as well as the equivalent pressure to balance the inner load at the end of the vessel and pipe, and the typical working temperature difference is imported from the thermal analysis shown in Fig. 7.13 (c), where the history of the loading combination is assumed to follow the identical rule defined by Fig. 7.13 (b).

Table 7.6. Load conditions of the hydrogenation reactor for the probabilistic creep-fatigue analysis

Parameter type	Design parameter	Mean value μ	Distribution type	Coefficient of variation CV
Loading conditions	Maximum cyclic inner pressure P (MPa)	10	Normal	0.1
	Maximum cyclic temperature difference ΔT (℃)	500	Normal	0.1
	Creep dwell time t (hours)	8760	Normal	0.1

7.4.2 Identification of creep-dominated failure mode of the hydrogenation reactor under cyclic thermo-mechanical load

Given the mean values of all the provided design parameters, Fig. 7.14 displays the predominant failure mechanism of the hydrogenation reactor under cyclic thermo-mechanical load. Although the maximum fatigue damage and creep damage take place at the same critical location on the forging component, the inner surface of the transition arc on the support side, compared with the case of the elbow pipe, the total damage is controlled by the creep damage. Three underlying factors contribute to this considerable creep damage. On the one hand, the geometric discontinuity combined with the higher temperature gradient leads to significant peak stress during the load cycle, which elevates the stress level at the start of dwell, consequently, increasing the mean stress during creep dwell and dropping the time to rupture during creep damage evaluations. On the other hand, it seems that the air chamber between the head side and the support transfers heat from the high-temperature side to the low-temperature side, making the temperature uniform in this area. Nevertheless, this design also raises the temperature of the stress concentration zone, and thus deteriorates the temperature-related material strengths of this part (including the resistances to both fatigue and creep).

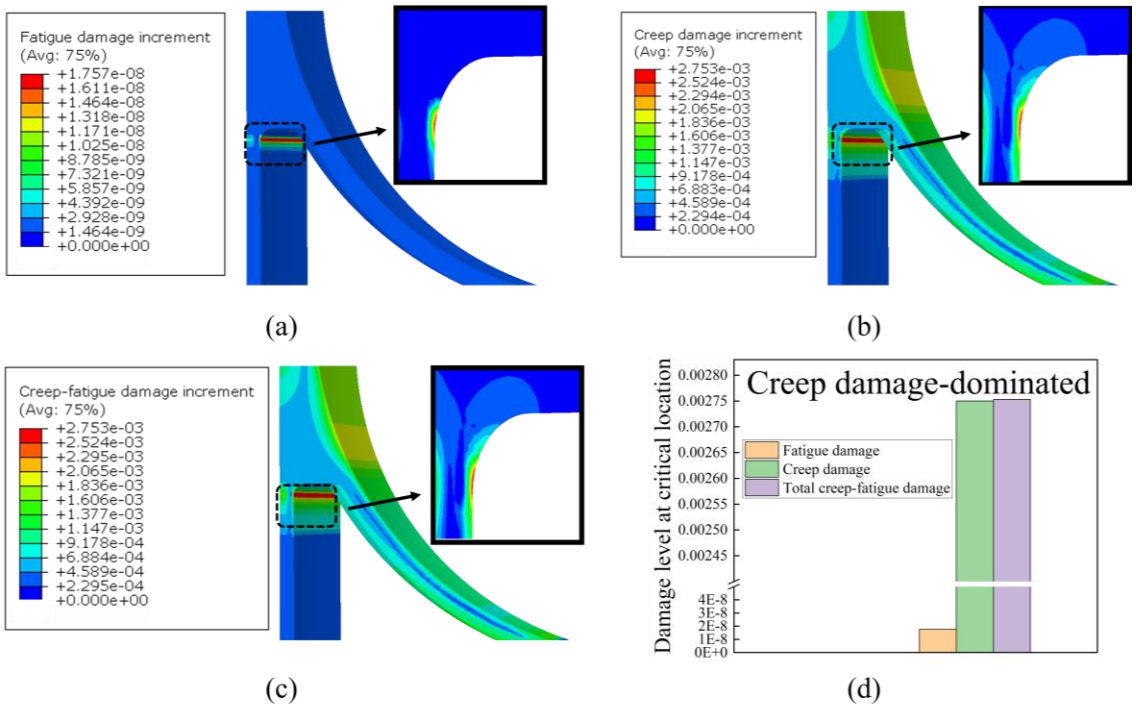

Fig. 7.14. Distributions of damage increment per cycle of the hydrogenation reactor component under the mean values of the design conditions: (a) fatigue damage increment; (b) creep damage increment; (c) creep-fatigue damage increment

7.4.3 Statistical distributions of creep-fatigue damage and lifetime

In this section, the probabilistic creep-fatigue analysis of the hydrogenation reactor investigates the uncertain structural responses, where the random variables existing in material plastic yield strength, the material creep property, the geometric dimension and the cyclic loading conditions are defined in Tables 7.3 to 7.6. And the sensitivity of each selected random variable to the creep-fatigue life of the reactor is illustrated in Fig. 7.15. Except for the equipment thickness (including the thickness dimensions of the lower head and the main shell), which has a positive correlation with the lifetime, all other parameters show a negative correlation. As an assessment with high temperature-related failures, the cyclic temperature difference exhibits the most marked negative effect on the creep-fatigue life, following are the Norton creep coefficient A^* and the height of the air chamber, both of which have an equally negative correlation with structural creep-fatigue life. It is worth noting that regarding the height of the air chamber and the emissivity, the conventional way is to increase them so as to alleviate the local temperature gradient and the thermal stress levels. However, in this case, the creep behaviour relieved by reducing thermal stress

is not able to compensate for the side effect of elevating the local temperature at the critical location of the forging component. This means that the local high temperature is more likely to promote the accumulation of creep-fatigue damage rather than suppress the local thermal stress level.

In Fig. 7.16, there are 160 training data points involved in the training process in terms of the structural creep-fatigue life. To explain the fitting quality, the comparison between the physical model-derived creep-fatigue life and the estimations by the EDDNN approach is provided, and it can be observed that in the zone of the ± 1.5 scattering band locate all the validation cases, with the R-squared coefficient of this built correlation equal to 0.98.

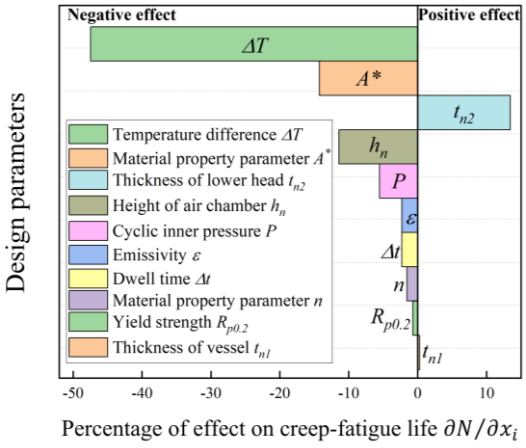

Fig. 7.15. Sensitivity of the design parameters on creep-fatigue life of the hydrogenation reactor

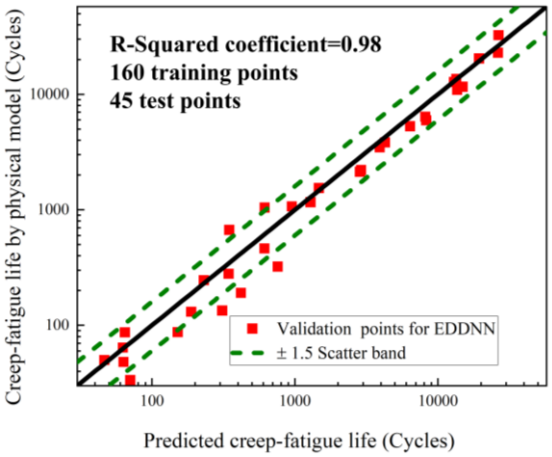

Fig. 7.16. Fitting quality of the EDDNN for creep-fatigue life estimation of the hydrogenation reactor

As plotted in Fig. 7.17, the creep-fatigue damage and the lifetime distributions of the hydrogenation reactor are acquired by the converged MCS with the EDDNN surrogate model. Quite different from the previous analysis of the elbow pipe bend, which is dominated by the fatigue failure pattern, in this case, both the creep-fatigue damage and the lifetime of the hydrogenation reactor tend to obey the normal distribution (with the mean value and the standard deviation fitted in Fig. 7.17). Under such design conditions, the potential failure of the high-temperature hydrogenation reactor is mainly caused by the accumulation of the creep-dominated damage, and this random variable of creep damage is closer to the trend of normal distribution, instead of the Log-normal distribution which is proved more suitable for describing the LCF damage.

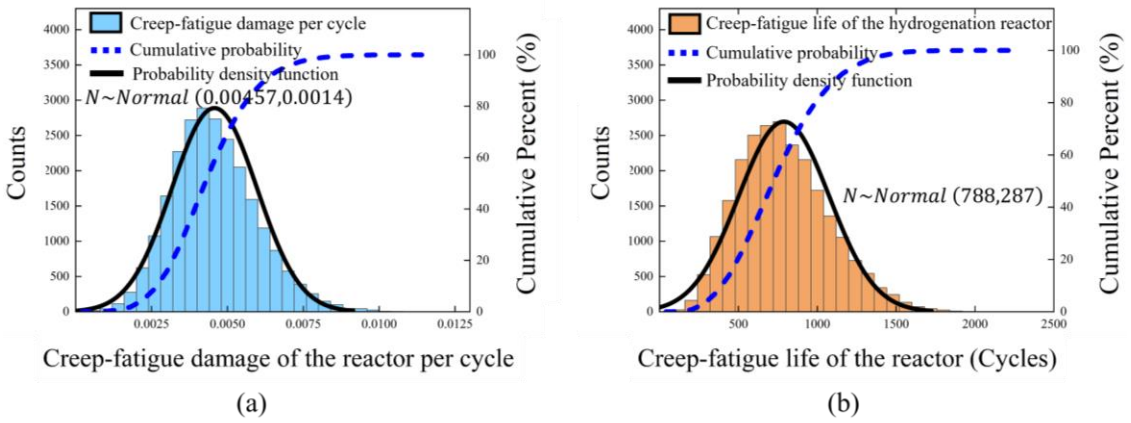

Fig. 7.17. Statistical distribution of the predicted creep-fatigue responses: (a) creep-fatigue damage per cycle of the hydrogenation reactor; (b) creep-fatigue life of the hydrogenation reactor

The reliability-based creep-fatigue design and evaluation diagram is constructed in Fig. 7.18, with the relationship between the structural reliability and the failure probability versus the minimum creep-fatigue life depicted. In respect of different considerations for reliability, three levels of acceptable creep-fatigue life regions are schemed by different colours, and the life span of the highest level for the critical facility (e.g., the nuclear level components) is highlighted by a red label to facilitate the decision making against creep-fatigue failure.

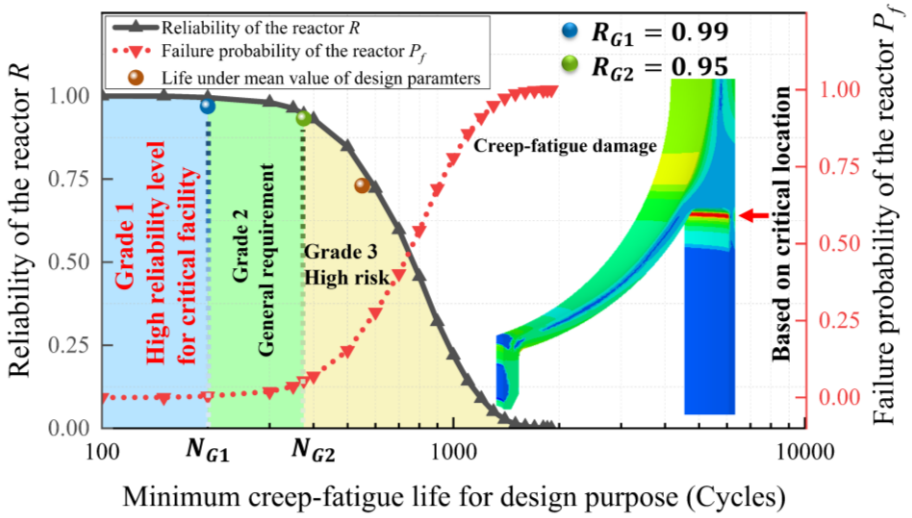

Fig. 7.18. Structural reliability and the failure probability of the hydrogenation reactor versus the minimum creep-fatigue life for design purposes

7.5 Reliability-based safety factor (RBSF) determination under the pLMM framework

7.5.1 Safety factor for design and evaluation against creep-fatigue failure

The traditional safety factor-based design to determine the structural required design life or the minimum acceptable life relies on expert experience more or less. For a variety of engineering cases, this may cause conservative schemes, thus undermining the efforts of detailed calculations. To avoid the arbitrary decision on structural creep-fatigue life, the reliability-based safety factor (RBSF) is necessary to reflect the potential reliability level and failure risk for engineering components with uncertain design conditions. In this section, the RBSF for high-temperature structures is derived from the proposed pLMM framework, and the probabilistic creep-fatigue analysis for the hydrogenation reactor is utilized to demonstrate the detailed derivation process.

7.5.2 Calibration of reliability-based safety factor (RBSF) for high-temperature component

As shown in Fig. 7.18, the brown data point is highlighted to express the analysis result based on the mean values of the design parameters adopted in Section 7.4.2, where the structural creep-fatigue life is 540 cycles, with the reliability equal to 0.72 if the calculated lifetime is taken as the structural design life (i.e., there is no effective safety factor used to reduce the current calculated lifetime). Given the divided reliability grades, this design falls into the region of lower reliability, facing a higher creep-fatigue failure risk. To further improve the robustness of the design proposal, setting a reasonable design life which should be located inside the high-reliability zones is indispensable for enhancing the structure resistance against creep-fatigue failure. According to different applications, two sensible high-reliability grades are recommended:

Grade 1

Inevitably, key facilities often pursue higher reliability such as the power plant in nuclear engineering and the design scheme for the aviation industry, for which the reliability is strictly guaranteed above 99%, corresponding to the lower-bound life N_{G1} in Fig. 7.18. And the RBSF is given out by the ratio of the lifetime N_m calculated by the mean values of design parameters to the lower bound N_{G1}, as described below:

$$n_{G1} = \frac{N_m}{N_{G1}} = \frac{540}{200} = 2.7 \tag{7.19}$$

Grade 2

For general requirements, the Grade 2 RBSF is determined by the lower-bound life N_{G2} with a reliability of 95%, which is calibrated by Equation (7.20).

$$n_{G2} = \frac{N_m}{N_{G2}} = \frac{540}{375} = 1.44 \tag{7.20}$$

In engineering evaluation, once the creep-fatigue life is calculated at the mean values of design parameters, the acceptable design lifetime is able to be evaluated according to the calibrated RBSF.

7.6 Multi-location-based correction for the creep damage-dominated probabilistic assessment

7.6.1 Uncertain critical location in the probabilistic creep-fatigue analysis

During the probabilistic creep-fatigue analysis for the hydrogenation reactor, as the uncertain design parameters fluctuate within a given range, especially for those sensitive to the structural creep-fatigue lifetime (e.g., the cyclic load conditions and the material creep property), the evolution of the creep damage makes the location of the critical node vary randomly. In Fig. 7.19, under the uncertain design parameters, the weakest part arising from the creep damage evolution may shift downward, from point A at the forging component to point B at the welding transition area between the lower head and bottom nozzle. Such a stochastic critical location poses a huge disturbance to building the ANN because of the irregular training dataset of the structural creep-fatigue response. Without recognizing the information of different susceptible positions, the poor quality estimation is pointed out in Fig. 7.20 (a), where a large number of validations are distributed outside the ± 2.0 error band, compared with the pertinent fittings addressed separately, according to critical points A (see Fig. 7.16) and B (see Fig. 7.20 (b)). Here, different critical locations may be relevant to different kinds of creep damage driving forces. At point A, the creep damage accumulation is mainly controlled by the temperature difference between the walls, whereas, the creep damage at point B is much more sensitive to the inner pressure.

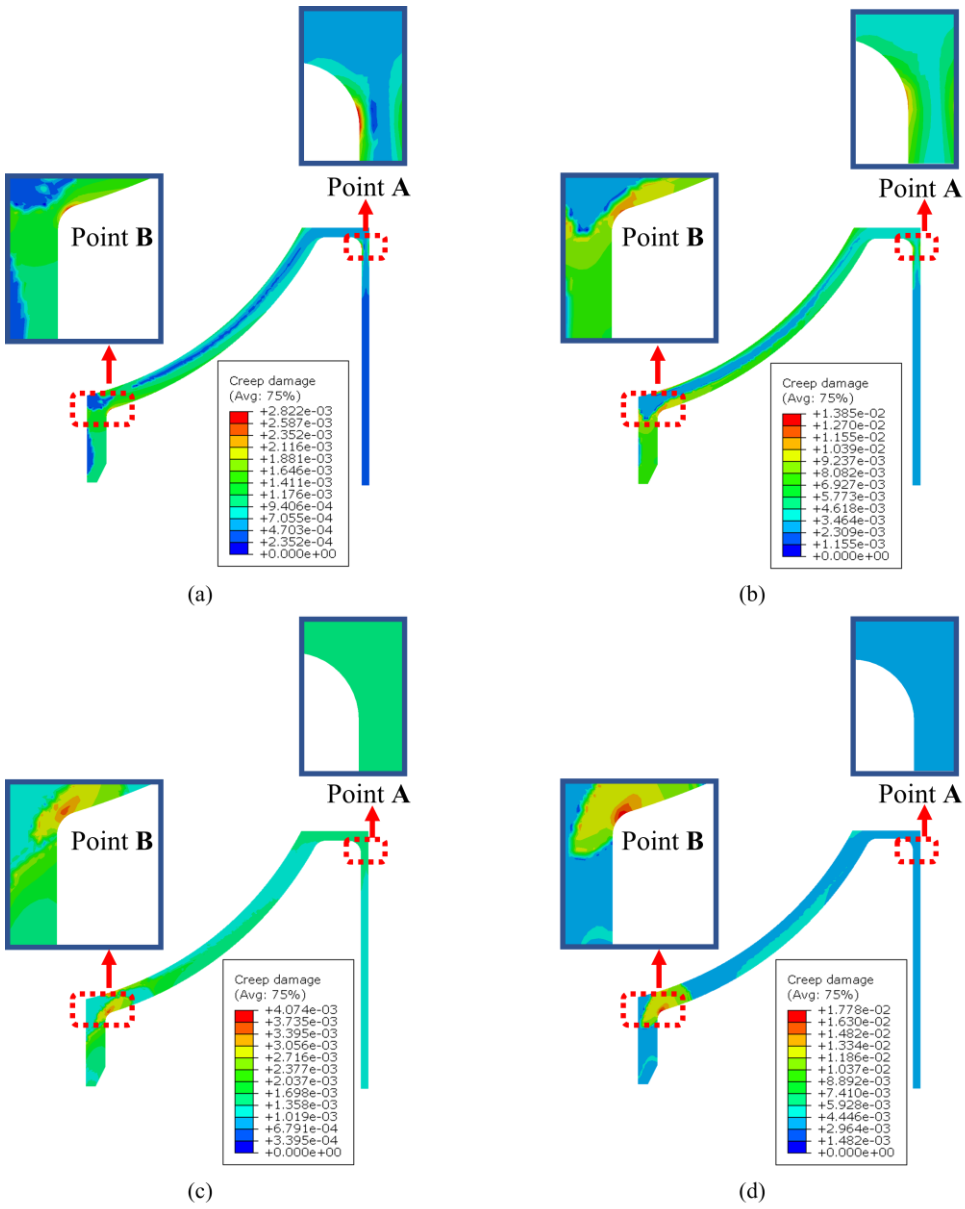

Fig. 7.19. Uncertain evolution of the creep-fatigue damage increment per cycle under the uncertain combination of the design conditions: (a) maximum cyclic temperature equal to 520 ℃ and maximum cyclic inner pressure equal to 8.5 MPa; (b) maximum cyclic temperature equal to 520 ℃ and maximum cyclic inner pressure equal to 9 MPa; (c) maximum cyclic temperature equal to 405 ℃ and maximum cyclic inner pressure equal to 12 MPa; (d) maximum cyclic temperature equal to 450 ℃ and maximum cyclic inner pressure equal to 11.6 MPa

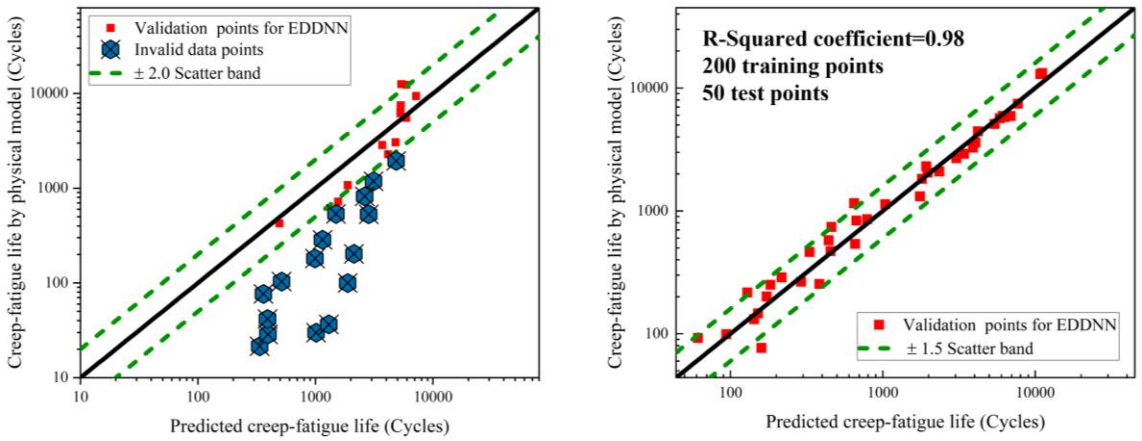

Fig. 7.20. Fitting quality of the EDDNN for structural creep-fatigue life estimation of the hydrogenation reactor: (a) the training process without distinguishing physically key locations; (b) the training process based on the critical location B

7.6.2 Novel data classification scheme to enhance data correlation for an adaptive and robust perception

To eliminate the interference of chaotic data noises and further improve the accuracy of the ANN estimation, a novel data classification scheme is proposed to deal with the randomness in creep damage-dominated probabilistic assessment. The correlation of the given dataset is enhanced by screening the potential critical locations within the design space, and the integrated training processes make the EDDNN robust and adaptive to different failure mechanisms.

This numerical strategy is implemented by the following steps:

Step. 1 Classification according to creep-dominated or fatigue-dominated failure mode.

Step. 2 Identification of the expected vulnerable locations by means of creep-fatigue analysis under a certain range of design parameters.

Step. 3 Training and validating the EDDNN for structural creep-fatigue life in terms of each critical location separately.

Step. 4 Determining the structural creep-fatigue life based on the minimum value among all the individual predictions of underlying candidate targets.

Benefiting from such a scheme, the estimation quality of creep-fatigue life in terms of the whole structure is improved considerably, which is illustrated by the validation in Fig. 7.21, with the lifetime depending on two critical points distinguished by different colours. Within the uncertain design space, the structural creep-fatigue life below 1,000 load cycles tends to be controlled by critical point A, compared with the larger lifetime ranging from 1,000 to 10,000 load cycles, where critical location B plays a more decisive role. This also proves that for structure-level probabilistic analysis, applying the enhanced data perception of the input dataset related to creep damage-induced fatigue is conducive to recognizing the effective lifetime.

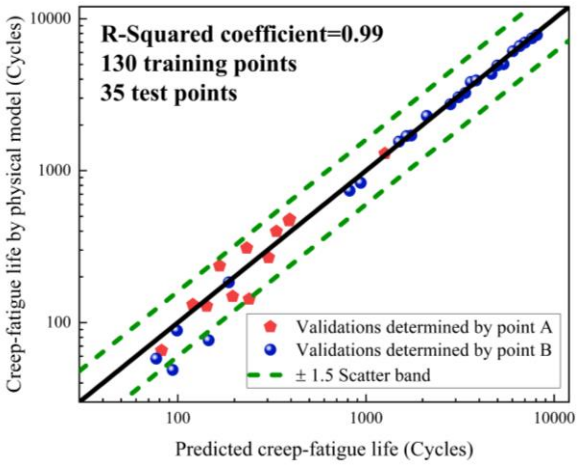

Fig. 7.21. Fitting quality of the EDDNN for structural creep-fatigue life estimation of the hydrogenation reactor with enhanced correlation perception of multi-locations (ECPML)

7.7 Conclusions

The deterministic method-based assessments use safety factors to maintain extremely safe designs under uncertain factors, which is an obstacle to implementing reliability-based design and risk management. In this chapter, a novel artificial neural network-driven probabilistic analysis strategy for creep-fatigue failure is proposed under the probabilistic Linear Matching Method (pLMM) framework with superior computational efficiency and accuracy. Two extreme creep-fatigue failure assessments of the pressurized structures that are dominated by fatigue damage and creep damage respectively are provided to discuss the applicability of the proposed approach. The main conclusions of this study are summarized and listed below:

1. The eDSCA-driven neural network (EDDNN) is built to generate the surrogate model for creep-fatigue damage and lifetime prediction, with the physics-based creep-fatigue model employed to prepare the training database.

2. The probabilistic analysis strategy for structural creep-fatigue failure is established to investigate the statistical information on the damage and lifetime, by which the failure risk is able to be estimated.

3. The comprehensive capability of the proposed probabilistic analysis is well demonstrated by the engineering benchmarks including the elbow pipe bend and the high-temperature hydrogenation reactor, with a wide range of uncertain design parameters involved.

4. With the two typical creep-fatigue damages considered, the reliability-based evaluation diagrams are constructed according to different reliability grades, which is conducive to the risk evaluation of infrastructures by introducing the reliability-based safety factor (RBSF).

5. The data classification scheme is proposed to deal with the randomness in creep damage-dominated probabilistic assessment and the correlation of the given dataset is enhanced by screening the potential critical locations within the design space, making the EDDNN adaptive to different failure mechanisms.

8 Conclusions

8.1 Summary of the thesis

In this thesis, the novel probabilistic Linear Matching Method (pLMM) framework is developed to deal with the reliability-centred structural integrity assessment for the high-temperature component. Based on the current Linear Matching Method (LMM) and Artificial Intelligence technology, the physics-based and data-driven numerical strategy of failure prediction and risk management regarding critical infrastructures is proposed, with a reasonable balance between the computational efficiency and accuracy achieved.

The main outcomes of the research are summarised below:

1. A comparative study of the creep rupture analysis approaches is performed to investigate the effectiveness of the selected rupture limit assessments.

2. The unified constraint parameter is proposed to describe the constraint effect in terms of the cyclic plastic behaviour of the structure containing defects.

3. A direct method-based probabilistic shakedown analysis is delivered under the new probabilistic Linear Matching Method framework (pLMM).

4. Under the pLMM framework, the physically based probabilistic low cycle fatigue and ratcheting assessments are implemented with the novel Linear Matching Method-driven neural network (LDNN).

5. The innovative physics-based probabilistic assessment for creep-fatigue failure is proposed under the pLMM framework, and the extended DSCA-driven neural network (EDDNN) is built with the superior fitting quality of damage and lifetime.

Major creep rupture assessment techniques are comparatively investigated, including the isochronous stress-strain (ISS) curve-based creep rupture limit analysis, the Omega creep damage model-based creep analysis and the direct method-based creep rupture assessment by an extended LMM. New virtual creep test curves are generated from the Omega creep model and chosen as the unified creep source data to derive the key material parameters used for different methods. Through a practical engineering application of a high-temperature pressure vessel component, a profound

insight into the techniques of creep rupture evaluation is delivered from different views. Several assessment curves are built based on a new understanding of the creep rupture failure mechanism, with an effective numerical plan to validate the creep rupture boundary illustrated.

The plastic shakedown load domain and low cycle fatigue (LCF) life are compressed dramatically by increasing the in-plane constraint effect, while the out-of-plane constraint effect elevates the capability to resist ratcheting failure. In addition, the unified constraint parameter A_p is suitable to measure the strength of compound constraint under cyclic loading conditions, and there is a salient linear relation between constraint parameter $\sqrt{A_p}$ and cyclic plastic responses (including ratchet limit and alternating plastic strain range) of the cracked specimen.

The risk of losing the shakedown state is predicted by the physics-based estimation model, where the efficient iteration is employed to derive the reliability index. In the benchmark, the probabilistic shakedown boundary is constructed, with the additional influence of the uncertain cyclic loading pattern on the reliability fully reflected.

The pLMM framework is capable of quantitatively predicting the statistical distribution of LCF life and ratchet limit. With the numerical investigations on the elbow pipe structure presented, the probabilistic assessment boundaries and reliability-centred evaluation diagrams in terms of LCF life and ratchet limit are established respectively, which are beneficial to get rid of the conservativeness of the traditional design schemes with safety factor.

The extended DSCA-driven neural network (EDDNN) is built to efficiently express the relationship between design parameters and structural creep-fatigue damage and lifetime. And the reliability-based evaluation diagram is established according to different requirements. Furthermore, a novel data classification scheme is given out to tackle the randomness in creep damage-dominated probabilistic assessment.

8.2 Future work

Although the reliability-based structural integrity assessment for the high-temperature component is fulfilled by the pLMM framework in this study, there are still several aspects that can be improved as shown below:

In the current version of the LMM framework, the creep-fatigue simulation procedure mainly relies on the Norton and Norton-Bailey laws to depict the material creep behaviour under high-

temperature conditions, which focus on the secondary stage creep. However, it is crucial to extend the creep constitutive relationship to incorporate a more detailed creep description covering the tertiary stage, since modern high-temperature engineering requires the operating unit with a long-term running that may lead to the creep behaviour exceeding the secondary stage and entering the more dangerous tertiary stage.

The implementation of probabilistic structural integrity assessment under the pLMM framework adopts the EBF neural network with the Isight software. And this neural network type has limitations when coping with different kinds of failure mechanisms. Hence, future work should explore more types of neural networks with versatile structures to enhance the applicability of the pLMM framework. More flexible computer languages should also be utilized to build efficient neural network models.

The optimization of the core parameters (including the weights and the level number of the neural network) of the LDNN and EDDNN should be addressed in the next stage. And with the pLMM framework applied to the probabilistic structural integrity assessment for practical engineering problems, the database based on failure mechanisms needs to be further updated. Therefore, the feedback in terms of the predicting quality is able to be provided to the current neural network, with optimization of the key parameters performed iteratively. The research results will be conducive to paving the way for the future development of digital twin technology for high-temperature structures.

References

[1] Woo T-H, Lee U-C. Safeguard assessment for life extension in nuclear power plants (NPPs) using a production function. Nucl Eng Des 2011;241:826-31.
[2] Hirano M, Yonomoto T, Ishigaki M, Watanabe N, Maruyama Y, Sibamoto Y, et al. Insights from review and analysis of the Fukushima Dai-ichi accident. Journal of Nuclear Science and Technology 2012;49:1-17.
[3] ASME. ASME Boiler & Pressure Vessel Code, Section III Rules for Construction of Nuclear Facility Components, Division 1, Subsection NH, Class 1 Components in Elevated Temperature Service. New York: The American Society of Mechanical Engineers; 2015.
[4] API. API 579-1/ASME FFS-1, Fitness-For-Service. Houston, TX: American Petroleum Institute; 2016.
[5] Ainsworth R. A. R5: an assessment procedure for the high temperature response of structures. Procedure R5: Issue 3. Gloucester: UK: British Energy Generation Ltd.; 2014.
[6] RCC-MRx Code, Design and Construction rules for Nuclear Power Generating Stations, 2015. AFCEN, France.
[7] Burdekin FM. General principles of the use of safety factors in design and assessment. Engineering Failure Analysis 2007;14:420-33.
[8] Stefanou G. The stochastic finite element method: Past, present and future. Comput Method Appl M 2009;198:1031-51.
[9] Tuck OCG, Pyke CK, Underwood NJ. A review of probabilistic creep assessment reporting relating to volume 2/3 of the R5 procedure. International Journal of Pressure Vessels and Piping 2021;190:104295.
[10] Marriott DL. Isochronous Stress/Strain Curves: Origins, Scope and Applications. ASME 2011 Pressure Vessels and Piping Conference: American Society of Mechanical Engineers Digital Collection; 2011. p. 373-9.
[11] Kim W-G, Lee H-Y, Hong H-U. Evaluation of tension and creep rupture behaviors of long-term exposed P91 steel in a supercritical plant. Engineering Failure Analysis 2020;116:104736.
[12] Zhao M, Koves W. Applications of isochronous data in creep analysis. ASME 2007 Pressure Vessels and Piping Conference: American Society of Mechanical Engineers Digital Collection; 2007. p. 223-30.
[13] Koves W, Zhao M. On Simplified Inelastic Method Using Material's Isochronous Stress–Strain Data for Creep Analysis. Journal of Pressure Vessel Technology 2013;135.
[14] Manu C, Birk A, Kim I. Uniaxial high-temperature creep property predictions made by CDM and MPC omega techniques for ASME SA 455 steel. Engineering Failure Analysis 2009;16:1303-13.
[15] Prager M. Development of the MPC Omega Method for Life Assessment in the Creep Range. Journal of Pressure Vessel Technology 1995;117:95-103.
[16] ASME. ASME Boiler and Pressure Vessel Code Case 2605-3, Fatigue Evaluation for SA-182 F22V, SA-336 F22V, SA-541 22V, SA-542 Type D, Class 4a, and SA-832 Grade 22V at Temperatures Greater Than 371°C (700°F) and Less Than or Equal to 482°C (900°F) Section VIII, Division 2. New York: American Society of Mechanical Engineers; 2017.
[17] Vivio F, Gaetani L, Ferracci M, Masia A. Detail investigation of Omega method for creep analysis of pressure vessel components. ASME; 2013.
[18] Prager M. The Omega Method–An Engineering Approach to Life Assessment. Journal of Pressure Vessel Technology 2000;122:273-80.
[19] Gurumurthy K, Srinivasan B, Krishna PS, Achary GGS, Subramanyam SVR. Creep-Fatigue Design Studies for Process Reactor Components Subjected to Elevated Temperature Service as per ASME-NH. Procedia Engineering 2014;86:327-34.

[20] Murakami S. Creep Damage and Creep-Fatigue Damage. Springer Netherlands; 2012. p. 217-51.
[21] Zuo F-J, Huang H-Z, Zhu S-P, Lv Z, Gao H. Fatigue life prediction under variable amplitude loading using a non-linear damage accumulation model. International Journal of Damage Mechanics 2015;24:767-84.
[22] Wang R-Z, Zhang X-C, Gong J-G, Zhu X-M, Tu S-T, Zhang C-C. Creep-fatigue life prediction and interaction diagram in nickel-based GH4169 superalloy at 650℃ based on cycle-by-cycle concept. Int J Fatigue 2017;97:114-23.
[23] Douzian G, Muránsky O, Kruzic JJ, Wright RN, Payten W. Assessment of modelling methodologies for prediction of high-temperature creep-fatigue behaviour of Alloy 617. International Journal of Pressure Vessels and Piping 2020;187:104150.
[24] Ragab R, Liu T, Li M, Sun W. Membrane stretching based creep damage analytical solutions for thin disc small punch problem. Journal of the Mechanics and Physics of Solids 2022;165:104928.
[25] Payten WM, Snowden KU, Bendeich P. The use of a simplified analytical expression for metastable thermal stress analysis and its application to creep–fatigue damage of a 2.25Cr 1Mo thick walled component. Int J Fatigue 2010;32:368-75.
[26] Huo J, Sun D, Wu H, Wang W, Xue l. Multi-axis low-cycle creep/fatigue life prediction of high-pressure turbine blades based on a new critical plane damage parameter. Engineering Failure Analysis 2019;106:104159.
[27] Yang YP, Mohr WC. Finite Element Creep-Fatigue Analysis of a Welded Furnace Roll for Identifying Failure Root Cause. Journal of Materials Engineering and Performance 2015;24:4388-99.
[28] Ortega J, Khivsara S, Christian J, Ho C, Dutta P. Coupled modeling of a directly heated tubular solar receiver for supercritical carbon dioxide Brayton cycle: Structural and creep-fatigue evaluation. Applied Thermal Engineering 2016;109:979-87.
[29] Wong EH, van Driel WD, Dasgupta A, Pecht M. Creep fatigue models of solder joints: A critical review. Microelectronics Reliability 2016;59:1-12.
[30] Skelton RP, Gandy D. Creep – fatigue damage accumulation and interaction diagram based on metallographic interpretation of mechanisms. Materials at High Temperatures 2008;25:27-54.
[31] Brocks W, Schmitt W. The second parameter in J-R curves: constraint or triaxiality? Constraint Effects in Fracture Theory and Applicatons: Second Volume: ASTM International; 1995.
[32] Liu Z, Wang X, Zhang Z, Jin P, Chen X. Solutions and applications of 3D elastic–plastic constraint parameters for clamped single edge notched tension (SENT) specimens. Engineering Fracture Mechanics 2022;272:108713.
[33] Larsson S-G, Carlsson AJ. Influence of non-singular stress terms and specimen geometry on small-scale yielding at crack tips in elastic-plastic materials. Journal of the Mechanics and Physics of Solids 1973;21:263-77.
[34] O'Dowd NP, Shih CF. Family of crack-tip fields characterized by a triaxiality parameter—II. Fracture applications. Journal of the Mechanics and Physics of Solids 1992;40:939-63.
[35] O'dowd N, Shih CF. Family of crack-tip fields characterized by a triaxiality parameter—I. Structure of fields. Journal of the Mechanics and Physics of Solids 1991;39:989-1015.
[36] Chao Y, Yang S, Sutton M. On the fracture of solids characterized by one or two parameters: theory and practice. Journal of the Mechanics and Physics of Solids 1994;42:629-47.
[37] Ma HS, Wang GZ, Liu S, Tu ST, Xuan FZ. Three-dimensional analyses of unified characterization parameter of in-plane and out-of-plane creep constraint. Fatigue & Fracture of Engineering Materials & Structures 2016;39:251-63.
[38] Guo W. Elastoplastic three dimensional crack border field—II. Asymptotic solution for the field. Engineering Fracture Mechanics 1993;46:105-13.
[39] Guo W. Elastoplastic three dimensional crack border field—I. Singular structure of the field. Engineering Fracture Mechanics 1993;46:93-104.

[40] Mostafavi M, Smith D, Pavier M. A micromechanical fracture criterion accounting for in-plane and out-of-plane constraint. Computational materials science 2011;50:2759-70.
[41] Mostafavi M, Smith D, Pavier M. Reduction of measured toughness due to out-of-plane constraint in ductile fracture of aluminium alloy specimens. Fatigue & Fracture of Engineering Materials & Structures 2010;33:724-39.
[42] Yang J, Wang G, Xuan F, Tu S. Unified correlation of in-plane and out-of-plane constraint with fracture resistance of a dissimilar metal welded joint. Engineering Fracture Mechanics 2014;115:296-307.
[43] Yang J, Wang GZ, Xuan FZ, Tu ST. Unified characterisation of in-plane and out-of-plane constraint based on crack-tip equivalent plastic strain. Fatigue & Fracture of Engineering Materials & Structures 2013;36:504-14.
[44] Xu JY, Wang GZ, Xuan FZ, Tu ST. Unified constraint parameter based on crack-tip opening displacement. Engineering Fracture Mechanics 2018;200:175-88.
[45] Wu D, Jing H, Xu L, Zhao L, Han Y. Analytical approaches of creep crack initiation prediction coupled with the residual stress and constraint effect. European Journal of Mechanics - A/Solids 2018;71:1-15.
[46] Wu D, Jing H, Xu L, Zhao L, Han Y. Enhanced models of creep crack initiation prediction coupled the stress-regime creep properties and constraint effect. European Journal of Mechanics - A/Solids 2019;74:145-59.
[47] Wu D, Jing H, Xu L. Engineering application of enhanced C*-Q* two parameter approaches for predicting creep crack initiation times. European Journal of Mechanics - A/Solids 2020;82:104013.
[48] Yang J, Wang G, Xuan F, Tu S. Unified characterisation of in-plane and out-of-plane constraint based on crack-tip equivalent plastic strain. Fatigue & Fracture of Engineering Materials & Structures 2013;36:504-14.
[49] ASTM E1820-08a. Standard test method for measurement of fracture toughness. Philadelphia: American Society for Testing and Materials; 2008.
[50] Simon J-W, Weichert D. Numerical lower bound shakedown analysis of engineering structures. Comput Method Appl M 2011;200:2828-39.
[51] Chen S, Liu Y, Cen Z. Lower bound shakedown analysis by using the element free Galerkin method and non-linear programming. Comput Method Appl M 2008;197:3911-21.
[52] Marriott D. Evaluation of deformation or load control of stresses under inelastic conditions using elastic finite element stress analysis. ASME PVP 1988;136:3-9.
[53] Seshadri R. Inelastic evaluation of mechanical and structural components using the generalized local stress strain method of analysis. Nucl Eng Des 1995;153:287-303.
[54] Mackenzie D, Shi J, Boyle J. Finite element modelling for limit analysis by the elastic compensation method. Comput Struct 1994;51:403-10.
[55] Yang P, Liu Y, Ohtake Y, Yuan H, Cen Z. Limit analysis based on a modified elastic compensation method for nozzle-to-cylinder junctions. International journal of pressure vessels and piping 2005;82:770-6.
[56] Muscat M, Hamilton R, Boyle J. Shakedown analysis for complex loading using superposition. The Journal of Strain Analysis for Engineering Design 2002;37:399-412.
[57] Peng H, Liu Y, Chen H, Shen J. Shakedown analysis of engineering structures under multiple variable mechanical and thermal loads using the stress compensation method. International Journal of Mechanical Sciences 2018;140:361-75.
[58] Chen H, Ure J, Tipping D. Integrated structural analysis tool using the Linear Matching Method part 2–Application and verification. International Journal of Pressure Vessels and Piping 2014;120:152-61.

[59] Ure J, Chen H, Tipping D. Integrated structural analysis tool using the linear matching method part 1–Software development. International Journal of Pressure Vessels and Piping 2014;120:141-51.
[60] Ma ZY, Wang XX, Chen HF, Xuan FZ, Liu YH. A unified direct method for ratchet and fatigue analysis of structures subjected to arbitrary cyclic thermal-mechanical load histories. International Journal of Mechanical Sciences 2021;194.
[61] Zhu TL. A reliability-based safety factor for aircraft composite structures. Comput Struct 1993;48:745-8.
[62] Galambos TV, Ravindra M. Load and resistance factor design. Engineering Journal, AISC 1981;18:78-84.
[63] Matos JC, Cruz PJS, Valente IB, Neves LC, Moreira VN. An innovative framework for probabilistic-based structural assessment with an application to existing reinforced concrete structures. Engineering Structures 2016;111:552-64.
[64] Maier HR, Lence BJ, Tolson BA, Foschi RO. First-order reliability method for estimating reliability, vulnerability, and resilience. Water Resources Research 2001;37:779-90.
[65] Hasofer AM, Lind NC. Exact and invariant second-moment code format. Journal of the Engineering Mechanics division 1974;100:111-21.
[66] Khuri AI, Mukhopadhyay S. Response surface methodology. Wiley Interdisciplinary Reviews: Computational Statistics 2010;2:128-49.
[67] Kleijnen JPC. Kriging metamodeling in simulation: A review. European Journal of Operational Research 2009;192:707-16.
[68] Majdisova Z, Skala V. Radial basis function approximations: comparison and applications. Applied Mathematical Modelling 2017;51:728-43.
[69] Erzurumlu T, Oktem H. Comparison of response surface model with neural network in determining the surface quality of moulded parts. Materials & Design 2007;28:459-65.
[70] Matheron G. Principles of geostatistics. Economic geology 1963;58:1246-66.
[71] Cressie N. Statistics for spatial data: John Wiley & Sons; 2015.
[72] Ardakani M, Shokry A, Saki G, Escudero G, Graells M, Espuña A. Imputation of Missing Data with Ordinary Kriging for Enhancing Fault Detection and Diagnosis. In: Kravanja Z, Bogataj M, editors. Computer Aided Chemical Engineering: Elsevier; 2016. p. 1377-82.
[73] Luo J, Lin S, Ni J, Lei M. An Improved Fingerprint Recognition Algorithm Using EBFNN. Proceedings - 2nd International Conference on Genetic and Evolutionary Computing, WGEC 2008 2008.
[74] Baker MR, Patil RB. Universal Approximation Theorem for Interval Neural Networks. Reliable Computing 1998;4:235-9.
[75] Lu Y, Lu J. A universal approximation theorem of deep neural networks for expressing probability distributions. Advances in neural information processing systems 2020;33:3094-105.
[76] Voigtlaender F. The universal approximation theorem for complex-valued neural networks. arXiv preprint arXiv:201203351 2020.
[77] EDF Energy. Assessment Procedure R5, Volume 2/3, Appendix A15: Advice on Probabilistic Assessments. 2018.
[78] Chen H, Ponter ARS. A Direct Method on the Evaluation of Ratchet Limit. Journal of Pressure Vessel Technology 2010;132.
[79] Horseman G. Parsons 500 and 660 MW steam turbines: operating experience and lessons learned. Energy Materials 2009;4:213-37.
[80] Ahmad J, Purbolaksono J, Beng L. Failure analysis on high temperature superheater Inconel® 800 tube. Engineering Failure Analysis 2010;17:328-33.
[81] Barbera D, Chen H. Creep rupture assessment by a robust creep data interpolation using the Linear Matching Method. European Journal of Mechanics-A/Solids 2015;54:267-79.
[82] Gorash Y, Chen H. A parametric study on creep–fatigue strength of welded joints using the linear matching method. Int J Fatigue 2013;55:112-25.

[83] Chen H, Engelhardt M, Ponter AR. Linear matching method for creep rupture assessment. International journal of pressure vessels and piping 2003;80:213-20.
[84] ASME. ASME Boiler & Pressure Vessel Code, Section II Materials Part D, Properties (Metric). New York: The American Society of Mechanical Engineers; 2015.
[85] Liu H, Xuan F-Z. A new model of creep rupture data extrapolation based on power processes. Engineering Failure Analysis 2011;18:2324-9.
[86] Gong J-G, Liu F, Xuan F-Z. On fatigue design curves for 2.25 Cr-1Mo-V steel reactors at elevated temperature in Code Case 2605. Journal of Pressure Vessel Technology 2018;140.
[87] Barbera D, Chen H, Liu Y. On Creep Fatigue Interaction of Components at Elevated Temperature. Journal of Pressure Vessel Technology 2016;138.
[88] Giugliano D, Barbera D, Chen H, Cho N-K, Liu Y. Creep-fatigue and cyclically enhanced creep mechanisms in aluminium based metal matrix composites. European Journal of Mechanics - A/Solids 2019;74:66-80.
[89] Chen H, Chen W, Ure J. A direct method on the evaluation of cyclic steady state of structures with creep effect. Journal of Pressure Vessel Technology 2014;136.
[90] Bradford R, Ure J, Chen H. The Bree problem with different yield stresses on-load and off-load and application to creep ratcheting. International Journal of Pressure Vessels and Piping 2014;113:32-9.
[91] Cochran KB, Dodds RH, Hjelmstad KD. The role of strain ratcheting and mesh refinement in finite element analyses of plasticity induced crack closure. Int J Fatigue 2011;33:1205-20.
[92] Paul SK, Tarafder S. Cyclic plastic deformation response at fatigue crack tips. International Journal of Pressure Vessels and Piping 2013;101:81-90.
[93] Li T, Chen H, Chen W, Ure J. On the Ratchet Analysis of a Cracked Welded Pipe. Journal of Pressure Vessel Technology 2011;134.
[94] Chen H, Chen W, Li T, Ure J. Effect of circular holes on the ratchet limit and crack tip plastic strain range in a centre cracked plate. Engineering fracture mechanics 2011;78:2310-24.
[95] Li TB, Chen HF, Chen WH, Ure J. On the Ratchet Analysis of a Cracked Welded Pipe. J Press Vess-T Asme 2012;134.
[96] Tong J, Cornet C, Lin B, Lupton C, Li HY, Bowen P, et al. Near-tip strain ratchetting and crack growth at elevated temperature. Int J Fatigue 2016;82:514-20.
[97] Bahloul A, Bouraoui C. The overload effect on the crack-tip cyclic plastic deformation response in SA333 Gr 6 C-Mn steel. Theoretical and Applied Fracture Mechanics 2019;99:27-35.
[98] Paul SK. Numerical models of plastic zones and associated deformations for a stationary crack in a C(T) specimen loaded at different R-ratios. Theoretical and Applied Fracture Mechanics 2016;84:183-91.
[99] Report BS. SINTAP. Structural assessment procedures for European industry, final procedure, project BE95-1426. Rotherham1999.
[100] Ltd BE. R6: Assessment of the integrity of structures containing defects. British energy generation report R/H/R6, revision 4. Gloucester, UK2007.
[101] Koçak M, Webster, S., Janosch, J.J., Ainsworth, R.A., Koers, R. FITNET Fitness-for-Service (FFS) - Procedure (Volume 1). Geesthacht, Germany: printed by GKSS Research Center; 2008.
[102] Koçak M, Hadley, I., Szavai, S., Tkach, Y., Taylor, N. FITNET Fitness-for-Service (FFS) - Annex (Volume 2). Geesthacht, Germany: printed by GKSS Research Center; 2008.
[103] Wang B, Siegmund T. Numerical simulation of constraint effects in fatigue crack growth. Int J Fatigue 2005;27:1328-34.
[104] Pandey VB, Samant SS, Singh IV, Mishra BK. An improved methodology based on continuum damage mechanics and stress triaxiality to capture the constraint effect during fatigue crack propagation. Int J Fatigue 2020;140:105823.
[105] Shen H, Guo W. 3D constraint effect on 3D fatigue crack propagation. Int J Fatigue 2005;27:617-23.

[106] Yang J, Liu Y, Chen H. A study on the matching of constraint between steam turbine blade and laboratory specimens. Advances in Mechanical Engineering 2020;12:1687814020922007.
[107] Tan JP, Wang GZ, Xuan FZ, Tu ST. Correlation of creep crack-tip constraint between axially cracked pipelines and test specimens. International Journal of Pressure Vessels and Piping 2012;98:16-25.
[108] Ponter ARS, Chen HF. A minimum theorem for cyclic load in excess of shakedown, with application to the evaluation of a ratchet limit. Eur J Mech a-Solid 2001;20:539-53.
[109] Chen HF, Ponter ARS. A method for the evaluation of a ratchet limit and the amplitude of plastic strain for bodies subjected to cyclic loading. Eur J Mech a-Solid 2001;20:555-71.
[110] Chen HF, Ponter ARS. A Direct Method on the Evaluation of Ratchet Limit. J Press Vess-T Asme 2010;132.
[111] Ma Z, Wang X, Chen H, Xuan F-Z, Liu Y. A unified direct method for ratchet and fatigue analysis of structures subjected to arbitrary cyclic thermal-mechanical load histories. International Journal of Mechanical Sciences 2021;194:106190.
[112] Chen HF, Ponter ARS. Shakedown and limit analyses for 3-D structures using the linear matching method. International Journal of Pressure Vessels and Piping 2001;78:443-51.
[113] Liu Z, Wang X, Shi S, Shen Y, Chen X. Application of modified normalization method for JR curve determination using clamped SENT specimens with varying in-plane and out-of-plane constraints. Engineering Fracture Mechanics 2020:106968.
[114] Liu Z, Wang X, Miller RE, Hu J, Chen X. Ductile fracture properties of 16MND5 bainitic forging steel under different in-plane and out-of-plane constraint conditions: Experiments and predictions. Engineering Fracture Mechanics 2020:107359.
[115] Wu XQ, Katada Y. Strain-amplitude dependent fatigue resistance of low-alloy pressure vessel steels in high-temperature water. Journal of Materials Science 2005;40:1953-8.
[116] ASTM. ASTM A508 / A508M-18, Standard Specification for Quenched and Tempered Vacuum-Treated Carbon and Alloy Steel Forgings for Pressure Vessels. West Conshohocken, PA2018.
[117] Beesley R, Chen H, Hughes M. A novel simulation for the design of a low cycle fatigue experimental testing programme. Comput Struct 2017;178:105-18.
[118] ASME. ASME Boiler & Pressure Vessel Code, Section VIII Rules for Construction of Pressure Vessels Division 2, Alternative Rules. New York: The American Society of Mechanical Engineers; 2015.
[119] Systèmes D. Abaqus 6.12 Abaqus User's Manual. USA2012.
[120] Gusella F. Effect of the plastic rotation randomness on the moment redistribution in reinforced concrete structures. Engineering Structures 2022;252:113652.
[121] Jiang F, Ding Y, Song Y, Geng F, Wang Z. Digital Twin-driven framework for fatigue life prediction of steel bridges using a probabilistic multiscale model: Application to segmental orthotropic steel deck specimen. Engineering Structures 2021;241:112461.
[122] Lantsoght EOL, van der Veen C, de Boer A, Hordijk DA. Probabilistic prediction of the failure mode of the Ruytenschildt Bridge. Engineering Structures 2016;127:549-58.
[123] Chuang W-C, Spence SM. Probabilistic performance assessment of inelastic wind excited structures within the setting of distributed plasticity. Struct Saf 2020;84:101923.
[124] Thomos GC, Trezos CG. Examination of the probabilistic response of reinforced concrete structures under static non-linear analysis. Engineering Structures 2006;28:120-33.
[125] Ayyub BM, Mccuen RH. Simulation-based reliability methods. Probabilistic structural mechanics handbook: Springer; 1995. p. 53-69.
[126] Engelund S, Rackwitz R. A benchmark study on importance sampling techniques in structural reliability. Struct Saf 1993;12:255-76.
[127] Harbitz A. An efficient sampling method for probability of failure calculation. Struct Saf 1986;3:109-15.

[128] Millwater H, Ocampo J, Crosby N. Probabilistic methods for risk assessment of airframe digital twin structures. Engineering Fracture Mechanics 2019;221:106674.
[129] Franchini A, Sebastian W, D'Ayala D. Surrogate-based fragility analysis and probabilistic optimisation of cable-stayed bridges subject to seismic loads. Engineering Structures 2022;256:113949.
[130] Halfpenny A, Chabod A, Czapski P, Aldred J, Munson K, Bonato M. Probabilistic Fatigue and Reliability Simulation. Procedia Structural Integrity 2019;19:150-67.
[131] Shi X, Teixeira AP, Zhang J, Guedes Soares C. Structural reliability analysis based on probabilistic response modelling using the Maximum Entropy Method. Engineering Structures 2014;70:106-16.
[132] Wong SM, Hobbs RE, Onof C. An adaptive response surface method for reliability analysis of structures with multiple loading sequences. Struct Saf 2005;27:287-308.
[133] Siemaszko A. Computational Methods for Shakedown and Limit Reliability Analysis. Inelastic Behaviour of Structures under Variable Repeated Loads: Springer; 2002. p. 345-59.
[134] Javidan MM, Kang H, Isobe D, Kim J. Computationally efficient framework for probabilistic collapse analysis of structures under extreme actions. Engineering Structures 2018;172:440-52.
[135] Hurtado JE, Alvarez DA. Neural-network-based reliability analysis: a comparative study. Comput Method Appl M 2001;191:113-32.
[136] Vlaicu D. Shakedown Analysis of Axisymmetric Nozzles Under Primary and Secondary Cyclic Loads. ASMEDC.
[137] Koeppe A, Bamer F, Markert B. An efficient Monte Carlo strategy for elasto-plastic structures based on recurrent neural networks. Acta Mechanica 2019;230:3279-93.
[138] Papadrakakis M, Papadopoulos V, Lagaros ND. Structural reliability analyis of elastic-plastic structures using neural networks and Monte Carlo simulation. Comput Method Appl M 1996;136:145-63.
[139] Papadrakakis M, Lagaros ND. Reliability-based structural optimization using neural networks and Monte Carlo simulation. Comput Method Appl M 2002;191:3491-507.
[140] Wang Q, Li Q, Wu D, Yu Y, Tin-Loi F, Ma J, et al. Machine learning aided static structural reliability analysis for functionally graded frame structures. Applied Mathematical Modelling 2020;78:792-815.
[141] Maier HR, Lence BJ, Tolson BA, Foschi RO. First-order reliability method for estimating reliability, vulnerability, and resilience. Water Resources Research 2001;37:779-90.
[142] Ning L, Jiashou Z. Reliability of elasto-plastic structure using finite element method. Acta Mechanica Sinica 2002;18:66-81.
[143] Augusti G, Baratta A, Casciati F. Probabilistic methods in structural engineering: CRC Press; 1984.
[144] Chou K, Galambos T. Reliability consideration in shakedown analysis. Proceedings of the 6th ASCE Specialty Conference on Probabilistic Mechanics, and Structural and Geotechnical Reliability: Publ by ASCE; 1992. p. 204-7.
[145] Marti K. Limit load and shakedown analysis of plastic structures under stochastic uncertainty. Comput Method Appl M 2008;198:42-51.
[146] Heitzer M, Staat M. Structural reliability analysis of elasto-plastic structures. Safety and Reliability AA Balkema, Rotterdam, Brookfield 1999;513:518.
[147] Staat M, Heitzer M. Part VII Probabilistic limit and shakedown problems. Numerical methods for limit and shakedown analysis 2003:217.
[148] Staat M. Limit and shakedown analysis under uncertainty. Int J Comp Meth-Sing 2014;11:1343008.
[149] Trần TN. Limit and shakedown analysis of plates and shells including uncertainties. 2008.
[150] Trần T, Phạm P, Vũ Đ, Staat M. Reliability analysis of inelastic shell structures under variable loads. Limit States of Materials and Structures: Springer; 2009. p. 135-56.

[151] Tran TN, Kreissig R, Staat M. Probabilistic limit and shakedown analysis of thin plates and shells. Struct Saf 2009;31:1-18.
[152] Trân TN, Staat M. An edge-based smoothed finite element method for primal-dual shakedown analysis of structures under uncertainties. Limit state of materials and structures: Springer; 2013. p. 89-102.
[153] Tran N, Tran TN, Matthies H, Stavroulakis G, Staat M. Shakedown analysis under stochastic uncertainty by chance constrained programming. Advances in Direct Methods for Materials and Structures: Springer; 2018. p. 85-103.
[154] Trần TN, Staat M. Uncertainty multimode failure and shakedown analysis of shells. Direct methods for limit and shakedown analysis of structures: Springer; 2015. p. 279-98.
[155] Liu Y, Zhang H, Liu Y, Deng Y, Jiang N, Lu N. Fatigue reliability assessment for orthotropic steel deck details under traffic flow and temperature loading. Engineering failure analysis 2017;71:179-94.
[156] Varelis GE, Karamanos SA, Gresnigt AM. Pipe Elbows Under Strong Cyclic Loading. Journal of Pressure Vessel Technology 2012;135.
[157] Takahashi K, Watanabe S, Ando K, Urabe Y, Hidaka A, Hisatsune M, et al. Low cycle fatigue behaviors of elbow pipe with local wall thinning. Nucl Eng Des 2009;239:2719-27.
[158] Moslemi N, Mozafari F, Abdi B, Gohari S, Redzuan N, Burvill C, et al. Uniaxial and biaxial ratcheting behavior of pressurized AISI 316L pipe under cyclic loading: Experiment and simulation. International Journal of Mechanical Sciences 2020;179:105693.
[159] Chen X, Chen X, Yu D, Gao B. Recent progresses in experimental investigation and finite element analysis of ratcheting in pressurized piping. International Journal of Pressure Vessels and Piping 2013;101:113-42.
[160] Hassan T, Rahman M, Bari S. Low-Cycle Fatigue and Ratcheting Responses of Elbow Piping Components. Journal of Pressure Vessel Technology 2015;137.
[161] Paul SK. A critical review of experimental aspects in ratcheting fatigue: microstructure to specimen to component. Journal of Materials Research and Technology 2019;8:4894-914.
[162] Takahashi K, Tsunoi S, Hara T, Ueno T, Mikami A, Takada H, et al. Experimental study of low-cycle fatigue of pipe elbows with local wall thinning and life estimation using finite element analysis. International Journal of Pressure Vessels and Piping 2010;87:211-9.
[163] Zheng X, Chen H, Ma Z, Xuan F. A novel fatigue assessment approach by Direct Steady Cycle Analysis (DSCA) considering the temperature-dependent strain hardening effect. International Journal of Pressure Vessels and Piping 2019;170:66-72.
[164] Chen H. Linear matching method for design limits in plasticity. Computers, Materials and Continua-Tech Science Press 2010;20:159-83.
[165] Hassan T, Rahman M. Constitutive Models in Simulating Low-Cycle Fatigue and Ratcheting Responses of Elbow. Journal of Pressure Vessel Technology 2015;137.
[166] Hassan T, Rahman SM. Simulation of Ratcheting Responses of Elbow Piping Components. ASME 2009 Pressure Vessels and Piping Conference2009. p. 103-8.
[167] Liu C, Yu D, Akram W, Cai Y, Chen X. Ratcheting behavior of pressurized elbow pipe at intrados under different loading paths. Thin-Walled Structures 2019;138:293-301.
[168] Foroutan M, Ahmadzadeh GR, Varvani-Farahani A. Axial and hoop ratcheting assessment in pressurized steel elbow pipes subjected to bending cycles. Thin-Walled Structures 2018;123:317-23.
[169] Cho N-K, Chen H. Shakedown, ratchet, and limit analyses of 90° back-to-back pipe bends under cyclic in-plane opening bending and steady internal pressure. European Journal of Mechanics - A/Solids 2018;67:231-42.
[170] Zhu S-P, Huang H-Z, Smith R, Ontiveros V, He L-P, Modarres M. Bayesian framework for probabilistic low cycle fatigue life prediction and uncertainty modeling of aircraft turbine disk alloys. Probabilistic Engineering Mechanics 2013;34:114-22.

[171] Avrithi K, Ayyub BM. A Reliability-Based Approach for Low-Cycle Fatigue Design of Class 2 and 3 Nuclear Piping. Journal of Pressure Vessel Technology 2010;132.
[172] Mishra J, Balasubramaniyan V. Evaluation of Implicit Reliability Level Associated with Fatigue Design Criteria of Nuclear Class-1 Piping. Springer Singapore; 2018. p. 335-50.
[173] Liao M, Shi G, Xiong Y. Analytical methodology for predicting fatigue life distribution of fuselage splices. Int J Fatigue 2001;23:177-85.
[174] Zhang Z, Qiu Z. Fatigue reliability analysis for structures with hybrid uncertainties combining quadratic response surface and polynomial chaos expansion. Int J Fatigue 2021;144:106071.
[175] Jimenez-Martinez M, Alfaro-Ponce M. Fatigue damage effect approach by artificial neural network. Int J Fatigue 2019;124:42-7.
[176] Durodola JF, Ramachandra S, Gerguri S, Fellows NA. Artificial neural network for random fatigue loading analysis including the effect of mean stress. Int J Fatigue 2018;111:321-32.
[177] Li X, Zhang Y, Abbassi R, Khan F, Chen G. Probabilistic fatigue failure assessment of free spanning subsea pipeline using dynamic Bayesian network. Ocean Engineering 2021;234:109323.
[178] Figueira Pujol JC, Andrade Pinto JM. A neural network approach to fatigue life prediction. Int J Fatigue 2011;33:313-22.
[179] Ma X, He X, Tu ZC. Prediction of fatigue–crack growth with neural network-based increment learning scheme. Engineering Fracture Mechanics 2021;241:107402.
[180] Mortazavi SNS, Ince A. An artificial neural network modeling approach for short and long fatigue crack propagation. Computational Materials Science 2020;185:109962.
[181] Hamedi M, Salleh S-H, Astaraki M, Noor A. EMG-based facial gesture recognition through versatile elliptic basis function neural network. BioMedical Engineering OnLine 2013;12:73.
[182] Xia C, Zhou L, Zhang Y, Wu L. Application of EBF Based Generalized Dynamic Fuzzy Neural Networks to Model Weather Impacts on Electrical Load Forecasting. Springer International Publishing; 2021. p. 1280-7.
[183] Wang X, Yang J, Chen H, Ma Z, Xuan F. Effect of constraint on cyclic plastic behaviours of cracked bodies and the establishment of unified constraint correlation. European Journal of Mechanics-A/Solids 2023;97:104857.
[184] Xiang K-L, Xiang P-Y, Wu Y-P. Prediction of the fatigue life of natural rubber composites by artificial neural network approaches. Materials & Design 2014;57:180-5.
[185] Jing L, Ping-Chen Z, Yun-Ni J. Fault diagnosis of power transformer based on ellipsoidal basis functional neural network. 2007 International Conference on Wavelet Analysis and Pattern Recognition2007. p. 695-8.
[186] Markou M, Singh S. Novelty detection: a review—part 2:: neural network based approaches. Signal Processing 2003;83:2499-521.
[187] Griffiths GW, Płociniczak Ł, Schiesser WE. Analysis of cornea curvature using radial basis functions – Part I: Methodology. Computers in Biology and Medicine 2016;77:274-84.
[188] Al-Mangour B, Vo P, Mongrain R, Irissou E, Yue S. Effect of Heat Treatment on the Microstructure and Mechanical Properties of Stainless Steel 316L Coatings Produced by Cold Spray for Biomedical Applications. Journal of Thermal Spray Technology 2014;23:641-52.
[189] Vojdani A, Farrahi GH, Mehmanparast A, Wang B. Probabilistic assessment of creep-fatigue crack propagation in austenitic stainless steel cracked plates. Engineering Fracture Mechanics 2018;200:50-63.
[190] Zhu S-P, Liu Q, Peng W, Zhang X-C. Computational-experimental approaches for fatigue reliability assessment of turbine bladed disks. International Journal of Mechanical Sciences 2018;142-143:502-17.
[191] Shabani MM, Shabani H, Goudarzi N, Taravati R. Probabilistic modelling of free spanning pipelines considering multiple failure modes. Engineering Failure Analysis 2019;106:104169.
[192] Vojdani A, Farrahi GH. Reliability assessment of cracked pipes subjected to creep-fatigue loading. Theoretical and Applied Fracture Mechanics 2019;104:102333.

[193] Mao H, Mahadevan S. Reliability analysis of creep–fatigue failure. Int J Fatigue 2000;22:789-97.
[194] Chavoshi SZ, Bradford R, Booker J. A validated approach for probabilistic structural integrity design code implementation. Engineering Fracture Mechanics 2021;257:108028.
[195] Hu D, Ma Q, Shang L, Gao Y, Wang R. Creep-fatigue behavior of turbine disc of superalloy GH720Li at 650℃ and probabilistic creep-fatigue modeling. Materials Science and Engineering: A 2016;670:17-25.
[196] Zhan Z, Li H. A novel approach based on the elastoplastic fatigue damage and machine learning models for life prediction of aerospace alloy parts fabricated by additive manufacturing. Int J Fatigue 2021;145:106089.
[197] Liu Z, Mavris D. A methodology for probabilistic creep-fatigue life assessment of hot gas path components. 45th AIAA/ASME/ASCE/AHS/ASC Structures, Structural Dynamics & Materials Conference2004. p. 1990.
[198] Song L-K, Bai G-C, Fei C-W. Dynamic surrogate modeling approach for probabilistic creep-fatigue life evaluation of turbine disks. Aerospace Science and Technology 2019;95:105439.
[199] Deng K, Song L-K, Bai G-C, Li X-Q. Improved Kriging-based hierarchical collaborative approach for multi-failure dependent reliability assessment. Int J Fatigue 2022;160:106842.
[200] Zhang X-C, Gong J-G, Xuan F-Z. A physics-informed neural network for creep-fatigue life prediction of components at elevated temperatures. Engineering Fracture Mechanics 2021;258:108130.
[201] Bartošák M. Using machine learning to predict lifetime under isothermal low-cycle fatigue and thermo-mechanical fatigue loading. Int J Fatigue 2022;163:107067.
[202] Gu H-H, Wang R-Z, Zhu S-P, Wang X-W, Wang D-M, Zhang G-D, et al. Machine learning assisted probabilistic creep-fatigue damage assessment. Int J Fatigue 2022;156:106677.
[203] Wang R-Z, Gu H-H, Zhu S-P, Li K-S, Wang J, Wang X-W, et al. A data-driven roadmap for creep-fatigue reliability assessment and its implementation in low-pressure turbine disk at elevated temperatures. Reliability Engineering & System Safety 2022;225:108523.
[204] Wang R, Liu X, Hu D, Meng F, Li D, Li B. Zone-based reliability analysis on fatigue life of GH720Li turbine disk concerning uncertainty quantification. Aerospace Science and Technology 2017;70:300-9.
[205] Shen H, Lin J, Mu E. Probabilistic model on stochastic fatigue damage. Int J Fatigue 2000;22:569-72.
[206] Wang X, Ma Z, Chen H, Liu Y, Shi D, Yang J. Creep rupture limit analysis for engineering structures under high-temperature conditions. International Journal of Pressure Vessels and Piping 2022;199:104763.
[207] Sato I, Suzuki K. Manufacturing and material properties of forgings for the reactor pressure vessel of the high temperature engineering test reactor. Nucl Eng Des 1997;171:45-56.
[208] Felemban B. Application of Multiaxial Cyclic Loading for Constitutive Model and Parameter Determination of Steels. 2017.

Appendix A: The calculation process of creep strain rate by the Omega model

The creep strain rate needed by the Omega model is able to be calculated through the equations as follows when implementing the creep simulation by coding the ABAQUS user subroutine. Firstly, in a calculation increment, the original creep rate, $\dot{\varepsilon}_{oc}$, in equation (A-1) is determined by the non-linear creep FEA procedure to produce the results of stress components in Equation (A-3).

$$log_{10}\dot{\varepsilon}_{oc} = -\left\{A_0 + \left(\frac{A_1 + A_2 S_l + A_3 S_l^2 + A_4 S_l^3}{273 + T}\right)\right\} \tag{A-1}$$

$$S_l = log_{10}(\sigma_e) \tag{A-2}$$

$$\sigma_e = \frac{1}{\sqrt{2}}[(\sigma_1 - \sigma_2)^2 + (\sigma_1 - \sigma_3)^2 + (\sigma_2 - \sigma_3)^2]^{0.5} \tag{A-3}$$

Next, the creep damage rate, $\dot{D}_c$, defined in equation (A-5) is dependent on the Omega parameter, Ω_m, which is given out through Equations (A-6) to (A-11). Here A_i and B_i $(i = 1,2,3,4)$ are creep data of strain rate parameters and Omega parameters of 2.25Cr-1Mo-V, and p refers to the hydrostatic stress.

$$D_C = \int_0^t \dot{D}_c dt \leq 1.0 \tag{A-4}$$

$$\dot{D}_c = \Omega_m \dot{\varepsilon}_{oc} \tag{A-5}$$

$$\Omega_m = \Omega_n^{\delta+1} \tag{A-6}$$

$$\Omega_n = max[(\Omega - n),\ 3.0] \tag{A-7}$$

$$log_{10}\ \Omega = B_0 + \left(\frac{B_1 + B_2 S_l + B_3 S_l^2 + B_4 S_l^3}{273 + T}\right) \tag{A-8}$$

$$n = -\left(\frac{A_2 + 2A_3 S_l + 3A_4 S_l^2}{460 + T}\right) \tag{A-9}$$

$$\delta = \beta\left(\frac{3p}{\sigma_e} - 1.0\right) \tag{A-10}$$

$$p = \frac{\sigma_1 + \sigma_2 + \sigma_3}{3} \tag{A-11}$$

Then in this analysis increment, the net increment of creep damage, D_C, is obtained by integrating the creep damage rate over a time increment, and finally, the creep strain rate is provided to compute the creep strain increment.

Appendix B: Configuration of the data-driven LMM analysis procedure in the Isight platform

The data-driven LMM analysis procedure in Isight contains three elements. Firstly, the Data Exchanger tool is utilized to recognize the LMM analysis script which is written by Python, with the input variables pointed out (shown in Fig. B1).

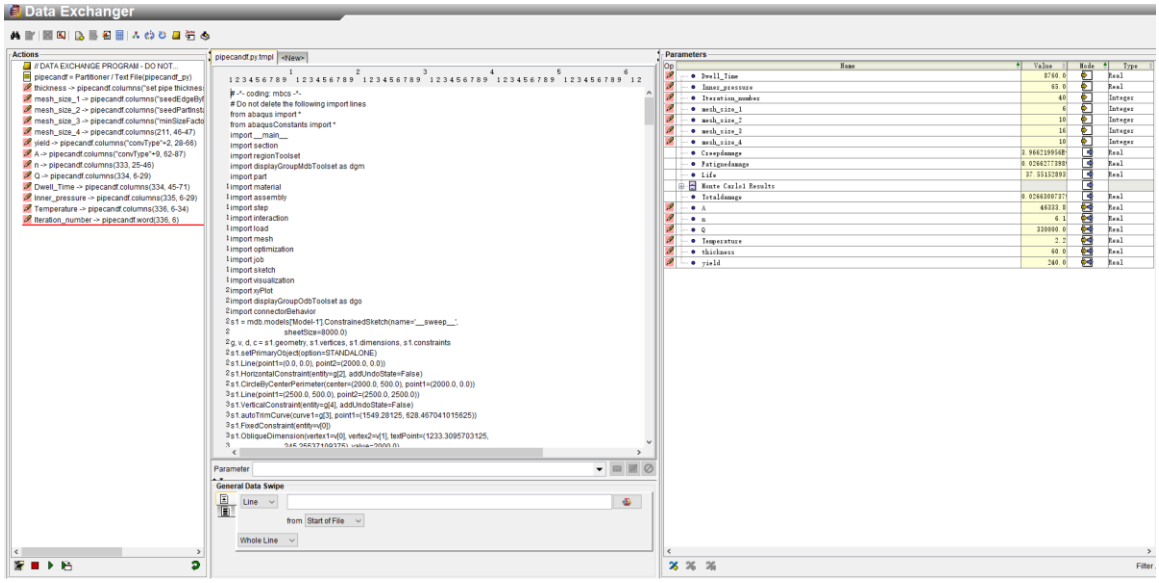

Fig. B1. Configuration of the input variables by Data Exchanger tool

The updated analysis script (by the Data Exchange tool) is then passed into the OS Command component, where the commands to call the ABAQUS program are compiled in Fig. B2.

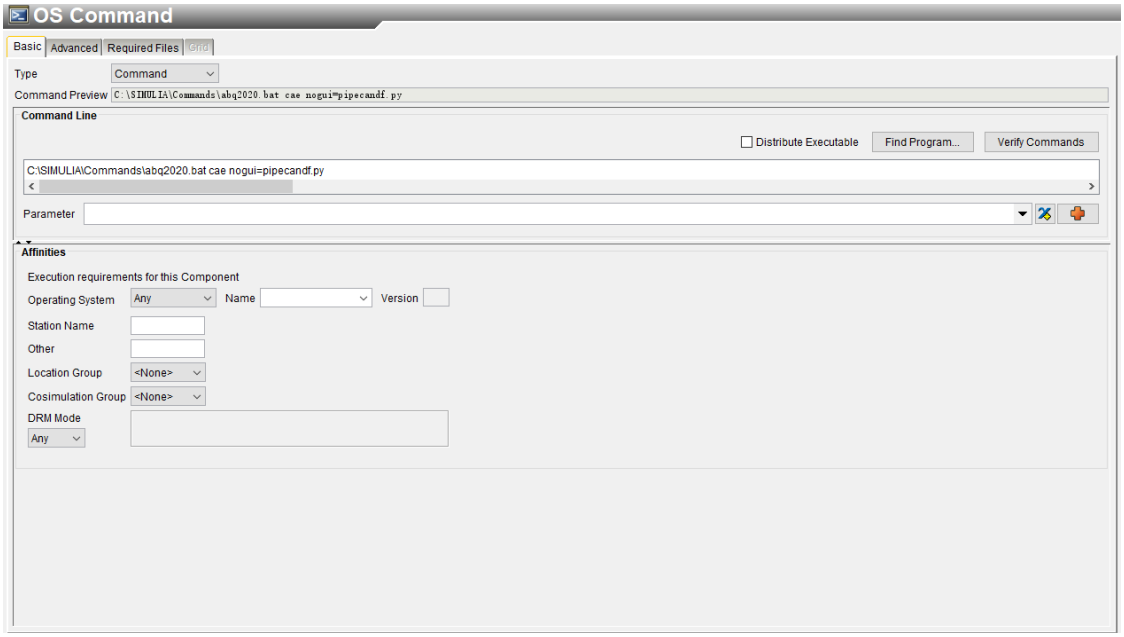

Fig. B2. Setup of the command to launch the ABAQUS program by OS Commond tool

The last step is to use the Data Exchanger tool to mark the output variables that are generated by the LMM analysis procedure. For instance, in Fig. B3 below, the creep damage, fatigue damage, creep-fatigue damage and creep-fatigue life are written into the text file after the LMM analysis and then passed into the Data Exchanger tool, with the output variables highlighted in green colour.

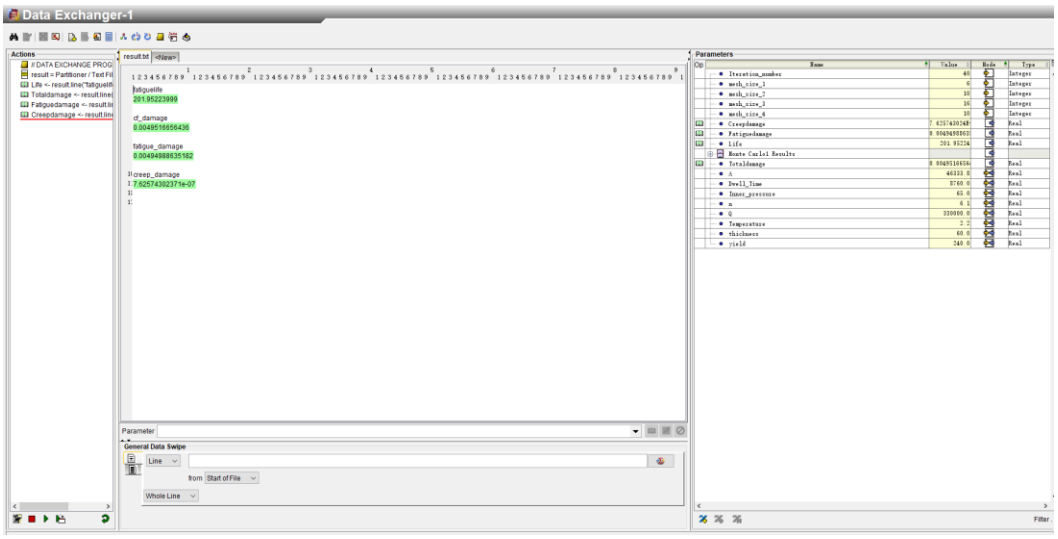

Fig. B3. Configuration of the output variables by Data Exchanger tool

Fig.

Appendix C: Configuration of the data-driven surrogate model by Isight

The data-driven surrogate model is established by adopting the Isight software, and the setup process is described below. The first step is to identify the input and output variables, which is displayed in Fig. C1.

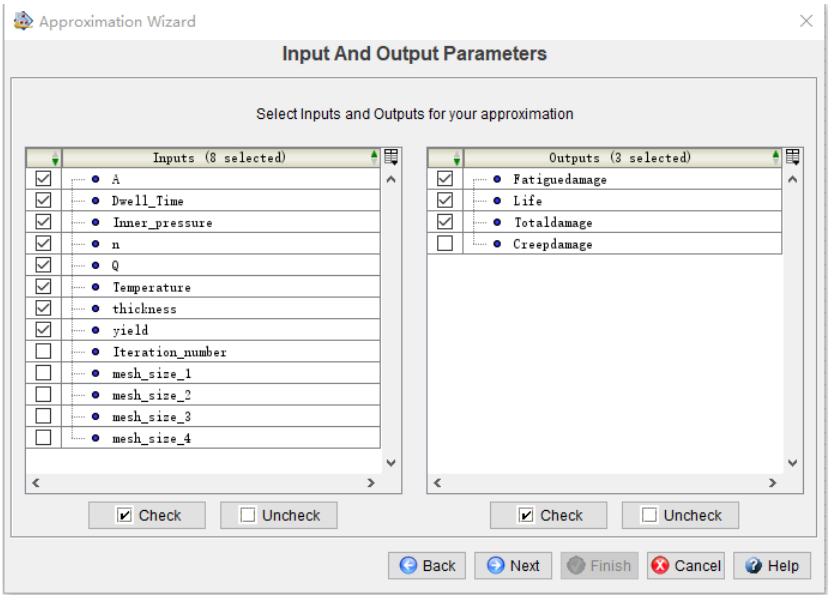

Fig. C1. Identification of input and output variables.

Next, the sampling approach and the amount of training data points are defined in Fig. C2.

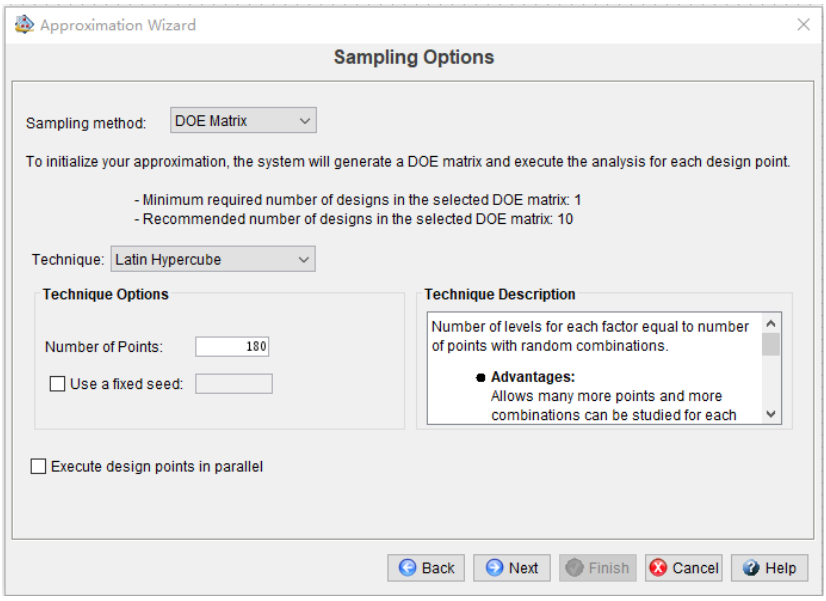

Fig. C2. Setup of sampling approach and amount of training data point

Before launching the training process, the lower bound and upper bound of the input parameters are given out in Fig. C3.

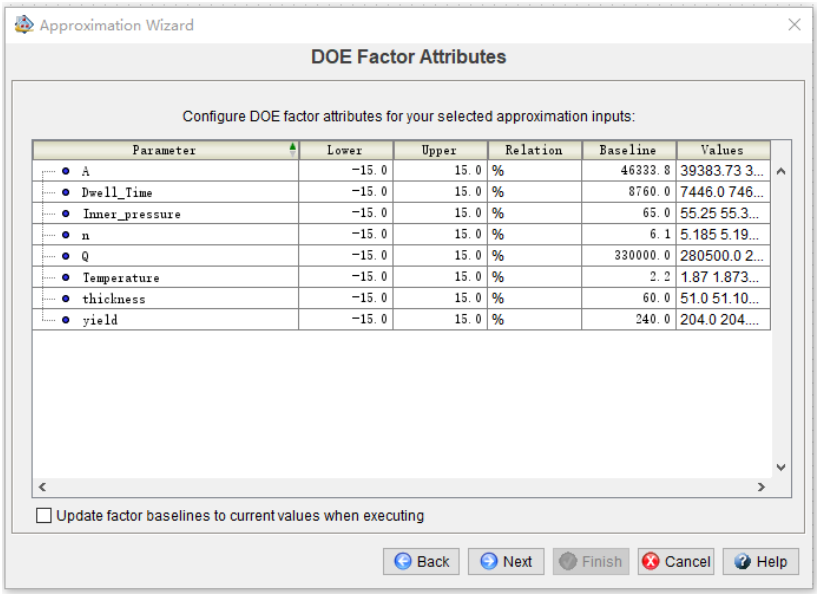

Fig. C3. Configuration of the lower bound and upper bound of the input parameters.

Finally, the error analysis method should be selected in Fig. C4, which is then implemented to validate the accuracy of the trained surrogate model.

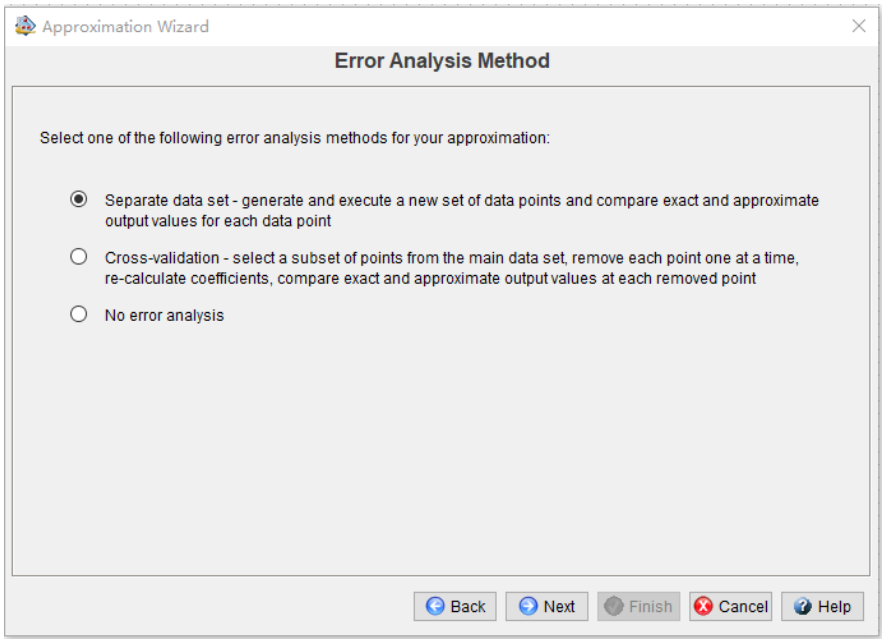

Fig. C4. Selection of the error analysis method

Appendix D: Configuration of the probabilistic analysis by Isight

The configuration of the probabilistic analysis by Isight is displayed in Fig. D1 below.

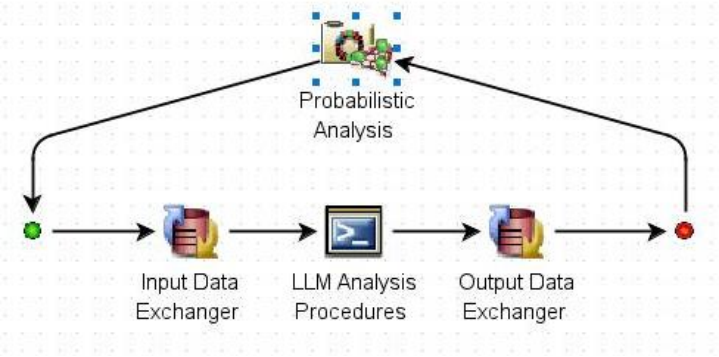

Fig. D1. Configuration of the probabilistic analysis by Isight

In the MCS controller, the sampling method, simulation numbers and the convergence tolerance are assigned firstly, which are exhibited in Fig. D2.

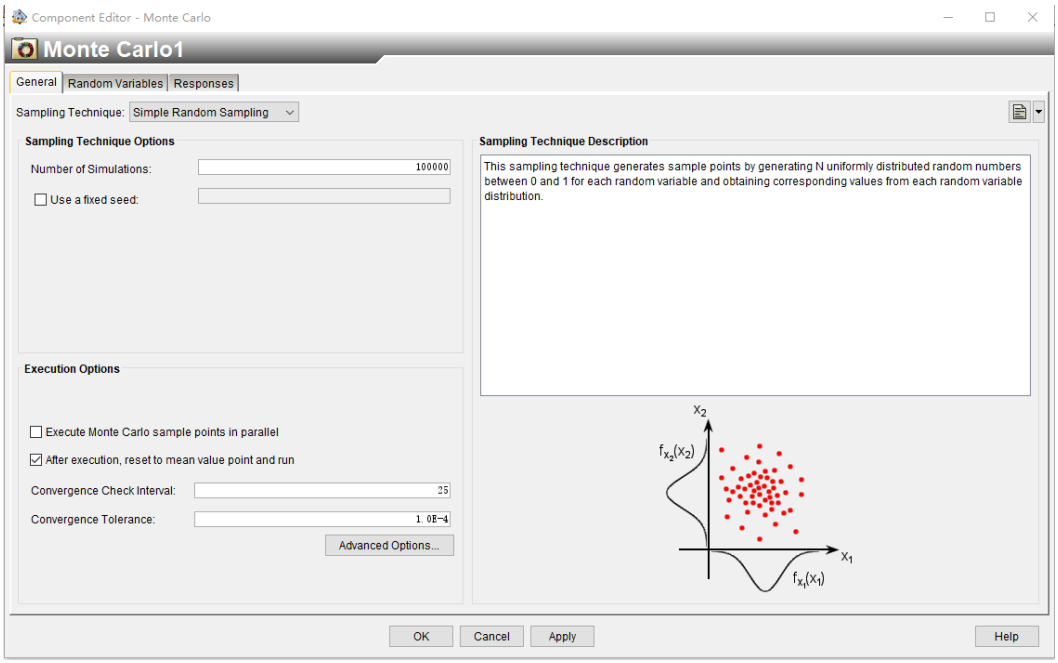

Fig. D2. Setup of the sampling method, simulation numbers and the convergence tolerance in MCS

Then, the statistic information of each random variable is predefined, including the distribution type, mean, standard deviation, as shown in Fig. D3.

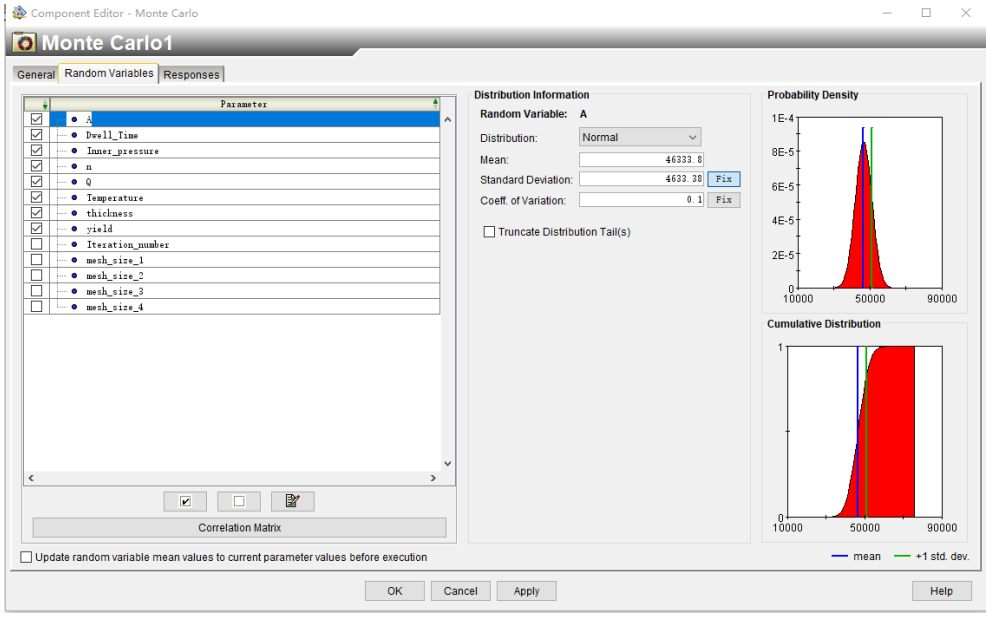

Fig. D3. Setup of the statistic information of random variables

Before performing the probabilistic analysis, the response variables are defined by Fig. D4.

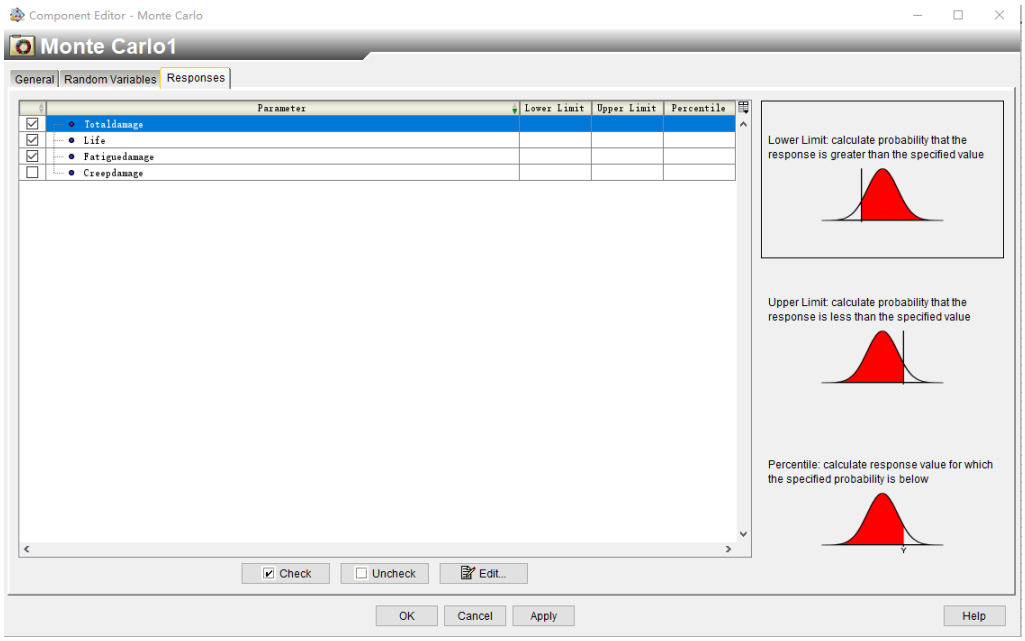

Fig. D4. Configuration of the response variables

Appendix E: Configuration of the reliability analysis by Isight

The configuration of reliability analysis by Isight is shown in Fig. E1, where the limit value of the key response is defined in terms of the adopted limit state function.